FABRICATION OF SURFACE MICRO- AND NANOSTRUCTURES FOR SUPERHYDROPHOBIC SURFACES IN ELECTRIC AND ELECTRONIC APPLICATIONS

A Thesis
Presented to
The Academic Faculty

by

Yonghao Xiu

In Partial Fulfillment
of the Requirements for the Degree
Doctor of Philosophy in the
School of Chemical and Biomolecular Engineering

Georgia Institute of Technology
December, 2008

FABRICATION OF SURFACE MICRO- AND NANOSTRUCTURES FOR SUPERHYDROPHOBIC SURFACES IN ELECTRIC AND ELECTRONIC APPLICATIONS

Approved by:

Dr. C. P. Wong, Advisor
School of Materials Science and Engineering
Georgia Institute of Technology

Dr. Dennis W. Hess, Advisor
School of Chemical and Biomolecular Engineering
Georgia Institute of Technology

Dr. William Koros
School of Chemical and Biomolecular Engineering
Georgia Institute of Technology

Dr. Victor Breedveld
School of Chemical and Biomolecular Engineering
Georgia Institute of Technology

Dr. Carson Meredith
School of Chemical and Biomolecular Engineering
Georgia Institute of Technology

Dr. Sankar Nair
School of Chemical and Biomolecular Engineering
Georgia Institute of Technology

Date Approved: October 29, 2008

This work is dedicated to my parents, Yumin Xiu and Wenmei Liang, and my wife, Yan Lu, for their unwavering love, support and kindness.

ACKNOWLEDGEMENTS

First, I would like to express my deepest thanks to my thesis advisors, Prof. C. P. Wong and Prof. Dennis W. Hess, for providing me with many opportunities to develop my professional and technical skills, and the guidance and resources for this research at Georgia Institute of Technology. I also wish to thank my committee members Prof. William Koros, Prof. Victor Breedveld, Prof. Carson Meredith, and Prof. Sankar Nair for their suggestions, feedback, and critique of my work. I thank Mr. Richard Hartlein, Mr. Frank Lambert and Dr. Nigel Hampton from National Electric Energy Testing, Research and Applications Center (NEETRAC) for collaborating on application of superhydrophobic coatings on high voltage insulators. I wish to thank Dr. Rudy Bukovnik from Tyco Electronics, Dr. Joon Han from Dow Chemical, Dr. Bill Taylor from 3M and many more for their helpful discussions and financial support from the companies. I would like to thank Prof. Clifford Henderson and Prof. Martha Grover for kindly allowing the use of AFM. I thank Paul Wissmann for training me on AFM. I would also like to thank Prof. Ajeet Rohatgi and Dr. Vijay Yelundur for their help on the photovoltaic properties and light reflection of textured Si surfaces. I would like to acknowledge my group members in both Prof. Wong and Prof. Hess's research groups for sharing their valuable insights on my research and help on my experiments: Dr. Lingbo Zhu, Dr. Jack K. Moon, Dr. Fei Xiao, Dr. Hai Dong, Dr. Glit Levitin, Dr. Jie Diao, Dr. Qian Luo, Dr. Ashwini Sinha Dr. Prabhakar Tamirisa, Dr. Ingu Song, Dr. Shantanu Pathak, Dr. Zhuqing Zhang, Dr. Jianwen Xu, Dr. Yangyang Sun, Dr. Brian Englert, Dr. Yi Li, Dr. Hongjin Jiang, Dr. Jiongxin Lu, Ms. Guseul Yun, Ms. Jessica

Berger, Mr. Qizhen Liang, Mr. Rongwei Zhang, Mr. Owen Hildreth, Mr. Wei Lin, Ms. Yan Liu, Ms. Anna-Sofia Kivelio, Ms Yiqun Duan, Mr. Balamurali Balu, Mr Ashish Pande, and Ms Fangyu Wu. I also thank Rentian Xiong, Yueming Hua, Reginald Thio, Genggeng Qi, Wei Zhang, Xinzhou Qin, Qingshan Li, Jun Chen and Kuang Zhang for their friendship and support during my stay in Atlanta. Finally, I would like to express my appreciation and deepest affection to my wife Yan Lu for her love and encouragement throughout this research.

This work has been partially supported by NSF and NEETRAC.

TABLE OF CONTENTS

LIST OF TABLES

LIST OF FIGURES

SUMMARY

In our study, the superhydrophobic surface based on biomimetic lotus leave is explored to maintain the desired properties for self-cleaning. Parameters in controlling bead-up and roll-off characteristics of water droplets were investigated on different model surfaces. The governing equations were proposed. Heuristic study is performed. First, the fundamental understanding of the effect of roughness on superhydrophobicity is performed. The effect of hierarchical roughness, i.e., two scale roughness effect on roughness is investigated using systems of 1) monodisperse colloidal silica sphere (submicron) arrays and Au nanoparticle on top and 2) Si micrometer pyramids and Si nanostructures on top from KOH etching and metal assisted etching of Si. The relation between the contact area fraction and water droplet contact angles are derived based on Wenzel and Cassie-Baxter equation for the systems and the two scale effect is explained regarding the synergistic combination of two scales. Previously the microscopic three-phase-contact line is thought to be the key factor in determining contact angles and hysteresises. In our study, Laplace pressure was brought up and related to the three-phase-contact line and taken as a key figure of merit in determining superhydrophobicity. In addition, we are one of the first to study the effect of tapered structures (wall inclination). Combining with a second scale roughness on the tapered structures, stable Cassie state for both water and low surface energy oil may be achieved. This is of great significance for designing both superhydrophobicity and superoleophobicity.

Regarding the origin of contact angle hysteresis, study of superhydrophobicity on micrometer Si pillars was performed. The relation between the interface work of function

and contact angle hysteresis was proposed and derived mathematically based on the Young-Dupré equation. The three-phase-contact line was further related to a secondary scale roughness induced.

Based on our understanding of the roughness effect on superhydrophobicity (both contact angle and hysteresis), structured surfaces from polybutadiene, polyurethane, silica, and Si etc were successfully prepared. For engineering applications of superhydrophobic surfaces, stability issues regarding UV, mechanical robustness and humid environment need to be investigated. Among these factors, UV stability is the first one to be studied. However, most polymer surfaces we prepared failed the purpose. Silica surfaces with excellent UV stability were prepared. This method consists of preparation of rough silica surfaces, thermal treatment and the following surface hydrophobization by fluoroalkyl silane treatment. Fluoroalkyl groups are UV stable and the underlying species are silica which is also UV stable (UV transparent). UV stability on the surface currently is 5,500 h according the standard test method of ASTM D 4329. No degradation on surface superhydrophobicity was observed. New methods for preparing superhydrophobic and transparent silica surfaces were investigated using urea-choline chloride eutectic liquid to generate fine roughness and reduce the cost for preparation of surface structures.

Another possible application for self-cleaning in photovoltaic panels was investigated on Si surfaces by construction of the two-scale rough structures followed by fluoroalkyl silane treatment. Metal (Au) assisted etching was employed to fabricate nanostructures on micrometer pyramid surfaces. The light reflection on the prepared surfaces was investigated. After surface texturing using KOH etching for micrometer pyramids and the following nanostructure using metal assisted etching, surface light reflection reduced to a minimum value which shows that this surface texturing technique is highly promising for improving the photovoltaic efficiency while imparting photovoltaics the self-cleaning feature. This surface is also expected to be UV stable due to the same fluoroalkyl silane used.

Regarding the mechanical robustness, epoxy-silica superhydrophobic surfaces were prepared by O_2 plasma etching to generate enough surface roughness of silica spheres followed by fluoroalkyl silane treatment. A robustness test method was proposed and the test results showed that the surface is among the most robust surfaces for the superhydrophobic surfaces we prepared and currently reported in literature.

CHAPTER 1

INTRODUCTION

1.1 Introduction to superhydrophobicity

Lotus effect or superhydrophobicity was described by Barthlott in 1996[1, 2]. When he studied lotus leaf surfaces, he found that the surface is rough instead of smooth. Combined with hydrophobic surface layers, a superhydrophobic state was observed. Water droplets falling on the surface bead up and roll off the surface instantaneously. Superhydrophobicity requires that both a surface hydrophobic layer and rough surface structures are present. This phenomenon is quite common in the biology arena, e.g., on some insects and plants leaves, shown in Figure 1. Artificial superhydrophobic surfaces were prepared before the phenomenon was widely acknowledged. In 1986, Sacher et al reported that very water repellent films were obtained by depositing hexamethyldisiloxane on silicon chips in a high-energy plasma at low temperature[3]. Drops of water had contact angles as high as 180° and rolled off the slightly inclined surfaces, which suggested a near-zero roll off angle. Morra et al had prepared a superhydrophobic surface by O_2 plasma etching on PTFE surfaces in 1989[4]. Actually after 5 min of treatment, water drops rolled easily across the surface. Due to the absence of hysteresis, no obstacle to their movement occurred. The first super water- and oil-repellent surface was developed in Tsujii's group[5] on anodically oxidized aluminum surface after a hydrophobic treatment.

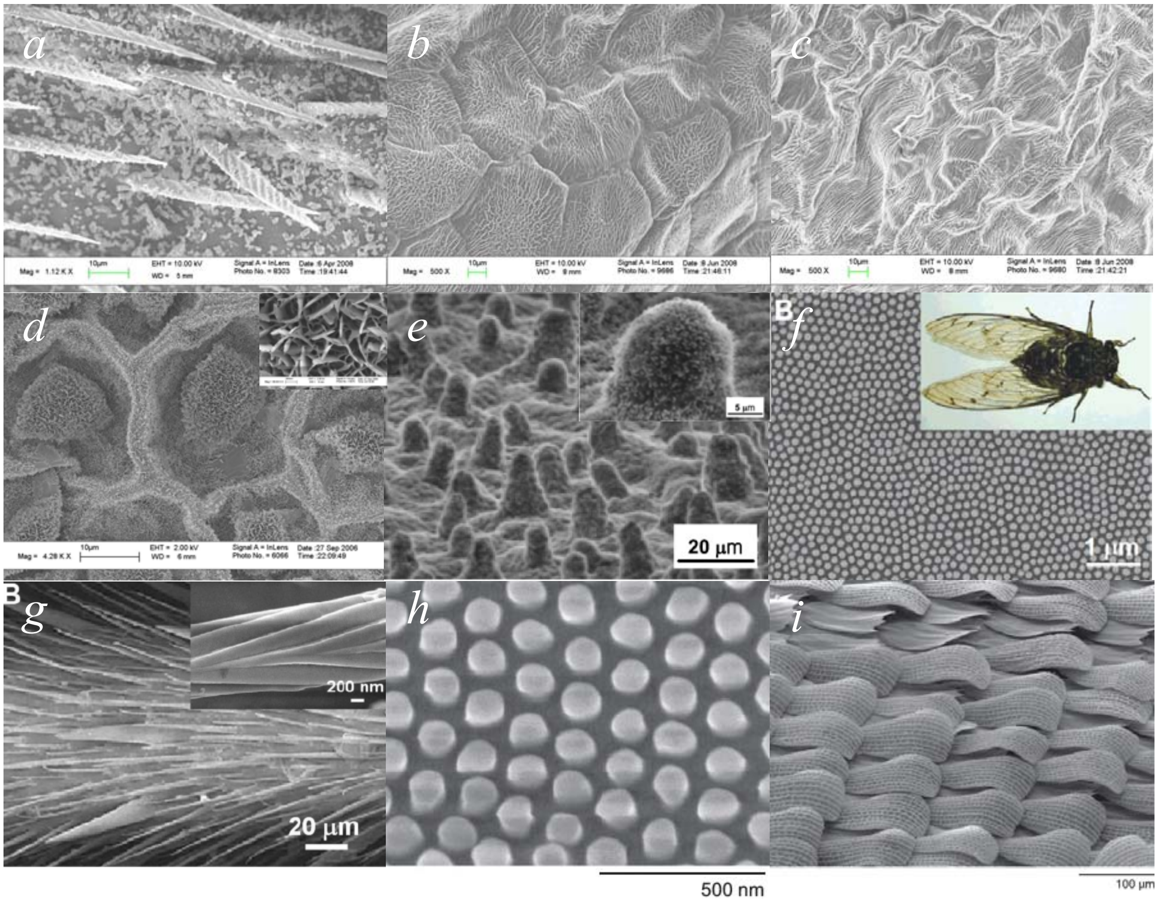

Figure 1. SEM images of different bio-surface structures: (a) Wasp wing, (b)Azaleas petal, (c) rose petal, (d) Colocasia esculenta leaf surface, (e)Micro- and nanostructures on the lotus leaf (Nelumbo nucifera)[6], (f) cicada wing[7], (g) water strider[8], the leg with numerous oriented spindly microsetae, (Inset) Nanoscale groove structure on a seta. (h) surface of mosquito (*culex pipiens*) eye[9], (i) The wings of *Papilio ulysses*; the way the tiles are displayed together with the detail of the texture confer anisotropy to the texture[10].

The effect of roughness on surface wetting is scale-dependent. Besides the surface hydrophobicity, the surface roughness can be more important in achieving dewetting surfaces even without the most hydrophobic materials (e.g., fluorine containing polymers). On flat surfaces oil repellency is difficult to achieve. However, with appropriate surface roughness with special geometry designs, a superoleophobic surface may result. This signifies the importance of surface wetting/dewetting control via flexible, fine-tuned surface structure design at micro and nano scales.

On a flat surface, the change in surface free energy, ΔG, accompanying a small displacement of the liquid such that the change in area of solid covered, ΔA, is

$$\Delta G = \Delta A_{SL}(\gamma_{SL} - \gamma_{SV}) + \Delta A_{LV}\gamma_{LV} \qquad (1)$$

$$\Delta G = \Delta A_{SL}(\gamma_{SL} - \gamma_{SV}) + \Delta A_{SL}\cos(\theta - \Delta\theta)\gamma_{LV} \qquad (2)$$

At equilibrium, $\Delta G = 0$

Therefore when $\Delta\theta$ goes to zero, Young's equation can be derived

$$\gamma_{SL} - \gamma_{SV} + \gamma_{LV}\cos\theta = 0$$

or

$$\cos\theta_Y = \frac{\gamma_{SV} - \gamma_{SL}}{\gamma_{LV}} \qquad (3)$$

On a smooth surface, this equation determines the contact angle of liquid droplets.

On a rough surface, Young's equation no longer holds for the apparent contact angle due to the introduction of a new factor: surface roughness. Water droplet/solid interface contact can be either in Wenzel state or Cassie state (shown in Figure 2), depending on the surface hydrophobicity and geometries of the surface structures.

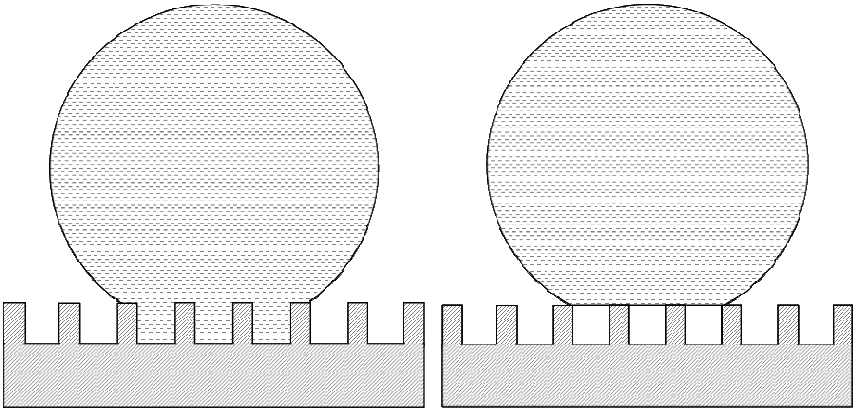

Figure 2. The two contact regimes of water droplet with rough surfaces, (a) Wenzel contact regime, (b) Cassie contact regime.

Usually two equations were used for the calculation of the apparent contact angles corresponding to the two regimes. One is the Wenzel equation as shown in equation (4):

$$\cos\theta_A = r\cos\theta_Y \qquad (4)$$

This equation described the relation between the surface roughness *r* and the apparent contact angle, where *r* is determined by the ratio of total surface area to the projected surface area. This equation is valid for a complete solid/liquid contact interface.

For heterogeneous surfaces, the Cassie equation can be used to describe the heterogeneity effect on the apparent contact angle[11],

$$\cos\theta_A = f\cos\theta_Y + f - 1 \tag{5}$$

where θ_A is the apparent contact angle on the rough surface, f is the projected surface fraction of solid, and θ_Y is the contact angle on a flat surface as per Young's equation.

On a rough surface, surface roughness can be determined by

$$r = \frac{A_{Actual}}{A_{\mathrm{Pr}\,ojected}} \tag{6}$$

The development of the Wenzel and Cassie equations are shown below.

For water droplets on rough surfaces, according to equation 2 and 6,

$$\Delta G = \Delta A_{Actual}(\gamma_{SL} - \gamma_{SV}) + \Delta A_{\mathrm{Pr}\,ojected}\gamma_{LV}\cos(\theta_A - \Delta\theta)$$

When $\Delta\theta$ goes to zero, the equation reduced to

$$r(\gamma_{SL} - \gamma_{SV}) + \gamma_{LV}\cos\theta_A = 0 \tag{7}$$

Therefore,

$$\cos\theta_A = r\frac{\gamma_{SL} - \gamma_{SV}}{\gamma_{LV}} = r\cos\theta_Y$$

The Wenzel equation is thus derived as shown in equation 4[12].

This equation describes the relation between the surface roughness r and the apparent contact angle, where *r* is defined by eq. (6). This equation is valid for complete solid/liquid contact interfaces.

Similarly for the Cassie equation, considering the fraction of solid(*S1*)/air(*S2*) and solid/liquid interface,

$$f_1(\gamma_{S1V} - \gamma_{S1L}) + f_2(\gamma_{S2V} - \gamma_{S2L}) - \gamma_{LV}\cos\theta_A = 0$$

or

$$\gamma_{LV}\cos\theta_A = f_1(\gamma_{S1V}-\gamma_{S1L}) + f_2(\gamma_{S2V}-\gamma_{S2L}) \qquad (8)$$

When *S2* is also air, $\gamma_{S2V} = 0$ and $f_1 + f_2 = 1$, equation (8) reduced to Cassie equation (equation 5)

Specifically, if the micropillar surface is composed of a second scale roughness, then the Cassie equation can be written as[13, 14],

$$\cos\theta_A = rf\cos\theta_Y + f - 1 \qquad (9)$$

where *r* is the Wenzel roughness factor (as shown in equation 6) of the structures at the solid-liquid contact interface, f is f_1 in eq 8 for short.

The Wenzel and Cassie equations describe the relationship between contact angle and surface roughness/solid contact fraction. For contact angle hysteresis, the investigation of mathematical description is still going on. The contact angle hysteresis of superhydrophobic surfaces can be characterized by the roll-off angle which is defined as the tilt angle at which a water droplet sitting on the surface starts to move; it can also be characterized by the contact angle hysteresis which is the difference between the advancing angle and the receding angle when the water droplet starts to move. They are illustrated in Figure 3.

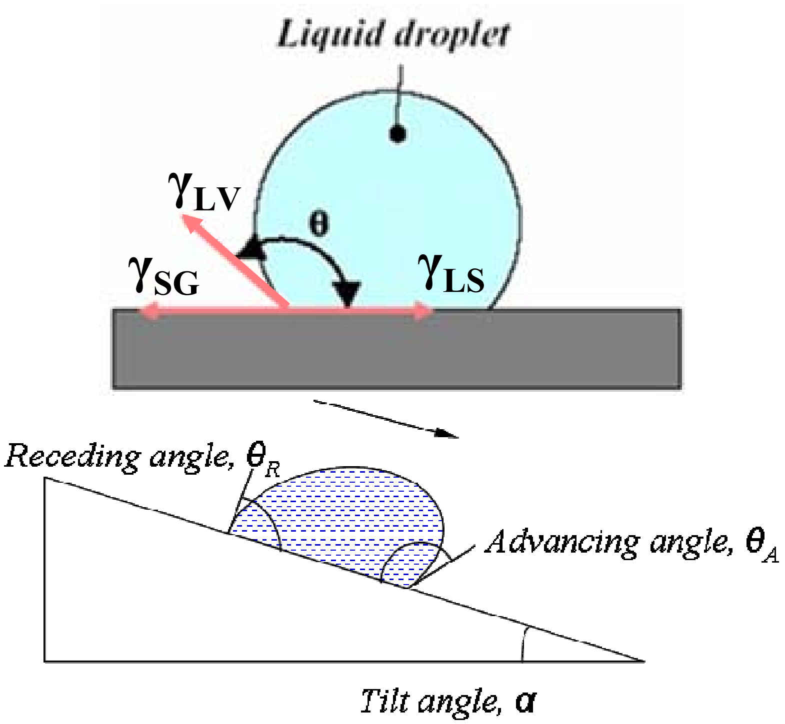

Figure 3. Illustration of the water droplet contact angle, tilt angle and advancing and receding angles.

The relationship between contact angle hysteresis and tilt angle can be illustrated by the following equation:

$$\sin\alpha = \frac{\gamma d(\cos\theta_R - \cos\theta_A)}{mg} \tag{10}$$

where d is the diameter of the moving droplet in the direction that is perpendicular to the droplet movement and m is the mass of the droplet.

To achieve roll-off superhydrophobicity, the contact angle hysteresis must be controlled. Only when the hysteresis is small is the surface self-cleaning.

1.2. Thermodynamics

In order to analyze the contact of the water droplet with the rough surface[15], Patankar gave an excellent discussion. First considering a Cassie drop on a rough substrate with negligible weight, the free energy, G_c, of the drop is represented by

$$G_c = \gamma_{LV} A_s + f_1 A_c(\gamma_{SL} - \gamma_{SV}) + (1 - f_1) A_c \gamma_{LV} \tag{11}$$

According to the Cassie equation, eqn (11) simplifies to

$$G_c = \gamma_{LV} A_s - \gamma_{LV} \cos\theta_c A_c \qquad (12)$$

where A_s is the area of the spherical liquid/air surface and A_c is the projected composite contact area, θ_c is the apparent contact angle on the surface that is in Cassie state.

By considering the volume of the droplet, and substituting appropriate expressions for As and Ac, eq 12 becomes[16]

$$\frac{G_c}{\sqrt[3]{9\pi}V^{2/3}\gamma_{LV}} = (1-\cos\theta_c)^{2/3}(2+\cos\theta_c)^{1/3} \qquad (13)$$

where V is the drop volume.

Similarly, for a Wenzel drop, the free energy G_w, of the drop is[15, 16]

$$G_w = \gamma_{LV} A_s - \gamma_{LV} \cos\theta_w A_w$$

where θ_w is the apparent contact angle on the surface that is in Wenzel state. The left-hand side denotes nondimensional energy. For the Wenzel state, the energy can also be described as eq 13 by replacing θ_c with θ_w. The generalized eq can be written as

$$\frac{G}{\sqrt[3]{9\pi}V^{2/3}\gamma_{LV}} = (1-\cos\theta)^{2/3}(2+\cos\theta)^{1/3} \qquad (14)$$

The equation 14 is then a monotonically increasing function of θ for $0^\circ \le \theta \le 180^\circ$. If $\theta_c > \theta_w$, the Cassie drop will have higher energy than the Wenzel drop. However, this does not necessarily mean that the Cassie state will always transition to the Wenzel state. In the transition from Cassie to Wenzel, the energy change during the process is given by the following eqn. 15 assuming a square pillar patterned surface. In this case, the liquid/vapor interface, initially at the top of the groove, moves down; that is, liquid begins to wet the sides of the pillars as shown in Figure 4.

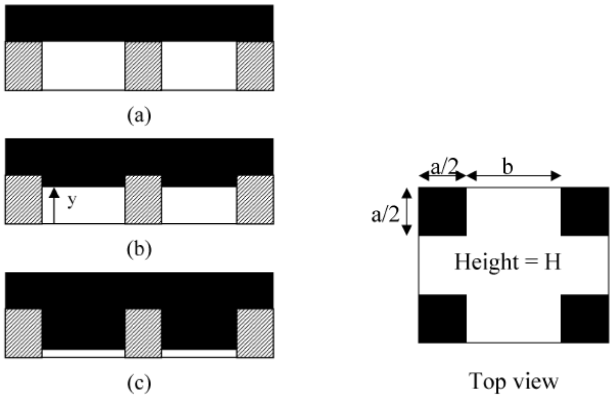

Figure 4. (a) Side view of liquid on top of pillars. The liquid interface is suspended from edge to edge on the pillars; (b) intermediate state in which the liquid enters the valley and therefore represents a transition from a Cassie to a Wenzel state; (c) intermediate state during transition where the liquid has not yet wetted the bottom of the valleys.

The transition is in general a nonequilibrium process where the local contact angle is not necessarily equal to the equilibrium value. The surface energy will change during transition. Assuming that the filling of the grooves occurs below the projected area, A_c, of the Cassie drop, the energy at any intermediate state is given by

$$G(y) = G_c - (1 - \frac{y}{H})(r - 1)\cos\theta_Y \gamma_{LV} A_c \qquad (15)$$

Where y is the location of the interface from the bottom of the groove (Figure 4b) r is the Wenzel roughness factor and $G(y)$ is the drop energy of that state. As the liquid fills the grooves, A_s and A_c should change because some volume is moving out of the spherical liquid cap above the substrate. This in turn should change the energy, G_c, but we will assume these changes to be negligible compared to the surface energy changes (the second term on the right-hand side of eqn (15)) due to the wetting of the grooves. This assumption is justified because the surface area per unit volume is much larger in the grooves compared to the spherical liquid cap. G_c and Ac are therefore assumed constants in eqn (15).

Eqn (15) implies that the energy of the drop at intermediate states is larger that G_c for $\theta_e > 90^\circ$. The maximum value is reached at $y = 0$ when the liquid has filled the grooves but the liquid-solid contact at the bottom of the valley is yet to be formed (Figure 4c). When the liquid wets the bottom of the valley, the corresponding change in energy is given by $-(1 + \cos\theta_e)\,\gamma_{LV}(1 - f)\,A_c$; that is, the energy of the system decreases. The liquid then wets a greater area of the substrate ($A_w > A_c$) and eventually reaches the equilibrium shape of a Wenzel drop at the energy G_w. Since we are assuming that $\theta_c > \theta_w$, we have $G_c > G_w$, as argued above.

The maximum energy state ($G(y)$ at $y = 0$) among all the intermediate states can be used to obtain an estimate of the barrier energy for the transition from Cassie wetting to Wenzel wetting, G_b,

$$G_b = G_c - (r-1)\cos\theta_e \gamma_{LV} A_c \tag{16}$$

Even if the Cassie drop, on a surface roughness established by pillars, is transitioning to a Wenzel state at lower energy, it has to go through a higher intermediate energy state. Hence, energy must be provided to the drop to enable transition. The transition can be enabled, for example, by depositing the drop from some height, by pushing/sliding the drop, or simply due to its own weight.

With respect to hysteresis, a gain factor has been introduced by Mchale et al. to establish a relationship between the contact angle on a flat surface and the contact angle on a rough surface[17]. The model developed did not seek to explain at a microscopic level how contact angle hysteresis arises but simply used the Cassie and Wenzel concepts to predict how a preexisting hysteresis on a flat, smooth material is transformed when a superhydrophobic surface is created from the material. An advantage of their approach is that it may be possible, using a series of liquids with varying contact angles on the flat, smooth surface, to determine experimentally the relationship between Young's contact angle and contact angle on rough surfaces as shown in Figure 5 and 6 and thereby numerically determine the gain factors required to predict changes in contact angle hysteresis.

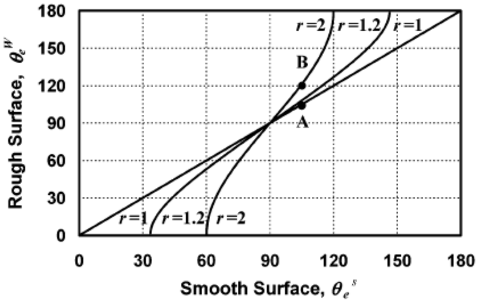

Figure 5. Contact angles predicted by Wenzel's equation for roughness factors of $r = 1$, $r = 1.2$, and $r = 2$. In the $r > 1$ cases, a linear region with a slope greater than 1 occurs close to 90°, surrounded by super-linear regions, which then convert to saturation values of 0° or 180°. An operating point, A, on the $r = 1$ smooth surface becomes an operating point, B, on the $r = 2$ rough surface. [17]

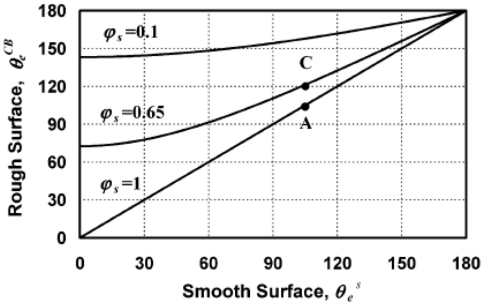

Figure 6. Contact angles predicted by the Cassie-Baxter equation (eq 3) using solid surface fractions of $f = 1$, 0.65, and 0.1. An operating point, A, on the $f = 1$ smooth surface becomes an operating point, C, on the $f = 0.65$ rough surface. [17]

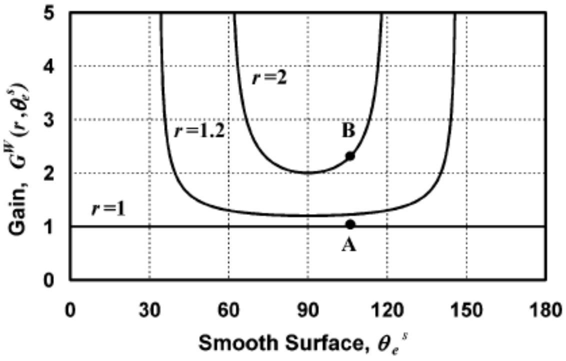

Figure 7. Gain factors, corresponding to curves in Figure 5, determining response of the contact angle on a Wenzel surface to a perturbation of the smooth-surface contact angle. [17]

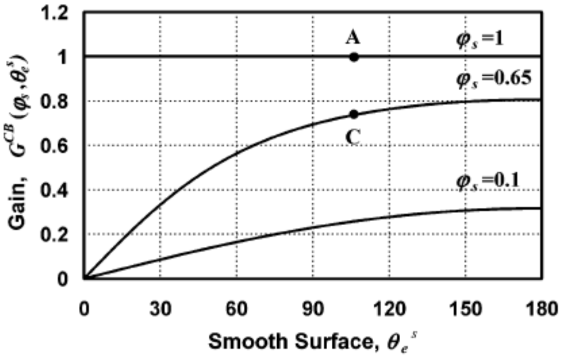

Figure 8. Gain factors, corresponding to curves in Figure 6, predict the response of the contact angle on a Cassie-Baxter surface to a perturbation of the smooth-surface contact angle. [17]

1.3. Low surface energy materials

A variety of materials have been used to prepare superhydrophobic surfaces including both organic and inorganic materials. For polymeric materials, which are generally inherently hydrophobic, fabrication of surface roughness is the primary focus. For inorganic materials, which are generally hydrophilic, a surface hydrophobic treatment must be performed after the surface structures are fabricated.

Most polymeric materials can be used to fabricate superhydrophobic surfaces. For instance, plasma etching has been employed to generate roughness on polymer surfaces to achieve superhydrophobicity; polyethylene has been etched by CF_4/O_2 plasmas to prepare superhydrophobic surfaces[18]; direct catalytic polymerization process for superhydrophobicity[19] etc. In addition, transparent and superhydrophobic surfaces can be achieved such as on poly(ethylene terephthalate) surfaces[20]. Examples of inorganic materials that have been used to create superhydrophobic surfaces are silica, alumina, hepatite, boehmite, titania, and copper etc. which can be roughened to create superhydrophobicity if the roughened surfaces are treated appropriately with a hydrophobic material[21, 22]. For inorganic materials, the top surface should be covered with an organic layer or monolayer for the reduced surface energy.

Low energy materials are particularly important in achieving stable superhydrophobic surfaces; among these materials, fluoropolymer/fluorocarbon is one of the lowest and F-C bonds are one of the most stable bonds. In addition, the bulky F atoms cover well the C atoms beneath the surface (compared to H atoms), thus preventing chemical attack of the weaker C-C bonds. These facts lead to the significant potential of fluorocarbon layers for self-cleaning coatings. Indeed, Teflon has been roughened to produce superhydrophobic surfaces. Short chain fluorocarbon silanes have also been investigated to form monolayers on a rough surface to achieve superhydrophobicity (10 Å thickness is enough to give a hydrophobic layer without any effect of the underlying substrates)[23]. Studies have shown that the surface energy with CF_3 groups is lower than that of CF_2 covered surfaces[24].

Another very important low surface energy material is silicone. The siloxane backbone shows very high bond energy and the side CH_3 gives the low surface energy.

1.4. Structure effect

For superhydrophobic surfaces, surface structure/roughness is essential; geometrical shape is also critical in achieving the desired surface superhydrophobicity. As discussed in section 1.2, Patankar investigated the energy barrier between a Cassie and Wenzel state for surface geometries of inclined structures. He demonstrated that an energy barrier to prevent the transition from a Cassie high energy state to a Wenzel low energy state as shown in Figure 9, may not necessarily be present; that is, the transition may be spontaneous.

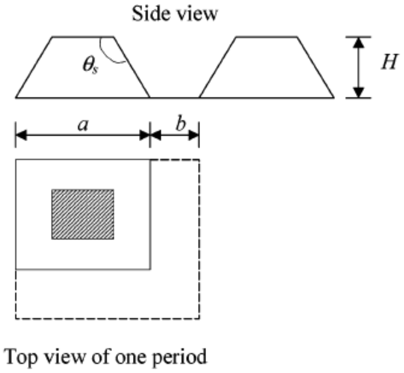

Figure 9. Side and top views of geometrical roughness obtained by periodically placed pillars with inclined side walls.

A Cassie drop will be formed only if a liquid-vapor interface can connect from pillar-to-pillar without touching the valleys. Such an interface can establish equilibrium at the top corners of the pillars only if $\theta_s \leq \theta_e \leq 180^\circ$. For other values of θ_e a Cassie drop is not possible and the valleys will always be filled with liquid.

A pyramidal Si surface represents a good model surface for the investigation of this structure inclination effect. It was shown mathematically that the inclination angle is very important in maintaining the Cassie state. Actually, as the inclination angle θ_s increases, the difficulty in achieving a Cassie superhydrophobic state increases. As predicted, the liquid-vapor interface on the composite surface cannot be maintained and the droplet is always in Wenzel state. However, by implementing a second scale of surface roughness on the pyramid surface, the liquid-vapor interface can be maintained on the pyramid top and a Cassie state can be effectively achieved.

A superoleophobic surface has also been reported by using the structure shown in Figure 10. In order to achieve oil repellency, a reentrant (or overhang) structure design was employed. On this surface, a high contact angle can be achieved even though the surface is hydrophilic ($\theta < 90^\circ$). The reentrant structure was also fabricated in electrospun polymer/POSS composite fibers as shown in Figure 10 and 11.

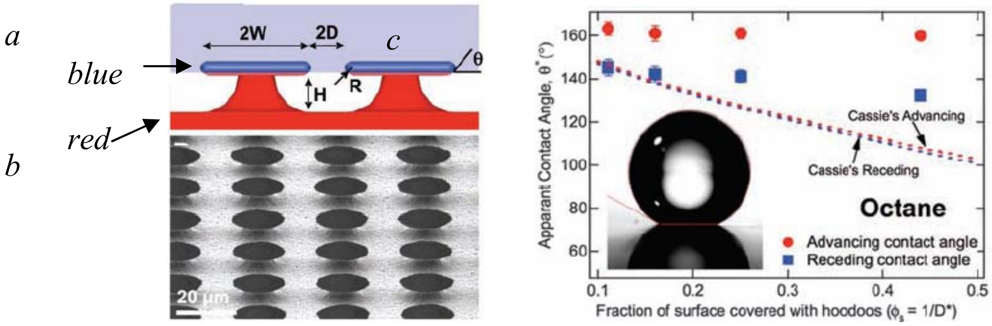

Figure 10. (a) Cartoon highlighting the formation of a composite interface on surfaces with re-entrant topography. The geometric parameters R, D, H, and W characterizing these surfaces are also shown. The blue(top) surface is wetted while the red(bottom) surface remains nonwetted when in contact with a liquid whose equilibrium contact angle is θ_Y (< 90°). (b) SEM micrographs for so-called micro-hoodoo surfaces having circular flat caps. The sample is viewed from an oblique angle of 30°. (c) Contact angles for octane on silanized micro-hoodoos as a function of f (φ_s).[25]

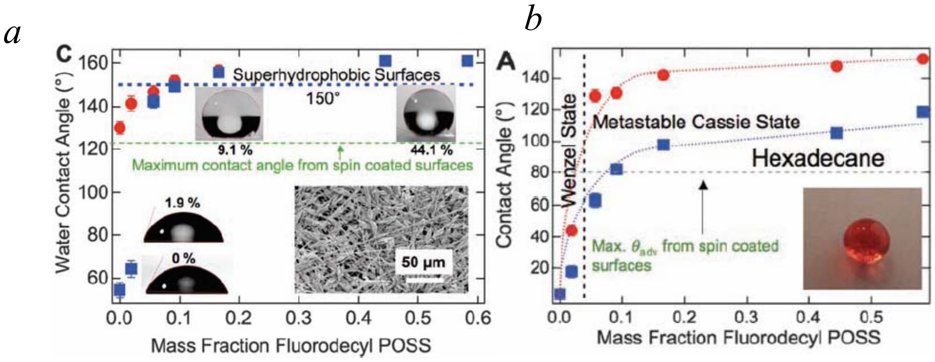

Figure 11. (a) θ_{adv} (red dots) and θ_{rec} (blue squares) for water on electrospun polymer surfaces. The inset shows a SEM micrograph for an electrospun surface containing 9.1 weight % POSS. (b) θ_{adv} (red dots) and θ_{rec} (blue squares) for hexadecane on the electrospun surfaces, the inset of (A) shows a drop of hexadecane (dyed with Red) on a 44 weight % fluorodecyl POSS electrospun surface.

Similar results have also been reported by fabrication of a nanonail structure on Si surfaces using plasma etching techniques[26]. Instead of attempting to guarantee that the Cassie-Baxter state always remains the minimum-energy state, this approach created a system in which the height of the energy barrier that separates the metastable Cassie-Baxter state from the stable Wenzel state is designed to be sufficiently high to achieve effective pinning of the liquid in the desired nonwetting state. The idea is to create a special type of 3D surface topography that normally inhibits transitions from the Cassie-

Baxter state to the Wenzel state but that would allow such transitions under the influence of external stimuli, such as electrical fields. A particular example of such topography is the “nanonail” structure in Figure 12.

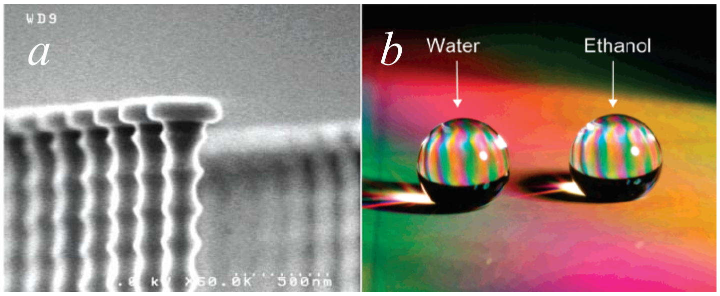

Figure 12. (a) Scanning electron microscopy (SEM) image of 2-µm-pitch nanonails [26]. The nail head diameter D is ~405 nm, the nail head thickness h is ~125 nm, and the nanonail stem diameter d is ~280 nm. (b) A nanonail-covered substrate in action. Droplets of two liquids with the very different surface tensions, 72mN/m (water) and 21.8 mN/m (ethanol), sit next to each other on the 2-µm-pitch nanonail substrate.

Porous Si surfaces from Au assisted electroless etching process have shown the ability to achieve an oil repellent surface[27, 28]. These structures show similar overhang character to that for nanonail structures as shown in Figure 13; droplet contact angles of water and various organic solvents are shown in Figure 14.

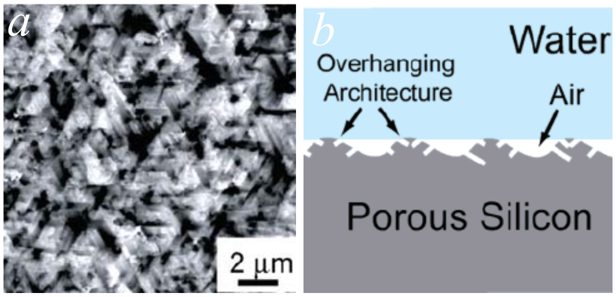

Figure 13. Porous silicon surface fabricated by Au-assisted electroless etching. (a) Top-view SEM image. (b) Schematic cross-sectional profile of water in contact with the porous silicon surface.[27]

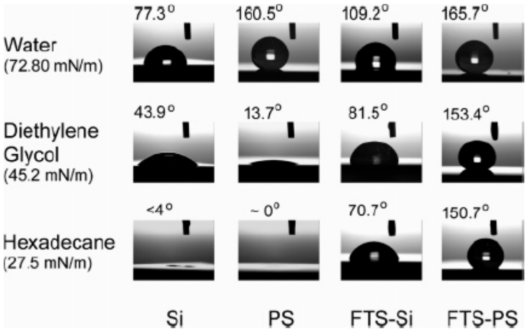

Figure 14. Static contact angles of water, diethylene glycol, and hexadecane on flat silicon (Si), porous silicon (PS) with tilted pores, flat silicon coated with FTS (FTS-Si), and porous silicon with tilted pores coated with FTS (FTS-PS). [27]

Achievement of high contact angles for both polar (water) and nonpolar droplets (e.g., hexadecane) requires the design of surface structures similar to those shown in Figure 14. In order to achieve mechanical stability and optimized hierarchical surface structures for enhanced self-cleaning on superhydrophobic surfaces, it is critical to understand the fundamental surface physics, especially the surface-structure effect on superhydrophobicity to improve control over the surface structures (geometrical shapes, pitch, height, aspect ratio, hierarchical design etc) present. These design criteria can then be used to achieve the requirements necessary for various applications.

As described previously, for surface superhydrophobicity, there are two requirements. The first is high contact angle (>150˚), which relates the contact angle to surface structure (expressed by the Wenzel surface roughness factor *r*) and can be described by the improved Cassie equation[13, 15]. The second parameter is the contact angle hysteresis, which is defined by the difference between the surface advancing contact angle and the surface receding contact angle.

1.5. Approaches to preparing surface structures for superhydrophobicity

Generally methods to prepare structures for superhydrophobic surfaces include 1) preparation of a rough surface by etching of hydrophobic substrates or hydrophilic substrates followed by a surface hydrophobization treatment, or 2) preparation of a rough surface by coating techniques using either hydrophobic materials or hydrophilic materials followed by hydrophobic treatment/coating. The hydrophobic treatment can be accomplished by techniques such as film or molecule deposition, solution coating or self-assembly of hydrophobic layers (e.g., silane coupling agent, thiol).

1.5.1 Etching approaches

1.5.1.1 Lithography techniques

Lithography is a method to transfer patterns from a mask onto a substrate surface or film. Therefore the geometrical surface structure can be designed on masks (generally chromium on glass) and the mask can be employed repeatedly. Generation of structures on a substrate using lithography can be realized by the following steps.[29] In photolithography, a photoactive polymer layer (photoresist) is irradiated through a mask followed by layer development where either the exposed or unexposed polymer is removed selectively, leaving a positive or negative image of the mask on the surface. Photolithography can be sub-divided into different categories depending on the radiation used: UV, X-ray, etc. Lithography is useful for generating superhydrophobic surfaces because the feature shape and pattern dimensions are well-defined. Therefore, model surfaces can be created for the investigation of fundamental effects, such as the relationship between surface structure shape, geometries and superhydrophobicity (high contact angle and low sliding angle/roll-off angle/hysteresis).

An extensive set of studies on superhydrophobic surfaces generated by photolithography was performed by Oner et al[29]. In these studies, they produced a large range of feature sizes with patterns etched in silicon, including square posts with feature height from 20-140 µm and side lengths 2-128 µm (Figure 15a-c) as well as staggered rhombus- and star-shaped structures. Bico et al. also investigated other structures such as shallow cavities and stripes on Si surfaces to understand the effect of isotropic and anisotropic structures on superhydrophobicity (Figure 15d, e). Choi et al. reduced Si structures to nanoscale dimensions (~200 nm in height) using interference lithography and showed that the structure shape can be controlled by the etching conditions[30] (Figure 15f, g). SU-8 features were also investigated using analogous lithography techniques to investigate the three-phase-contact-line effect on superhydrophobicity[31] as shown in Figure 15h.

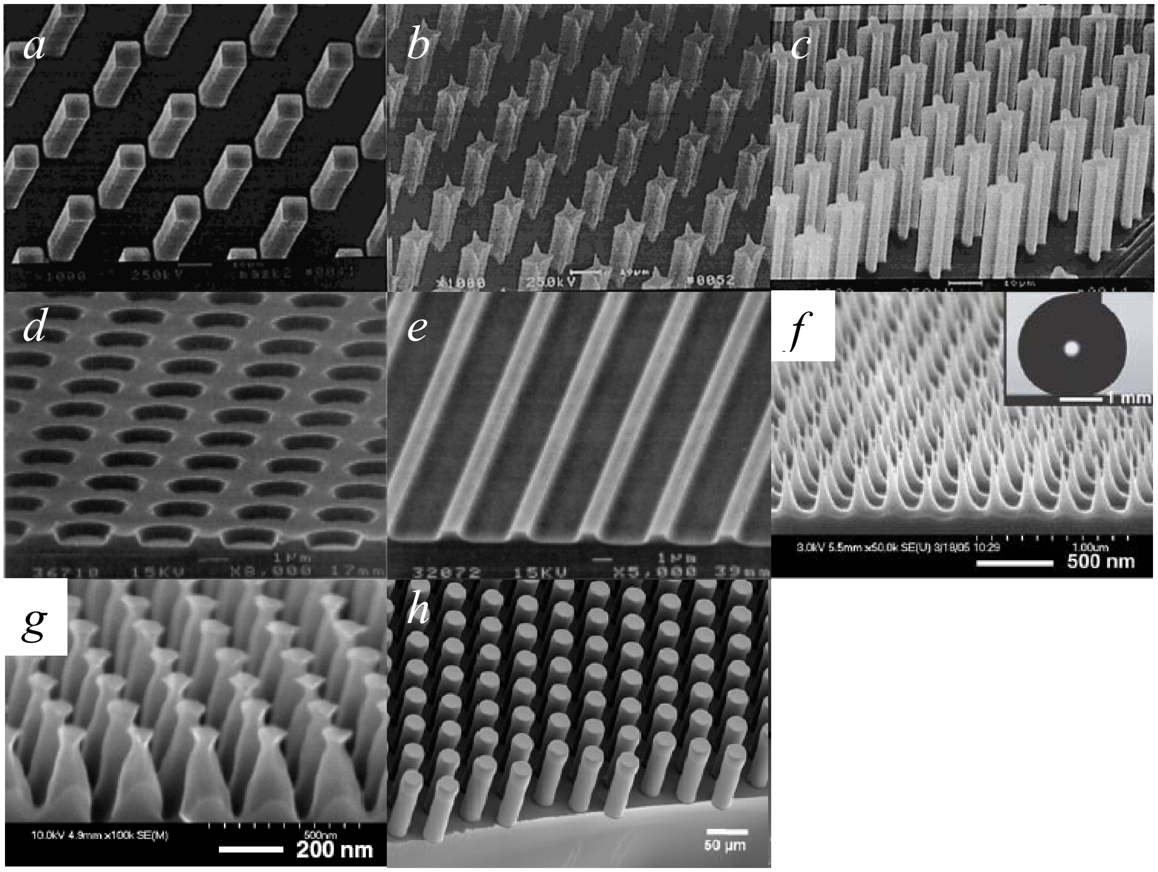

Figure 15. SEM images of surface structures from lithography techniques: a) Si square posts[29]; b) four-armed star-shaped posts[29]; c) indented square posts[29]; d) shallow cavities[32]; e) Si stripes[32]; f) sharp tip Si nanoposts[30]; g) Si reentrant structures[30] and h) patterned SU-8 surfaces of circular pillars[31].

1.5.1.2 Differential Plasma Etching

Plasma techniques are widely employed in microelectronics processing (Si surface pattern etching), cleaning, removal of photoresists, and dielectric film deposition such as inorganic or polymer materials)[33]. Plasma etching techniques are also capable of surface roughness generation and therefore offer a method to fabricate superhydrophobic surfaces.

Plasma etching of fluoropolymers

Using plasma etching techniques, polymer materials ranging from PTFE to silicones to polyethylene can be etched to produce a rough surface. To roughen PTFE, the technique of radio-frequency sputtering has been reported[4, 34]. For long sputtering times, a superhydrophobic Teflon surface was prepared by use of an O_2 plasma; the resulting surface showed a water contact angle of 168˚[35]. Plasma ion beam treatment using O_2 and Ar have also been reported in preparation of superhydrophobic PTFE coatings[36] with a surface morphology as shown in Figure 16.

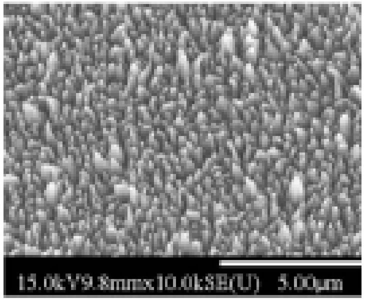

Figure 16. The SEM surface morphology of plasma treated PTFE surface by Ar/O2 (2sccm/2sccm) 1.5KeV.

Using a simple plasma based technique that combines etching and plasma polymerization on silicon substrates, superhydrophobic surfaces have been fabricated by tailoring their surface chemistry and surface topology[37]. This technique showed the capability of large area processing and good reproducibility. Using SF6 as an etchant, surface roughness can be produced by over-etching the photoresist layer. Overall, the method to generate superhydrophobic surfaces consisted of 3 steps. First, a 2.3 μm thick photoresist polymer layer (microposit S1813 supplied by Shipley Company) is deposited by spin coating on a silicon wafer. Then, photoresist layers are etched using an inductively coupled plasma with a magnetic pole enhanced ICP (MaPEICP) source. Third, the CFx layer is deposited on etched photoresist/Si wafer from C4F8 using the same plasma reactor but with the 13.56MHz r.f. capacitive plasma mode. The key step of this process is etching of the surface topography into the substrate to create high roughness before deposition of the fluorocarbon coating. Superhydrophobicity is achieved after the C_4F_8 plasma polymer deposition process.

Plasma etching of silicon with micromask

SF_6 and CHF_3 plasmas were used to investigate the surface roughness generation on silicon surfaces for surface wettability modification[38]. Due to the nonuniform removal of photoresist (Microposit S 1813, Shipley, spincoating at 2000rpm), the reside that remains on the surface acts as localized masks to create roughness on the silicon surface. After the surface roughness was formed as shown in Figure 17, a CFx layer was deposited on top of the rough surface using plasma-enhanced chemical vapor deposition (PECVD). The surfaces treated by the CHF_3 plasma are all superhydrophobic up to 10 min of etching, while SF_6 etching will not produce superhydrophobic after 2.5 min etching; these results are due to differences in Si etch rate with the two fluorocarbon gases. After 5 min etching for SF_6, the surface contact angle becomes 116˚, which is approximately the contact angle on a flat surface for CFx coatings.

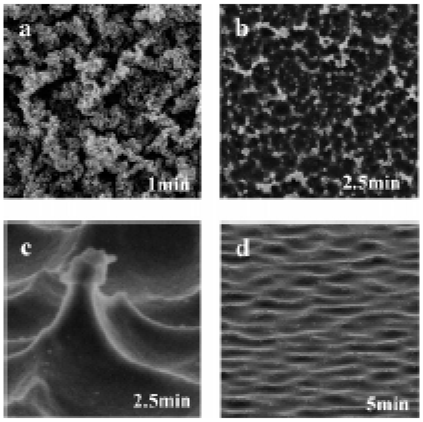

Figure 17. SEM image of silicon surface etched by SF_6 for (a) 1, (b,c) 2.5, and (d) 5 min. Image c is a magnified view (with an observation angle of 45°) of one residual photoresist particle on a peaked feature. The areas in images a, b, and d are 20 μm x 20 μm; The area of image c is 2 μm x 2 μm[38].

The roughness morphology at these process conditions shows a crystallographic anisotropy, where (111) planes are revealed. When an oxide mask was used, the surface roughness was reduced compared to that for a photoresist mask. When there is no mask, the surface roughness is very low which suggests an effect due to the photoresist mask layer (which redeposits during etching) on the surface roughness.

Plasma etching of poly(dimethylsiloxane)

Polydimethylsiloxane is a very low surface energy material with a surface energy of 21-22mJ/m2, only slightly higher than PTFE (~18mJ/m^2). However, after plasma treatment, the surface may show much higher surface energy. For instance, superhydrophobic PDMS has been fabricated by an SF6 plasma treatment followed by fluorocarbon film deposition that generated hydrophobic high aspect ratio columnar-like nanostructures as shown in Figure 18[39].

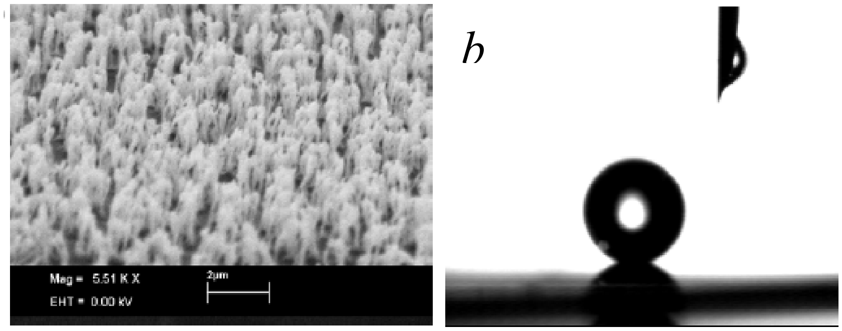

Figure 18. SEM image of a PDMS elastomer (Sylgard 184) surface after a 6 min SF_6 plasma treatment. 1.45 µm-high nano-columns are shown. (b) Image of a water droplet rolling off the surface in (a) after being conformally coated with a 20 nm-thick FC film[39].

In addition, under appropriate plasma processing conditions (SF_6 plasma etching for a sufficient time to generate the appropriate surface roughness), superhydrophobic and simultaneously transparent surfaces can be produced[39], which is of great practical importance. In particular, nanostructured PDMS surfaces are visibly transparent for treatment times up to 2 min (height of column: 130 nm), although they become opaque for etching times longer than 4 min. However, the transmittance data were not shown.

Domain selective plasma etching

To establish superhydrophobicity of PET, a method consisting of a two-step process comprised of nanotexturing by an oxygen plasma treatment and subsequent deposition of a hydrophobic coating by means of low temperature chemical vapor deposition or plasma-enhanced chemical vapor deposition, was employed to form ultra water-repellent polymer sheets [20, 40, 41]. After oxygen etching, many protrusions are observed on the polymer surface. Since PET has two domains, that is, noncrystalline domains are more readily etched than the crystalline domains, these protrusions were probably formed as a result of domain-selective plasma etching. This surface nanotexture remained after deposition of the hydrophobic coatings using organosilane precursors; surface topologies are shown in Figure 19. The surface-modified substrate was transparent (the polymer is optically transparent) and ultra water-repellent, showing a water contact angle greater than 150 degrees.

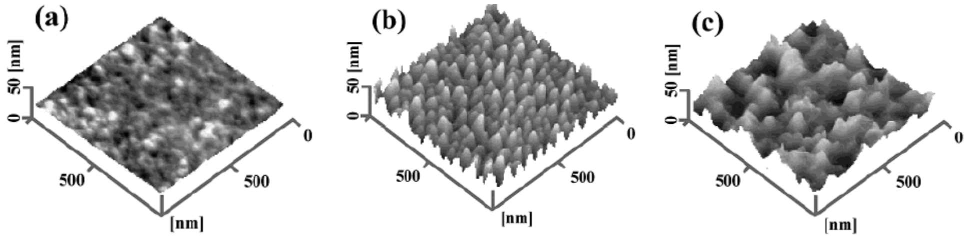

Figure 19. AFM of PET (a) untreated, (b) O2 plasma treatment (c) FAS coating after O2 plasma.

By selectively patterning a surface (deposited fluorocarbon polymer) a micro-patterned polymer substrate with superhydrophobic/superhydrophilic domains as shown in figure 20 can be prepared. Such surfaces are extremely useful in chemical and biological sciences to keep surfaces from retaining or being fouled by samples and reagents.

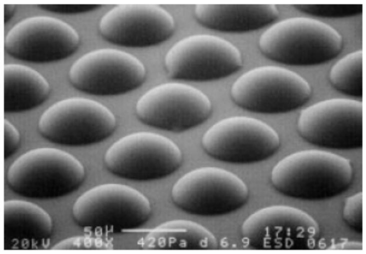

Figure 20. Environmental Scanning Electron Microscope (ESEM) image of micro-patterned water droplets on a superhydrophobic/superhydrophilic surface prepared by a multi-step drying process[42].

To achieve superhydrophobicity on LDPE surfaces, a similar process has been employed due to the fact that LDPE also shows non-crystalline and crystalline domains [43-45]. Two routes to achieve superhydrophobicity are possible. The first corresponds to a one-step synthesis (CF4 plasma modification of LDPE). The second route involves two steps (O2 plasma treatment followed by CF4 plasma deposition onto LDPE). However, these surfaces tend to lose their superhydrophobic behavior after water vapor condensation.

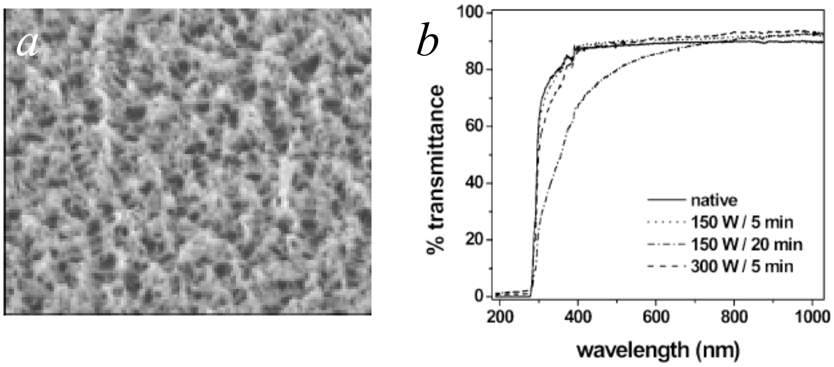

Figure 21. a) SEM image of PS samples treated with a CF_4-O_2 discharge with 17% O_2 for 5 min[46]; 300W 5 min plasma etching; b) transmittance of the prepared surfaces.

Superhydrophobicity can also be achieved by polystyrene (PS) etching in CF4-O2[46]. By controlling the etching parameters, the surface wetting characteristics can be tailored from sticky to slippery superhydrophobicity. Using this process, the optical transparency can be maintained on the PS surfaces (Figure 21).

Woodward et al. used a two step CF_4 plasma etching and fluorination process followed by sample curing to prepare a fluorinated rough polybutadiene surface (Figure 22) [47]. This surface exhibited superhydrophobicity with a water contact angle of ~175° and contact angle hysteresis of 0.4°.

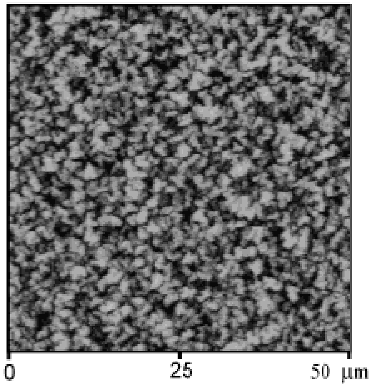

Figure 22. AFM height image of polybutadiene in CF_4 plasma (power 50 W) for 900 s [47].

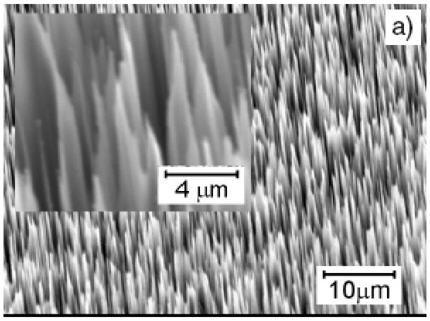

Figure 23. Electron microscopy images of a nanograss surface coated with a PFA thin film. [48]

Dorrer et al. reported a method to manipulate superhydropobicity/superhydrophilicity by precise control of the surface chemistry using various polymer coatings on Si nanograss surfaces generated by anisotropic plasma etching (Figure 23) [48]. When a hydrophobic polymer poly(heptadecafluorodecylacrylate) (PFA) was used to coated Si nanograss surfaces, superhydrophobicity (179°, no observable hysteresis) was achieved and the surface showed "condensation resistance" to water vapor.

1.5.1.3 Metal assisted etching

The metal assisted etching process on Si surfaces involves: 1) deposition of metal nanoparticles (Au, Pt, Ag, Pd etc) on the Si surface, and 2) etching of the metal coated Si in HF/oxidant solutions[49]. During this process, Si is continuously etched away at the site of the metal/Si contacts and surface roughness formed by control of the metal particle density. Deposition methods including direct metal deposition by sputtering or electron beam evaporation and electrochemical deposition of metal particles from reactive metal precursors. Figure 24 shows the result of using different metals for assisted etching on Si surfaces. Metal has been deposited onto Si surfaces by reduction of metal precursors such as $HAuCl_4$[28], $AgNO_3$[50], $Ni(NO_3)_2$ [51]. E-beam evaporation or DC sputtering can also be used to deposit metal onto silicon surfaces for this etching process[49].

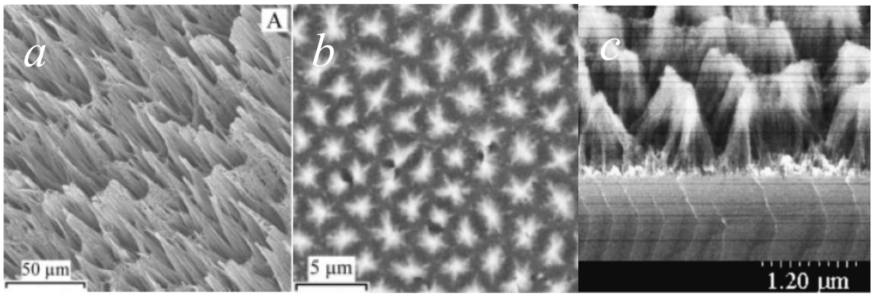

Figure 24. SEM images of etched Si surfaces: a. from $AgNO_3$/HF etching, 0.02/5.0; b. from $Ni(NO_3)_2$/HF etching 0.08/5.0[51]; c. evaporated Pt on Si, etching in HF/H_2O_2[49].

1.5.1.4 Dislocation selective chemical etching and other etching methods

Dislocation selective chemical etching can be performed on the surface of polycrystalline metals such as aluminum, copper and zinc, to prepare rough surfaces as shown in Figure 25 [52-55]. The key to this etching technique is the use of a dislocation selective etchant that preferentially dissolves the dislocation sites in the grains. Water droplet contact angles higher than 150° and roll-off angles of less than 10° were obtained when surfaces were treated with fluoroalkylsilane.

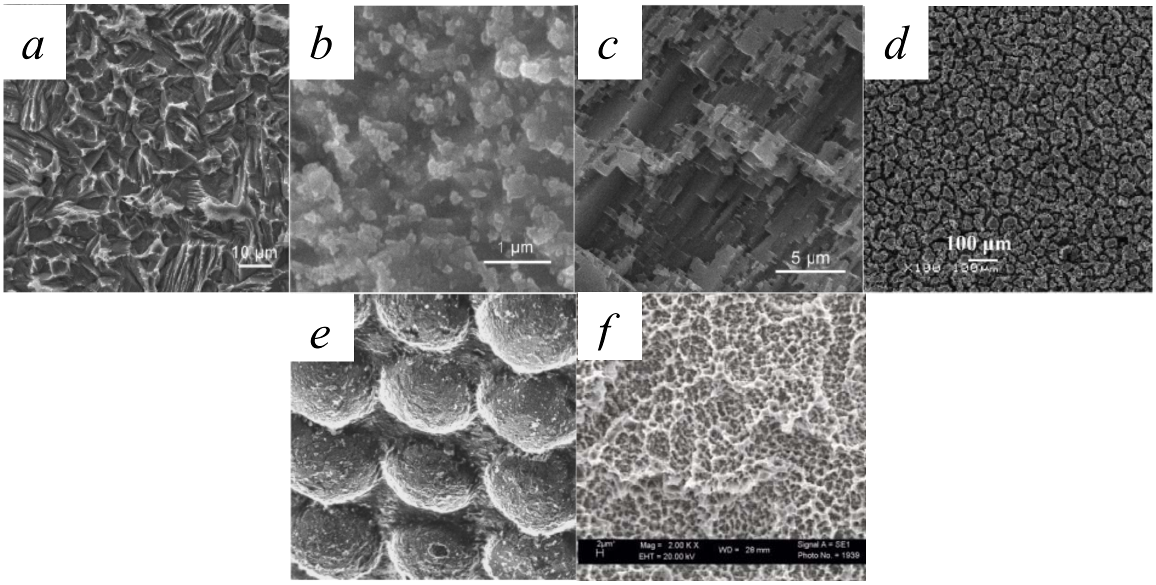

Figure 25. SEM images of different etched surfaces: a) zinc surface etched with 4.0 mol/L HCl solution for 90 s at room temperature[52]; b) copper surface etched with a modified Livingston's dislocation etchant for 24 h at ambient temperature[52]; c) Al etched by Beck's dislocation etchant for 10 s; d) Al alloy (2024Al, 92.8wt% Al, 5.5wt% Cu) etching by NaOH[53]; e) Cu surface[54], Cu etching was carried out in a potassium persulfate solution. rough etched top and pits; f) Ti surfaces from sandblasting and acid etching.[55]

Superhydrophobicity can also be achieved by Al alloy etching using NaOH. Etching mainly occurred in the Al domain because of preferential dislocation etching; roughness is due to the remaining Cu and other elements on the surface. The as prepared surface shows a contact angle of 154° and sliding angle of ~3° after hydrophobic treatment. [53] On Cu surfaces, the microstructures can be prepared by photolithography and subsequent etching using a potassium persulfate solution[54]. A Ti surface with low surface energy was prepared by sandblasting and acid etching (HCl/H_2SO_4) after a hydrophobic treatment[55] (Figure 25f). The initial advancing contact angle on the surface is 139.9° without any hydrophobic treatment, which is the highest contact angle considering that there is no more hydrophobic treatment on the surface. However, the receding contact angle is < 5° and repeated measurement gave a contact angle of 0°.

Electrochemical anodization can also be used to generate surface roughness. For example, Ti was treated by electrochemical anodization to form a sponge-like nanostructured TiO_2 film on the surface[56] (Figure 26a). After a hydrophobic surface treatment, the advancing angle on the surface was 160.1° and the hysteresis was only 0.8°.

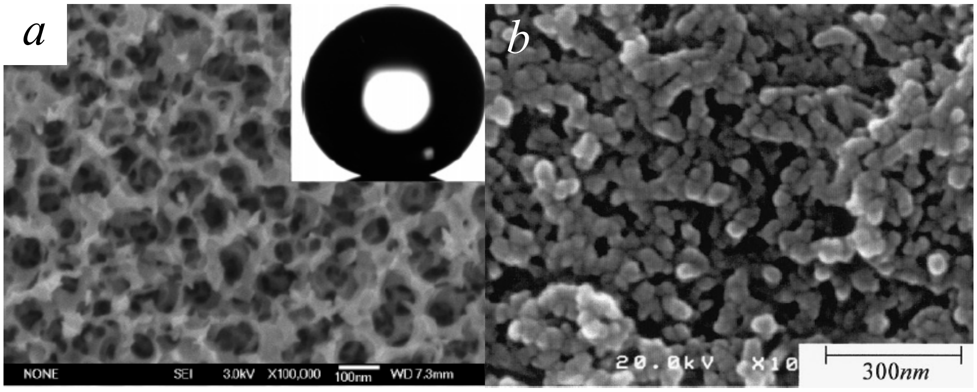

Figure 26. Anodized surfaces: a) Ti anodization, TiO_2 formed on surface[56]; b) Al anodized surface[5].

Al surfaces can also be anodized to prepare a fractal surface[5] (Figure 26b). After a fluorinated monoalkyl phosphate (F-MAP) treatment, the surface showed a water droplet contact angle of 163° and rapeseed oil contact angle of 150°. The fluorination chain length is very important in this case and the oil repellency for the silane coupling agent was much less than that of F-MAP.

1.5.2 Coat-on/cast approach

This approach uses gas or liquid phase deposition or coating processes to deposit a thin film on substrates; during the deposition, rough solid structures evolve. Depending on the surface energy of the coating materials, the surface may (high surface energy materials) or may not (low surface energy materials, e.g. fluoropolymer, silicone, hydrocarbon etc) require a hydrophobic treatment to achieve superhydrophobicity.

1.5.2.1 Plasma deposition

Particulate formation in atmospheric plasma process can be used for the generation of superhydrophobic surfaces[57]. Among many treatments that can be utilized to impart hydrophobic and superhydrophobic character to surfaces, plasma based processes have been widely studied and developed. Plasma-based treatment methods provide the advantages that no liquid waste is generated and the efficiency of surface activation by the dual action of radicals and charged particles (electrons and ions) is high. There are several reports of the use of atmospheric plasma processes, but plasma stability, low power operation, and high flow rates of precursors/diluents remain as challenges that must be solved for practical applications. One method of atmospheric plasma polymerization to form superhydrophobic surfaces on a wide range of substrates has been demonstrated[57]. The superhydrophobic coating was produced by an in-line atmospheric radio frequency (rf, 13.56MHz) plasma process using a mixture of CF_4, H2 and He gases. Roughness can be minimized while maintaining the superhydrophobicity to achieve transparent film on glass slides. The process can be applied to flat substrate surfaces such as metal, silicon wafers, and glass as well as rough surfaces such as Kimwipe paper and cotton without the need for separate micro-roughening steps. The system does not require reduced pressure and is operated in an in-line mode,rather than a batch mode. As a result, it can be scaled up for applications to large substrate surfaces or continuous processing, which is preferred for industrial manufacturing. Two parameters were important: the speed at which the sample was moved through the plasma and the use of hydrogen. The speed must be optimized and hydrogen is used to achieve effective polymer deposition. After more than 5 passes, the surface showed superhydrophobicity. XPS and AFM analyses showed that on the surface there are CFx particulates formed which are responsible for the high contact angle and low hysteresis. It is known that for microelectronics manufacturing, particulates are detrimental to device properties and reliability and should be avoided. However, for superhydrophobicity applications, particulates are intentionally produced. At a relatively high pressure and so a low mean free path of neutrals and ions, particles will be formed in the gas phase, which leads to the deposition of particulates onto substrates.

1.5.2.2 Chemical Vapor Deposition (CVD) process

Silicone nanofilaments have been formed from trichloromethylsilane (TCMS) precursor via a gas phase reaction route at room temperature and pressure without a carrier gas[58]. Silanes with hydrolysable groups (chloride) react with water to form silanols, which then couple to hydroxyl groups at the surfaces, and subsequently polymerize to a silicone layer, depending on the reaction conditions. When dry reaction conditions with only traces of water were maintained, monolayers or nearly monolayer thick coatings resulted. When equimolar amounts of liquid TCMS and water vapor were used in the reaction vessel, a superhydrophobic surface was achieved; the coating then consisted of polymethylsilsesquioxane nanofilaments. This technique can be used to coat a variety of surfaces such as cotton fiber, wood, polyethylene, ceramics, titanium and aluminum. In addition, on glass surfaces, a transparent coating can be achieved as shown in Figure 27. When the as deposited surface was treated in an O_2 plasma followed by a treatment with fluoroalkylsilane, oil repellent surfaces resulted[59] as shown in Figure 27c.

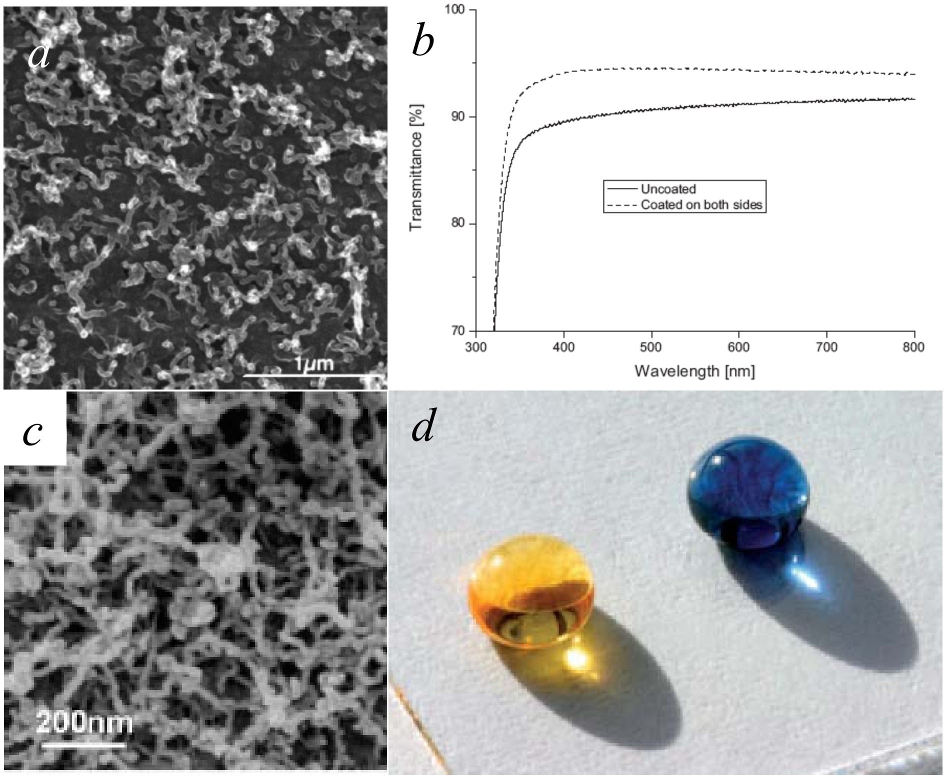

Figure 27. Scanning electron microscopy images of silicone nanofilaments on silicon. b. UV-vis spectra of coated and uncoated glass slides[58]; d. 10 ml drop of colored hexadecane (yellow) and colored water (blue) on a PFOTS modified silicone nanofilament coating on glass.[59]

Zhu et al. reported a method of superhydrophobic materials preparation using two-tier CNT surfaces formed by growing patterned CNT arrays on CNT covered Si surfaces via CVD (Figure 28a)[60]. Because of the presence of nanoroughness on the CNT film/array surface, a two tier roughness can be achieved. Therefore, after coating the surfaces with a fluorocarbon film, superhydrophobicity was achieved with a contact angle of 167° and a hysteresis of 1°. A CNT nanoforest has also been prepared by

PECVD (Figure 28b).[61] After the surface was coated with PTFE, superhydrophobicity was achieved down to the microscopic level. Even micrometer-sized water droplets can be suspended on top of the nanotube forest.

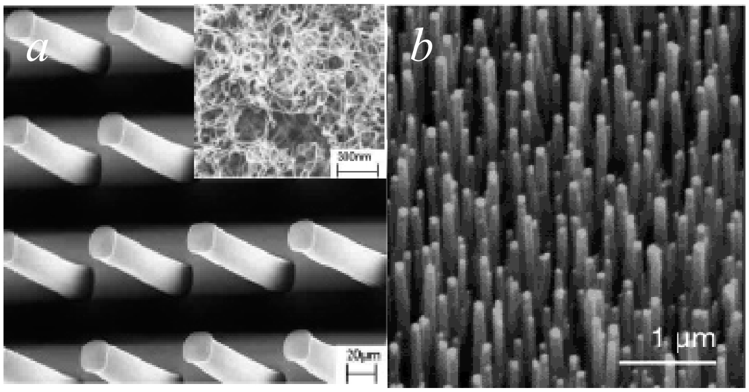

Figure 28. a) Typical SEM images of CNT arrays on silicon substrates; b) SEM images of carbon nanotube forests prepared by PECVD with nanotube diameter of 50 nm and a height of 2 μm. [60, 61]

1.5.2.3 Sol-gel process

Sol-gel processes can also produce rough surfaces on a variety of oxides such as silica, alumina, and titania[62, 63]. This approach is a very versatile process for the preparation of superhydrophobic thin films or bulk materials. Sol-gel process can form a flat surface coating, xerogel coating or aerogel coating depending on the process conditions; both xerogel and aerogel show rough or fractal surfaces.

Silica aerogels can contain up to 15 wt% of absorbed air and water vapor. In order to decrease the pore affinity to absorption and thus make aerogels less hydrophilic, a number of strategies have been used, such as avoiding the presence of terminal hydroxyl groups by co-gelling certain silicon precursors containing at least one non-polar chemical group i.e., CH_3-Si[64]. Superhydrophobic silica aerogels can also be obtained by surface modification of standard silica gels with a heavily fluorinated silyl chloride followed by supercritical fluid solvent removal.[62] After either ambient drying or supercritical drying, both surfaces show superhydrophobic properties (Figure 29).

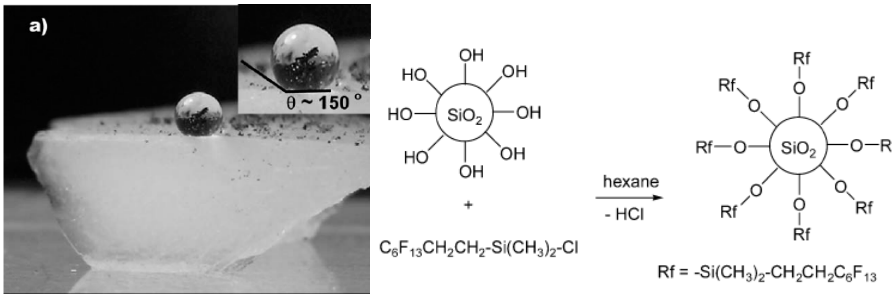

Figure 29. Drop of water on top of fluorinated aerogel, inset shows a close-up.[62]

Attempts have been made to synthesize highly flexible and superhydrophobic silica aerogels using methyltrimethoxysilane (MTMS) as a precursor by a two-step acid-base sol-gel process[65] (Figures 30 and 31). The aerogels consist of cross-linked networks of silica polymer chains extended in three dimensions. Due to the presence of non-polar alkyl groups (i.e. methyl) attached to the silica polymer chains, the inter-chain cohesion is minimized resulting in an elastic and flexible three-dimensional network. Increased dilution of the MTMS precursor with methanol solvent yielded a silica network with a low degree of polymerization which exhibited higher flexibility. In contrast, for lower dilution of the MTMS precursor, an extensive polymerization resulted in dense and rigid structures. Because of the new property, i.e. flexibility, imparted to the aerogel, it can be bent into a variety of shapes and acts as a good shock absorber as well. A water droplet contact angle of 164˚ can be achieved on such aerogel surfaces.

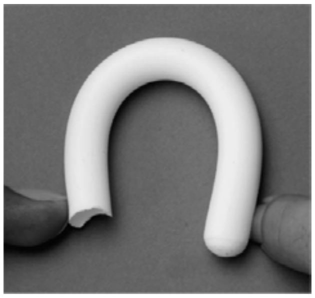

Figure 30. Flexible silica aerogels prepared at two different MeOH/MTMS molar ratio of 35.[65]

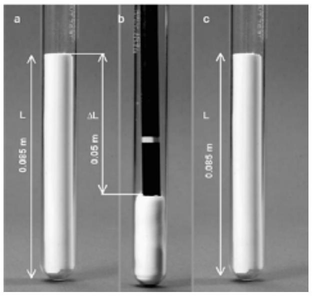

Figure 31. Photograph of the three states of a flexible aerogel sample: (a) without stress, (b) with stress, (c) after releasing the applied stress.[65]

Another method to produce superhydrophobic silica materials is the phase separation method in which a hardening process ‘freezes’ a phase separation that occurs concurrently with hardening of one of the phases[66]. This method produced co-continuous materials consisting of a solid phase and a liquid phase. When the liquid was removed, a porous structure remained. The materials system was comprised of condensed organo-triethoxysilane in a mixture of organic solvent and water. Such sol-gel materials show promise as stronger superhydrophobic surfaces and as bulk materials and are relatively cheap to produce. Reaction occurs through hydrolysis of the ethoxy groups and polymerization of the resulting silanol groups. Polymerization causes a decrease in dipole moment, leading to hydrophobic phase separation. The dried material has the organic groups on its surface, causing the foams to be superhydrophobic (Figure 32).

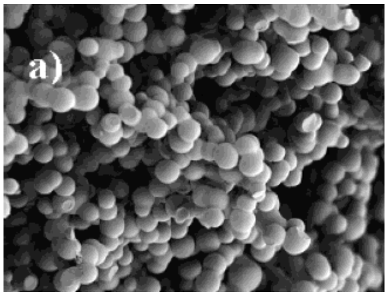

Figure 32. Electron micrographs of gold-coated foams: MTEOS with 1.1 M ammonia, heated to 300 °C. [66]

Despite abrasion of these sol-gel surfaces, the high water droplet contact angle can be maintained. This result is significant for applications wherein handling and mechanical abrasion are inevitable. Even at temperatures as high as 300˚C, no loss of superhydrophobicity is detected.

Another facile process involves initial formation of silica particles followed by surface fluorination in situ using trichlorosilanes[67]. Stable superhydrophobic surfaces with water contact angles over 170˚ and sliding angles below 7˚ have been produced by simply coating a particulate silica sol solution of co-hydrolyzed TEOS/fluorinated alkyl silane with NH_3-H_2O onto various substrates, including textile fabrics (e.g. polyester, wool and cotton), electrospun nanofiber mats, filter papers, glass slides, and silicon wafers (Figure 33).

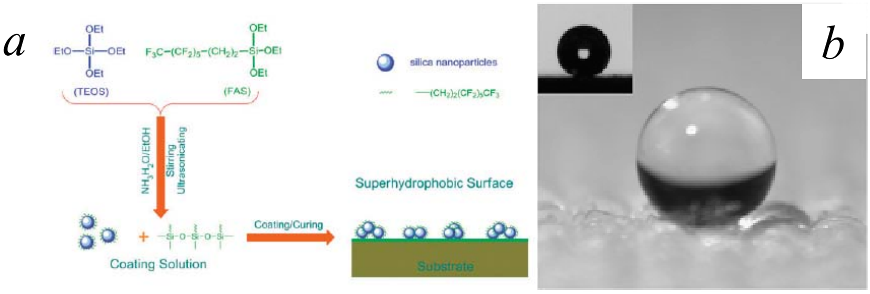

Figure 33. a) Reaction route of silica sol preparation and coating procedure; b) Photographic images of the coated polyester fabrics. [67]

Gao et al. reported a method to fabricate a perfect superhydrophobic surface (θ_A/θ_R = 180˚/180˚) by immersion of a Si wafer into CH_3SiCl/toluene solution, rinsing with toluene, ethanol and water and drying the surface coating[68]. The surface morphology generated is shown in Figure 34.

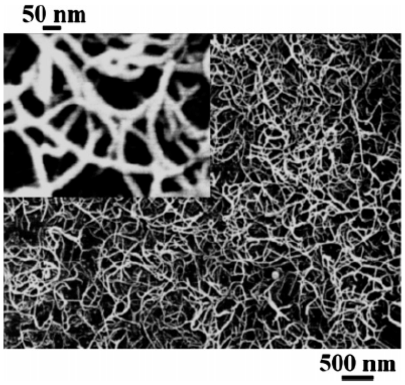

Figure 34. SEM images of a superhydrophobic surface from CH_3SiCl_3.[68]

Alumina is a hard material that is abrasion resistant. Using a sol-gel process, nanoscale surface structures can be generated by various methods (Figure 35). Tadanaga et al. showed that by immersing the porous alumina gel films prepared by the sol-gel method in boiling water, alumina thin films with a roughness of 20 to 50 nm were formed[63]. As a result, high optical transparency can be achieved. After a surface hydrophobic treatment, a superhydrophobic surface with a contact angle of 165° resulted.

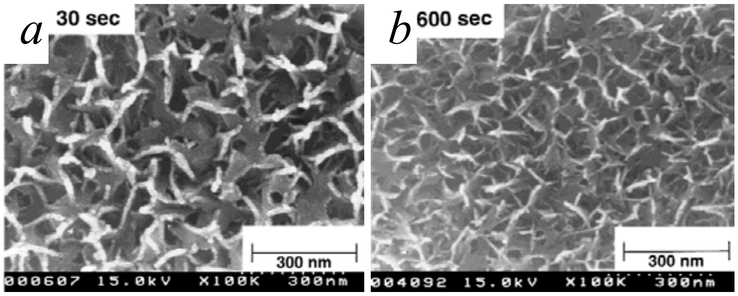

Figure 35. FE-SEM photographs of the surface of the Al_2O_3 films immersed in boiling water for (a) 30, and (b) 600 s. [63]

1.5.2.4 Layer-by-layer self-assembly

Layer-by-layer (LbL) self-assembly, which is based on the alternating physisorption of oppositely charged building blocks, represents a method to immobilize polyelectrolytes, colloid nanoparticles and biomacromolecules, such as enzymes, extracellular matrices (ECM), and DNA[69]. The sensitivity of the LbL multilayer towards its environment (e.g., pH, ionic strength) further provides new approaches to adjust the layered nanostructure with a tailored composition and architecture. The use of the LbL technique for constructing superhydrophobic coatings from poly(acrylic acid) (PAA) and polyethyleneimine (PEI), especially using Ag^+ to enhance the exponential growth of the PEI/PAA multi-layers has been explored[70]. It was found that the addition of Ag^+ can significantly improve the surface roughness as shown in Figure 36. On such surface, a high contact angle of 172° can be achieved after surface fluorination by (tridecafluoroctyl)triethoxysilane.

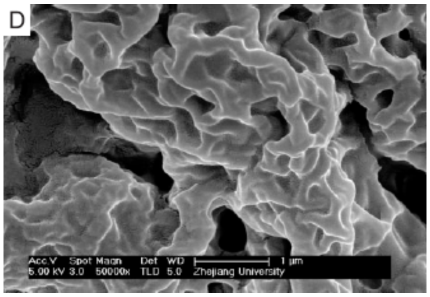

Figure 36. SEM image of (PAA/PEI-Ag+)7.5 film[70]

Zhai et al. prepared a polyelectrolyte multilayer surface by LbL assembly and then overcoated the surface with silica nanoparticles to mimick the hierarchical scale present on lotus leaf surfaces[71] (Figure 37). Superhydrophobicity was achieved after surface fluorination with a fluoroalkyl silane.

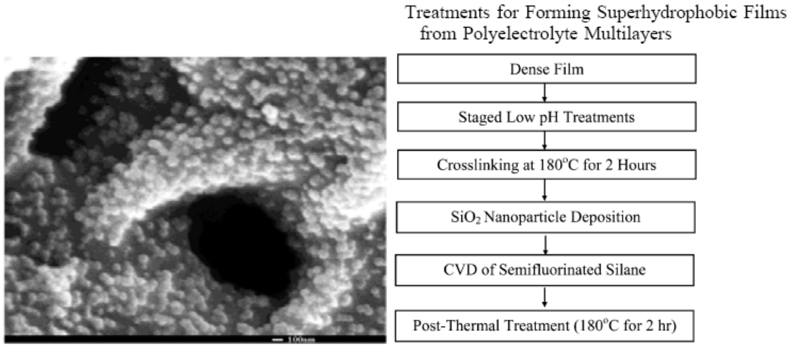

Figure 37. SEM image of the fully treated polyelectrolyte structure (a 2 h immersion in a pH 2.7 solution followed by a 4 h immersion in a pH 2.3 solution, with no water rinse) with silica nanoparticles. [71]

1.5.2.5 Monodisperse nanoparticles

Shiu et al. fabricated superhydrophobic surfaces by employing polystyrene (PS) monodisperse nanosphere lithography[72]. This method involves the formation of close-packed nanosphere arrays, O_2 plasma etching of the spheres, coating of the surface with Au, followed by octadecanethiol (ODT) treatment. The contact angle of the resulting surface was 168˚; images of the final surface are shown in Figure 38.

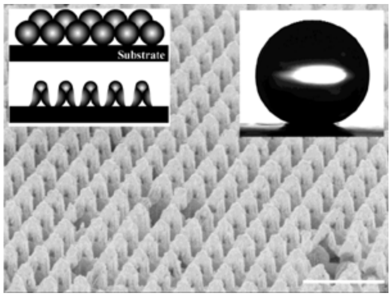

Figure 38. SEM image of a 440-nm-diameter double-layer polystyrene surface after 120 s of oxygen plasma treatment; Bar: 1 μm.[72]

1.5.2.6 Electrospinning

Electrospinning has become a popular method to generate continuous ultrathin fibers with micrometer and sub-micrometer diameters from a variety of polymeric materials. Electrospun fibers intrinsically provide at least one length scale of roughness for superhydrophobicity because of the small fiber size. The fiber mats composed solely of uniform fibers could be obtained by electrospinning a hydrophobic material (i.e., poly(styrene-block-dimethylsiloxane) block copolymer) blended with homopolymer polystyrene (PS)[73]. The roughness of the nonwoven mat, that resulted from the small diameters of the fibers (150–400 nm), combined with the enrichment of the dimethylsiloxane component at fiber surfaces yielded superhydrophobic surfaces (Figure 39). The construction of hierarchical roughness improves the superhydrophobicity with improved water droplet contact angles and reduced contact angle hysteresis[74].

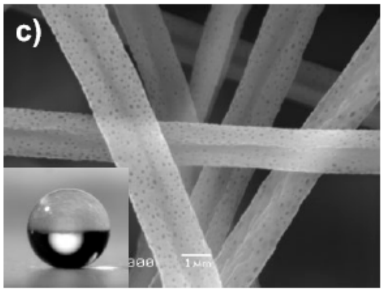

Figure 39. SEM images of electrospun and poly(perfluoroalkyl ethyl methacrylate) (PPFEMA)-coated PMMA fibers with surface pore structures; electrospinning process

was performed from a chloroform solution in ambient conditions with 44% relative humidity. [73]

Superhydrophobic surfaces were also prepared from electrospinning of polyaniline/polystyrene webs[75] (Figure 40). This surface is conductive and stable in many corrosive solutions, including acidic or basic solutions over a wide pH range, and oxidative solutions.

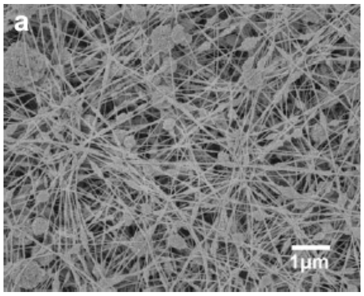

Figure 40. SEM image of an electrospun PANI/PS composite film with lotus-leaf-like structure.[75]

1.5.2.7 Electrochemical deposition method

Two-dimensional gold nanostructures have been fabricated by electrochemical deposition of gold nanoparticles onto indium tin oxide (ITO) glass substrates modified with thin polypyrrole (PPY) films[76] (Figure 41a). Different structures can be formed depending upon the deposition conditions; e.g., dendritic rods, sheet, flower-like and pinecone-like structures. The contact angle after dodecanethiol treatment on pinecone-like structures is 153.4°, at a tilt angle of 4.4°. Zinc oxide conductive surface structures were also prepared by cathodic electrochemical deposition from aqueous solutions of $ZnCl_2$/KCl[77] (Figure 41b). Hierarchical spherical cupreous microstructures have been reported on an indium tin oxide (ITO) substrate by using $Cu(NO_3)_2$ aqueous solutions (Figure 41c).[78] Further chemisorption of a self-assembled monolayer of n-dodecanethiol resulted in a superhydrophobic surface with a contact angle of 152°.

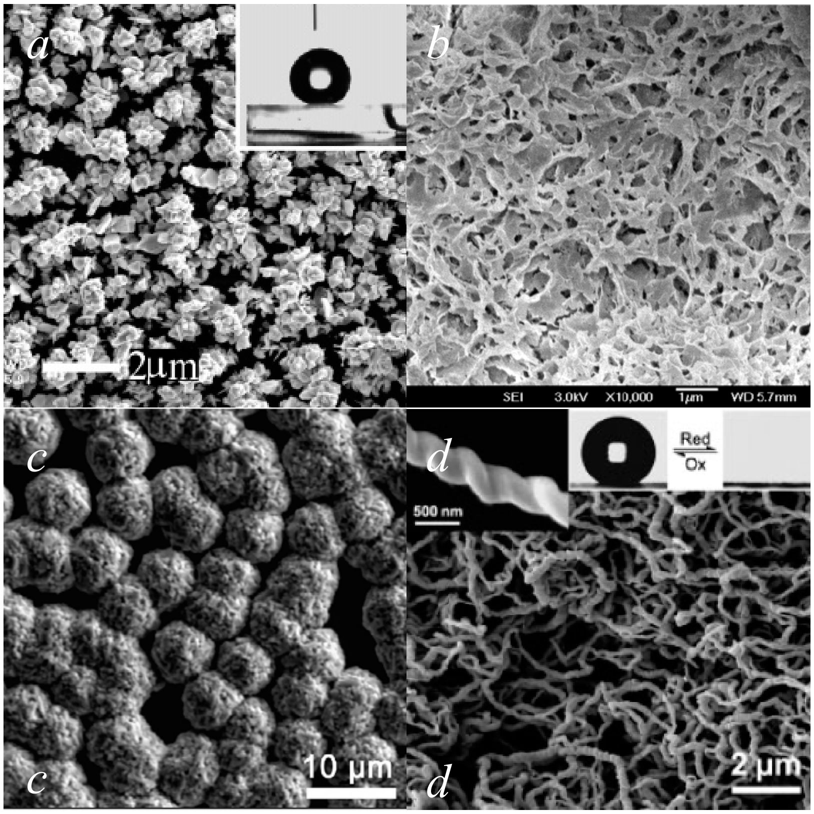

Figure 41. SEM images of a) Au nanoparticles deposited on a 14-nm-thick PPY for 2000 s[76]; b) ZnO thin films prepared by electrochemical deposition[77]; c) hierarchical spherical cupreous microstructures after 30 min deposition on ITO substrate[78]; d) perfluorooctanesulfonate-doped polyaniline film on Au coated glass surface from electrochemical deposition. [79]

Conductive PANI have also been reported[79] (Figure 41d), where superhydrophobic conducting polyaniline (PANI) films were electrochemically deposited in acetonitrile-H_2O electrolyte containing aniline monomer and perfluorooctanesulfonic (PFOS) acid. By controlling the electrical potential, PANI films were changed between the doped state and un-doped state, resulting in reversibly switchable superhydrophobic and superhydrophilic surfaces.

1.5.5 Other formation methods

1.5.5.1 Templating and imprinting

One of the simplest reproducible methods to prepare structured surfaces is the templating approach. Lee et al. reported that using AAO templating, PS superhydrophobic surfaces with well-defined nanostructures could be fabricated (Figure 42a).[80] Templates from lotus leave have also been reported[81]. In this case, lotus leaves were used as a mold to make negative structures on PDMS surfaces by a replica molding process. This molded PDMS surface can be used as template to fabricate polymer surface structures similar to those on lotus leaf surfaces (Figure 42b).

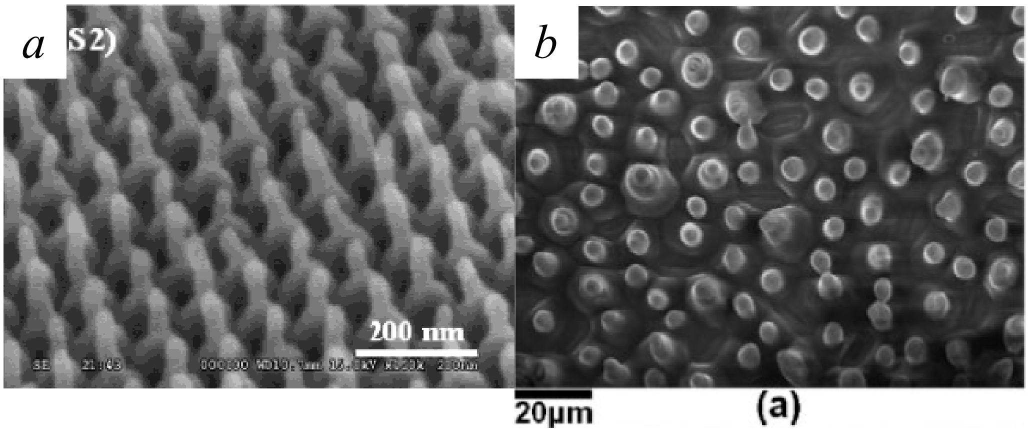

Figure 42. SEM images of a) nanostructured PS surfaces of nanopost arrays with an embossed base[80]; b) imprinted layers of epoxy-based azo polymer.[81]

1.5.5.2 Sublimation method

Nakajima et al. prepared superhydrophobic and transparent boehmite and silica films by sublimation of aluminum acetylacetonate (AACA)[22]. After sublimation, surface roughness was generated (Figure 43) and superhydrophobicity was achieved by an appropriate fluoroalkyl silane surface treatment.

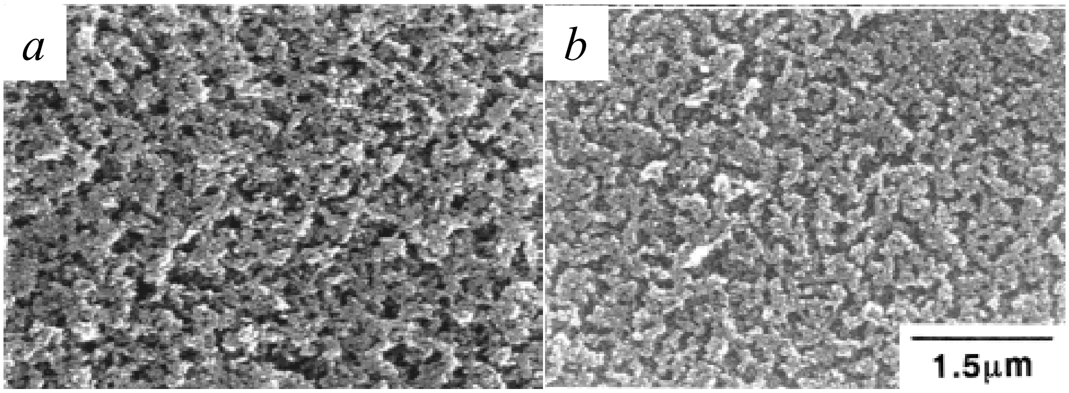

Figure 43. SEM micrographs of prepared films. a) Film prepared from a suspension containing boehmite and AACA; b) film prepared from a suspension containing silica and AACA. [22]

1.5.5.3 Honey comb structures by moisture condensation

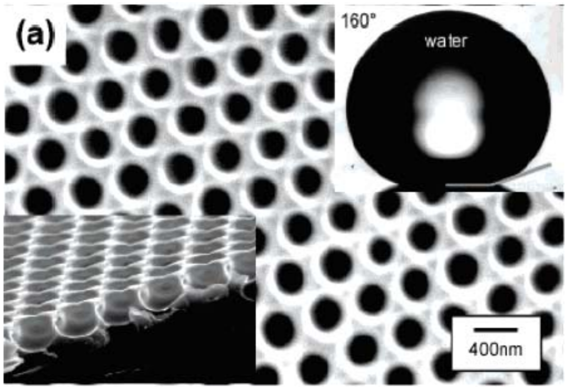

Figure 44. Scanning electron micrograph of the 300-nm-sized honeycomb patterned film (top image and cross section) and the water contact angle on this film. [82]

Honeycomb-like microporous polymer films with 500 nm to 50 μm pores (diameter) have been prepared by casting polymer solutions under humid conditions(Figure 44). If a fluoropolymer was used, superhydrophobicity was achieved.[82] In this process, water droplets condensed on the solution film surface act as templates. Depending on the drying rate of solvents, pore size can be controlled by controlling the water droplet size. This surface can also be optically transparent under the proper formation conditions.

Combination approaches using several formation techniques to create surface structures at different length scales to mimick lotus leaf surfaces has been reported. The combination of LbL and electrochemical deposition of Au is one example[83].

1.6. Potential Applications

Superhydrophobicity is a relatively recent term that has been used to describe extreme water repellency of rough hydrophobic surfaces. However, such techniques have been practiced for a long time. Early products include breathable fabrics and certain membrane filters, which use the same structure effects as superhydrophobic surfaces, but these are rarely referred to as being superhydrophobic. For example, Gore-Tex®, which was patented in 1972, is superhydrophobic.

The number and scope of techniques to generate superhydrophobic surfaces has greatly increased in recent years with possible applications expanding with them. The main barrier that prevents implementation of self-cleaning surfaces is that the surfaces are easily damaged or contaminated during normal use, such as abrasive wear and washing cycles. Despite this limitation, over 200 patens have been granted that use or produce superhydrophobicity in some form and products are becoming commercially available. Specific applications that do not involve abrasion or contact with oils that may cause contamination, such as self-cleaning building walls and windows have made use of these super-water-repellent surfaces. Commercially, one of the greatest limitations to the use of such surfaces is the stability over time under outdoor conditions. Investigations to improve resistance to scratching are underway which could lead to useful products. As research continues, methods of production and materials used to form superhydrophobic surfaces will broaden and offer new applications.

Potential uses for self-cleaning surfaces are wide-ranging. Indeed, we are surrounded by many surfaces that we want to keep clean, from window panels to roof tiles to bathroom surfaces and house walls. For example, cleaning of windows is expensive and cumbersome, especially if the windows are on skyscrapers. Water-related corrosion processes can also be prevented by such superhydrophobic surfaces.

The hydrophilic route to self-cleaning windows has been realized by several companies (PPG, Pilkington, TOTO) and has just been released to market. To what extent these windows will be a commercial success clearly remains to be seen; to some, a water film running off the glass may appear to be a nuisance. The main advantage of these surfaces is the combined hydrophilicity-photodegradation effect, which significantly aids in the cleaning process by decomposing organic moieties on the surface when illuminated under UV radiation. Furthermore, the fact that a controlled roughness is not needed in this approach is a clear technological advantage. Although the superhydrophilic effect is reversible in principle, the ageing of these surfaces under actual conditions is not known. Others argue that coatings for windows and mirrors should be superhydrophilic, causing water to form a transparent film which does not block the vision. However, superhydrophobic coatings on transparent windows may be problematic due to the fact that raindrops rolling off the surface can be distracting.

The alternative superhydrophobic approach, has not yet been realized in practice, but work in this direction is now underway. An ambitious attempt has been made by combining the basic elements of superhydrophobicity with biomimetic surface design[84]. A system under industrial development contains a reservoir with a hydrophobic polymer that is intended to mimic the wax of the lotus leaf: the outcome would be a self-cleaning surface that heals itself. The concept relies on a replenishment layer embedded in a glass that serves as a surface-repairing reservoir, refueling a hydrophobic cover layer when it has been depleted at the surface, and hence restores superhydrophobicity to the roughened surface.

Another important application for superhydrophobic surfaces may be in the field of oil/water separation[85]. Feng et al. demonstrated that a mesh coated with PTFE showed two extremes in wettability for water and oil. For water, it is an extremely nonwetting surface (superhydrophobic), while for oil, it changed to complete wetting (superoleophilic). The extreme difference in wettability for water and oil showed the possibility to separate oil and water. When a mixture of oil and water is put on the mesh film, the water remains on the upper part of the film, while the oil penetrates through the mesh and can be collected underneath.

Corrosion induced failure plays an important role in microelectronic devices and electronic packaging failures[86, 87]. In order for microelectronic components and devices to perform their functions properly, highly reliable packaging is necessary. Failures of microelectronic devices and packages not only cause malfunction of the devices but also sometimes lead to catastrophic consequences for entire systems. Among all microelectronic device failures, corrosion related failure is responsible for more than 20%. Corrosion in microelectronic packaging depends on the package type, electronic materials, fabrication and assembly processes, and environmental conditions such as moisture condensation, ionic or organic contaminants, temperature, residual and thermal stress and electrical bias. With the ever-shrinking feature sizes of microelectronic components and devices, susceptibility to corrosion-induced failures increases. Better performance and reliability requirements drive improved corrosion-resistance of packaging systems.

There are basically three types of packages for microelectronic components and devices: ceramic, metal and plastic. Ceramic and metal packages are hermetic packages mainly used in military, aerospace and automobile applications where high reliability is required. Plastic packaging is non-hermetic, but is widely used because of its low cost and easy manufacturability. Compared to other package types, plastic packaging systems have more corrosion-related problems because the polymeric materials used in plastic package systems are more permeable to moisture which can then reach die, wires, bond pads, lead frames and solder joints. Therefore, corrosion problems are long-term issues in microelectronic packages.

Corrosion involves electrochemical processes unless oxidation can take place at elevated temperature and dry environments. The basic requirements for electrochemical corrosion include an electrically conductive anode, cathode, interconnecting electrolyte (humidity environment) and driving force[88]. There are three major corrosion types: galvanic corrosion, pitting corrosion and stress corrosion cracking[89]. Under most of circumstances, water/moisture is a key in the corrosion process. Corrosion prevention is a matter of preventing moisture condensation on sensitive areas such as die interfaces, wires, bond pads, and solder joints. In order to prevent corrosion for improved device reliability, superhydrophobic coatings on microelectronic devices offer great potential for water-repellent and moisture resistant applications.

In microelectromechanical systems (MEMS), adhesion failure due to bonding and capillary force between moving parts and substrates is the major failure mechanism[90]. Superhydrophobic surfacea are promising to achieve antistiction in these applications due to the low surface energy. Reduction of friction using superhydrophobic surfaces to achieve slip flow in microfluidic channels is also of considerable interest[91].

Control or transfer of fluid droplets containing biologically relevant molecules (DNA and proteins) while minimizing contamination is of much significance in biotechnology and biomedical fields. Specifically, the construction of complementary DNA (cDNA))-microarrays prepared by spotting techniques requires specific wetting properties of the substrates. Glass slides-the substrates most commonly used-are usually only mildly hydrophobized, such that the drops of drying cDNA-solution produce unwanted ring-like structures, a nuisance known in the field as the ‘doughnut-effect’, (Figure 45a). This effect is related to the well-studied ‘coffee-stain effect’: an evaporation-driven convection mechanism that drives dissolved or dispersed particles inside the drop to the surface-pinned contact line where evaporation occurs rapidly[92].

Superhydrophobicity is advantageous in this application since the nearly spherical drops on a superhydrophobic surface can shrink exactly like a drop in air. The positioning and shape of spotted drops can be steered by combining hydrophilic and hydrophobic patterns. The utility of this idea can be demonstrated by consideration of an actual biosystem: some desert beetles capture their drinking water by a hydrophobically-hydrophilically structured back[93]. By prepatterning a substrate, hydrophilic prespotting (anchoring) on an otherwise hydrophobic or superhydrophobic surface results in new possibilities for improvements in spotting and analyzing DNA and proteins by avoiding wall contact.

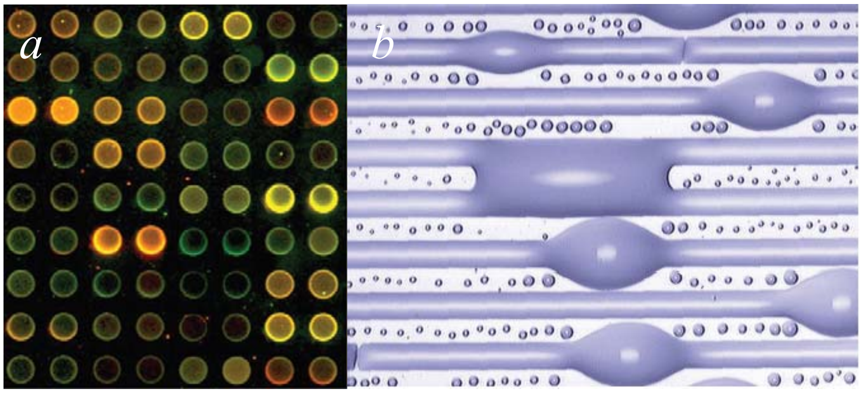

Figure 45. a) Complementary DNA microarray on a silanized glass plate. The doughnut-like shapes of the deposits are clearly visible; b) liquid channels on a hydrophilically–hydrophobically patterned substrate: a possible pathway to surface-tension controlled microfluidics[92].

Beyond the possibility of improving fluid shapes on substrates, the possibility of guided motion of droplets on superhydrophobic surfaces offers the opportunity to develop a droplet-based microfluidics system, in contrast to the classical concept based on microfluidic channels. Driving the liquid along the channels and causing merger at predefined locations offers a novel way to mix reactants or direct biochemical reactions; this approach defines the concept of a ‘liquid microchip’ or ‘surface-tension confined microfluidics’[94]. One advantage of the open structures over capillaries, in addition to their ease of cleaning, is that blocking of the capillary by unforeseen chemical reactions is inhibited.

To conclude this introduction into the vast number of approaches and applications for superhydrophobicity, an indication of the greatest challenge facing all self-cleaning or contaminant free surface applications must be offered: ageing and degradation of the artificial surfaces. For biotechnology applications, this is not so relevant; the surfaces will often be used for analytic purposes and hence designed as disposables. If one thinks of contaminant-free surfaces for use in medicine, the issues of reusability and hygiene are complex and at present unresolved. However, a different issue is the use of self cleaning surfaces in outdoor applications. Examples are known already in which an initially improved product lost its advertised self-cleaning property too rapidly, and thereby did not justify the initial investment (Lotusan^{TM}private communiation). Clearly, failed products bear the risk of discrediting an entire field of applications. Ageing will remain difficult to foresee - pure empiricism reigns in its description - but the benefits to investors and product users require that ageing be under control. In addition, stability under high humidity conditions also needs improvement by designing small features with cost-effective approaches. The dew point may be reduced on superhydrophobic surface with small features[95]. Oil or surfactant repellent or superoleophobic surfaces may also be desirable which add more constraints to superhydrophobicity design. As coatings improve and prices fall, use of superhydrophobic surfaces is likely to increase, particularly as understanding of many of the limitations is developed and perhaps mitigated by careful selection of coatings.

1.7. Challenges and research objectives

1.7.1 Challenges

Although very promising, successful application of superhydrophobic surfaces has a long way to go. Despite the fact that a variety of surfaces can be made superhydrophobic based on the principle of surface structuring and hydrophobization, practical issues such as robustness (e.g., mechanical robustness, chemical stability, UV stability, thermal stability), adhesion of nanostructures or coatings to substrates, moisture condensation and oil-repellency still require significant research efforts for both fundamental understanding and technical breakthroughs.

Robustness

Robustness refers to both a stable high contact angle on the superhydrophobic surface over time and UV stability under UV illumination, e.g., outdoor applications. Superhydrophobicity is a surface sensitive property, and change of chemistry in the surface layer with a thickness of only 10 Å will significantly alter the surface energy, leading to failure of the superhydrophobicity. Under this situation, instead of cleaning the surface, contamination will accumulate (be trapped in the surface structures). Thus, chemical species present in the surface layer should have strong chemical bonds in addition to low surface energy. The two most investigated low surface energy materials (fluorocarbon polymers/chains and polydimethylsiloxane) both show high bond strength and therefore very good UV stability. Plasma-assisted deposition of fluorocarbon polymers using different precursors is preferred due to the cross-linked nature of the resulting layers and the improved adhesion observed[96]. Deposition of PDMS is more difficult as shown in reference [97]; the surface lost hydrophobicity after the plasma deposition process due to the energetic plasma species (plasma ions 250eV) and the surface roughness was not high enough to achieve superhydrophobicity even after hydrophobic surface treatment.

Good abrasion resistance is also one of the most important characteristicsparameters for the practical application of superhydrophobic surfaces. One disadvantage of polymers is that they are soft so that surface structures can be easily deformed under exposure to mechanical force and heat. If this deformation is non-reversible, the superhydrophobicity will be permanently lost. One method is to promote crosslinking in the polymer for hard surface structures by plasma deposition process such as those used to form highly crosslinked fluorocarbon polymers. The other method is to use hard inorganic materials e.g., ceramics, for the creation of the surface roughness, and after formation of self-assembled-monolayers on the rough surface, hard superhydrophobic surface may be possible. Reference[97] shows a promising approach to achieve water repellency by diamond like carbon and PDMS. However, it these results suggest that the surface roughness is not adequate, although the surface hardness may be greatly improved. Further investigation of the effect of plasma deposition conditions on the creation of sufficient roughness is necessary.

Adhesion

In order to achieve superhydrophobic surfaces that are stable over long periods of time, the adhesion of deposited films is also a critical parameter. As shown in reference [37], after deposition of CFx species on the structured surface, the surface was superhydrophobic, however, when the surface was cleaned in an ultrasonic acetone bath, the contact angle dropped to 120˚. Adhesion between the deposited species and the substrate was very weak. However, good adhesion is expected between the deposited polymer and the substrate materials through appropriate control of plasma species and deposition conditions.

Oil repellency

For a superhydrophobic surface, oil will always display a lower contact angle than that of water[25]. Therefore it is difficult to achieve self-cleaning of oil on superhydrophobic surfaces. Usually, reentrant/overhang structures are critical in achieving superoleophobicity [25]. However, there is another self-cleaning mechanism based on the photocatalytic property of crystalline TiO_2 (especially anatase TiO_2). Reference [98] showed the possibility of preparing a superhydrophobic TiO_2 film by plasma etching followed by a hydrophobic surface treatment. Unfortunately, the surface lost superhydrophobicity due to oxidation of the surface hydrophobic species when irradiated with UV light. Despite this limitation, it may be possible to impart photocatalytic self-cleaning properties to a superhydrophobic surface for organic or oil cleaning by etching and deposition of a passivation layer with reduced amounts of TiO_2 exposed on the surface.

Optical transparency

Transparency of superhydrophobic films can be achieved by plasma etching or sol-gel processes[20, 39, 99], but most of the time, only the contact angle is reported or the hysteresis is very high. Further research should be performed to keep the surface structure sizes small while maintaining roll-off behavior that is characteristic of superhydrophobic surfaces.

1.7.2 Research objectives

1.7.2.1 Understanding the effect of surface structure on superhydrophobicity

As described above, two requirements exist for the establishment of surface superhydrophobicity. The first is high contact angle (>150˚). The relationship of contact angle to surface structure (expressed by the Wenzel surface roughness factor *r*) is described by the Cassie-Baxter equation. The second parameter is the contact angle hysteresis, which is defined by the difference between advancing and receding contact angle. By careful design of the surface structure, superhydrophobicity can be controlled for a specific surface tension and surface structure, which will be helpful in optimization of self-cleaning properties.

1.7.2.2 Developing UV stable superhydrophobic surfaces: Sol-gel process to prepare inorganic superhydrophobic surfaces

Polymeric materials, including polybutadiene, polypropylene (PP), polystyrene (PS), acrylate polymer, and polytetrafluoroethylene (PTFE) have been the primary materials utilized to prepare superhydrophobic surfaces. However, complications exist when polymeric materials are exposed to both atmospheric conditions where degradation occurs due to UV irradiation, and to impurities such as O_2 and moisture present in the environment. The resulting changes to hydrophilic surfaces will result in a loss of superhydrophobicity. In order to achieve stable Lotus effect surfaces for outdoor applications, the UV stability should be addressed first. Thus, we focused on inorganic surfaces from sol-gel process, which are more UV resistant, to achieve this objective.

1.7.2.3 Transparent superhydrophobic surface coatings through eutectic liquid templating

We propose the use of eutectic liquids to form silica aerogel films with optical transparency and superhydrophobic characteristics. Indeed, by careful control of film thickness, surface roughness, and a fluoroalkylsilane surface treatment, superhydrophobicity and transparency can be achieved from the use of a eutectic liquid composed of urea and choline chloride (2:1 molar ratio) with a melting point of 12 ˚C.

1.7.2.4 Metal assisted HF/H_2O_2 etching of silicon wafers for surface structure fabrication and multifunctional surfaces

Si surface texturing is used in quite a few applications such as Si nanowire fabrication, non-reflecting solar cell surfaces, sensors, biochips, and microfluidics devices. In this thesis we describe the use of a metal assisted etching technique to prepare surface structures for superhydrophobicity, while retaining other properties such as non-reflection for multifunctional surfaces.

1.7.2.5 Mechanically robust superhydrophobic surface

In the case of applications where handling of coated devices and abrasion of the superhydrophobic surface is inevitable, research on robustness improvement is critical. Thus, in this thesis, we investigate the preparation of superhydrophobic surfaces using polymer/silica nanoparticle coatings for improved robustness.

CHAPTER 2

FUNDAMENTAL UNDERSTANDING OF SUPERHYDROPHOBICITY

Regarding superhydrophobic surface preparation, biomimetic method of creating hierarchical surface structures similar to lotus leave surfaces is frequently employed. Here we will focus on the preparation of two scale structures (micro- or submicro-structures together with nanostructures) to achieve a self-cleaning superhydrophobic surface for the fundamental understanding of the superhydrophobic surface formation and the water droplet rolling-off (Cassie) and sticking (Wenzel) mechanism on a hydrophobic and rough surface.

Research into the creation of superhydrophobic surfaces, especially with respect to mimicking the two scale structure of lotus leaves, has received much attention. Recent studies suggest that topography at two length scales may not be necessary for superhydrophobicity. That is, even with only one nano scale-size feature, if the solid surface fraction (relative to air) is very small, and the surface contact angle is smaller than 90˚, superhydrophobicity can still be effectively achieved[100]. However, such surfaces are not in a thermodynamically stable state. After extended times, water can still penetrate inside the nanostructures, indicating that surface hydrophobicity is required to achieve a stable state. With only micron scale-size features, superhydrophobicity can also be achieved on a macroscopic scale; But when dealing with micro-droplets of water, this approach is not effective[101]. In contrast, nature has designed lotus leaves with hierarchical length scales, there by supplying reproducibility, requisite mechanical properties, and geometrical optimization for a non-fouling and self-cleaning surface.

Indeed, use of this biomimetic approach from nature is a successful way to develop different applications of superhydrophobicity[93].

Considerable effort has been expended to create hierarchically structured surfaces that mimick the surface structure of lotus leaves. For example, superhydrophobic surfaces with hierarchical structures can be formed by a number of techniques, including layer by layer process[71, 102], phase-separation micro molding methods using soluble polymers[103], binary colloidal assemblies[104], sol-gel silica[105], micellar solution casting of propylene-MMA diblock copolymer[106], polystyrene film preparation by the electrohydrodynamics method[107], carbon nanotube pattern generation [60, 61], laser etching of polydimethylsiloxane (PDMS) surfaces[108], and galvanic cell corrosion of a copper foil with aqueous phosphorus acid solution[76], nanosphere lithography[72], and adsorption of charged submicrometer polystyrene latex particles[109]. In addition, the relationship between surface structure, contact angle and hysteresis has also been widely studied[101, 110, 111]. Despite the extensive work reported, we are not aware of studies that illustrate a clear relationship between superhydrophobicity and the surface two scale roughness.

2.1 Investigation into Hierarchical Surface Structures by Combining Colloidal Self-Assembly and Au Sputter Deposition

Colloidal crystals can be formed on a substrate from monodisperse nano spheres, e.g., SiO_2 spheres and polystyrene spheres, as a result of assembly into arrays of hexagonal close packed or FCC layers. In this scenario, the as-formed surface is rough due to the regular arrangement of the monodisperse spheres. Although this surface is not superhydrophobic even after a surface treatment with hydrophobic surface modification agents[72], superhydrophobicity can be achieved by imparting nano scale structures on/in the surface to achieve multiscale roughness. Furthermore, this surface can serve as a model surface for the investigation of the effect of surface roughness on superhydrophobicity. In this study, we use monodisperse silica particles to form a thin layer on a glass slide. After deposition of a Au layer on top of the spheres followed by heat treatment to form Au nanoparticles, surface nanoroughness was generated. By controlling the Au deposition conditions, the necessary nanoroughness can be effectively designed into the surface. Such tunability of the structures furthers the understanding of the effect of surface nanostructure on superhydrophobicity and suggests specific ways by which superhydrophobic surface properties such as mechanical stability and durability can be achieved.

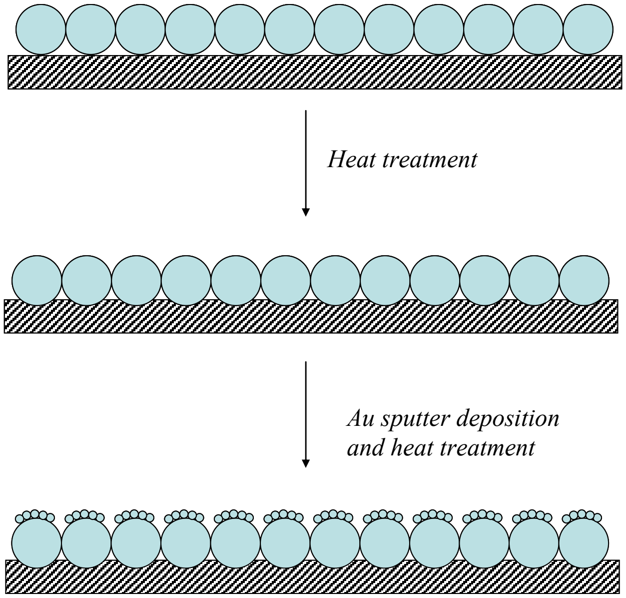

Figure 46. Schematic of the surface SiO_2 layer; for simplicity, only one layer of silica spheres is illustrated. It should be noted that the surface roughness will be the same for a monolayer and for a multilayer.

2.1.1 Experimental section

Materials. All solvents and chemicals are reagent grade and are filtered through 0.22 μm syringe filters (Gelman) except for tetraethyl oxysilane (TEOS, 99% Aldrich) which was distilled under vacuum condition before use. Absolute ethanol is obtained from VWR and 29% ammonium hydroxide is purchased from Fisher. Ultrapure water (18.2MΩcm-1) is used directly from a Milli-Q water system. Microscope slides (75×25×1mm, Fisher) are cut in half lengthwise and used as substrates, cleaned in Piranha solution (2:1 (vol/vol) mixture of 96% sulfuric acid and 30% aqueous hydrogen peroxide) at 80˚C for 30 min and subsequently rinsed extensively with de-ionized water and ethanol. The surface hydrophobicity modification agent trichloro(1H,1H,2H,2H-perfluorooctyl) silane (PFOS) is purchased from Aldrich.

Colloidal silica nanosphere synthesis. Monodisperse silica nanospheres are synthesized following the Stöber-Fink-Bohn method[112]. Nanospheres with diameters ranging from 200 to 700 nm and relative standard deviation <8% are obtained through strict control of the reaction conditions[113]. The size and size distributions of these samples are obtained from SEM and Beckman Coulter Model LS 13 320 laser diffraction particle size analyses. After the silica spheres were prepared, the colloidal suspension was centrifuged using an IEC multi centrifuge at 5000 rpm and washed and redispersed in absolute ethanol by ultrasonication. Five cycles were performed in order to achieve high purity colloidal suspensions.

Self-assembly of silica spheres. Silica sphere dispersions (10ml) with concentrations of 5wt% were placed in a cylindrical opticlear glass vial (Fisher Scientific, 3DR). The vial containing the sphere dispersion was immersed in an isothermal oil bath maintained at 75 ± 0.5 ˚C by a hotplate. The entire apparatus is placed on a vibration free bench. Prior to use, the microscope slides were soaked in a freshly prepared piranha solution (H_2SO_4/H_2O_2, 2:1) at 80˚C for 30 min, and rinsed with water followed by ethanol, and finally dried with a N_2 stream. A clean microscope slide was then placed into a vial containing the heated 10 ml silica sphere dispersions. The vial was then covered with a glass dish to allow ethanol evaporation, while minimizing convection from room air.

Au nanoparticle formation. The film of silica spheres was heated to 620 ˚C for 4 hrs to partially sinter the spheres and to improve adhesion between the silica spheres and the glass slide. A Au thin film was sputter deposited on the as-prepared silica sphere layer using an Ernest Fullam sputter coater. The sample was then placed in a Lindberg oven and heated to 620 ˚C at a rate of 20˚C/min to form Au nanoparticles.

Surface treatment by 1-pentadecanethiol (PDT) and PFOS. Samples with Au nanoparticles on their surface were placed in a PFOS/n-hexane solution (5mM) for 30 min to permit adsorption of a PFOS layer on the SiO_2 surface; subsequently the samples were treated at 150˚C in air for 1hr and at 220˚C for 5 min to promote silane hydrolysis and condensation, thereby forming a stable silanated layer on the silica surfaces. The samples were then placed in PDT/ethanol solution (1mM) overnight to form an organic monolayer on the Au surface.

Characterization. The as-prepared samples were characterized by high resolution field-emission scanning electron microscopy (FESEM; LEO 1530 FEG at 10 kV). For contact angle measurements, water droplets (4μl size) were formed with a 0.5 μl step on a microsyringe at a predefined height and static images were recorded; advancing contact angle of the droplet on the solid surface was determined from these images. Receding angles were measured by increasing the volume of the 4 μl water droplet to 6 μl and bringing it back to 4 μl by extracting the extra water with a volumetrically controlled pipette with the same 0.5 μl step.

2.1.2. Results and discussion

2.1.2.1 Contact angle changes of silica sphere arrays by chemical surface treatment

As shown schematically in Figure 46, monodisperse silica particle layers can be effectively formed on a glass slide by controlled evaporation of solvent[114, 115]. The particles are hexagonally ordered due to assembly through attractive capillary forces caused by solvent evaporation[116-118]. These structures can be considered a hemispherical close packed model for the study of water droplet wetting/dewetting behavior on rough surfaces[119].

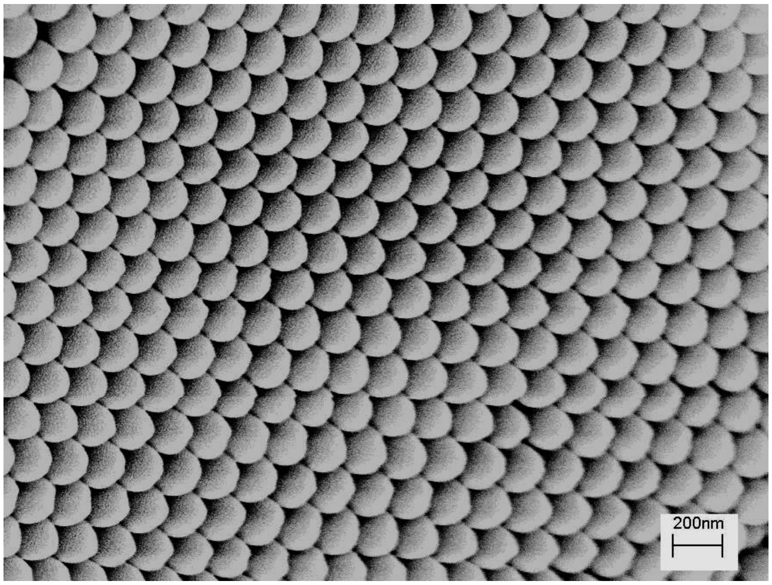

Figure 47. Self organized silica particle layer formed through controlled solvent evaporation (particle size: 200nm)

From Figure 47, it is obvious that the surface is periodic due to the regular sphere array on the glass slide. It is this order that allows the creation of structured surfaces as a result of the hexagonal packing of monodisperse spheres.

Using silica spheres with a diameter of 360 nm, we investigated the surface hydrophobicity by surface treatment with several silanes including: trichloro(1H,1H,2H,2H-perfluorooctyl) silane (PFOS), trichloro(3,3,3-trifluoropropyl)silane (TFPS), n-dodecyl trichlorosilane (DDTS), and octadecyl trichlorosilane (ODTS). As a result of soaking in a 5 mM solution of silane/n-hexane, a silanated layer was adsorbed onto the silica surface. After heat treatment at 150˚C for 1 hr and 220˚C for 5 min, a uniform layer of silylating agent was formed on the silica particle surface with the hydrophobic chains protruding outward; this chemical moiety imparts hydrophobic properties to the surface. The resulting contact angle data are shown in Table 1.

Table 1. Experimental contact angles and theoretical predictions.

silane	Advancing contact angle on flat (glass) surface (˚)	Advancing contact angle on silica sphere surface (˚)	Calculated advancing contact angle according to Cassie equation (˚)
TFPS	102.5	120.0	119.1
DDTS	107.9	134.4	130.6
ODTS	110.6	142.2	137.0
PFOS	115.3	157.2	150.3

When glass slides were treated with silanating agents, the contact angles ranged from 102.5˚ to 115.3˚ due to the different physical (chain length) and chemical (fluorinated) structures of various organic moieties on the silanes. For the same chemical structures, the chain length effect can be seen from the higher contact angle of ODTS (C18) than DDTS (C12). And for PFOS, when a layer was formed on glass, the CF_3 groups protrude outward from the surface. As a result, the CF_3-modified surface gave the lowest surface energy and highest hydrophobicity compared to the other three. On a roughened surface formed by colloidal silica particles, the contact angles were amplified relative to those of a smooth surface.

According to the Cassie equation for a heterogeneous surface,

$$\cos\theta_A = f_1 \cos\theta_1 + f_2 \cos\theta_2 \tag{17}$$

where $f_1 + f_2 = 1$

When the surface is composed of solid (designated as1) and air (designated as 2), eq. 17 applies. However, Cassie also indicated that when the solid surface is rough, eq. 17 can be formulated as[11]

$$\cos\theta_A = rf_1 \cos\theta_1 + f_1 - 1 \tag{9}$$

where the parameter r is the ratio of the actual solid-liquid contact area to its vertical projected area (Wenzel roughness factor).

We should point out that most previous studies used the Cassie equation in the form as in eq. 17

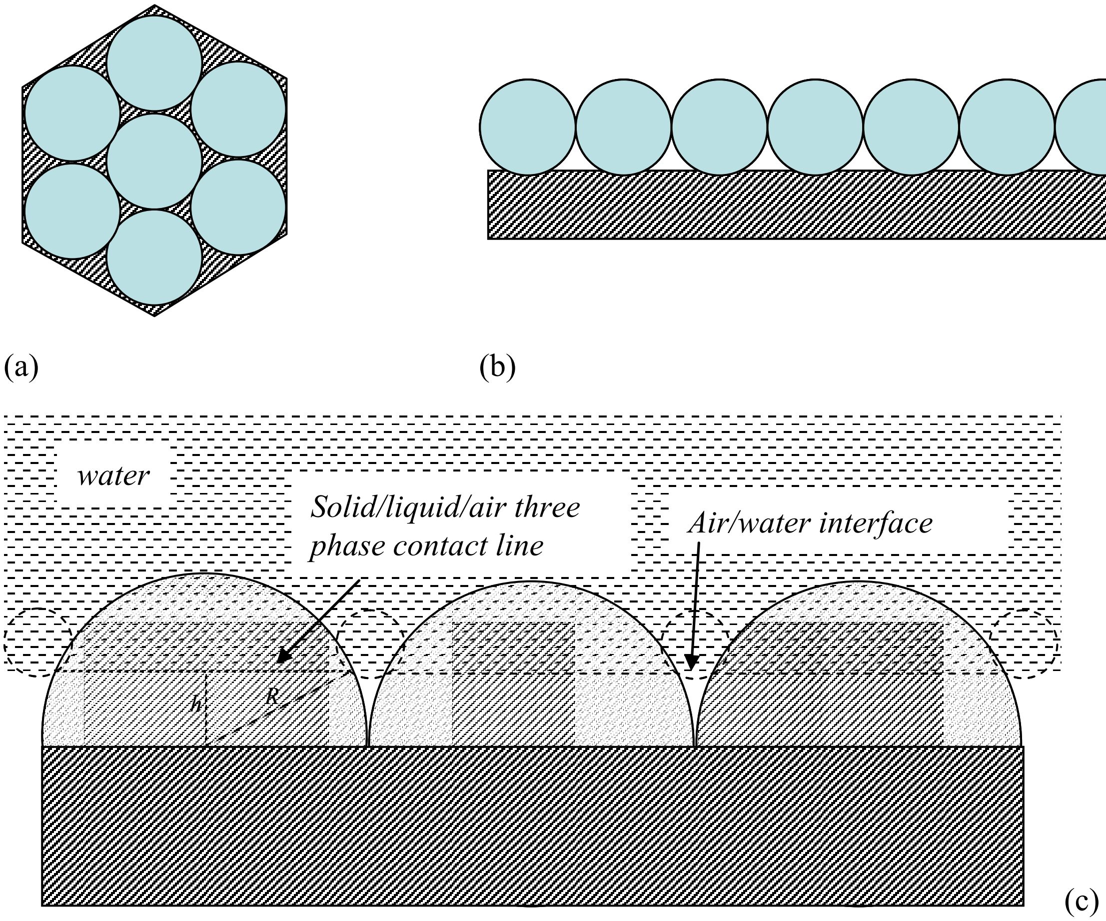

Figure 48. Top view (a) and side view (b) of silica spheres on glass substrates (note that the contact line should not be a perfect circle on the sphere surface); (c) Illustration of water contact with silica spheres; where *R* is the radius of the silica sphere, and *h* is the distance of the solid/liquid/air three phase contact line to the center plane of the spheres, here we just draw a hemisphere array on substrate for simplicity.

That is, the roughness factor was not included, although it plays a crucial role in the apparent contact angle; in order to more accurately describes the observations, we used eq. 9 to incorporate the surface roughness factor *r*. For the silica sphere arrays as shown in Figure 48, r is 2, assuming that water contacts the entire top hemisphere. Since $f_1 = \frac{\pi}{2\sqrt{3}}$ for hexagonally arrayed spheres as shown in Figure 48 (a), eq. 9 becomes

$$\cos\theta_A = \frac{\pi}{\sqrt{3}}\cos\theta_1 + \frac{\pi}{2\sqrt{3}} - 1 \tag{18}$$

Table 1 compares the experimental contact angles with those predicted from eq. 17. It is clear that with an increase of the Young's contact angle, θ_1 or θ_Y, the contact angle on the rough surface is increasingly higher than the calculated value; this trend is shown in Figure 49. These comparisons indicate that the initial assumption of water contacting the entire hemisphere is not valid. Rather the fraction of the sphere surface in contact with air at the edge of the water-solid interface increases with r, so that f_1 decreases. In addition, the experimental data cannot be fitted accurately to the Cassie equation if f_1 or r is constant. This fact suggests that the deviation of the measured contact angle from the calculated value results from the relationship of f_1 to r, not from the deviation between the true value of f_1 and the value used in the calculation. Such considerations further indicate that when the surface hydrophobicity increases (θ_1 increases), the amount of air trapped at the interface also increases, resulting in an increase in h and a decrease in r and f_1 as shown in eq. 20 and 21; Overall, the surface contact angle increases. For better description of the relationship between apparent contact angle, Young's contact angle and surface roughness, the distance h of the solid/liquid/air three phase contact line to the center plane of sphere array needs to be incorporated.

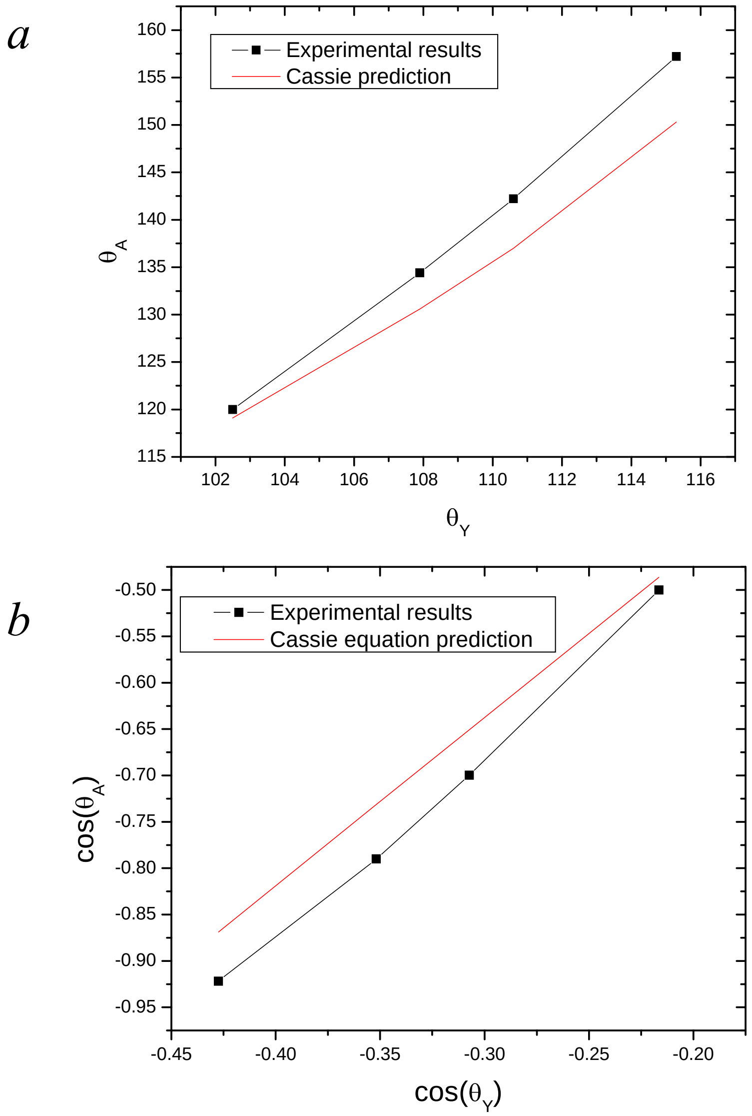

Figure 49. (a) Comparison of the contact angle data to that predicted by the Cassie equation; (b) the relationship of the contact angles on rough surface (cos(θ_A)) and smooth surface (cos(θ_Y)).

Geometrically, we can express f_1 and r as

$$f_1 = \frac{\pi(R^2 - h^2)}{2\sqrt{3}R^2} \tag{19}$$

$$r = \frac{2R}{R + h} \tag{20}$$

The Cassie equation can therefore be written in the form

$$\cos\theta_A = \frac{\pi(R-h)}{\sqrt{3}R}\cos\theta_1 + \frac{\pi(R^2-h^2)}{2\sqrt{3}R^2} - 1 \tag{21}$$

where *h* is the height of the water/air/silica surface three phase contact line referenced to the center line of the silica spheres as shown in Figure 48(c).

We note here that unlike previous reports[119, 120], in the composite contact interface of water with each silica sphere and air, the microscopic water/air interface should not be tangent to the silica sphere (if it were tangent, the water contact angle on the silica surface would be 180˚). Rather, the water/air interface is non-tangent to silica spheres so that the contact angle is <180˚, as illustrated in Figure 48(c). And the three phase contact line on a silica sphere is not a perfect circle due to the periodic arrangement of silica spheres and the air cushion around the silica spheres. Correspondingly, there should be a periodic distortion of the microscopic three phase contact line on the composite contact surface.

As the surface hydrophobicity increases, the length of the three phase contact line over each individual silica sphere decreases, which increases the macroscopic apparent contact angle at the silica sphere array surface [121, 122]. For the PFOS treated surface, the contact angle is the highest relative to the surfaces modified with the other three silanes. However, the contact angle hysteresis for the PFOS surface is too high (>30˚) to achieve superhydrophobicity due to the relatively long three phase contact line, which leads to pinning of the water droplets.

2.1.2.2 Effect of Au nanoparticle deposition

These above observations indicate that by grafting extremely hydrophobic materials (e.g., fluoro-silanes), on the silica colloidal sphere roughened surface, superhydrophobicity is still not attained. In order to achieve contact angles >150˚ with hysteresis <10˚ by structural approaches similar to those of lotus leaves, we altered the other important factor described in the Cassie equation: surface nanoroughness (r, as expressed in eq. 4) on the silica sphere surface. Nanoroughness can be imparted by fabricating hierarchical structures on top of the silica spheres, for example, by sputter deposition of a thin Au film which is composed primarily of Au nanocrystals with diameters <5 nm. Due to the small particle size, the melting point is dramatically reduced relative to that of bulk Au[123, 124]. As a result, heat treatment of the Au nanocrystals will cause melting at a temperature much below the temperature at which the silica particles are altered. Furthermore, due to the surface tension, the small particles will aggregate to form larger Au particles with a size range of 30-50nm after re-solidification. By this method, nanosized Au particles can be successfully introduced on top of the silica spheres.

2.1.2.2.1 Conditions of Au nanoparticle deposition

Heat treatment temperature effect on the nanostructure formation. We investigated three heat treatment temperatures for Au nanoparticle formation: 570, 620 and 670˚C. From Figure 50, it is evident that when the Au film was heated to 570˚C, no obvious structure was formed. When heated to 620˚C, Au nanoparticles were formed, while when heated to 670˚C, the Au nanoparticles sintered, thereby leaving no nanoparticles.

At a heat treatment temperature of 620˚C, treatment time was also investigated in order to determine the time needed to form appropriately sized Au nanoparticles; results are shown in figure 52. After the surface was treated for 10 min, Au nanoparticle formation had begun and surface roughness existed. When the heat treatment time was increased to 30 min, Au nanoparticles were clearly observed but were not evident on the sides of the silica spheres (Figure 52.b). At a heat treatment time of 2hrs, Au nanoparticles on the silica spheres attained a particle size between 30 and 50 nm, which is similar to the two scale structure characteristic of lotus leaves. For longer treatment times, the structure showed no change; thus, a heat treatment time of 2 hrs was used for subsequent studies.

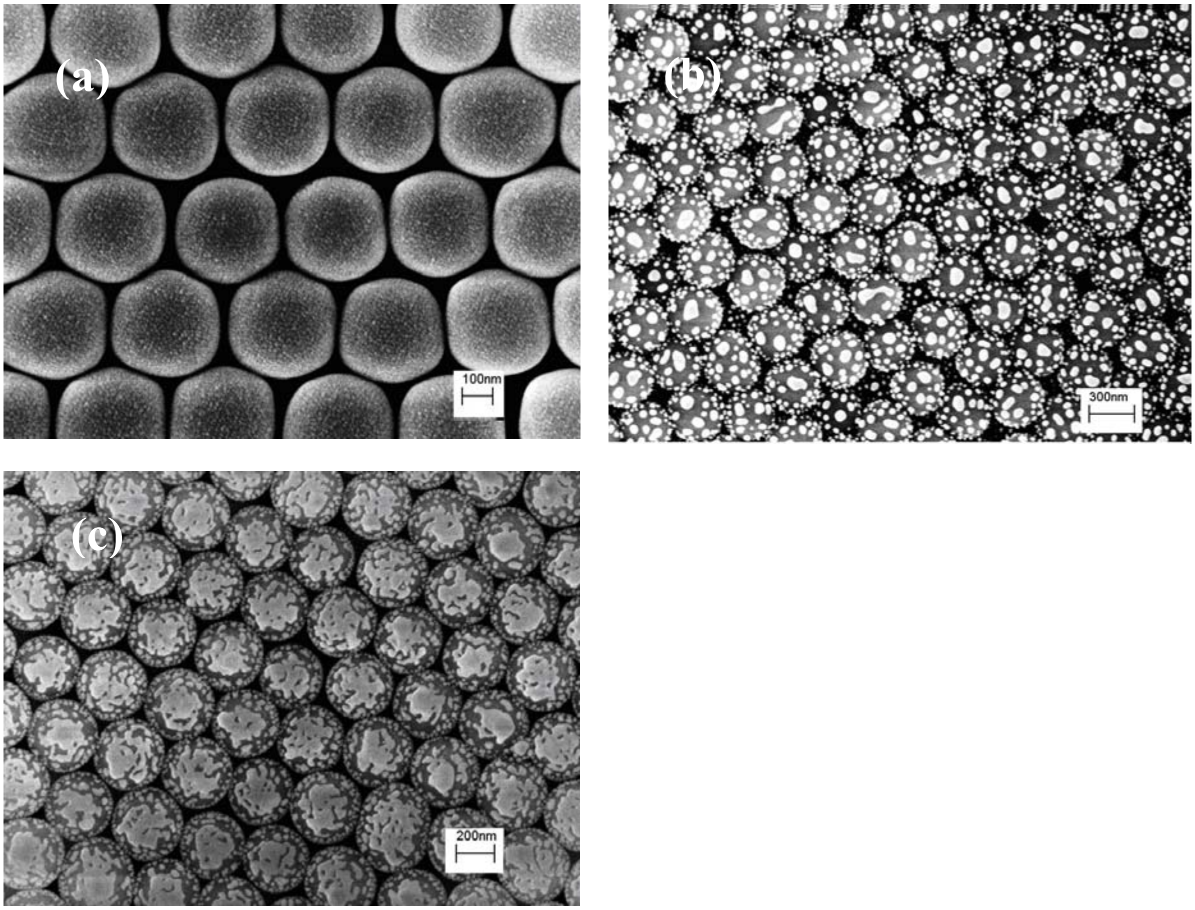

Figure 50. Temperature effect on Au nanoparticle formation; Au deposition for 90 sec, followed by heat treatment for 2 hrs in air at a) 570˚C, b) 620˚C, c) 670˚C.

Heat treatment time

Au sputter deposition time. As shown in supporting information in Figure 53, when the Au sputter deposition time is 40sec and is followed by a heat treatment at 620˚C for 2 hrs, the particle size is less than 10 nm). When the Au deposition time reaches 60 sec, ~10 nm Au nanoparticles are observed (some larger ones are formed, but they are a few in number) on the silica sphere surfaces; however, this particle size is not large enough to significantly increase the surface roughness factor r. At a deposition time of

120 sec, Au nanoparticles are sintered, and the nanoroughness is eliminated due to the existence of more Au on the silica sphere surface.

2.1.2.2.2 Relation between two-scale structures and contact angles

Water contact angles were measured for the samples shown in figures 52 and 53 to determine if the surfaces displayed superhydrophobicity or superhydrophilicity. For surfaces shown in figures 52, the contact angles are <15˚. In fact, for sample 53.c, the water droplet fully wet the surface (contact angle <10˚) due to the large capillary forces generated by the two scale structure. These observations, demonstrate that if the surface is hydrophilic, the contact angle on the hierarchical surface is reduced still further by the introduction of roughness. This indicates that the as-prepared surfaces are described well by Wenzel's roughness factor[12] (as shown in eq. 1). In order to achieve superhydrophobicity, it is necessary to treat the hydrophilic surface with modification agents to convert the surface into one that is hydrophobic. After the surfaces were treated with PFOS and PDT, the water contact angle increased substantially; the contact angles as a function of Au deposition time are shown in Figure 51. The highest contact angle observed was 167.3˚C when the Au deposition time was 90 sec. In addition, for the highest contact angle surface, the contact angle hysteresis is 8.5˚, which indicates that a superhydrophobic surface is achieved (hysteresis <10˚). However, for all other surfaces, the hysteresis values are >10˚, which is too large to be designated as a superhydrophobic surface; such observations result from the long three phase contact line. And compared to the bare silica sphere, according to the surface roughness definition, the sphere with Au nanoparticles showed higher values of r due to the increased surface area after the Au nanoparticles were formed on the silica sphere surface. Figure 54 shows a picture of a water droplet on the silica sphere/Au nanoparticle surface shown in Figure 53.c. From Figure 51 it is clear that surface contact angle hysteresis can be effectively reduced by the construction of a surface with two scale roughness using Au nanoparticles on SiO_2

spheres. The phenomena observed are primarily due to the effect of surface geometry on the prevention of water penetration and to a reduction of the three phase contact line (discontinuity) that results from the introduction of nanostructures, which lower the energy barrier between metastable states during the movement of a water droplet. The increase of the apparent contact angle can be explained by eq. 4 as a result of the formation of Au nanoparticles which increased the surface area and thus an increased roughness factor *r*, and resulted in an increase in the apparent contact angle.

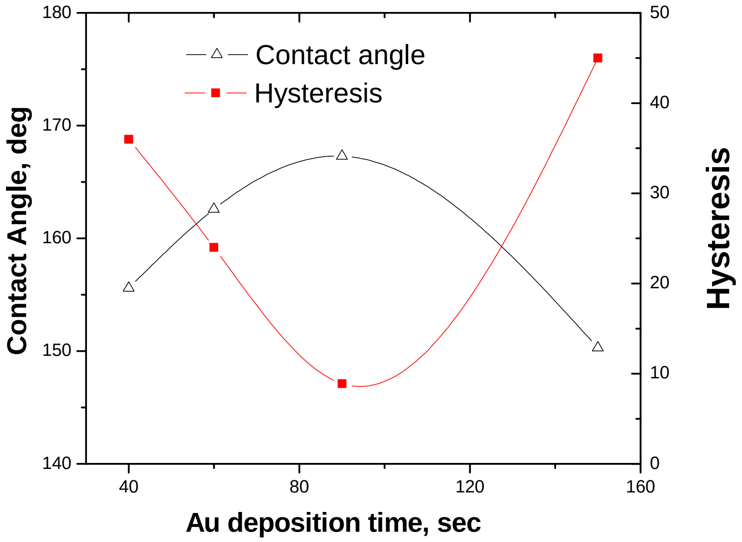

Figure 51. Dependence of contact angle on Au sputtering time for PFOS-treated two scale rough surfaces; the heat treatment was performed at 620˚C for 2hrs.

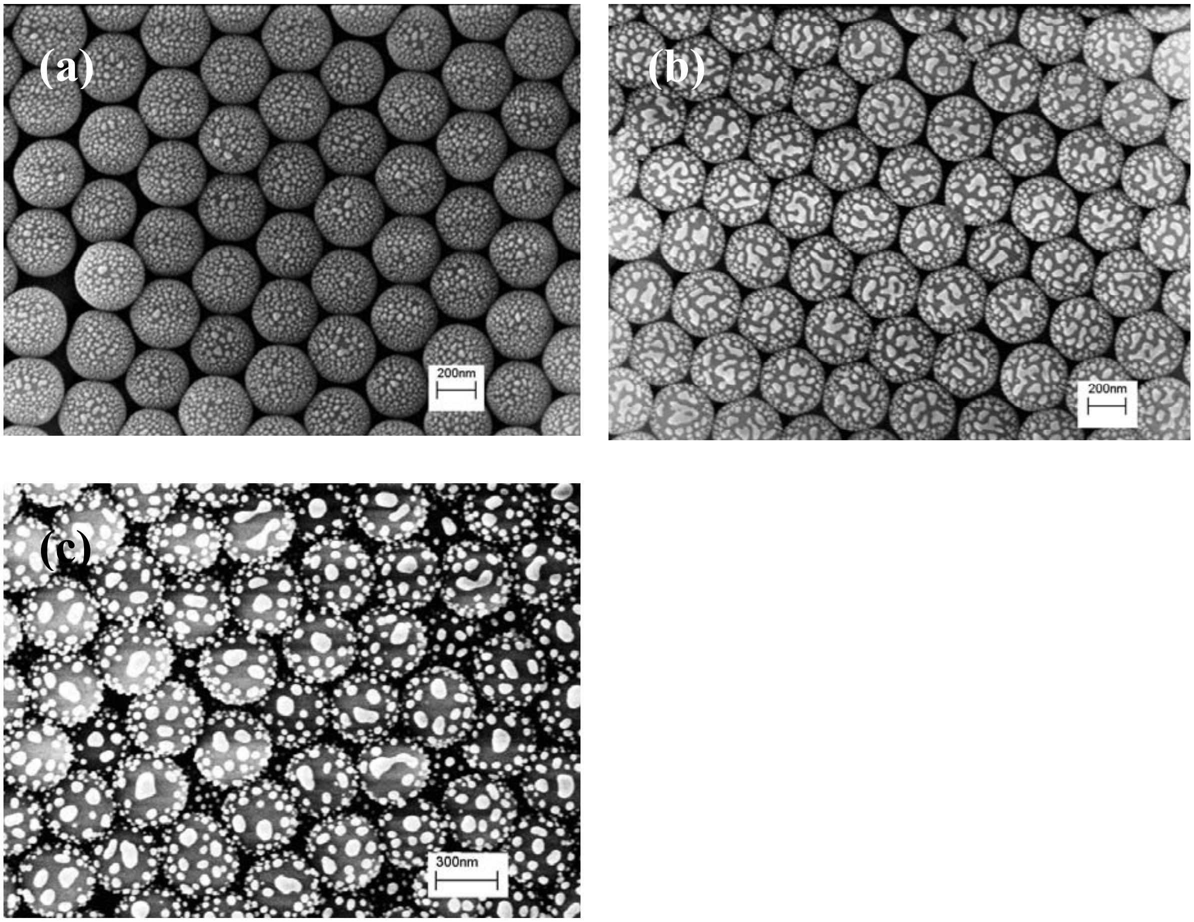

Figure 52. Effect of heat treatment time for a Au sputter deposition time of 90 sec; a) 10 min, b) 30 min, c) 2 hrs, all at 620˚C.

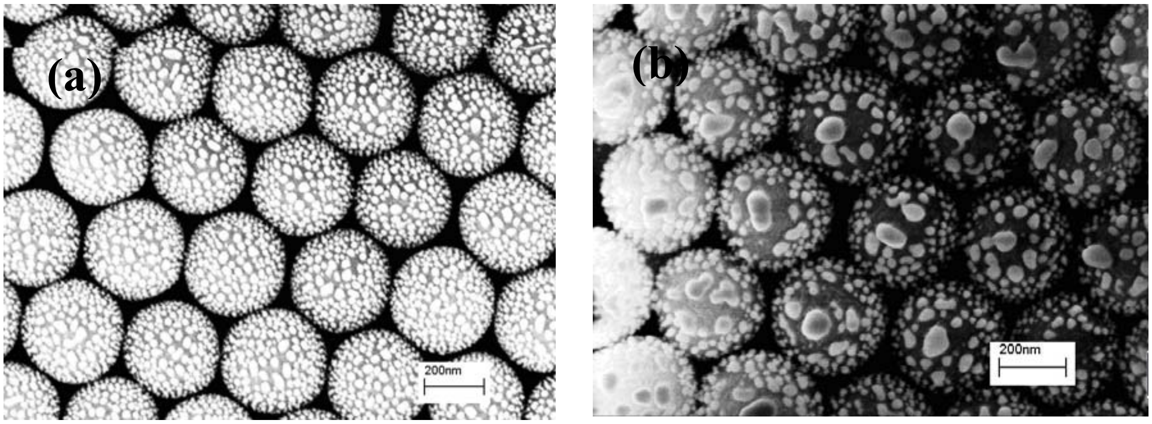

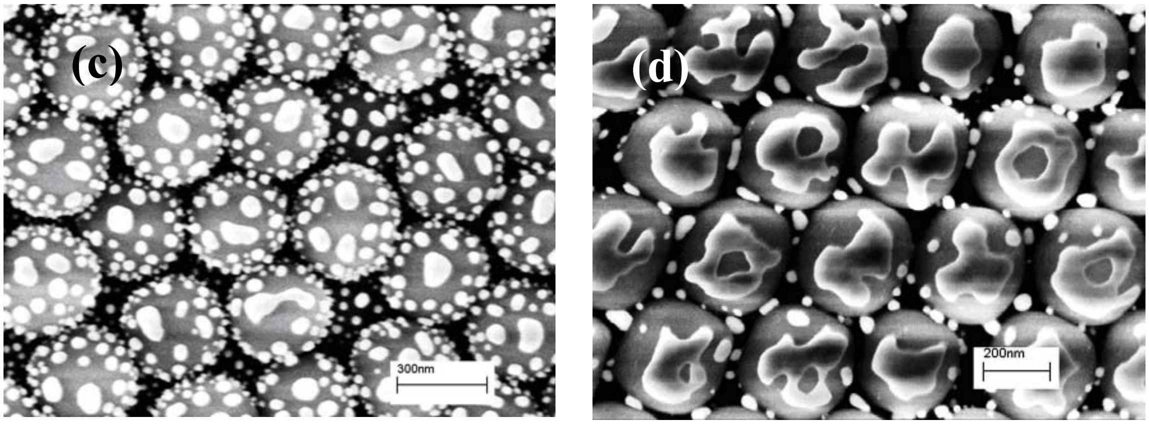

Figure 53. SEM images of two-scale structured silica/Au surface morphology at various Au sputter deposition times; a) 40sec, b) 60 sec, c) 90 sec, d) 120 sec.

Figure 54. Photograph of the superhydrophobic surface from silica sphere/Au nanoparticle sample shown in figure 53(c).

Conclusions

Using a controlled evaporation method, densely packed monodisperse silica spheres were organized onto a glass slide to create a rough surface for superhydrophobicity investigations. After silanation of the sphere surfaces, the contact angle dependence on the surface roughness was fitted to a modified form of the Cassie equation that included a roughness factor. Different surface hydrophobicity, generated by attaching different silanes containing various hydrocarbon or fluorocarbon chains to the sphere surfaces, led to variation in contact angles, but superhydrophobicity was not achieved. Increased contact angles were achieved by employing a biomimetic approach similar to that of Lotus leaves to create a two scale rough structure. The two scale roughness was realized by sputter deposition of a thin Au nanocrystalline layer on the as-prepared silica spheres followed by heat treatment at 620˚C; this process sequence caused Au nanoparticles to form on the sphere surfaces. The water contact angle observed on this biomimetic surface was >160˚, and the hysteresis was <10˚. These studies demonstrate that an increase of the roughness factor can be realized by creation of nanoscale roughness on an initially rough surface, thereby enhancing superhydrophobicity. Such surfaces may serve as model biomimetic surfaces and can be appropriate for applications that require mechanically stable superhydrophobic surfaces that resist fouling, dust incorporation, or inhibit corrosion.

2.2 Wall Inclination Effect on Hierarchical silicon etched structures

The effect of surface structure on superhydrophobicity is of much interest due to the dependence of structure on the attainment of a high water contact angle and reduced contact angle hysteresis. Superhydrophobicity was first observed on lotus leaves where high water contact angle and low hysteresis cause water that falls on the surface to bead and roll off the surface, thereby leading to water repellency and self-cleaning characteristics[2, 125, 126]. Such surface properties are also critical in MEMS antistiction[127], friction reduction[128], and anti-corrosion[129] applications. In addition, superhydrophobic surfaces offer much promise for the formation of high performance micro/nano structured surfaces with multi-functionality that can be used in optical[130, 131], photoelectric[132], microelectronic, catalytic and biomedical applications.

Superhydrophobicity is generally achieved on a hierarchically structured surface. For instance, although both the Wenzel state and the Cassie state display a high contact angle, transition from a Wenzel state to a Cassie state is required for reduced adhesion, and this transition occurs at a critical contact angle θ_c.[133] Substantial effort has been expended on the generation of micron-scale structured surfaces that also possess nanoscale roughness,[14, 60, 110, 134, 135] since superhydrophobicity can be achieved based on such hierarchical structures. However, most of the micron structures reported are structures with vertical walls[110, 136]; generally, these structures alone can maintain a Cassie state. Although the Cassie state does not ensure superhydrophobicity, addition of nanoscale roughness can facilitate the desired superhydrophobicity. For micron-scale structures in the Wenzel state, the ability to achieve superhydrophobicity is even more limited. That is, after a hydrophobic surface treatment, nano-scale structures are needed to first transition from the Wenzel state to the Cassie state, and then to enhance the contact to achieve superhydrophobicity. The effect of roughness on superhydrophobicity can be shown clearly from the Wenzel and Cassie-Baxter equations. However, the detailed effect of hierarchical structure especially on the Laplace pressure of water meniscus and thus the work of adhesion, both of which are crucial to maintain a high contact angle and low contact angle hysteresis, is not delineated by the two equations. Lafuma et al. have demonstrated that the Wenzel to Cassie transition can be induced by applying a pressure on the water droplet[133]. Recently Bormashenko et al. also showed that the transition can also be induced by vertical vibrating a water droplet on rough surfaces[137].

In this study, we mimick the hierarchical structure of lotus leaves by preparing an artificial superhydrophobic surface by simple silicon etching techniques to demonstrate and quantify the effect of two scale roughness on superhydrophobicity. The micron pyramid structures were prepared from anisotropic KOH etching. The nanostructures were prepared from metal assisted HF/H_2O_2 etching[130, 132, 138]. The transition from Wenzel state to Cassie state for superhydrophobicity was demonstrated by controlling the surface structures and surface hydrophobicity.

2.2.1 Experimental Details

n-type silicon (100) wafers with a resistivity of 3-10 Ω cm were used in all experiments. KOH etching was performed in a solution of KOH (3%wt), water and isopropyl alcohol (20% by volume) at 85˚C for 20-30 min. Prior to etching, a thin discontinuous layer of Au with a thickness of 5 nm was deposited by e-beam evaporation. Etching was then performed for various times in a HF/H_2O_2 solution (49%HF, 30%H_2O_2 and H_2O with a volume ratio of 1:5:10). Subsequently, the Au nanoparticles of diameter ~ 5-10 nm were removed by immersing the samples in KI/I_2 (100 g KI and 25g I_2 per 1L H_2O) for 60 seconds.

Contact angle measurements were performed with a Rame-Hart goniometer that has a CCD camera equipped for image capture. Scanning Electron Microscopy (SEM) was used to investigate the surface morphology. After fabrication of the surface structure, surface fluorination was performed by treatment with various fluoroalkylsilanes. Ten millimolar solutions of 3,3,3-trifluoropropyl-trichlorosilane, dodecyltrichlorosilane, octadecyltrichlorosilane and perfluorooctyl trichlorosilane (PFOS) were formed in hexane. For a specific treatment, the structured silicon wafer was soaked in one of these solutions for 30 min followed by a heat treatment at 150˚C in air for 1 hour, to complete the hydrophobic surface modification.

2.2.2 Results and Discussion

When surfaces are randomly roughened, the surface structures are not vertically oriented to the substrate; thus, they often show inclined walls as shown schematically in Figure 55. The contact angle dependence on such surface structures is very important when considering superhydrophobicity. The studies described below generated silicon pyramids to serve as a model surface to investigate the effect of inclined side wall angles on hydrophobic and superhydrophobic behavior. Micron-sized surface pyramids were prepared by anisotropic KOH etching of silicon substrates with (100) orientation; the bases on these pyramids result from the intersection of (111) orientated crystallographic planes. An SEM image of the surface is shown in Figure 56a. This surface was treated with PFOS which yielded a contact angle of 146.3˚ and a contact angle hysteresis >60˚. Deposition of nanometer sized Au particles on this pyramidal surface was followed by silicon etching in HF/H_2O_2 for 60 seconds, and then removal of the Au nanoparticles in KI/I_2 for 60 seconds. These treatments resulted in the production of surface nanostructures directly on the pyramid surfaces. After PFOS treatment, the surface displayed superhydrophobicity with a contact angle as high as 165.8˚.

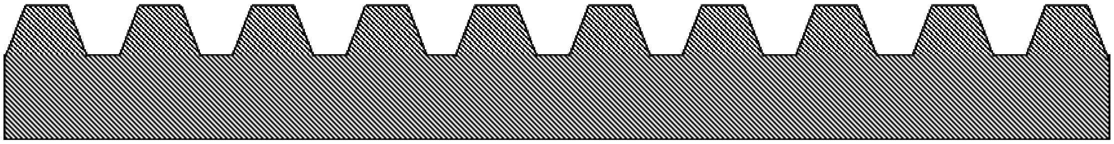

Figure 55. Model structure of inclined side walls on a substrate surface.

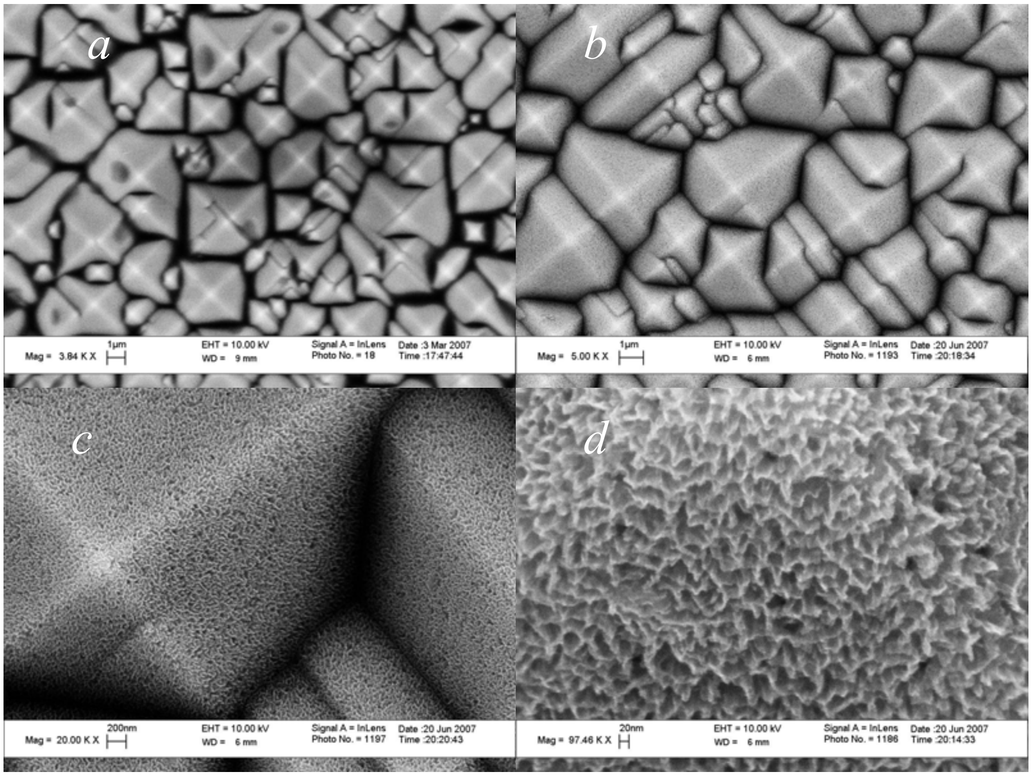

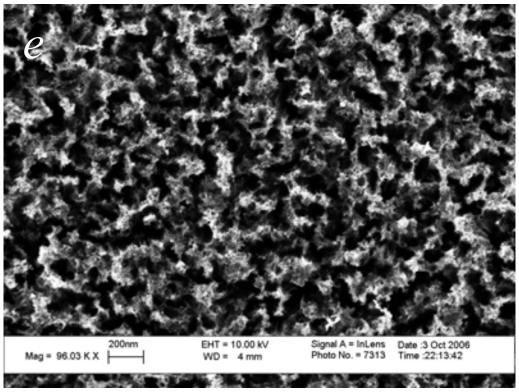

Figure 56. Surface structures of silicon after etching in KOH at 80˚C for 25 min (a), two scale rough surfaces resulting from pyramid and nanostructure from Au assisted HF/H_2O_2 etching; different magnifications (b,c,d), and nanostructures on a flat silicon surface with (111) orientation (e) from Au assisted etching are shown.

Superhydrophobicity is usually achieved through the formation of a composite interface (solid/water and air/water interfaces) with air trapped within the structure[16]. Figure 57 illustrates the geometry involved when water contacts surface structures with inclined walls. The Laplace pressure of the meniscus from water droplet/surface contact plays an important role in maintaining the composite interface by confining the water at the air/water interface. The relationship between the Laplace pressure and the inclination angle α is given by equation.(22)[139]

$$\Delta p = p - p_0 = -\frac{\gamma \cos(\theta - \alpha)}{R_0 + h \tan \alpha} \tag{22}$$

where γ is the surface tension of water, θ is the Young's contact angle of liquid on the surface, α is the inclination angle as illustrated in Figure 57, p is the pressure on the liquid side of the meniscus (drop internal pressure), and p_0 is atmospheric pressure. From this equation it is clear that the Laplace pressure is dependent on water height h, Young's contact angle θ and inclination angle α. The height h is dependent upon the hydrostatic pressure of water on top of the structured surface. It should be noted that for vertically walled structures, the Laplace pressure is dependent only on Young's contact angle.

Equation (22) indicates that the Laplace pressure is reduced due to the inclination angle α; the higher the inclination angle, the lower the Laplace pressure on the meniscus. When the inclination angle is sufficiently high for a particular surface structure (depending on θ), water wets the structured surface completely without air entrapment. In a metastable Cassie state, application of pressure to the water droplet can affect the hysteresis if the drop adheres to the surface. This can lead to a transition from a Cassie state to a Wenzel state. The transition pressure is related to the Laplace pressure which holds the droplet upon the composite surface. For a surface structured with an inclination angle, the conversion takes place at a much lower pressure.

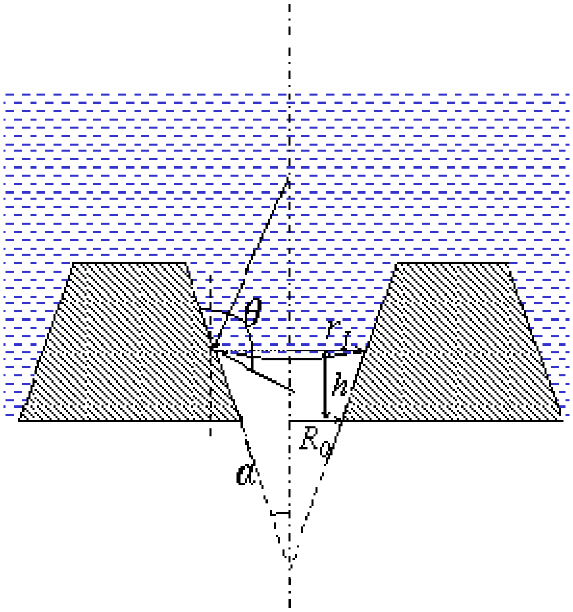

Figure 57. Water contact interactions with surface structures with inclined walls.

The range of possible situations with varying inclination angles is illustrated in Figure 58. This phenomenon inhibits the ability to achieve a superhydrophobic state to a greater extent than experienced on vertical structures. Interestingly, this scenario is the one most likely encountered in nature. For structures with vertical walls, the water meniscus either remains on top of the structure or moves to the bottom of the structure when pressure is applied to the water. However, because of the inclination angle, the Laplace pressure increases when the meniscus approaches the structure bottom (decreasing h, as shown in Figure 57). Equation (22) also shows that when the surface hydrophobicity increases (increase of θ), the Laplace pressure increases and more air can be trapped between the structures, leading to an increase in apparent contact angle and reduced contact angle hysteresis as illustrated in Figure 58.

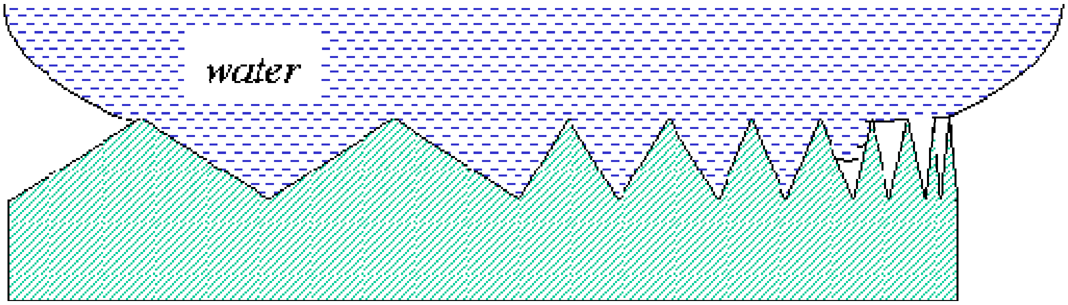

Figure 58. Water droplet on a hydrophobic surface with inclined wall structures of various angles.

The dependence of the apparent contact angle on Young's contact angle and surface roughness is shown in Figure 59 as calculated from the Wenzel and Cassie-Baxter equations. For the Cassie state, the surface solid/liquid contact fraction f_1 is critical to establishing the apparent contact angle, while Young's contact angle is not an important factor. However, the Wenzel state is more dependent on the Young's contact angle. That is, surface hydrophobicity can be used to increase the apparent contact angle for Wenzel states, while for Cassie states, a reduction of the fraction of solid/water contact is needed.

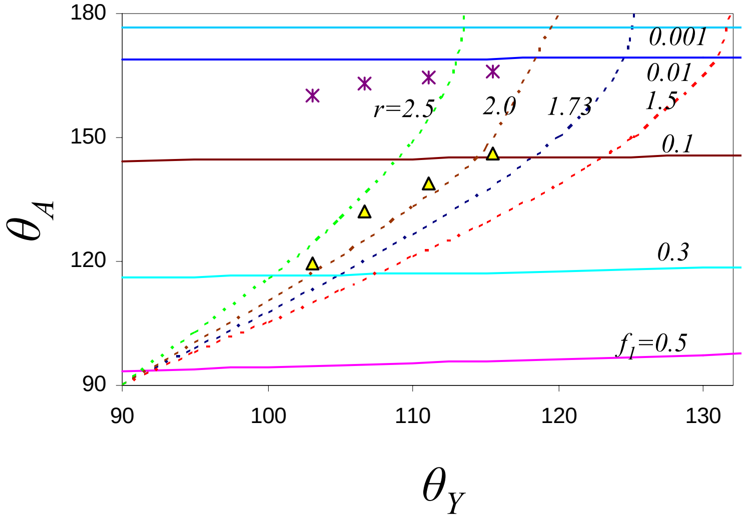

Figure 59. Contact angle calculations based on the Wenzel equation: $\cos\theta_A = r\cos\theta_Y$ (dotted lines) and the Cassie-Baxter equation: $\cos\theta_A = f_1\cos\theta_Y + f_1 - 1$ (solid lines). Data points: stars represent the contact angles on two scale rough silicon surfaces; triangles represent the contact angles on micron-scale pyramid surfaces; both surfaces have undergone silane treatment as described in Table 2.

Table 2. Contact angles resulting from different silane treatment.

Silane used	Sessile drop contact angles on a flat Si surface (degree)	Sessile drop contact angles on a silicon pyramid surface (degree)	Advancing contact angles on a two scale structured Si surface (degree)	Contact angle hysteresis (degree)
TFPS	103.1	119.7	160.2	28.2
DTS	106.7	132.1	162.9	17.9
ODTS	111.0	139.1	164.7	4.4
PFOS	115.5	146.3	165.8	2.1

For silicon surfaces with micron-sized pyramids, the effect of surface hydrophobicity on contact angle was investigated by performing surface treatments with a variety of different silanes that display different Young's contact angles on the surface (Table 2).

The triangles in Figure 59 designate the contact angles observed after silicon pyramid surfaces were treated with the four different silanes listed in Table 2. Clearly, with an increase in surface hydrophobicity (Young's contact angle), the apparent contact angles increase consistent with the Wenzel equation. According to the data in Figure 59, the Wenzel surface roughness is ~2.0. Previous studies[15] have suggested that for surface structures with inclined side walls, there is no energy barrier for the transition between the Cassie state and the Wenzel state if Young's contact angle $\theta_Y < 90° + \alpha$. Therefore, the Cassie state will always transition to the Wenzel state because it is a lower energy state. Indeed, our observations indicate that although the contact angle is higher (Cassie state) when the water droplet initially touches the pyramid surface, the contact angle drops quickly to a lower value (Wenzel state) as a result of the absence of an energy barrier between the two states.

An effective way to increase the Laplace pressure for superhydrophobicity is to generate nano-structures on the silicon pyramid surface as shown in Figure 60; SEM images of the surface hierarchical structures are shown in Figures 56b, c, and d. For a surface with inclined wall structures, the wetting behavior represents a combination of air entrapment, surface hydrophobicity and wall inclination. For the two scale structures on silicon surfaces, we presume that the nano-structure, as shown in Fig 2d, merely improves the surface hydrophobicity since the contact angle after PFOS treatment is 148.1°, which was obtained on nanostructures from Au assisted etching of a Si (111) surface, as shown in Fig 2e. But if the surface has only micron scale pyramids showing a Young's surface contact angle of ~115° after PFOS treatment, the surface is not superhydrophobic According to Equation (1), the Laplace pressure is greatly enhanced when a high contact angle θ exists. In addition, the extended three phase contact line on smooth surfaces is segmented into smaller ones on pyramid surfaces with nanostructures.

As a result, the surface exists in a stable Cassie state and is superhydrophobic. This leads to an improvement in the superhydrophobic stability on micron-scale pyramid surfaces with air entrapment at the composite contact interface. The result of forming a hierarchical structure is to achieve/enhance the Cassie state and thus surface superhydrophobicity through the interplay of surface hydrophobicity, air entrapment and inclination angle. Such effects cannot be achieved readily by structures with only one size scale. On two-scale rough surfaces, the increase of surface hydrophobicity also improves the apparent contact angle, but the effect is not a large, since these surfaces already show very high contact angles in the Cassie state as shown in Table 2 and Figure 59 (stars).

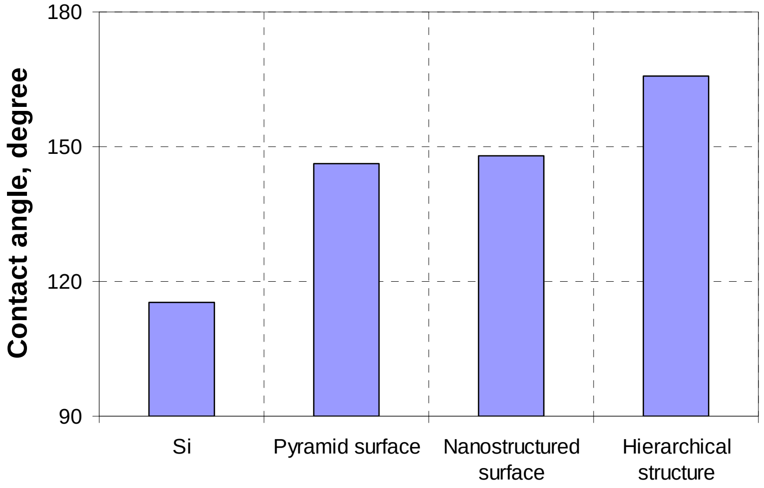

Figure 60. Contact angles on silicon surfaces with different surface texturing after PFOS treatment. For a silicon pyramid surface that possesses a hierarchical structure, a superhydrophobic surface with minimum hysteresis results after PFOS treatment. Nanostructures were formed by Au assisted etching of silicon surfaces in HF/H2O2 for 60 seconds with a Au layer of 5 nm on the silicon (111) surface.

The hierarchical structures not only facilitate improvement of the apparent contact angle, but also reduce the contact angle hysteresis as shown in Table 3.

Table 3. Contact angle hysteresis on different textured surfaces after PFOS treatment.

Surfaces	Hysteresis
Si	–
Silicon pyramids	>60°
Silicon nano-structured surface*	>60°
Hierarchically structured pyramid surface*	2.1°

*Nanostructures formed from Au assisted etching of silicon surfaces in HF/H_2O_2 for 60 seconds with Au layer of 5 nm on the silicon (111) surface.

For contact angle hysteresis related to water/solid adhesion, the hydrophobic surface plays two roles. First, adhesion of the solid/water contact interface is reduced due to the lowered surface tension of the solid surface γ_S; the work of adhesion can be estimated as $w_{ad} = 2\sqrt{\gamma_w \gamma_s}$ [23]. Second, the increased hydrophobicity of the surface gives a higher water contact angle (θ) on the surface due to the change in surface free energy. This results in a higher Laplace pressure, and so the meniscus moves away from the bottom of the structures. Therefore, the water/solid contact area is reduced leading to reduced adhesion between water and the solid surface. This fact is manifested in a difference in contact angle hysteresis of two-scale rough surfaces that have different silane treatments as shown in Figure 55. Such observations also confirm the proposal that hysteresis is more important than structure in achieving superhydrophobicity[121].

.

Conclusions

Surface structures with inclined wall angles are important in establishing superhydrophobicity since they inhibit the ability to achieve a stable Cassie state from a thermodynamic point of view. This consideration is related to the Laplace pressure on the water meniscus, which helps to maintain a composite contact interface. The Laplace equation was used to derive a relationship between Young’s contact angle and the geometry of surface structures. Surface hydrophobicity was varied by using different silane treatments on silicon pyramid surfaces to demonstrate that for these structured surfaces the stable state is the Wenzel state. By changing the surface hydrophobicity, the apparent contact angle changed according to the Wenzel equation for surface structures with inclined side walls. Superhydrophobicity can only be achieved if a second scale nano rough surface was constructed on top of the silicon pyramid surface to maintain a stable Cassie state. Contact angle hysteresis was related to surface adhesion between the liquid and the solid surface which is a function of liquid surface tension according to the Young-Dupré equation. The surface liquid/solid contact area, hydrophobicity and geometry of surface structures are thus inter-related in achieving superhydrophobicity. An increase in the surface hydrophobicity (Young’s contact angle) leads to a decrease in the water/substrate contact area fraction and therefore a reduction in contact angle hysteresis and an increase in the apparent contact angle.

CHAPTER 3

RELATIONSHIP BETWEEN WORK OF ADHESION AND CONTACT ANGLE HYSTERESIS

For a superhydrophobic surface, in addition to the high contact angles, the contact angle hysteresis is also critical in achieving a roll-off characteristics. Contact angle hysteresis of a superhydrophobic surface is generally attributed to surface roughness and chemical heterogeneity[140], which result in a variation of contact angles across a surface. The difference between advancing and receding contact angles of a water droplet is termed contact angle hysteresis. Lower contact angle hysteresis corresponds to an enhanced ability for the water droplet to move on a surface[141], a process of great importance for the application of superhydrophobic surfaces to non-fouling applications. It is generally unclear whether contact angle hysteresis, analogous to other hysteretic phenomena (e.g., magnetism), can be described by irreversible transitions or “jumps” between domains of equilibrium states.

The effect of roughness on apparent contact angles can be modeled by the Wenzel and Cassie equations[11, 142]. Various model surfaces containing patterned structures (e.g., Si, polymers) with different shapes have been invoked for the investigation of the relationship between contact angle and surface roughness[14, 101, 122, 143, 144]. Furthermore, a relationship between the contact angle hysteresis on a smooth surface and on a rough surface has also been established[17]. In some cases, the drop contact perimeter or three phase contact line, has been proposed as a defining parameter[122]. Such considerations involve the effect of surface structure on the movement of the contact line around the drop, because most of the friction is experienced in the region of the contact line[145]. However, reported data on a patterned surface with various feature sizes but a constant solid contact surface area and surface area fraction displayed no significant change in hysteresis with pattern scaling despite a change in the perimeter by a factor of 8; rather, the superhydrophobic contact angle remained constant to within 2°.[31]

Besides the water contact angle, the hysteresis should also be considered in determining the surface hydrophobicity. The sliding angle and driving force needed to start a drop-moving over a solid surface can be described as Equations 3 and 4, respectively:

$$\sin\alpha = \frac{\gamma_{LV}(\cos\theta_R - \cos\theta_A)w}{mg} \tag{23}$$

$$F = \gamma_{LV}(\cos\theta_R - \cos\theta_A) \tag{24}$$

In equation 23, α is the sliding angle, m is the weight of the water droplet, w is the width of the droplet, γ_{LV} is the surface tension of the liquid, and the θ_A and θ_R are the advancing and retreating contact angles, respectively. In equation 24, F is the critical line force per unit length of the drop perimeter. These equations indicate how the difference between the contact angles on a sliding surface (the hysteresis) affect the water repellence (hydrophobicity).

In this chapter, a model to establish a relationship between the equilibrium state (work of adhesion) and the dynamic state (contact angle hysteresis in the form of $\cos\theta_R - \cos\theta_A$) is proposed and predictions compared with previously published data. We also prepared patterned Si pillar arrays and treated them with different silanes to allow comparison to trends predicted by the model.

According to Young-Laplace eq,

$$\Delta p = \frac{2\gamma}{R} \tag{25}$$

where γ is the surface tension of liquid, and R is the radius of curvature for the liquid meniscus, concave: minus, convex: plus; $\Delta p = p - p_0$, the difference between the pressure under liquid surface and the atmospheric pressure. A certain curvature will lead to a pressure difference on the liquid meniscus. In the case of a cylindrical capillary, as shown in Figure 61, the shape of a meniscus (concave or convex) determines whether the surface tension holds a water droplet up (water repellency) or draws it down (water attraction). And the shape of a meniscus only depends on the surface tension of water and capillary materials. When the capillary is non–cylindrical and shows a tilt angle, the shape of liquid meniscus is dependent on the surface structures as shown in Figure 62. Even for a hydrophobic capillary surface, it may also show concave meniscus as illustrated in Figure 62b. Therefore the wetting property is surface structure dependent. In order to achieve water repellency, the convex meniscus in capillary is desirable and the surface tension will hold up the water droplet sitting on top of the structure. In contrast, the concave meniscus (Figure 62b) will extract water deep into the structures which will increase the adhesion of water on the structured surface and fail to achieve superhydrophobicity. Unfortunately, b is the most commonly seen scenario. In order for *b* to have the same meniscus as a, the surface should be either more hydrophobic than that of *a* or there is a second scale of roughness on the surface to increase the contact angle like lotus leaves. The former surface clearly will have an increased contact angle on the capillary surface and the latter one will also show an increased apparent contact angle due to the surface 2nd-roughness amplification of the Young’s contact angle. Therefore for both cases a convex meniscus will result. In addition to the surface physics parameters such as structure height, diameter and pitch size effects on superhydrophobicity, the tilt angle is also very important.

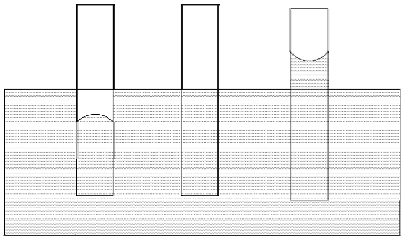

Figure 61. Three cases of water meniscus in capillaries with different surface tensions.

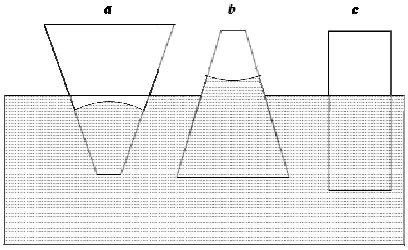

Figure 62. Illustration of the shape dependency of water meniscus on a surface with young's contact angle of 90˚.

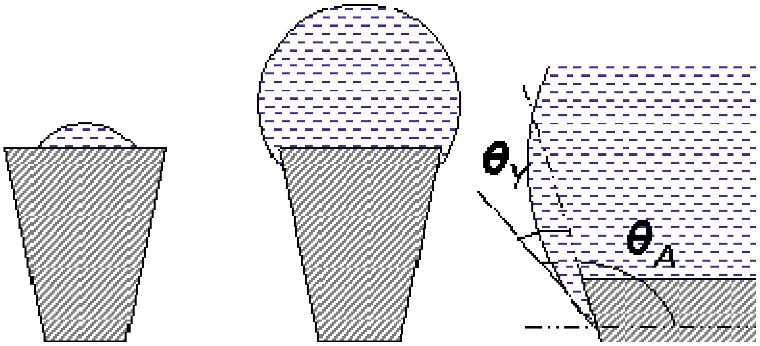

Figure 63. Illustration of the relation between apparent contact angle (θ_A) and Young's contact angle (θ_Y).

The geometrical effect on apparent contact angle is illustrated in Figure 63. Although the flat surface is hydrophilic, when on a pillar top surface, the apparent contact angle can be the sum of the Young's contact angle and the tilt angle of the surface structure wall. This demonstrated how a hydrophilic surface can also be made superhydrophobic if the surface structures are properly designed. In addition, surface structures defined in such a way can be made even oleophobic as shown in Figure 64. Based on this research, the understanding of structure design for achieving a Cassie state contact (composite contact for superhydrophobicity) can be illuminated. This is of great significance for achieving superhydrophobicity on a moderate hydrophilic surface, and superoleophobic surface for oil self-cleaning.

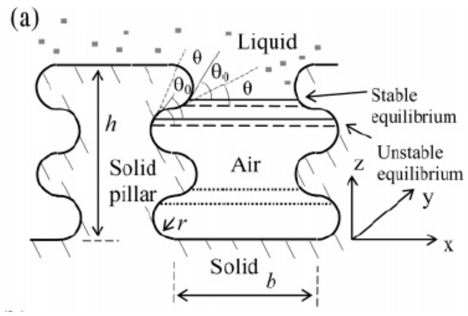

Figure 64. Two-dimensional pillars with semicircular bumps/grooves. (a) Schematic of the structure. The bumps may pin the triple line because an advancing liquid-air (LA) interface results in a decrease in the contact angle ($\theta < \theta_0$), making the equilibrium stable. Grooves provide equilibrium positions that satisfy the Young equation; however, the equilibrium is unstable because an advancing LA interface results in an increase in the contact angle ($\theta > \theta_0$).[146]

3.1 Experimental Details

Photolithography was employed for the fabrication of micron-sized silicon pillars on silicon wafers. A CEE 100CB Spinner Spin coater was used to apply a 2 μm thick photoresist (Shipley Microposit SC1813) layer. Exposure using a Karl Suss MA-6 Mask Aligner operating at 365 nm generated a pattern that was developed with Microposit 319 Developer. A Plasma-Therm ICP plasma reactor was invoked to perform silicon trench etching using the Bosch process with SF_6 and C_4F_8 [147]. The photoresist was subsequently removed by rinsing in acetone. Resulting surfaces were treated in UV/ozone for 3 min and rinsed with acetone. Surfaces were then treated with a fluoroalkyl silane, either trichloro-(1*H*,1*H*,2*H*,2*H*-perfluorooctyl) silane (PFOS) or dodecyltrichlorosilane (DTS), to form a hydrophobic layer and thereby establish superhydrophobicity. Samples were placed in a PFOS/n-hexane (or DTS/n-hexane) solution (3 mM) for 30 min for adsorption of a PFOS (or DTS) layer on the patterned surface; subsequently the samples were treated in air at 150˚C for 1hr and at 220˚C for 5 min to promote silane hydrolysis and condensation, thereby forming a stable silanated layer on the surfaces. After the fluoroalkyl silane treatment, the films formed by this process on a flat Si surface displayed a Young's contact angle of 115˚ (PFOS) and 106˚ (DTS). The surface area fraction of the pillars was determined using image processing and analysis software ImageJ from NIH. The height of the pillars (30 μm) is sufficient to ensure a composite contact during the contact angle measurement.

Characterization. The as-prepared samples were characterized by high resolution field-emission scanning electron microscopy (FESEM; LEO 1530 FEG at 10 kV). Contact angle measurements were performed using a digital automated contact angle goniometer (Rame-Hart Inc., model 100) with water droplets (4μl size) formed using a 4 μl step on a microsyringe at a flow rate of 25 μl/s and at a predefined height; static images of the droplets were then recorded and advancing contact angles of the droplet on the solid surface determined from these images. Receding contact angles were measured by increasing the volume of the 4 μl water droplet to 10 μl and subsequently reducing the volume to 4 μl by extracting the extra water with a volumetrically controlled pipette using a 0.2 μl step changes with a flow rate of 5 μl/s. Fifteen measurements were performed at different locations on the surfaces and the values averaged to obtain the reported advancing and receding contact angles.

3.2 Results and discussion

It is well-known that a heterogeneous surface (chemically or geometrically) usually shows a contact angle hysteresis[122, 148]. That is, for a geometrically rough surface, contact angle hysteresis originates primarily from the rough contact interface which depends upon the contact area of water with the structured surface. The contact area can be represented by the solid/liquid contact fraction (f_1) as demonstrated in the Cassie-Baxter equation.

$$\cos\theta_A = f_1 \cos\theta_Y + f_1 - 1$$

where f_1 is the solid surface fraction and $(1-f_1)$ represents the air surface fraction with water, θ_A is the apparent contact angle and θ_Y is the Young's contact angle on a flat/smooth surface.

The determining factor during movement of a water droplet on a superhydrophobic surface may be considered the microscopic work of adhesion at the surface of an individual structure. According to the Young-Duprè equation[149], the work of adhesion can be expressed as

$$w_{ad} = \gamma_{LV}(1+\cos\theta_Y) \tag{26}$$

where γ_{LV} is the surface tension of water on the solid surface; as a result, contact angle hysteresis can be related to γ_{LV} and θ_Y. Macroscopically, the hysteresis can be expressed using advancing and receding contact angles.

3.2.1 Theory

The contact angle hysteresis was initially discussed based on contact line density[143]; subsequently, a gain factor was used to correlate the contact angle hysteresises between a flat surface and a rough surface[17]. A thermodynamic approach was also invoked to predict equilibrium contact angles and contact angle hysteresis[150]. Little information has been reported concerning the explanation of the relationship between dynamic contact angles (advancing and receding contact angles), the surface geometrical features and surface chemistry. The following discussion focuses on an investigation of the relationship between contact angle hysteresis and the work of adhesion which is dependent upon surface geometrical parameters and surface chemistry. For a water droplet moving on a tilted surface, the relationship between the force on a water droplet and the contact angle hysteresis on a surface has been described by[141],

$$mg\sin\varphi / w (or F / w) = \gamma_{LV}(\cos\theta_R - \cos\theta_A) \tag{27}$$

where φ is the tilt angle of the surface relative to horizontal surface and w is the droplet width where the drop contacts the surface.

The energy barrier to droplet movement gives rise to contact angle hysteresis on a surface as a result of surface non-uniformity from either chemical (distribution between polar and nonpolar regions) or physical (roughness) properties.

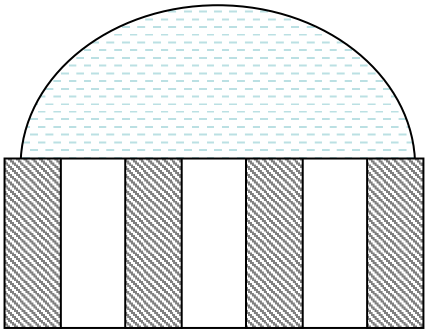

Figure 65. Water droplet on top of a structured surface.

Figure 65 shows a water droplet positioned on top of patterned pillars. For the flat top surface, equation (26) becomes

$$w_{ad} = \gamma_{LV} f_1 (1 + \cos\theta_Y) \tag{28}$$

It is reasonable to assume that the force needed to move a water droplet on a rough surface is that required to overcome the work of adhesion. Previous studies have suggested that for an advancing droplet, there is no energy barrier, but an energy barrier is experienced when the droplet recedes[110]. Therefore, the energy required to overcome the barrier at the receding edge of the water droplet can be expressed as

$$F \cdot \delta = w_{ad} \cdot \delta \cdot \pi R \tag{29}$$

where the left hand side of equation (29) represents the work done by the force (*F*) needed to move the droplet a distance δ and *R* is the drop/surface contact radius. We postulate that this energy is equal to the work of adhesion involved in the movement of the drop.

Therefore,

$$\gamma_{LV} (\cos\theta_R - \cos\theta_A) \cdot 2R = \gamma_{LV} f_1 (1 + \cos\theta_Y) \cdot \pi R \tag{30}$$

$$\cos\theta_R - \cos\theta_A = \frac{\pi}{2} f_1 (1 + \cos\theta_Y) \tag{31}$$

where $w = 2R$, and a circular three phase contact line has been assumed.

From the above development, the factor $\cos\theta_R - \cos\theta_A$ may be more appropriate than is the difference in contact angles in describing contact angle hysteresis. For a superhydrophobic surface, even if the difference between advancing and receding contact angles is the same, the force needed to move two droplets of the same size is different if the surface has a different advancing contact angle as shown in Figure 66.

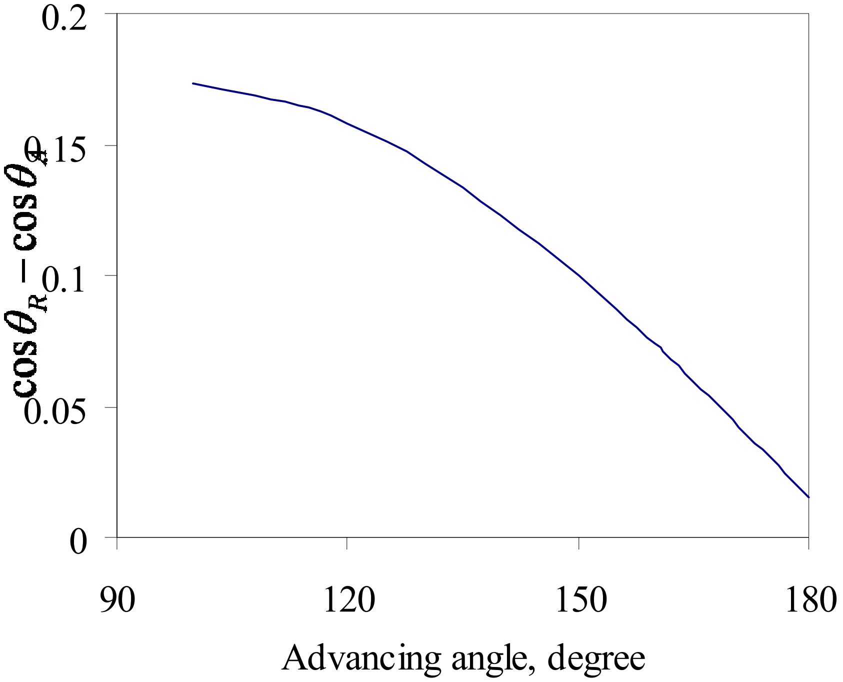

Figure 66. Difference of the cosines of advancing versus receding contact angles on advancing contact angles based on a constant contact angle hysteresis of 10°.

That is, the general concept of contact angle hysteresis defined as the difference between the advancing and receding angles is not adequate to precisely correlate hysteresis with surface self-cleaning. To overcome this limitation, we use the cosine form of the contact angle hysteresis, i.e., $\cos\theta_R - \cos\theta_A$, as a measure of the hysteresis.

3.2.2 Relationship between work of adhesion and the contact angle hysteresis

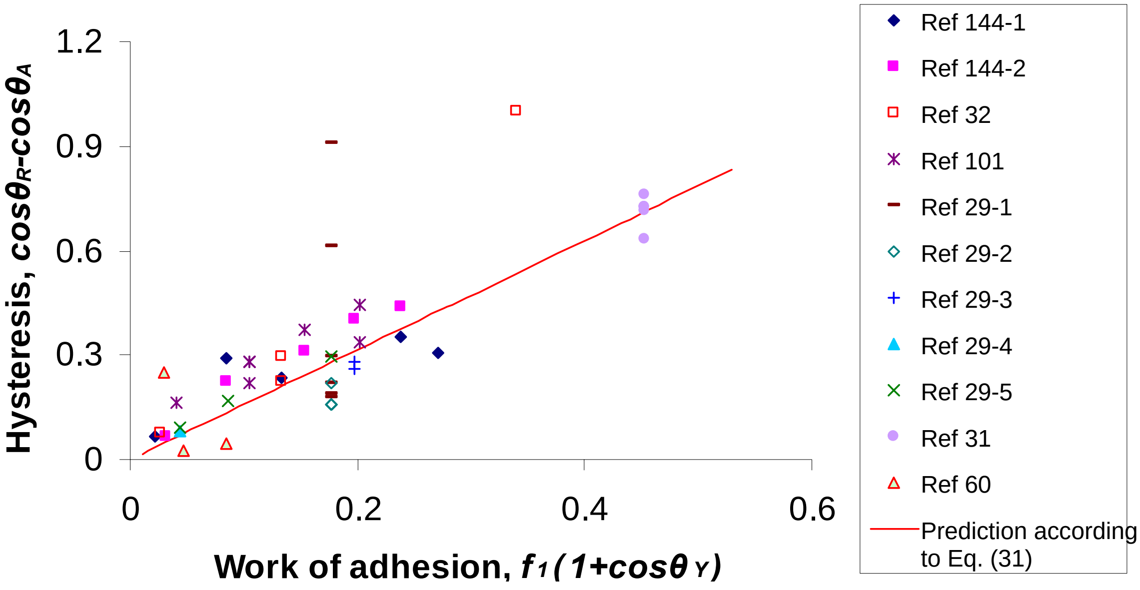

Figure 67. Relationship between contact angle hysteresis expressed as $\cos\theta_R - \cos\theta_A$ and work of adhesion. (eq 31)

In order to verify our approach, we compared our predicted correlations with previously published data [29, 31, 32, 60, 101, 144] as shown in Figure 67 Clearly, most of the data are consistent with the linear relationship shown, which suggests that the contact angle hysteresis as described by the difference in the cosines of the respective angles is related to the surface work of adhesion between the solid surface and the liquid droplet. Although some of the data in Figure 67 show marked deviations (references 29-1 and 32 shown as dashes and open square), these specific studies used unique geometrical surface structures. For instance, although the fit for pillar structures is quite reasonable, the surface containing holes shows a high deviation (open circle in Figure 67). When the hysteresis $\cos\theta_R - \cos\theta_A$ on such surfaces is sufficiently large, we can see from Figure 67 (stars) that the deviation from equation (31) is also large. Under these circumstances, the droplet-surface contact may be in the Wenzel state instead of the Cassie state. Since equation (31) is based on the Cassie state, correlation of the work of adhesion with the difference of the cosines of the contact angles is inappropriate.

In order to further verify our correlations (equation 31), we generated patterned Si pillars of different sizes arranged in square arrays with varied pitches, to serve as model surfaces for the study of geometrical effects on superhydrophobicity; the surface structures are shown in Figure 68 and the geometrical parameters are shown in Table 4.

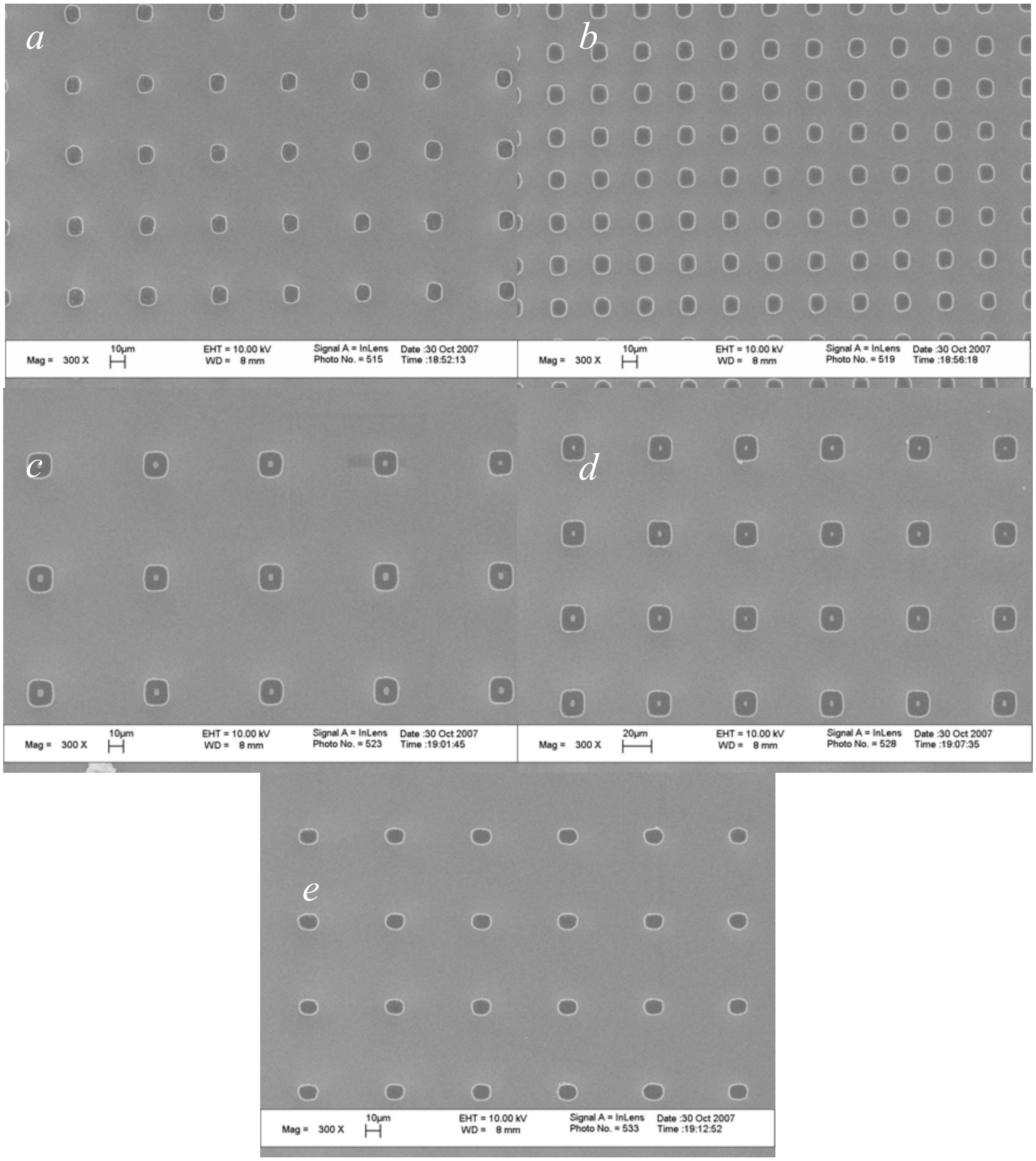

Figure 68. SEM images of model silicon pillar surfaces.

Table 4. Geometrical parameters describing the prepared Si pillars.

No.	Nominal side length (μm)	Nominal pitch size (μm)
a	12	50
b	12	30
c	18	80
d	18	60
e	12	60

[*] Note: the actual surface area fraction was measured using image processing and analysis software ImageJ from NIH

In order to achieve a superhydrophobic state, a surface treatment with (fluoro)alkyl silanes (PFOS, DTS) was performed. That is, on these structured surfaces, the surface roughness can be controlled by geometrical structure design, and hydrophobicity can be varied by surface treatment with different silanes. Thus, the parameters in equation (31) can be varied in a controlled fashion. The resulting contact angles and hysteresis (contact angle hysteresis and $\cos\theta_R - \cos\theta_A$) are shown in Table 5 and 6 and plotted in Figures 69 and 70 as a function of solid surface contact fraction f_1. An increase in f_1 for both PFOS and DTS treated surfaces causes the receding angles to decrease and contact angle hysteresis to increase while advancing angles remained essentially constant. The relationship between the work of adhesion and hysteresis as defined by ($\cos\theta_R - \cos\theta_A$) is shown in Figure 71.

Table 5. Advancing and receding contact angles for PFOS treated Si surfaces.

No.	f1	Advancing contact angle, degree	Receding contact angle, degree
a	0.055	167.6 ± 1.2	156.8 ± 1.3
b	0.156	167.1 ± 1.5	146.6 ± 3.2
c	0.051	165.9 ± 1.5	156.7 ± 2.7
d	0.091	166.2 ± 1.3	151.6 ± 3.3
e	0.044	165.7 ± 0.5	158.6 ± 2.0

Table 6. Advancing and receding contact angles for DTS treated Si surfaces

Number	Surface solid fraction	Advancing contact angle, degree	Receding contact angle, degree
a	0.055	163.1 ± 0.8	151.9 ± 1.2
b	0.156	165.9 ± 0.6	142.6 ± 1.1
c	0.051	164.2 ± 0.6	154.5 ± 1.1
d	0.091	164.5 ± 0.6	149.4 ± 3.0
e	0.044	165.0 ± 0.5	156.6 ± 1.6

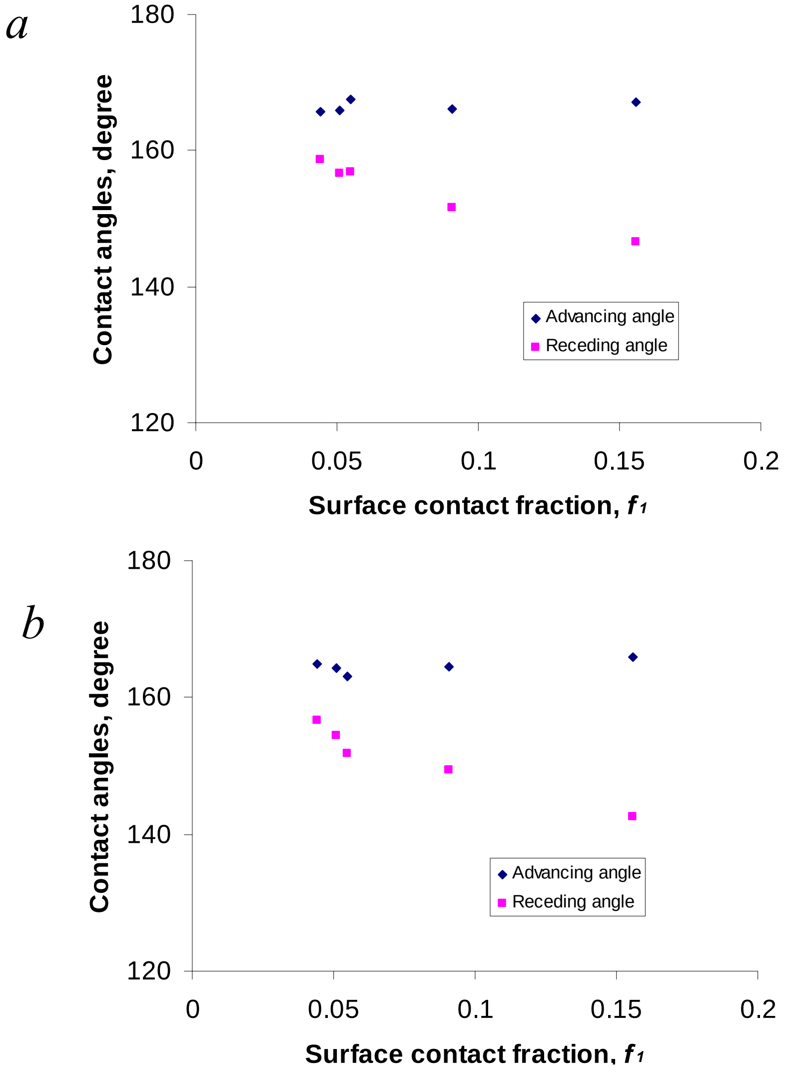

Figure 69. Advancing and receding contact angles on Si pillar surfaces, a. PFOS treated surfaces; b. DTS treated surfaces.

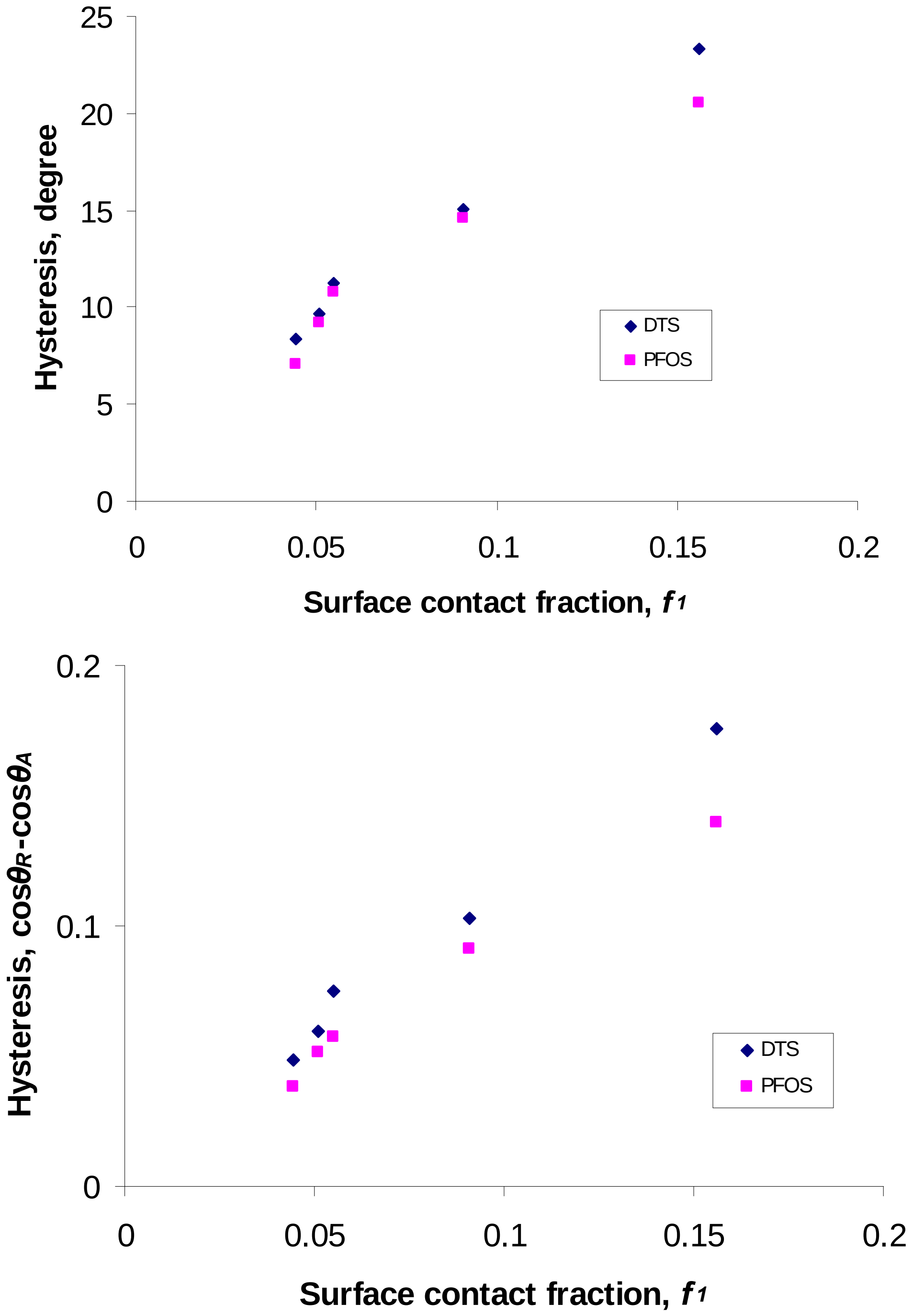

Figure 70. The contact angle hysteresis (angle and $\cos\theta_R - \cos\theta_A$) of PFOS and DTS treated Si pillar surfaces.

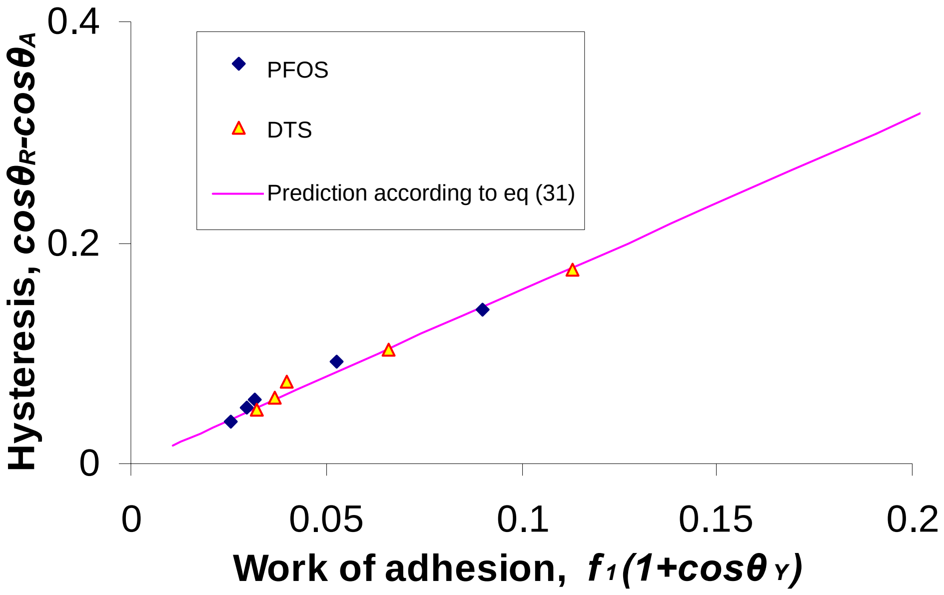

Figure 71. Hysteresis ($\cos\theta_R - \cos\theta_A$) vs. work of adhesion ($f_1(1+\cos\theta_Y)$) for patterned Si pillar surfaces treated with fluoroalkyl silanes.

From Figure 71, it is clear that the experimental data fit equation (31) quite well. It is reasonable that the hysteresis as defined by ($\cos\theta_R - \cos\theta_A$) mostly originates from the work of adhesion between the water droplet and the solid surface. In addition, some studies have proposed the incorporation of a line tension (one-dimensional surface tension) term in Young's equation to investigate the effect of surface structures (roughness) on contact angle and to modify the Cassie and Wenzel equations[151, 152]. However, it has been suggested that for surfaces with features larger than 100 nm, which is the case in our study, the line tension is not significant [153]. Therefore, for micron-sized surface structures such as pillars the line tension should be negligible. Thus, we assumed all contributions to the contact angle are from surface tension without considering the line tension effect.

For solid/water interfaces, small values of contact angle hysteresis are critical to achieve superhydrophobicity with reduced adhesion. In the current studies, the work of adhesion, which is dependent on Young's contact angle and the surface tension according to the Young-Duprè equation (Eqn (26)), have been used to characterize the surface behavior.

For contact angle hysteresis related to water/solid adhesion, the hydrophobic surface plays two roles. First, adhesion of the solid/water contact interface is reduced due to the lowered surface tension of the solid surface γ_s (the work of adhesion can be estimated as $\gamma_{ad} = 2\sqrt{\gamma_w \gamma_s}$ [23]); therefore, contact angle hysteresis is reduced and the receding contact angle is increased. Second, the increased hydrophobicity of the surface yields a higher water contact angle (θ) on the surface which results in a higher apparent contact angle.

For air/liquid contact surfaces, the Laplace pressure is critical in establishing a stable superhydrophobic surface[154]. In addition, the three phase contact line may play an important role in maintaining the air/water interface of a composite contact since it has a significant effect on superhydrophobicity due to the effect on the Laplace pressure, primarily at the air/water interface. For an irregular three phase contact line, we postulate that the equivalent radius of a capillary is related to the three phase contact line. Therefore, the Laplace pressure on the water meniscus will vary depending upon the length of the three phase contact line for a specific solid fraction f_1. The shorter the three phase contact line, the easier the transition from a Cassie state to a Wenzel state. Specifically, when the three phase contact line averaged over unit solid area (irregular, fractal, etc) is longer, the edge area of the solid pillars can be considered a composite surface as illustrated in Figure 72. This situation will result in a higher contact angle on the edge[155, 156] than is predicted from the Cassie-Baxter equation due to the formation of a composite contact at the edge.

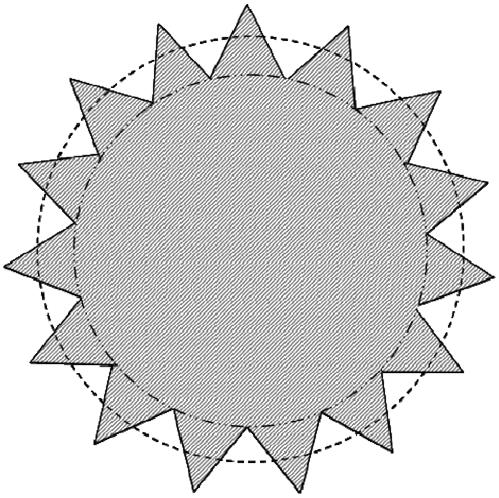

Figure 72. Surface structure illustration of top view of a microscopic pillar surface with rough edges.

Conclusions

A relationship has been proposed between the surface work of adhesion and the dynamic contact angle hysteresis; this model was subsequently correlated with previously reported data. In order to evaluate both the surface geometrical effects and chemical effects on hysteresis, patterned Si pillars with different pillar size and pitch were prepared. These surfaces were modified with different (fluoro)alkyl silanes to vary the hydrophobicity. The hysteresis-work of adhesion model was consistent with contact angle measurements. This result implies that the droplet adhesion originates mostly from the work of adhesion at the water/solid contact interface. The hysteresis as defined by the difference in cosines of the advancing and receding contact angles ($\cos\theta_R - \cos\theta_A$) appears to be related to the work of adhesion which is a function of surface solid contact fraction f_1 and Young's contact angle. The Laplace pressure at the air/water interface may be dependent upon the three phase contact line to maintain a stable superhydrophobic state.

CHAPTER 4

UV STABILITY IMPROVEMENT OF SUPERHYDROPHOBIC SURFACES

4.1 Introduction

The bulk of power delivery from the generating sites to the load centers is done by overhead transmission lines. To minimize line losses, power transmission over such long distances is more often carried out at high voltages (several hundred kV). The energized high voltage (HV) line conductors have to be physically attached to the support structures. Also the energized conductors have to be electrically isolated from the support structures. The device used to perform the dual functions of mechanically support and electrical isolation is the insulator. Since transmission lines are often in remote locations that are hard to reach, it is desirable that once the line has been constructed that it will work satisfactorily, without maintenance, for the expected life of the line, generally exceeding 30 years. The quality of raw materials, processing, design, and quality control of the insulator are all important.

In many parts of the world, insulator contamination has become a major impediment to the interrupted supply of electrical power. Contamination on the surface of insulators gives rise to leakage current, and if high enough, flashover[1].

So far, various techniques have been applied to address this problem:

a) Cleaning with water, dry abrasive cleaner, or dry ice can effectively remove loose contamination from insulator, but it is expensive, labor intensive and only a short term solution;

---

[1] A flash over is a disruptive discharge through air around or over the surface of insulation produced by the application of voltage wherein the breakdown path becomes sufficiently ionized to maintain an electric arc.

b) Mobile protective coatings, including oils, grease and pastes surface treatment, can prevent flashover, but have damaging results to the insulator during dry band arcing[2] (in wetted and polluted areas);

c) Grease-like silicone coating components, usually compounded with alumina tri-hydrate (ATH), provide a non-wettable surface and maintain high surface resistance, and have been used as protective coatings for the past 30 years. The major strength of the silicone grease lies in their ability to maintain a mobile water repellent surface, thereby controlling leakage current;

d) Fluorourethane coatings were developed for high voltage insulators, but the field test was not successful, and its low adhesion to the insulators has been a problem;

Since 1970s, room temperature vulcanizing (RTV) silicone coatings has gained considerable popularity, and become the major products available in the market, such as Dow Corning’s Sylgard High Voltage Insulator Coatings (HVIC), CSL’s Si-Coat HVIC, and Midsun’s 570 HVIC. Service experience has indicated that of the various types of insulator coatings, the time between maintenance and RTV coating reapplication is the longest.

The techniques described above cannot prevent contamination, such as dust, accumulation on coating surfaces, thus these serve to manage the problem, yet none of

---

[2] Dry-band arcing has been observed in highly polluted areas, mostly close to the sea. The wind from the sea drives saltwater droplets onto the fiber-optic-cable surface, which covers the cable with a thin layer of salt. Morning and evening fog or dew wets the pollution layer and forms a conductive layer on the cable surface. The layer resistance can vary between 100 k ohm/m to 100 M ohm/m. Capacitive coupling between the phase conductors and fiber-optic cable induces current along the wet pollution layer. The current magnitude increases from mid-span toward the towers, and the current maximum is usually near the armor rods. This current dries the layer and forms small dry bands. The dry band interrupts the current and generates a high voltage across the band. This voltage produces a flashover across the band and forms an arc. The heating effect of the arc extends the dry-band length, which stops the arcing. However, condensation and wind-driven saltwater from the sea wet the cable and reinitiate the arcing. Dry-band arcing is a periodic phenomenon that occurs when the cable is simultaneously wet and polluted.

the above techniques has satisfactory performance in heavy contamination environments. Table 7 showed water droplet contact angles on commercially available insulator material surfaces. In this work, a self-cleaning Lotus Effect coating is proposed and investigated as a novel protective coating for external electrical insulation systems.

Table 7. Contact angles on outdoor insulator surfaces.

Insulator materials	Contact angles on the surfaces, degree
Silicone	110
Ethylene-vinyl acetate (eva)	120
Ethylene propylene dimer (epdm)	75
Glass	56
Cycloaliphatic epoxy	55-60

Although the Lotus Effect was discovered in plants, it is essentially a physicochemical property rather than a biological property. Therefore, it is possible to mimic the lotus surface structure. To mimic the lotus surfaces, a Lotus Effect surface should be produced by creating a nanoscale rough structure on a hydrophobic surface or coating thin hydrophobic films on nanoscale rough surfaces.

Compared with superhydrophobicity of Lotus Effect, the mechanism of self-cleaning is not completely investigated. In fact, the self-cleaning can be achieved if two conditions can be met:

a) The surface is superhydrophobic so that water drops have very large contact angle and small sliding angle, and

b) The adhesion between the water drop and dust particles is greater than the adhesion between the surface and dust particles.

Adhesion of two components, such as adhesion of dust or dirt to a surface, is generally the result of surface-energy-related parameters representing the interaction of the two surfaces which are in contact. In general, the two contacted components attempt to reduce their free surface energy. Strong adhesion is characterized by a large reduction in free surface energy of two adhered surfaces. On the other hand, if the reduction in surface free energy between two components is intrinsically very low, it can generally be assumed that there will only be weak adhesion between the two components. Thus, the relative reduction in free surface energy characterizes the strength of adhesion. Usually dust particles consist of materials have higher surface energy than the surface materials, and they are generally larger than the surface microstructure and just contact with the tips of these microstructures. This reduced contact area minimizes the adhesion between the lotus leaf surface and dust particles, so the particles can be picked up and removed from the leaf surface by the water droplet. Based upon the self-cleaning mechanism, it is likely that hydrophobic particles are less likely be removed by water droplet than hydrophilic dust particles on a lotus leaf, and small particles, which have a size close to or even smaller than the microstructures, will possibly be pinched in the microstructures instead of be removed by water droplet.

4.2 Learnings from polymer Feasibility Study

In the proof of concept research, understanding the mechanism and developing superhydrophobic polybutadiene protective electrical coatings with the purpose that it could keep the surface of heavy electrical insulation devices dry and clean, minimizing the chances of surface degradation and surface contaminant-induced breakdown of the insulation devices, and significantly enhancing the electrical performance.

As proposed to use superhydrophobic coating as a protective coating for external insulators, various superhydrophobic coatings were prepared on insulating materials. Self-cleaning of contaminants were demonstrated on these superhydrophobic coatings. However, the UV stability is a big obstacle for the successful application on insulator surfaces. In fact, for polybutadiene superhydrophobic surfaces prepared from SF6 plasma etching, after UV aging test according to ASTM D 4329, the self-cleaning surfaces failed completely as shown in Figures 73 and 74.

As can be seen from the SEM image (Figure 73) and EDX (Figure 75), after the surface was irradiated under UV light for as little as 2 days, the surface changed. The change can be seen by the growth of the smooth areas that destroyed the surface roughness. The loss of roughness causes a fall in the contact angle. And the surface chemistry changed as a result of the oxidation of the polymer surface (oxygen content increased to ~30 atom%). This effect continued even when UV protection was included; presumably this was ineffective as the damage is very highly localized to the surface layers.

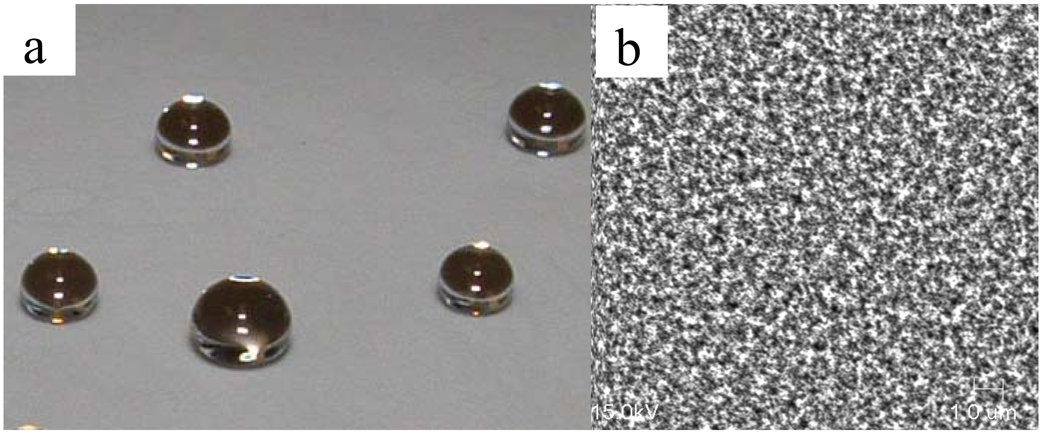

Figure 73. (a) Water droplets on Superhydrophobic Coatings; (b) SEM images of SF_6 etched polybutadiene thin films.

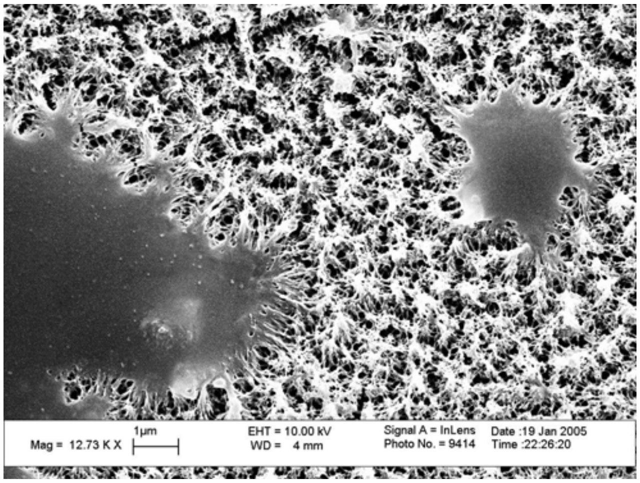

Figure 74. The UV degradation of polymeric superhydrophobic surface; the superhydrophobic polybutadiene surface after UV aging for 48 hs. Water droplet contact angle on this surface: ~ 70˚; polybutadiene surface treated with SF_6 plasma (150w 10 min).

According to literature, in order to create effective superhydrophobic coatings, biomimetic synthesis of hierarchical structure (two scale roughness) was optimized as the final goal in order to achieve a surface that right in Cassie regime with high contact angle and very low hysteresis so that self-cleaning surface is resulted. The surface hydrophobicity can be achieved by surface treatment like fluoroalkylsilane treatment (to form a Self Assembly Monolayer) or fluorocarbon thin film deposition etc.

Standard UV exposure and condensation tests following ASTM D 4329 were conducted on the prepared hydrophobic coatings, and the results in Table 8 suggest that the UV degradation poses one serious barrier in the successful application of the outdoor coatings. As such, in this study, the UV stability of the superhydrophobic coatings was emphasized.

Table 8. Contact angles of different materials before and after UV test according to ASTM D 4329.

Name	Contact angle before weathering test	Contact angle after weathering test*
EVA	115-120°	75 °
PTFE	115 °	112 °
TEFLON AF	125°	120°**
Silicone/PTFE	155°	138°***
polydimethylsilane	153°	80°
Polybutadiene (SF_6 treated)	162°	70°
Anodized Al surface treated with PFOS	175.6	120-130°***

* UV tested for 200 hrs; ** UV tested for 2500 hrs; ***UV tested for 1000 hrs.

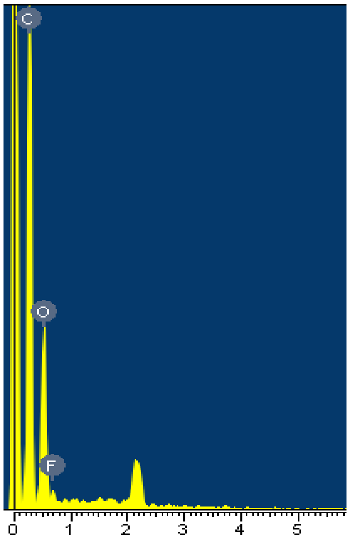

Figure 75. The EDX of the degraded superhydrophobic surface; polybutadiene surface treated with SF_6 plasma (150w 10 min).

For polybutadiene, UV stabilization using UV stabilizers and free radical scavengers were also performed. The results were shown in Figure 76. It showed that even with UV stabilizers, the surface cannot achieve an applicable self-cleaning surface.

The application requires that the UV aging test time should at least be 1000 h without any degradation on the surface property for possible outdoor applications.

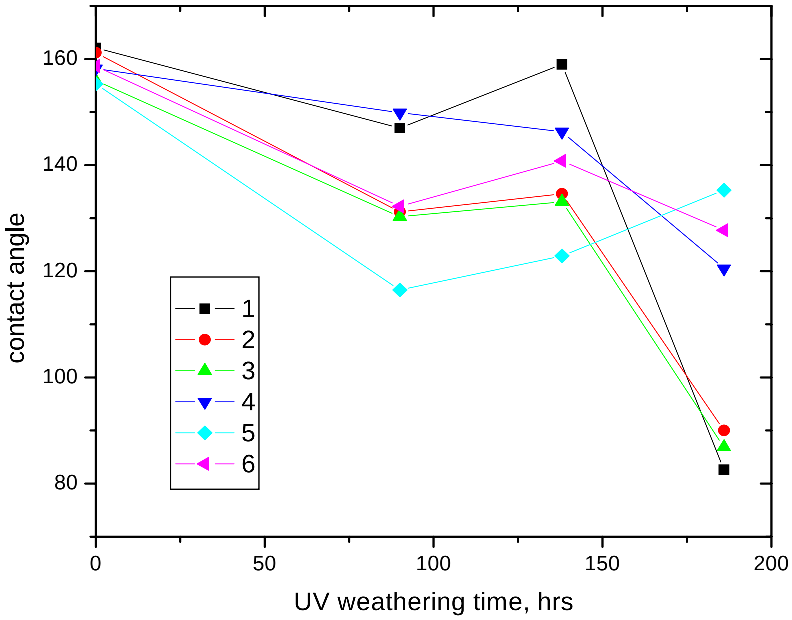

Figure 76. UV stability of polybutadiene superhydrophobic surfaces from SF_6 plasma etching, stabilized with different UV stabilizers; 1) Polybutadiene + UV 5411, 2) Polybutadiene + UV 1164, 3) Polybutadiene + UV 3346, 4) Polybutadiene + UV 1577FF, 5) Polybutadiene + 10%wt TiO_2, 6) Polybutadiene + 5% carbon black.

On the basis of UV test results, we tried two methods of UV stabilization. One is to try using inorganic materials as the coating material to create two scale structures, followed by a surface treatment with low surface energy and UV stable materials, such as fluoroalkylsilane. The other method is to create a surface self-healing mechanism as the lotus leaves possess. When the low surface energy material molecules were depleted, the underlying layer can continuously supply the molecules to the surface to maintain the surface hydrophobicity. i.e., the surface superhydrophobicity can be well maintained and UV stability is achieved. The second approach will be discussed in detail in chapter 8

4.2.1 Problem definition and research objectives

Although there have been numerous research efforts in creating such superhydrophobic surfaces, with various applications envisioned, there have been no commercial routines or products available on markets. Potential applications in the field of heavy electrical insulation have not been explored, while there is a great promise for such applications. In addition, to develop a Lotus Effect coating, a fundamental understanding of the Lotus Effect is critical. However, the understanding of Lotus Effect surfaces is still empirical/semi-empirical at present. Lack of theoretical framework of Lotus Effect/superhydrophobicity limits its potential application as a self-decontamination and self-cleaning coating material applications. In addition, to develop reliable Lotus Effect coatings as insulating coatings, the following criteria must be met:

The coatings should be stable under harsh environmental conditions;

The coatings should have good compatibility with practical insulation materials (silicone and porcelain – glassy);

The coatings should remain adhered to the insulator after expansion and contraction of the device:

The coatings must be capable of application to insulators in a simple and practical way.

The basic premise of this work is to devise a coating that both inhibits the formation of a continuous film of water and removes dust with the high water flow.

4.3 Coprecursor method from sol-gel processing

The sol-gel approach involves the creation of surface roughness by the evaporation of solvent (ethanol) after the formation of silica gel skeleton (gelation through silanol condensation), usually in the forms of particles, xerogel and aerogel depending on the processing and drying conditions. The reactions are shown in Figure 77. The surface hydrophobicity was achieved by the incorporation of the hydrophobic groups. The individual components are termed precursors (e.g. tetraethoxysilane, tetramethoxysilane, isobutyl trimethoxysilane etc.). When two or more precursors are combined to make the process more practical the process are termed coprecursor process. The second precursor contains the hydrophobic hydrocarbon/fluorocarbon group, e.g., TEOS-IBTMOS, TEOS-TFPS, etc, at least one of the precursors contributes hydrophobic groups, such as isopropyl, trifluoropropyl groups, etc.

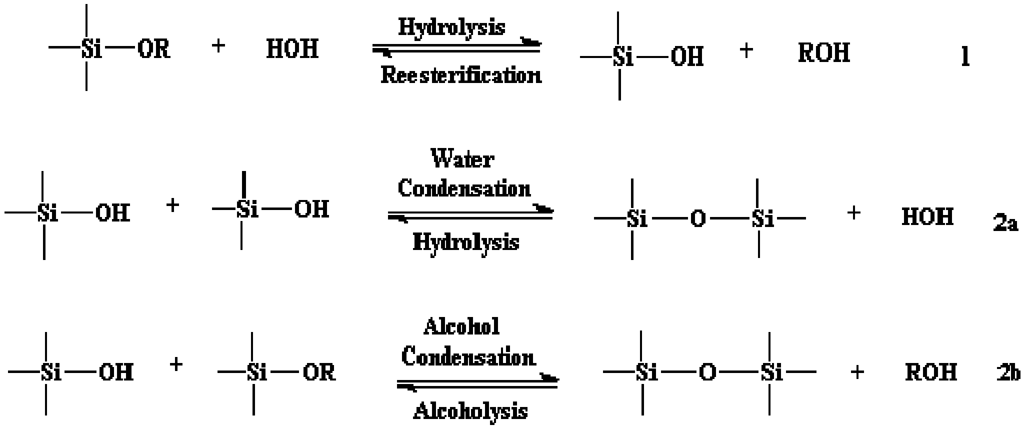

Figure 77. The generalized reaction mechanism for pre cursors

Self-cleaning surfaces have many potential applications, for example, surface decontamination on microelectronic equipment or devices, water repellent coatings, biocompatible surfaces, and friction reduction. Such surfaces have been created on a variety of materials such as silicon[154], silicones [157], alumina [21, 22, 158], polyelectrolytes[102],carbon nanotubes[159, 160], polystyrene[72, 161], PTFE (polytetrafluoroethylene) [4], polybutadiene[162], fluorocarbons[163]and mono-dispersed silica particles[14]. Several criteria have been established to characterize the surface including contact angle (>150˚), contact angle hysteresis (<10˚) and roll-off angle. However, complications exist when polymeric materials are exposed to atmospheric conditions where degradation occurs due to UV irradiation and to exposure to impurities, O_2, and moisture present in the environment. Also, because organic polymers are easily deformed when a force is applied, the surface structure is not stable when the surface undergoes abrasion from friction, handling, or dust particles. Recently, superhydrophobic silicone nanofilaments were fabricated for improved environmental durability[164, 165]. Sol-gel processes offer an alternative method to fabricate porous glass films under ambient conditions for improved durability. The mild preparation conditions offer the ability to incorporate a wide range of labile organic species into a glass composite. In addition to the mild processing conditions, sol-gel derived materials exhibit tunable porosity[66, 166-168], transparency[105], hardness, and good thermal stability[66, 166-171]. To achieve superhydrophobicity, different surface treatment was performed including silane treatment, fluorocarbon deposition or coprecursor methods[169, 170, 172, 173]. However, UV stability has not been addressed extensively, especially for long times, which is a requirement for outdoor applications. Such applications are especially problematic, since the surface hydrophobicity imparted is usually due to the presence of hydrocarbons[65, 66]. In this chapter, porous silica generated by sol-gel processing is invoked to improve the UV stability of superhydrophobic films. This approach to the fabrication of inorganic superhydrophobic silica films uses tetraethoxysilane and trifluoropropylmethoxysilane (TFPS) as precursors. When TFPS is incorporated into silica, the surface contains hydrophobic trifluoropropyl groups, resulting in hydrophobicity. Furthermore, the sol-gel process allows the generation of rough surfaces which is ideal to establish surface roughness. By incorporating both surface hydrophobicity and controlled structure into the surface, an inorganic film with excellent superhydrophobic properties can be fabricated.

4.3.1 Experimental Details

Silica monolith formation. The starting solution was prepared using a two-step (acid/base catalyzed) procedure. Tetraethoxysilane (TEOS, from Aldrich), trifluoropropyl trimethoxysilane (TFPS, from Aldrich), ethanol, and water were mixed in a 30 ml vial with varying ratios. The pH was adjusted to 1.8-2.0 by adding hydrochloric acid, and the mixture stirred for 120 min at 60˚C to make silica sol. Then NH4OH (1.0M) was added to the sol, (volume ratio of NH4OH solution to sol is 1:50) followed by mixing for 5 min at room temperature. The resulting gel was allowed to age for 48 hours. Incorporation of a small slit (6mm×3mm) in the vial cap allowed ethanol and water to evaporate slowly from the sol to form bulk silica.

Silica film formation by casting. Glass slides were cleaned in Piranha solution (70:30 (vol/vol) mixture of 96% sulfuric acid and 30% aqueous hydrogen peroxide) at 80˚C and subsequently rinsed extensively with de-ionized water and ethanol. The cleaned glass slides were used as substrates for the casting of silica films. The casting fixture was comprised of two glass slides. One slide acted as the substrate, and the other, which was treated with trimethylchlorosilane (TMCS) to prevent gel bonding, served as the cover. A chromium film of ~300 nm thickness was sputtered onto the surface of the substrate glass slide prior to gel formation. The procedure described above was used to prepare bulk silica sol; after NH_4OH was added to the sol, the mixture was stirred for 3 min. Several drops of the sol were then dispensed onto the substrate glass slide and covered with the TMCS treated glass slide. After gelation, aging for 1 week and evaporation of the solvent, a silica film resulted with surface groups shown in Figure 78.

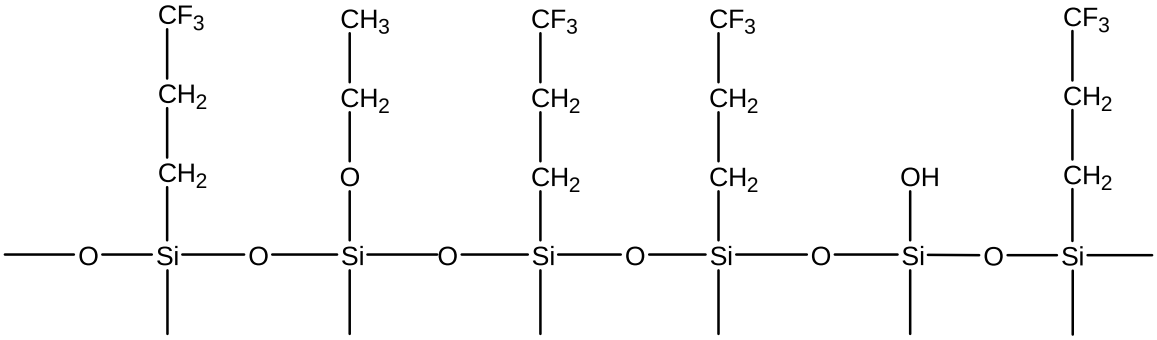

Figure 78. The surface chemical structure of TFOS & TEOS.

Characterization. Contact angle measurements, Scanning Electron Microscopy (SEM), Atomic Force Microscopy (AFM), and Thermogravimetric Analysis (TGA), were used to characterize the superhydrophobic surfaces. Contact angle measurements were performed with water droplets (4μl size) formed using a 0.2 μl step on a microsyringe at a predefined height; static images of the droplets were then recorded and advancing contact angles of the droplet on the solid surface determined from these images. Receding contact angles were measured by increasing the volume of the 4 μl water droplet to 10 μl and subsequently reducing the volume to 4 μl by extracting the extra water with a volumetrically controlled pipette using the same 0.2 μl step changes.. For SEM inspection, the samples were fixed to aluminum stubs with conductive tape before being coated with ~20 nm of gold in an Ernest Fullam sputter coater. The samples were then imaged using a LEO 1530 FEG SEM with Energy Dispersive X-ray Spectroscopy (EDS) capability. TGA analysis was performed with a TGA 2050 thermogravimetric analyzer from TA Instruments. A silica sample of ~10 mg was placed in a ceramic pan, and the pan positioned in the TGA furnace; a temperature ramp at a rate of 10˚C/min was used to heat the sample from room temperature to 800˚C in an air flow of 100 SCCM.

UV exposure testing. UV exposure tests were performed by adhering to standard procedures for the fluorescent UV exposure of plastics (ASTM D 4329). A UVA-340 lamp (xenon lamp) simulated the short and middle UV wavelength region corresponding to daylight exposure. The test cycle was 8 h UV with the uninsulated black panel temperature controlled at 60 ± 3˚C, followed by 4 h condensation with the uninsulated black panel temperature controlled at 50 ± 3˚C. A radiometer monitored and controlled the amount of radiant energy that impinged on the sample. A thermometer was used to monitor the temperature in the test chamber.

4.3.2 Results and Discussion

The existence of TFPS on the sample surface generates hydrophobicity due to the presence of CF3 from the trifluoropropyl groups (-Si-(CH2)3CF3). Indeed, the fluorine content is an indicator of surface hydrophobicity. The fluorine content of the surface can be quantified using EDS as shown in Figure 79; Table 9 gives the atomic fluorine percentage. When the ratio of TFPS to TEOS increases, the fluorine content increases and surface contact angle increases concomitantly.

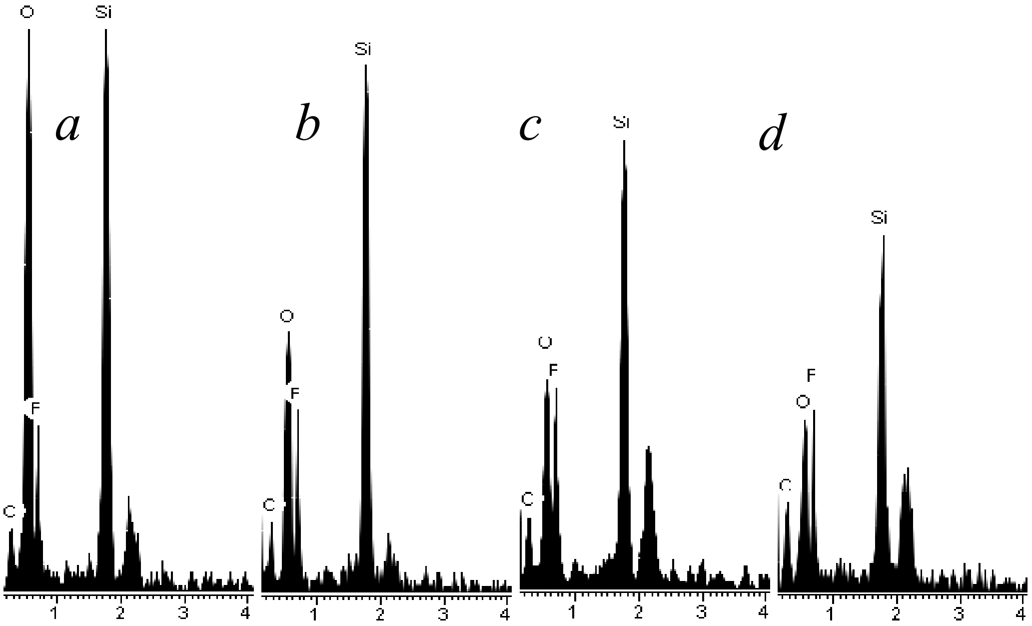

Figure 79. EDS spectra of the silica from different ratios of TFPS:TEOS, (a) 1:3; (b) TFPS:TEOS=1:1; (c) 2:1; (d) 3:1.

Table 9. Fluorine content in the as prepared hydrophobic silica materials.

TFPS/TEOS ratio	Fluorine content (atom.%)
1:3	10.26
1:1	15.19
2:1	18.25
3:1	23.23

In the TFPS/TEOS sol-gel process, the hydrophobic nature of trifluoropropyl groups causes these groups to migrate to the surface. This process again increases the hydrophobicity of the surface. The dependence of surface contact angle on the molar ratio of precursors for the preparation of silica is shown in Figure 80. The contact angle increased with an increase in the ratio of TFPS/TEOS. The hydrophobic surface resulting from TFPS, together with a ratio dependent surface morphology[174], yields an increase in the apparent contact angle with the increase in precursor ratio.

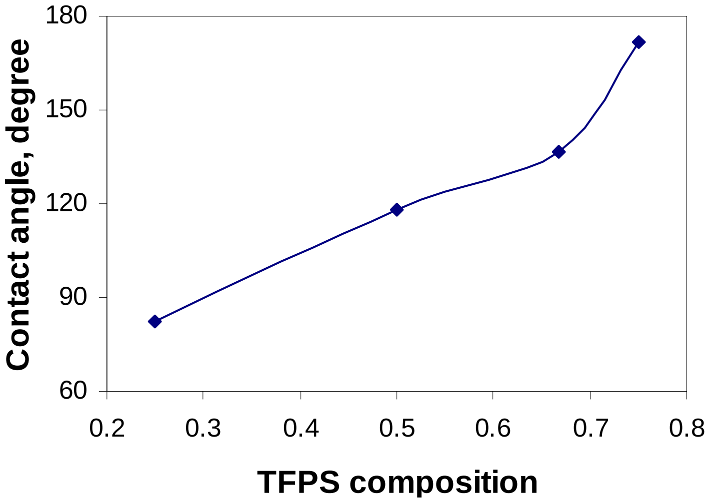

Figure 80. Dependence of water droplet contact angle on the composition of TFPS coprecursor in TEOS.

During the hydrolysis and condensation of TFPS/TEOS, TFPS acts as a coprecursor. TFPS has only three functional groups that can undergo hydrolysis and condensation, while TEOS has four. Thus, as the ratio of TFPS increases, the rate of hydrolysis and condensation diminishes due to the decrease in density of the functional groups as shown in Table 10. However, the methoxy groups in TFPS are more reactive than the ethoxy groups in TEOS. This means that during the reaction, TFPS hydrolyses first to form hydrophobic clusters; TEOS clusters then attach to the TFPS cluster. From Table 10, it is clear that the gelation time does not vary significantly for the different molar ratios of the two precursors. This result is different from that obtained when using coprecursors with ethoxy groups as reported previously[175]; in that study, when increasing the coprecursor ratio, the gelation time increased dramatically. With an increase in coprecursor ratio, reduced surface bonding and therefore poor adhesion generally results. Through the attachment of TEOS clusters to TFPS clusters, it is expected that this process can increase the adhesion between the substrate and the sol. When TEOS is attached to TFPS clusters, adhesion originates mainly from the substrate and TEOS clusters. However, this process does not limit the hydrophobicity of the silica surface formed on the substrate as was demonstrated in Figure 80.

Table 10. Effect of TFPS/TEOS molar ratio on the gelation time of silica alcosols (weight ratio of sol to NH4OH solution is 50:1)

TFPS/TEOS molar ratio	Gelation time, min
1:3	13
1:1	15
2:1	18
3:1	20

When a flat surface is treated with TFPS, the resulting contact angle is 102-105˚. Due to the surface roughness generated during the sol-gel process, the contact angle is much higher than that on a flat surface covered with trifluoropropyl groups. Indeed, with the combination of surface hydrophobicity and surface roughness, a superhydrophobic surface (contact angle of 172˚ and hysteresis of 2˚) results when the ratio of TFPS/TEOS is increased to 3. The silica surface morphologies from the TFPS/TEOS sol-gel process are shown in Figure 81. At low TFPS ratio, the surface is rough at the nanoscale (Figure 81a); the surface particle size is ~50nm. When the TFPS ratio increases, the surface roughness scale increases, and when the ratio reaches 3, the surface is a combination of micro and nano structures.. The roughness generated combined with the surface hydrophobicity, yields a superhydrophobic surface with reduced contact angle hysteresis.

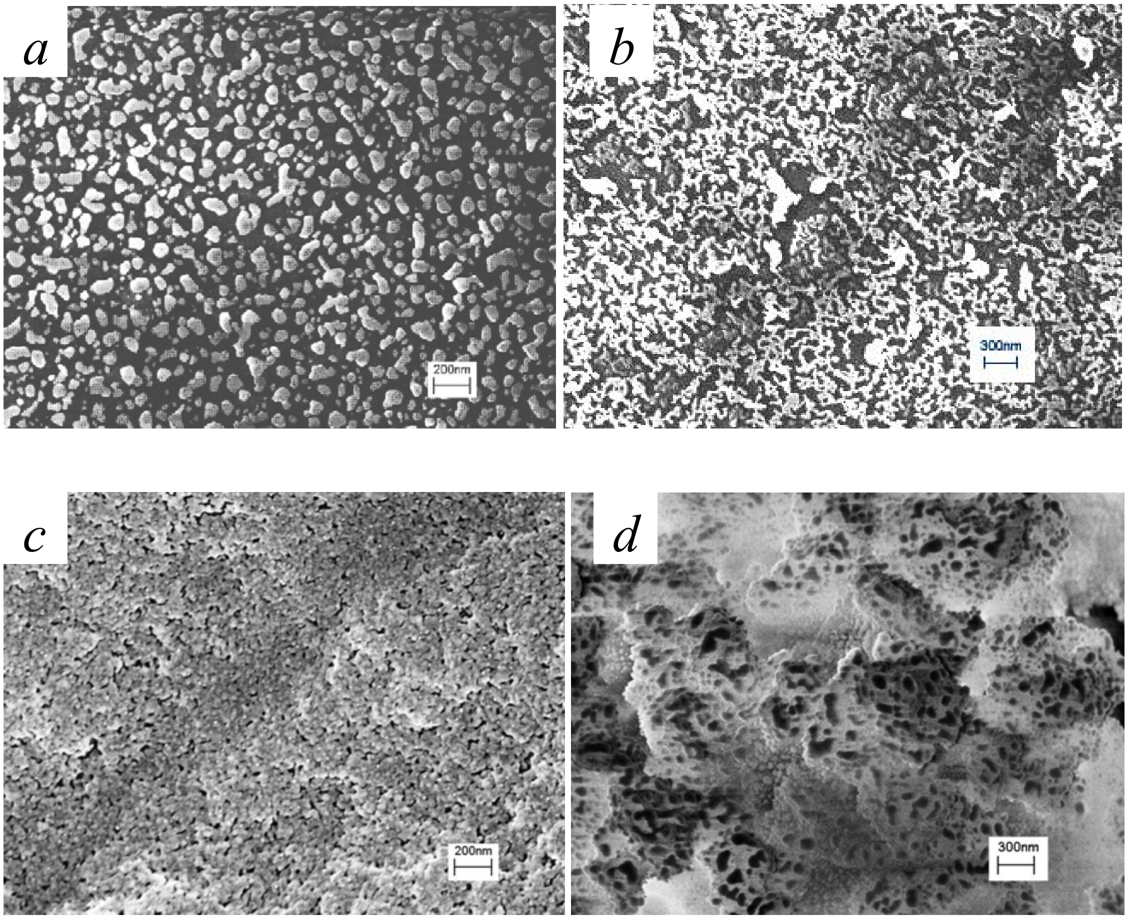

Figure 81. SEM images of as prepared hydrophobic silica monolith (bulk silica). TFPS:TEOS ratio: a, 1:3, b, 1:1, c, 2:1, d, 3:1.TFPS:TEOS=1:3, 1:1, 2:1, 3:1.

Silica films were also prepared on glass microscope slides following the procedure described in the experimental section; similar contact angle results to those shown in Fig. 2 were observed. The water droplet shapes on the as prepared silica films with different TFPS/TEOS ratios are shown in Figure 82. Clearly, the film results follow exactly the same trend as does the silica monolith. SEM images of the surface morphologies for these TFPS/TEOS ratios are shown in Figure 83; again, the morphologies display the same roughness trend. For the superhydrophobic surface of

Figure 83d, the surface is a combination of micro- and nano-scale structures. In addition to the differences in surface hydrophobicity, the surface morphology (roughness) differences are enhanced, thereby generating a superhydrophobic surface. For the silica surfaces in Figure 83b, when a hydrophobic fluorocarbon film of 30 nm thickness is deposited to achieve a hydrophobic surface while maintaining the surface roughness, the contact angle is only 142.3˚. Such results confirm that establishing the requisite surface roughness is critical in achieving the superhydrophobic surfaces in these sol-gel processes.

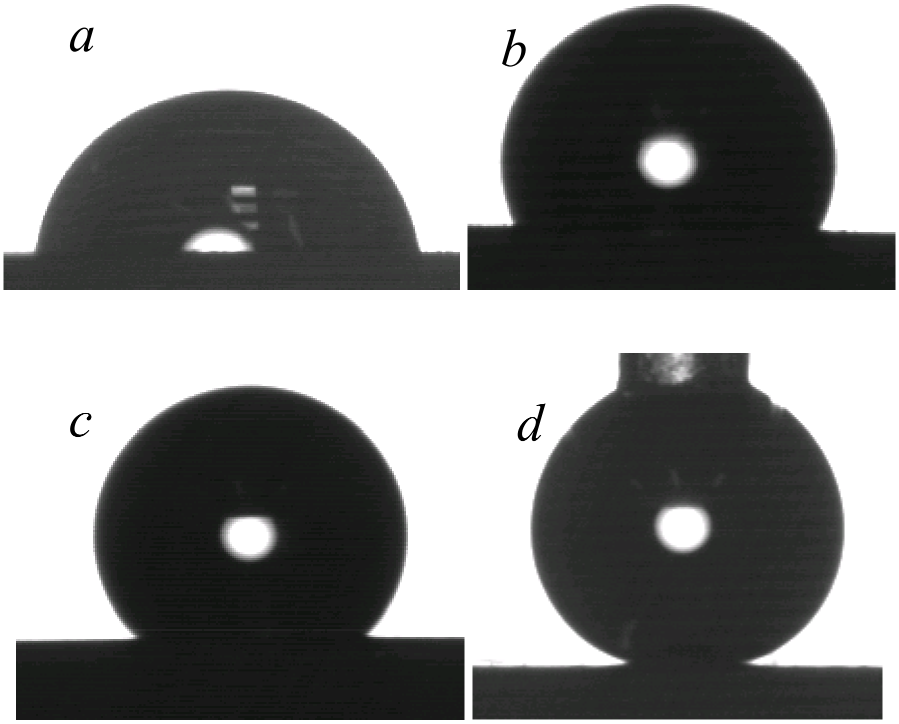

Figure 82. Water droplet contact on as prepared hydrophobic silica films. TFPS:TEOS ratio: a, 1:3, b, 1:1, c, 2:1, d, 3:1.

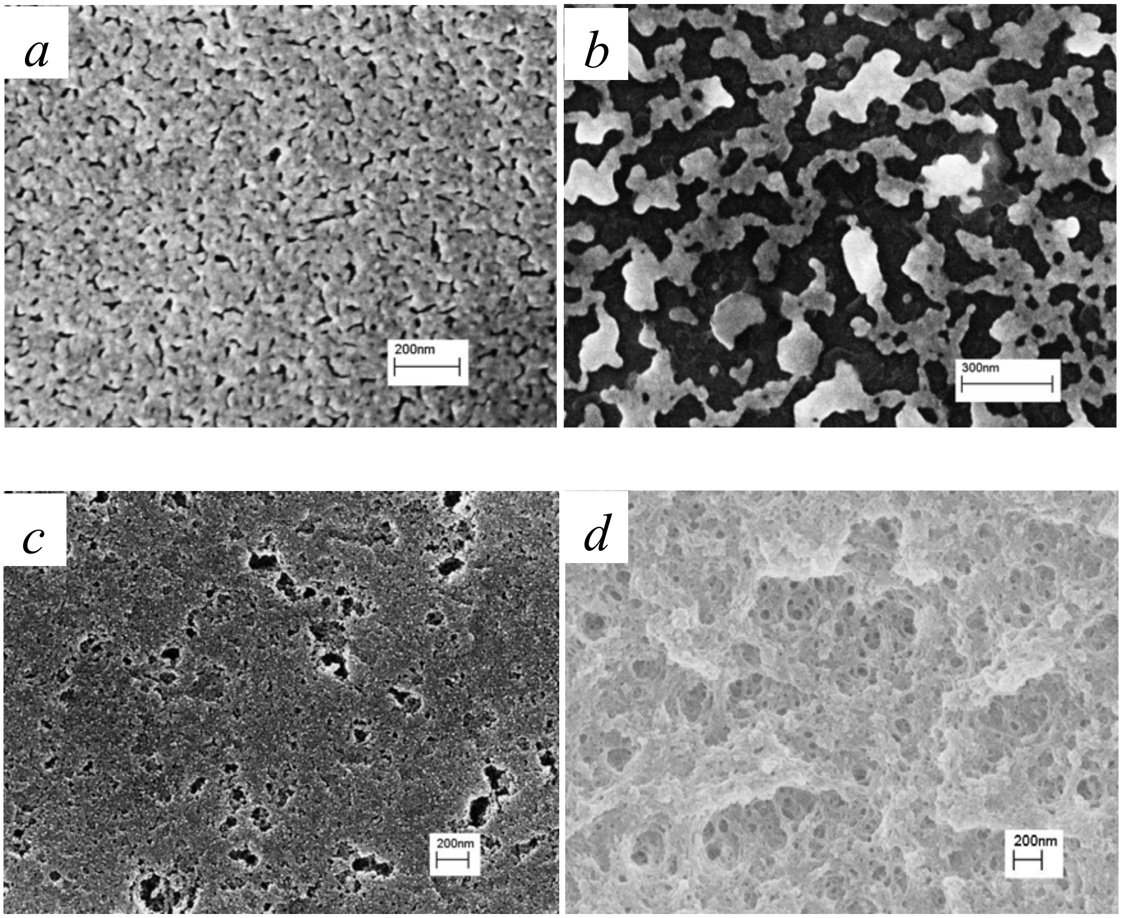

Figure 83. SEM images of as prepared hydrophobic silica thin film. TFPS:TEOS ratio: a, 1:3, b, 1:1, c, 2:1, d, 3:1.

The thermal stability of the as prepared hydrophobic silica monolith was tested using TGA; relative weight changes are shown in Figure 84. It has been reported that for the weight loss of a silica gel, three weight loss regions exist[66, 176]. Below ~150˚C, weight loss is due to the removal of chemisorbed water molecules. At 225˚C to 500˚C, weight loss is due to reaction and binding of silanol groups, thereby releasing water. The final mass loss is due to the loss of hydrophobic groups in the material; this mechanism sometimes overlaps with the second loss range. The measurements in Figure 84 indicate that the hydrophobic materials with a TFPS/TEOS molar ratio of 1:1 can withstand temperatures up to 370˚C without releasing water. When the ratio of TFPS/TEOS increases, the onset of binding of silanol groups decreases. When the temperature exceeds this critical point, the hydrophobic groups begin to decompose and the material undergoes further cross-linking and slow densification to form Si-O-Si linkages resulting in a loss of superhydrophobicity. A superhydrophobic surface prepared from TFPS:TEOS=3:1 is stable below 400˚C for 3 hours without any detectable contact angle and hysteresis changes. But after heating to 510˚C for 1 hour, the surface is no longer superhydrophobic (rather, it is superhydrophilic) possibly due to decomposition of the hydrophobic species on the surface[171]. Since PTFE has a degradation temperature of ~400˚C[177], the as prepared hydrophobic silica materials display similar thermal stability as PTFE, and thus offer the possibility of high temperature applications for these superhydrophobic materials.

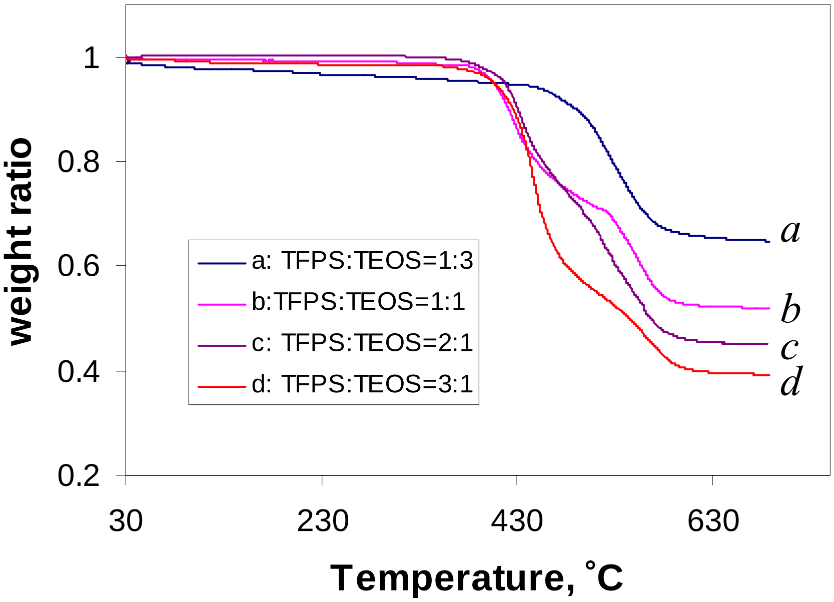

Figure 84. Thermal stability (TGA) evaluations of hydrophobic silica materials prepared from TFPS/TEOS mixtures.

Superhydrophobic surfaces fabricated from organic polymers are susceptible to degradation by UV radiation. The presence of UV labile segments, impurities (i.e., catalyst) and UV absorbing groups establishes sites where the polymer can undergo photo-oxidation to form carbonyl or hydroxyl groups in the bulk polymer and on the surface leading to degradation (i.e., unzipping) into smaller chains[178]. The introduction of these hydrophilic groups on the surface leads to a loss of superhydrophobicity. However, outdoor applications for superhydrophobic materials require that the surface be UV resistant. For organic superhydrophobic surfaces, the standard UV test time according to ASTM D 4329 cannot exceed 500 hours without significant degradation of surface properties such as apparent contact angle and contact angle hysteresis. As shown in Figure 85, the superhydrophobic silica films fabricated in this study exhibit extended UV stability, which is much improved relative to that of organic polymers. The superhydrophobic surface is retained even after 1000 hours of UV exposure; in addition, as shown in Figure 85, the contact angle hysteresis is $<5^\circ$ throughout the test period which implies improved stability of the surface fluoropropyl groups to UV irradiation. This result suggests that these superhydrophobic surfaces may be stable in outdoor environments, which offers an advantage over polymeric materials used for this purpose. For the hydrophobic silica material, only side groups ($-Si-(CH_2)_3CF_3$) exist on the material surface; these moieties are more UV stable than are polymers because of the strong $Si-(CH_2)_3CF_3$ bond, and the negligible UV labile groups on the silica surface, In addition, the silica main chain is comprised of Si-O bonds, which have higher bond strength and thus better UV stability than do organic polymer materials.

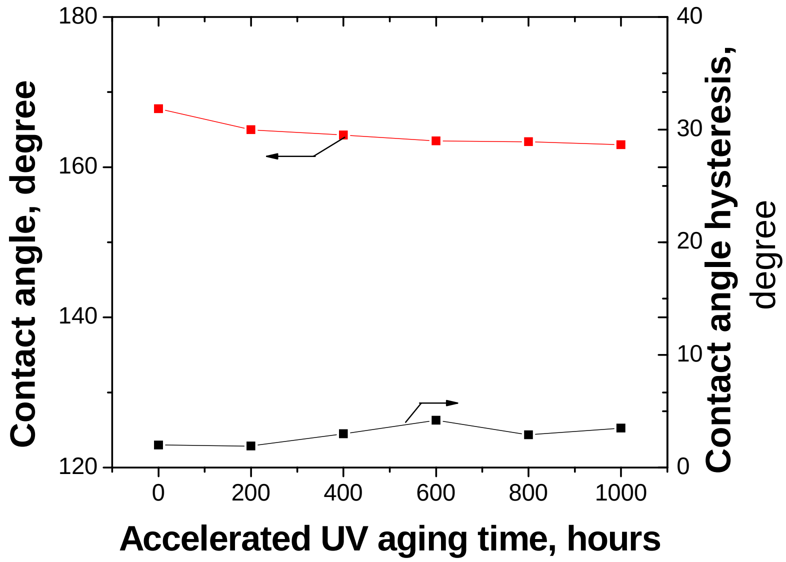

Figure 85. UV stability test of superhydrophobic silica films formed from a TFPS:TEOS ratio of 3:1; contact angle deviation ± 0.7˚, contact angle hysteresis deviation: ± 1.5˚.

Conclusions

The use of sol-gel processing with TEOS and TFPS as precursor and coprecursor at different molar ratios, superhydrophobic surfaces have been prepared that display a surface water droplet contact angle of 172˚, and a contact angle hysteresis 2˚ for a TFPS:TEOS ratio of 3. SEM analyses of the surface showed that the hydrophobicity is dependent on both the ratio of TFPS:TEOS and the surface roughness, which varied with TFPS:TEOS ratio. Thermogravimetric analyses and elevated temperature treatments indicated that the superhydrophobic silica materials are stable to temperatures of 400˚C. In addition, these superhydrophobic silicas show excellent UV stability with respect to contact angle and contact angle hysteresis for a test (ASTM D 4329) time of 1000 hours due to the strong Si-$(CH_2)_3CF_3$ bond, which suggests possible outdoor applications where UV exposure is prevalent.

4.4 Improved UV and thermal stability from sol-gel processing

In the current section, porous silica generated by sol-gel processing followed by surface fluoroalkyl substitution is invoked to improve the thermal and long term UV stability of superhydrophobic films. This approach to the fabrication of inorganic superhydrophobic silica films uses tetramethoxysilane and isobutyltrimethoxysilane as precursors. When isobutyltrimethoxysilane is incorporated into silica, the surface contains hydrophobic isobutyl groups, resulting in the ability to fine tune hydrophobicity and adhesion. Furthermore, this method does not use supercritical drying which is frequently employed for the preparation of superhydrophobic materials[65]. The porosity and thus surface structure can be controlled by parameters such as reaction conditions, solvent evaporation rate and precursor ratio. In addition, due to the fact that C-F bonds are stronger than C-H bonds, it is expected that the incorporation of fluoroalkyl groups will impart improved UV stability to the coating and thereby make possible a variety of outdoor applications. Therefore, by designing both surface hydrophobicity and surface structure into the film, it should be possible to prepare an inorganic coating with stable superhydrophobicity.

4.4.1 Experimental Details

<u>Bulk silica formation</u>

The initial solution was prepared using a two-step (acid/base catalyzed) procedure. Tetramethoxysilane (TMOS), isobutyltrimethoxysilane (IBTMOS), ethanol, and water were mixed in the volumetric ratio of 1:1:2:1 in a 30 ml vial. The pH was adjusted to 1.5-1.8 by adding hydrochloric acid, and the mixture stirred for 120 min at 60˚C to form silica sol. Ammonium hydroxide (NH_4OH) was subsequently added to the sol, followed by mixing for 5 min at room temperature. The resulting gel was allowed to age for 1 week. Slow evaporation of ethanol and water was permitted through a small slit (6mm×3mm) in the vial cap, thereby forming bulk silica within the vial.

Silica film formation by casting

Glass slides were used as substrates for the casting of silica films. The slides were cleaned in Piranha solution (70:30 (vol/vol) mixture of 96% sulfuric acid and 30% aqueous hydrogen peroxide) and subsequently rinsed extensively with de-ionized water and ethanol. Film casting was performed by invoking two glass slides. One slide served as the substrate, and the other, which was treated with trimethylchlorosilane (TMCS) to prevent gel from bonding to it, served as the cover. A chromium film of ~300 nm thickness was sputtered onto the surface of the substrate glass slide prior to gel formation. Bulk silica sol was prepared according the procedure described above; after NH4OH was added to the sol, the solution was stirred for 3 min. Several drops of the sol were then dispensed onto the substrate glass slide and the sol covered with the TMCS treated glass slide. After gelation, aging and evaporation of the solvent, a silica film resulted.

Preparation of superhydrophobic poly-butadiene films

A polybutadiene/toluene solution (5%wt. with 2% UV stabilizer TINUVIN 1577FF from Ciba and 1.5% antioxidant IRGANOX 1010FF from Ciba) was dispensed onto a silicon substrate at a spin speed of 2000 rpm to cast polybutadiene films (~10 μm). The film surface was subsequently exposed to an SF_6 plasma at 150 mTorr and 150 W for 10 min to form a superhydrophobic fluorinated polybutadiene surface as shown in Figure 73b.

Characterization

Contact angle measurements, Scanning Electron microscopy (SEM), Atomic Force Microscopy (AFM), Thermogravimetric Analysis (TGA), and Fourier Transform Infrared (FTIR) were used to characterize the superhydrophobic surfaces. Water droplets of 1 mm diameter were placed onto surfaces using a microsyringe and static images were recorded from which the contact angle of the droplet on the solid surface was determined. For SEM inspection, samples were fixed to aluminum stubs with conductive tape prior to coating with ~20nm of gold in an Ernest Fullam sputter coater. The samples were then imaged using a LEO 1530 SEM. An Explorer AFM from Veeco was invoked for roughness determination; measurements were performed in contact mode. A cantilever with a nominal spring constant of 0.1 N/m was used with minimum force. For TGA analysis, a TGA 2050 thermogravimetric analyzer from TA Instruments was used. An approximately 10 mg silica sample was placed in a ceramic pan, and the pan positioned in the TGA furnace; a temperature ramp was applied from room temperature to 800˚C with an air flow of 100 SCCM. FTIR spectra were obtained using a Nicolet Magna IR 560 with an ATR accessory. Samples were stored in a drybox to prevent moisture absorption. The spectrometer was flushed with dry air continuously before and during FTIR measurements.

Accelerated UV Weathering test

UV tests were performed by adhering to standard tests for the fluorescent UV exposure of plastics (ASTM D 4329). A UVA-340 fluorescent lamp was used to simulate the short and middle UV wavelength region corresponding to daylight exposure. The test cycle was 8 h UV with the uninsulated black panel temperature controlled at 60 ± 3˚C, followed by 4 h condensation with the uninsulated black panel temperature controlled at 50 ± 3˚C. A radiometer was used to monitor and control the amount of radiant energy that impinged on the sample. A thermometer was used to monitor the temperature in the test chamber.

4.4.2 Results and Discussion

Solvent evaporation of the solution-cast coating results in film surface roughness. The presence of hydrophobic chemical groups on the silica surface as illustrated schematically in Figure 86, along with the surface roughness generated from solvent evaporation, yields an enhanced surface contact angle. As described below, a superhydrophobic silica film can be prepared from sol-gel processing using TMOS and IBTMOS.

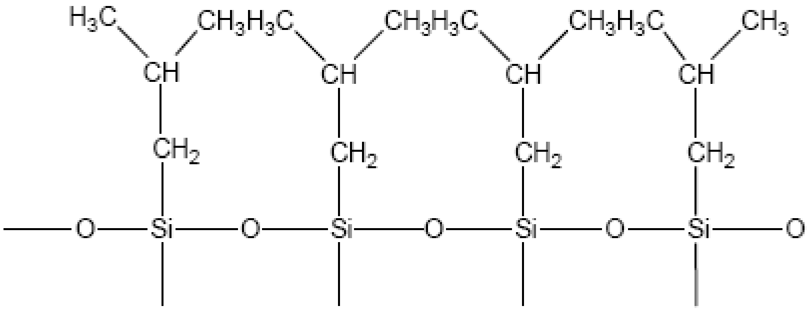

Figure 86. Illustration of hydrophobic groups on a treated silica surface.

4.4.2.1 Acid-Base Catalyzed Sol-Gel Process

Table 11. Physical characteristics of solutions resulting from different sol formulations.

TMOS: IBTMOS:ethanol:H_2O (Volume ratio)	Phase separation during hydrolysis	Transparency during Gelation	Precipitation after gelation
3:1:4:2	No	Yes	No
1:1:2:1	No	No	No
1:3:4:2	Yes	No	Yes

Table 12. Contact angles on surfaces resulting from various formulations of bulk silica.

TMOS (ml)	IBTMOS (ml)	Ethanol (ml)	H_2O (ml)	1M HCl (ml)	NH_4OH 1.1 M (ml)	Contact angle (˚)
1	3	4	2	0.03	0.5	160.8
2	2	4	1.9	0.1*	1	156.1
3	1	4	2	0.03	1	75.3

* HCl concentration is 0.1392 M.

Table 11 indicates that chemical reactions can occur that result in changes in the physical solution characteristics during the bulk silica formation process. When the concentration of IBTMOS was increased, e.g., TMOS:IBTMOS ratio of 1:3, phase separation occurred during hydrolysis as evidenced by the fact that the solution became cloudy (white) upon stirring. After the addition of ammonium hydroxide and equilibration, a separate viscous phase appeared at the bottom of the vial. After removal of the upper liquid phase, the viscous solution remaining in the vial underwent slow gelation and bulk silica formed. For a TMOS:IBTMOS ratio (v/v) of 1:1, no phase separation occurred; even after 120 min of reaction, the sol was still transparent. After gelation by addition of the ammonium hydroxide solution (1.1M), the sol became turbid/white and the solution gelled to form bulk silica. The time needed for this to occur depended on the amount of ammonium solution added; the more ammonium, the shorter the time to develop a turbid sol. During the controlled evaporation of solvent, the volume of silica was gradually reduced. Table 12 indicates the sol-gel process conditions and the final contact angles on the as-prepared silica surfaces.

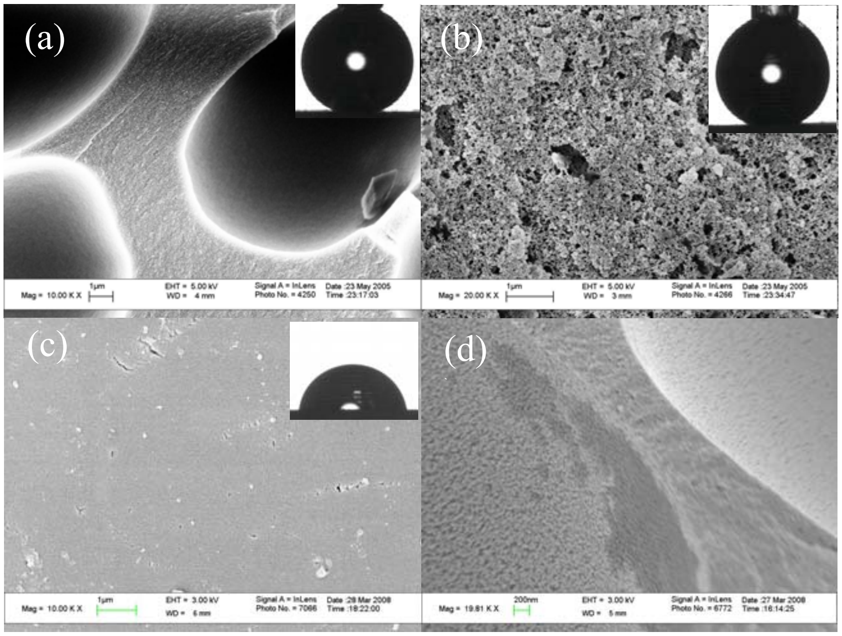

Figure 87. SEM images of surfaces of as-synthesized bulk silica, (a) TMOS:IBTMOS = 1:3, 1M hydrochloric acid: 0.03ml, 1.1M ammonia: 0.5ml (b) TMOS:IBTMOS = 1:1, 0.1392 M hydrochloric acid: 0.1ml, 1.1M ammonia: 1ml; (c) TMOS:IBTMOS = 3:1, 1M hydrochloric acid: 0.03ml, 1.1M ammonia: 1 ml; (d) High resolution SEM image of the structures on a superhydrophobic silica surface from a mixture of TMOS/IBTMOS = 1:3. Inset: images of the shapes of water droplets in contact with the prepared silica surfaces.

The creation of superhydrophobic surfaces requires control of the surface roughness. For surfaces formed from mixtures of TMOS/IBTMOS with a ratio of 1:3, superhydrophobicity was achieved with large pore sizes of ~10 µm as shown in Figure 87. In addition to the pores generated by evaporation of solvent, the particle size also contributes to the surface roughness as shown in Figure 87d. Surfaces from mixtures of TMOS/IBTMOS with a ratio of 1:1 still show superhydrophobicity although the isobutyl trimethoxysilane content is reduced. Furthermore, the pores are not spherical due to the increase of solvent solubility in the silica and the pore size is much reduced. Surfaces from mixtures of TMOS/IBTMOS with a ratio of 3:1 did not display superhydrophobicity because of the lower ratio of IBTMOS used; that is, the surface is generally flat with insufficient voids, and the contact angle is only 75.3˚.

After fracture of bulk silica formed from a 1:1 mixture of TMOS:IBTMOS, the fractured surface still displayed superhydrophobicity because the surface remained rough; the water contact angle on this fractured surface was also above 150˚.

4.4.2.2 Creation of Superhydrophobic Thin Films by Sol-Gel Processing

In addition to bulk silica, cast silica thin films were also prepared. Water droplet contact angles on different thin film surfaces are shown in Table 13. For a TMOS:IBTMOS ratio of 1:3, although superhydrophobicity was observed on bulk silica, ~300 nm films cast from this mixture were not superhydrophobic. A possible reason for this result is that large pores such as those observed in the bulk materials cannot form in thin films. However, with a TMOS:IBTMOS ratio of 1:1, a superhydrophobic thin film with a contact angle of 165-170˚ was achieved. Figure 88 shows the surface microstructure of a 300 nm silica film cast onto a glass slide from a TMOS/IBTMOS ratio of 1:1; the surface consists of globules (20-50 nm in diameter) surrounding a network of pores (submicron size) formed by evaporation of solvent from the sol. These observations also indicate that surface roughness exists in two scales: the pores contribute to the submicron scale roughness, and the silica particles contribute to the nanoscale roughness. This two-scale surface roughness combined with the hydrophobic surface that resulted from the isobutyl groups in IBTMOS, generated a superhydrophobic film surface.

Table 13. Thin silica films cast from different ratios of TMOS/IBTMOS.

TMOS:IBTMOS (v/v)	Contact angle, degree	Contact angle hysteresis, degree
1:3	101.0	Not measurable
1:1	167.8	2-3
3:1	73.6	Not measurable

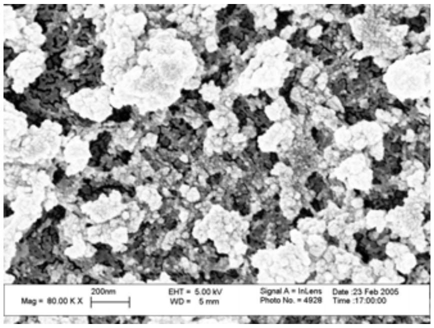

Figure 88. High resolution SEM image of a silica film cast from TMOS:IBTMOS = 1:1.

4.4.2.3 Stability of Superhydrophobic Surfaces

The hydrocarbon side group contained in the superhydrophobic silica can decompose (or be oxidized in air) at elevated temperature and thus cause the loss of superhydrophobicity. TGA studies of samples synthesized with TMOS/IBTMOS ratios of 1:1 and 1:3, demonstrate that the onset of weight loss is ~200˚C and ~207˚C, respectively, as shown in Figure 89. With continued heating above the onset temperature, the organic groups in the silica structure begin to degrade due to oxidation or bond cleavage of the isobutyl groups. TGA results showed that 27.7% loss is observed for a TMOS/IBTMOS ratio of 1:1. EDS results in Table 14 and Figure 90 also indicated that the isobutyl group content was 28.5%wt in the 1:1 silica (H atoms were included in the calculation) which agrees well with TGA data. For a TMOS/IBTMOS ratio of 1:3, similar results were observed to those with a TMOS/IBTMOS ratio of 1:1. Table 15 shows the contact angle data on the heat-treated surfaces at different temperatures. Contact angle decreased with increasing heat treatment temperature and contact angle hysteresis increased. When the heat treated surface was again treated with IBTMOS/hexane solution, the surface superhydrophobicity was recovered (CA ~165˚ and hysteresis < 5˚). This suggests that thermal degradation of the surface is primarily due to a change in surface chemistry rather than to a change in the surface roughness.

FTIR analysis of the silica film after a heat treatment at 400˚C indicated that hydrocarbon absorptions were absent as shown in Figure 91; CH3 and CH2 stretching vibration (2975-2840 cm-1) and deformation vibration (1232 cm-1, 1173 cm-1 894 cm-1 and 839 cm-1) intensities were below the detectability limit after the heat treatment, confirming decomposition of the organic groups.

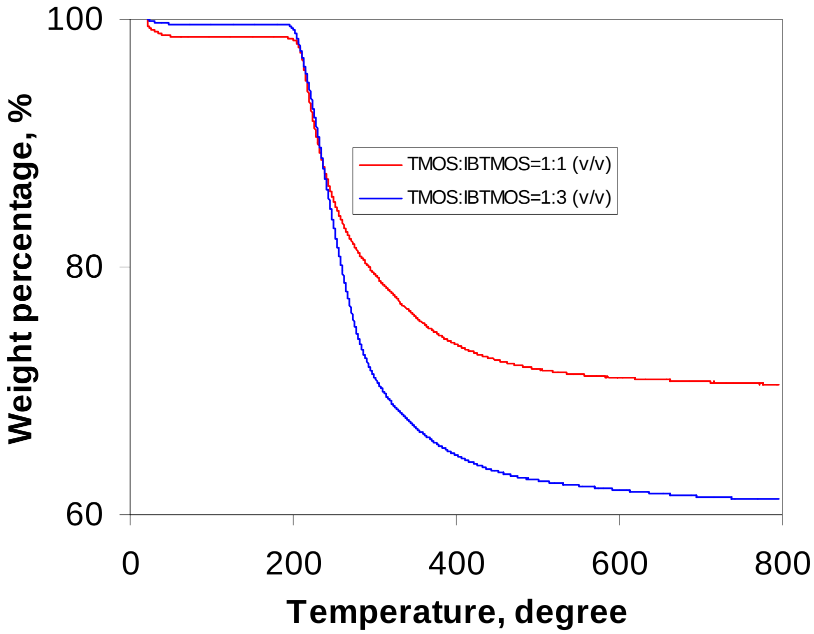

Figure 89. TGA results for silica from different TMOS/IBTMOS ratios. Temperature ramping rate: 4˚C/min.

Table 14. EDS analysis results of the thin film from TMOS/IBTMOS = 1:1

Element	Weight%	Atomic%
C	25.13	35.13
O	44.56	46.76
Si	30.31	18.11
Totals	100.00	100.00

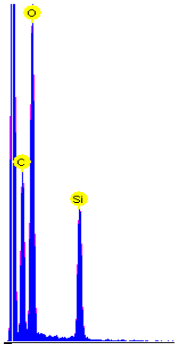

Figure 90. EDS spectrum of the thin film from TMOS/IBTMOS = 1:1.

Table 15. Thermal stability of the as-prepared superhydrophobic surfaces after heating for 2 hours at different temperatures.

Heat treatment temperature, ˚C	Contact angle, degree	Contact angle hysteresis, degree
200	165.3	12.6
300	91.7	>60
400	15.2	Not measurable

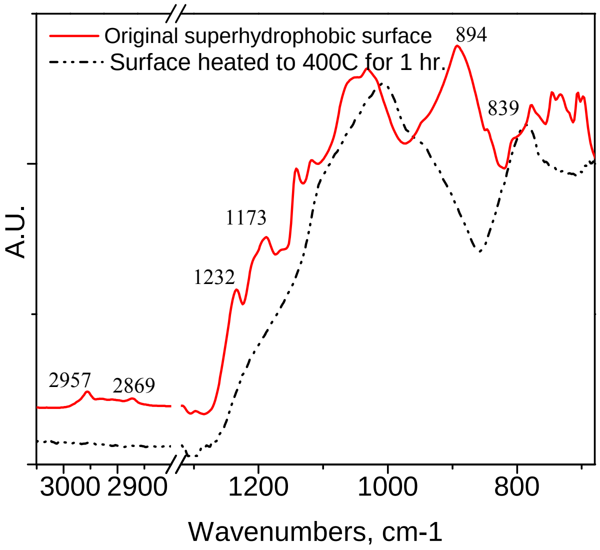

Figure 91. FTIR spectra of the silica superhydrophobic silica thin film before and after heat treatment at 400˚C for 1 hour.

Organic polymers with reactive (e.g., double bonds) or low energy (e.g., tertiary hydrogen) structures in the polymer main chain, are vulnerable to UV irradiation. When impurities (i.e., catalyst) and UV absorbing groups are present, the polymer can undergo a photo-oxidation process to form carbonyl or hydroxyl groups on the surface and thus degrade (unzip) into smaller chains[179]. The introduction of these hydrophilic groups leads to the loss of superhydrophobicity. As described previously, when the surface is hydrophilic, surface roughness enhances the hydrophilicity to superhydrophilicity. For the silica film, only small side groups (isobutyl groups) exist on the surface; these moieties are more UV stable than are polymers because negligible impurities and less UV-fragile defects exist on the silica surface; thus the silica film exhibits better UV stability than do organic polymers (polybutadiene fluorinated in SF6 plasma) as shown in Figure 92. In addition, the silica main chain is comprised of Si-O bonds, which have higher bond strength and thus better UV stability than organic polymer materials. Other commercially available polymers such as ethylene-vinyl acetate copolymer, polydimethyl siloxane and Teflon, all show surface degradation after long time UV aging tests.

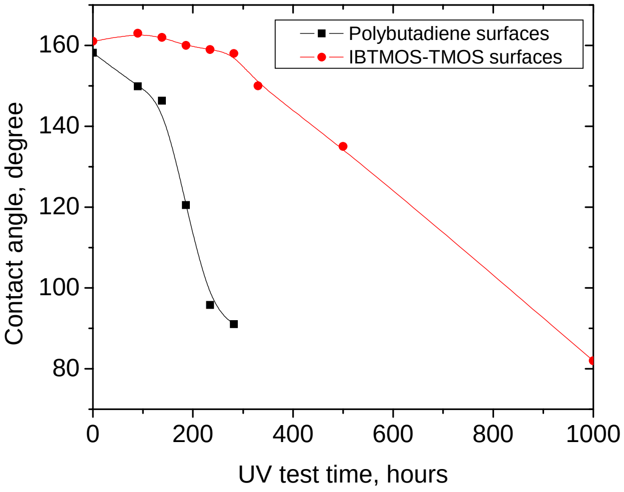

Figure 92. UV moisture weathering of superhydrophobic PB and silica thin film surfaces. Bottom curve: SF6 RIE etched PB + UV absorber TINUVIN 1577FF (2%) + antioxidant IRGANOX 1010FF (1.5%); Top curve: silica film from TMOS/IBTMOS (1:1) using a two step acid-base catalyzed sol-gel process.

When a superhydrophobic surface begins to degrade, the hysteresis changes more rapidly than does the contact angle. This observation is shown in Table 16, where contact angles changed very little, while hysteresis changed significantly. Therefore, contact angle hysteresis can be used to evaluate the surface chemistry change when the contact angles remain almost unaltered. The surface fraction that is air beneath the water drop becomes smaller and smaller, until it ultimately disappears, and the Cassie model no longer accurately describes the surface/water contact. Instead, the contact interface is better described by the Wenzel state. The FTIR spectrum in Figure 93 shows that after UV irradiation, the SiO-CH3 deformation vibration band at 1444 cm-1 disappeared due to continued hydrolysis. The ≡CH deformation vibration band at 1352 cm-1 also disappeared while the OCH2 vibration band at 1330 cm-1 appeared after UV irradiation because of oxidative degradation of the isobutyl groups specifically on tertiary carbons.

Table 16. Effect of UV irradiation on contact angle and hysteresis for a thin film formed from TMOS/IBTMOS = 1:1.

UV weathering test of silica film	Contact angle	Hysteresis
8 days	159-162°	3-5°
12 days	158°	15-20°

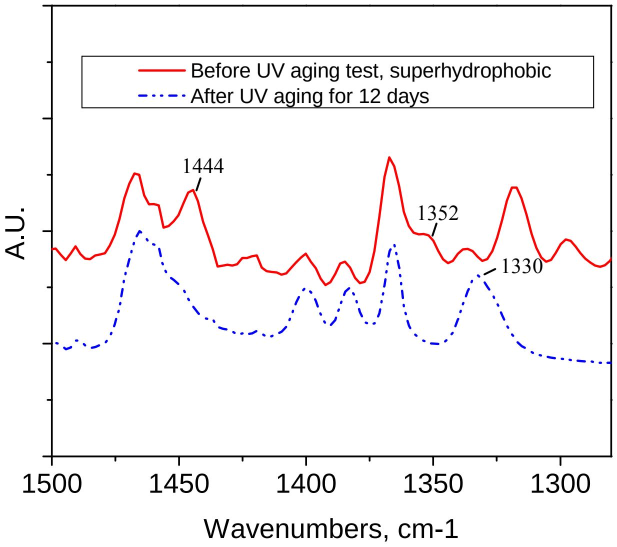

Figure 93. FTIR comparison of silica thin films before and after prolonged UV irradiation. Top curve: silica film from TMOS:IBTMOS=1:1 before UV test; bottom curve: the same silica film after UV testing for 12 days.

In order to mitigate the thermal and UV stability degradation of the superhydrophobic TMOS/IBTMOS surfaces, a heat treatment was performed on the silica thin films immediately after formation, to decompose/oxidize the organic moieties; subsequently, a fluoroalkyl silane treatment was carried out. AFM was used to probe the surface morphology of PFOS-treated superhydrophobic silica films. Figure 94 shows the surface morphology of a silica film produced from a 1:1 TMOS:IBTMOS mixture, that was heat treated at 500˚C and then PFOS treated; the root mean square (RMS) surface roughness from AFM was 330 nm. On the rough surface, air can still be effectively trapped between the water droplet and the substrate. Thus, the Cassie state can be maintained to achieve a superhydrophobic surface with both high contact angle and low hysteresis as shown in the inset in Figure 94.

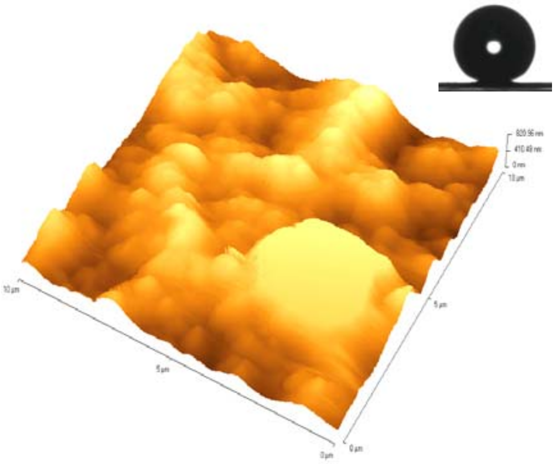

Figure 94. Superhydrophobic silica thin film AFM surface image after PFOS treatment; inset, water droplet image on the surface; Contact angle, ~168˚, hysteresis, 2˚.

Accelerated UV and thermal stability test results are shown in Figure 95 and Table 17. Because of the attachment of fluoroalkyl groups on the surface, improved thermal and UV stability were achieved due to the presence of a linear fluorocarbon chain on the silica surface. UV tests showed a stable superhydrophobic surface after a 5500 hour testing period without degradation of either contact angle or contact angle hysteresis. A thermal treatment at 400˚C demonstrated that the surface is stable to this temperature, which is a significant improvement relative to the results obtained with a superhydrophobic surface that contained isobutyl groups. Further temperature increases resulted in a decrease of the contact angle and an increase of contact angle hysteresis. When the treatment temperature was 500˚C, the surface was no longer superhydrophobic (contact angle ~ 0˚) as a result of the decomposition/oxidation of the surface fluoroalkyl groups. To our knowledge, this is one of the most stable superhydrophobic surfaces reported to date. This finding demonstrates that it may be possible to use superhydrophobic/self-cleaning surfaces in harsh environments such as high UV irradiation, high temperature, and outdoor applications.

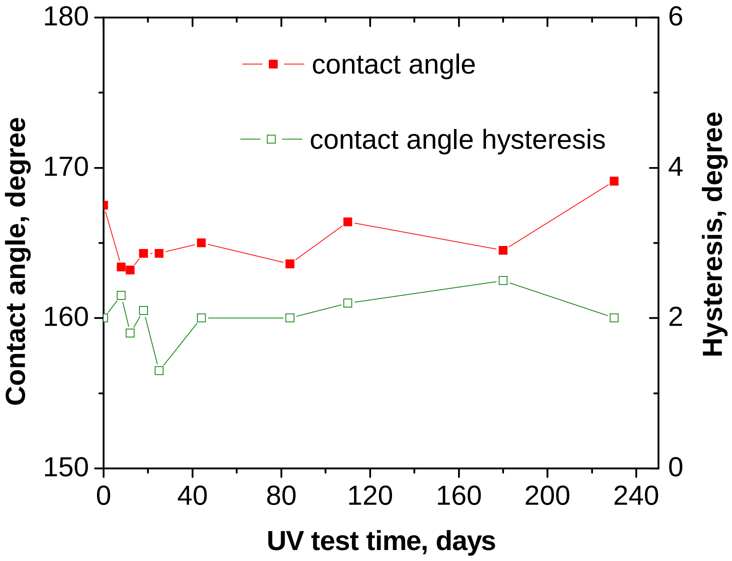

Figure 95. UV stability of a PFOS-treated rough silica thin film surface.

Table 17. Thermal stability of a PFOS-treated superhydrophobic thin film surface after heating for 2 hours at different temperatures.

temperature, ˚c	contact angle, degree	contact angle hysteresis, degree
400	166.3	2.1
450	160.4	>30
500	~0	not measurable

Conclusions

Superhydrophobic bulk silica materials and analogous silica thin films were prepared by TMOS/IBTMOS two-step acid base catalyzed sol-gel processing. Thermal analysis shows that these superhydrophobic materials begin to lose superhydrophobicity when heated above 200˚C. UV weathering tests (ASTM D 4329) indicate that the silica materials demonstrate better stability compared to SF6 plasma etched polybutadiene films but lost superhydrophobicity due to the oxidative degradation of the isobutyl groups. When the superhydrophobic surfaces from TMOS/IBTOMS mixtures were heated to 500˚C, the surface became superhydrophilic. When a PFOS treatment was performed on the surface, the attachment of fluoroalkyl groups resulted in superhydrophobicity. This surface is much more stable than a surface with isobutyl groups; after a UV testing time of 5500 hours, no degradation of either contact angle or contact angle hysteresis was observed for the PFOS-treated surface. Thermal stability of the PFOS-treated rough silica surfaces was also much improved at temperatures up to 400˚C. The PFOS-treated superhydrophobic surface is one of the most stable surfaces reported to date. This approach to the generation of superhydrophobic surfaces may have much significance for the successful application of self-cleaning surfaces in a variety of environments.

CHAPTER 5

TRANSPARENT SUPERHYDROPHOBIC SURFACES AND WATER VAPOR CONDENSATION

In this chapter, the preparation of superhydrophobic surface from sol-gel process with eutectic liquid (urea and choline chloride) will be investigated. After the preparation of the superhydrophobic surface, properties such as adhesion on the surface with AFM measurement, optical transparency and water vapor condensation will be examined.

5.1. Introduction

The formation of superhydrophobic coatings with properties similar to those of lotus leaves is of interest for many applications. Achievement of optically transparent superhydrophobic coatings would make possible self-cleaning surfaces in application areas such as window coatings, anti-dust screens and optical devices. Lotus leaves display excellent water repellent surface properties with a high (>150˚) water droplet contact angle. The superhydrophobicity is based on two indispensable factors, a hydrophobic surface and hierarchically ordered surface structures[2, 142, 180]. Recently, insights into the hierarchical structures and the structural/ chemical properties required for superhydrophobicity have been greatly improved[14, 25, 28, 110, 154, 181]. In order to achieve light transparency, the surface roughness must be minimized to reduce the light scattering, while for superhydrophobicity, surface roughness is necessary. Therefore, establishment of the appropriate surface structure length scale, i.e., the trade off between superhydrophobicity and transparency, is critical to the preparation of films that display both properties. Previous studies of the optical transparency of superhydrophobic layers utilized formation methods such as the sublimation of aluminum acetylacetonate for the preparation of titania and boehmite films[22, 182], and the fabrication of honeycomb-like microporous polymer films[82]. Formation of optically transparent films from organically modified silica sol [105] or silica particles using the Stöber method has also been reported[183]. Transparent nanoporous alumina surfaces have been fabricated using anodization followed by surface treatment in a gas phase (fluoro) alkyl silane[184]; in addition, superhydrophobic alumina layers derived from a sol-gel process have been described[63, 185]. The largest static contact angle reported was in the range of 146-153˚, but no hysteresis data were offered. A method of preparing flower like alumina surfaces was also reported by treating the alumina film in boiling water[185]. In these studies, although optical transparency was achieved, the reported contact angles were only ~150˚ and the hysteresis was either not reported or was significantly above 10˚ due to the dichotomy between the surface roughness needed for superhydrophobicity and the smooth surface required for optical transparency. Recently, a layer-by-layer technique has been reported for the preparation of transparent and superhydrophobic films using SiO_2 nanoparticles of various sizes[186].

A eutectic liquid, which shows similar properties to those of ionic liquids[187], is a eutectic combination of salts that yields a reduced melting temperature for the salt mixture. Halide salts can form complexes with hydrogen donors and in at least one extreme case, choline chloride and urea (C-U) with a molar ratio of 1:2, form a non-volatile deep eutectic liquid, with a melting point of 12 ˚C[188]. For choline chloride, only those compounds that form hydrogen bonds with chloride ions form a homogeneous liquid with a significant decrease in the freezing point. Compounds with greater ability to form hydrogen bonds display an enhanced freezing point depression when choline chloride and a hydrogen donor are mixed.

Due to the extraordinary water repellency properties of lotus leaves, superhydrophobicity has been studied intensively. Superhydrophobicity on lotus leaf surfaces is due to the particular surface structure on the lotus leaves along with the presence of waxy hydrophobic coatings. Applications of superhydrophobic surfaces include self-cleaning, anti-dust, anti-corrosion, fluid friction reduction in microfluidic devices, anti-stiction in MEMS devices, anti-bacterial coatings, and transparent coatings [22, 125, 129, 189-193]. Numerous methods have been developed to prepare superhydrophobic coatings, including layer by layer film formation[71, 102], electro-spinning [73, 194], carbon nanotube modification [61, 195, 196], photolithographic methods[29], chemical vapor deposition (CVD) [197], and self assembly [14, 198]; all of these approaches have generated contact angles >150°. Superhydrophobicity requires two factors: surface hydrophobicity, which is according to the definition by Young's equation, higher than 90°, and appropriate surface structure, often designated surface roughness. When a surface has both of these factors in appropriate ranges, we can achieve superhydrophobic surfaces with contact angles (CAs) >150° and CA hysteresis <10°. This property of superhydrophobicity has the potential for application to antistiction in MEMS devices.

Microelectromechanical systems (MEMS) have been used extensively to perform basic signal transduction operations in sensors and actuators. However, autoadhesion, or spontaneous sticking (stiction) between MEMS structures, remains a major limitation in bringing this new class of engineering devices to the broader market. Freestanding mechanical structures fabricated from polycrystalline silicon may strongly adhere to each other when brought into contact, due to hydrogen bonding between surface hydroxyl groups[199]. In a high humidity ambient, this problem is exacerbated by adsorption of water and capillary condensation. Water capillaries or condensation can cause catastrophic failure of MEMS devices[90]. Low surface energy coatings for anti-moisture condensation and thus antistiction are required for many practical MEMS devices[90, 199, 200].

Two primary methods have been invoked to prevent these failures. One method uses a surface treatment with low surface energy coatings, e.g., octadecyl trichlorosilane

(OTS), to inhibit surface condensation of water[201]. The other method involves the fabrication of structured surfaces in order to reduce the contact area and thereby reduce the adhesion force between the free standing structures and the substrate[202].

We have prepared superhydrophobic silica surfaces using sol-gel processing and demonstrated for the first time antistiction by AFM adhesion tests using tipless probes. This approach greatly reduces the stiction of MEMS moving parts which will help to reduce stiction failures of MEMS devices. Water does not condense on this superhydrophobic surface thus eliminating capillary forces. Furthermore, the adhesion force between the free standing structures and the substrate can also be effectively reduced due to the presence of surface nano-structures.

In the current chapter, we demonstrate the use of a eutectic liquid in a sol-gel process following the procedure described in Figure 96 to form silica films with optical transparency and superhydrophobic characteristics. We previously reported the fabrication of a silica film with excellent UV stability that demonstrated that superhydrophobic silica surfaces may be appropriate for outdoor self-cleaning applications[203]. Unlike the conventional sol-gel process, the process described in this report uses a unique solvent, a eutectic liquid with a melting point of 12 ˚C that is composed of urea and choline chloride (2:1 molar ratio). Relative to common sol-gel solvents such as ethanol, this eutectic liquid has an extremely low vapor pressure and so will remain in the film throughout the process under ambient conditions. As a result, porous silica thin films can be formed after gelation in the presence of a base catalyst and subsequent extraction of the eutectic liquid. This porous film formation approach is also advantageous compared to that of aerogel silica formation using supercritical drying[65] because no specialized equipment or procedures are required for eutectic liquid processes. The, eutectic liquid can be used to control film thickness and surface roughness, and after a fluoroalkylsilane surface treatment, superhydrophobic, transparent films can be achieved.

5.2. Experimental Details

5.2.1 Silica film formation

The general eutectic solution formulation is: tetraethoxysilane (TEOS): 0.6 g, choline chloride-urea (C-U): 2.4 g, ethanol: 3 g, 1M HCl aqueous solution: 0.3 g, ethylene oxide propylene oxide triblock copolymer P123 ($EO_{20}PO_{70}EO_{20}$): 0.12 g. Hydrolysis and condensation to form the sol solution occurred after addition of HCl to the mixture followed by stirring for 3 hrs at room temperature. The sol solution was then diluted with ethanol and spin-cast onto one square inch precleaned glass microscope slides at 3000 rpm to form uniform films with thicknesses between 100 and 500 nm. The spincast procedure was: 1000 rpm for 5 seconds followed by a ramp to 3000 rpm (ramp speed: 1000 rpm/second) and finally hold at 3000 rpm for 15 seconds. The coated glass slide was placed in a desiccator with a container of 1 ml ammonia (29%) at the bottom, to promote gelation. After 2 weeks, the glass slide was removed from the desiccator and rinsed extensively with ethanol to remove the eutectic liquid in the film and thus yield a porous thin film on a glass microscope slide.

5.2.2 Surface fluoroalkylsilane treatment

Substrates with spin-cast silica films were placed in a fluoroalkylsilane (trichloro(1*H*,1*H*,2*H*,2*H*-perfluorooctyl) silane, PFOS)/n-hexane solution (10 mM) for 30 min to allow adsorption of a PFOS layer onto the SiO_2 surface; subsequently the samples were heated to 150 ˚C in air for 1hr and at 220 ˚C for 5 min to promote silane hydrolysis and condensation, thereby forming a stable fluorosilanated layer on the silica surfaces.

5.2.3 Water vapor condensation experiments

Water vapor condensation was conducted by placing a substrate on a plate maintained at ~0 ˚C and exposing the substrate to water vapor that was generated by bubbling N2 through water (40˚C) to establish an environment of 100% humidity on the surface. Condensation was performed for a specific time period (0.5-30 min). The longer the exposure time, the larger the droplet size; typical droplet sizes over the times investigated ranged from 1 μm to 200 μm.

5.2.4 Characterization

Scanning Electron Microscopy (SEM), contact angle measurements, Atomic Force Microscopy (AFM) and UV-Visible spectroscopy (UV-Vis) were used to characterize the superhydrophobic silica films. The as-prepared samples were characterized by high resolution field-emission scanning electron microscopy (FESEM; LEO 1530 FEG at 2-10 kV). Six contact angle measurements were performed on each sample (for average values) at different sample spots with water droplets (4 μl size) formed using 0.5 μl step changes on a microsyringe at a predefined height and static images recorded; advancing contact angles of the droplet on the solid surface were determined from these images. Receding contact angles were measured by increasing the volume of the 4 μl water droplet to 6 μl and subsequently reducing the volume to 4 μl by extracting the extra water with a volumetrically controlled pipette using the same 0.5 μl step changes; deviations of the measured contact angles were within ± 1˚. The difference between the measured advancing angle and the receding angle is termed the contact angle hysteresis, and is related to the sliding angle; the hysteresis value can be used to characterize the self-cleaning effect of a superhydrophobic surface. Surface roughness was measured with a Veeco NanoScope IIIa/Dimension 3000 AFM system in contact mode. The Si tip spring constant is 0.2 N/m. AFM force curves were measured with a tipless silicon nitride coated probe with a tip spring constant of 0.12 N/m.

5.3. Results and Discussion

On a rough surface, two different loss mechanisms are operative when light is incident on the surface. One is the (diffuse) reflection of light from a surface with a surface roughness greater than the wavelength of the light, and the other is light scattering. In order to overcome reflection losses, film thickness and surface roughness must be reduced. For this purpose, a two step acid-base catalyzed sol-gel process was employed to prepare films with the appropriate roughness using a eutectic liquid as shown in Figure 96. To allow the preparation of ultrathin silica films, a tri-block copolymer P123 was used to enhance wetting between the sol and the substrate during spin-casting; incorporation of this material improves the ability of the film to uniformly cover the substrate. Several different dilutions of the sol with ethanol were investigated in order to investigate changes in the optical transparency of the resulting thin film coatings. After spin-casting, gelation and extraction of the eutectic liquid and tri-block copolymer from the film, the desired roughness necessary for superhydrophobicity was achieved.

5.3.1 Preparation of silica thin films

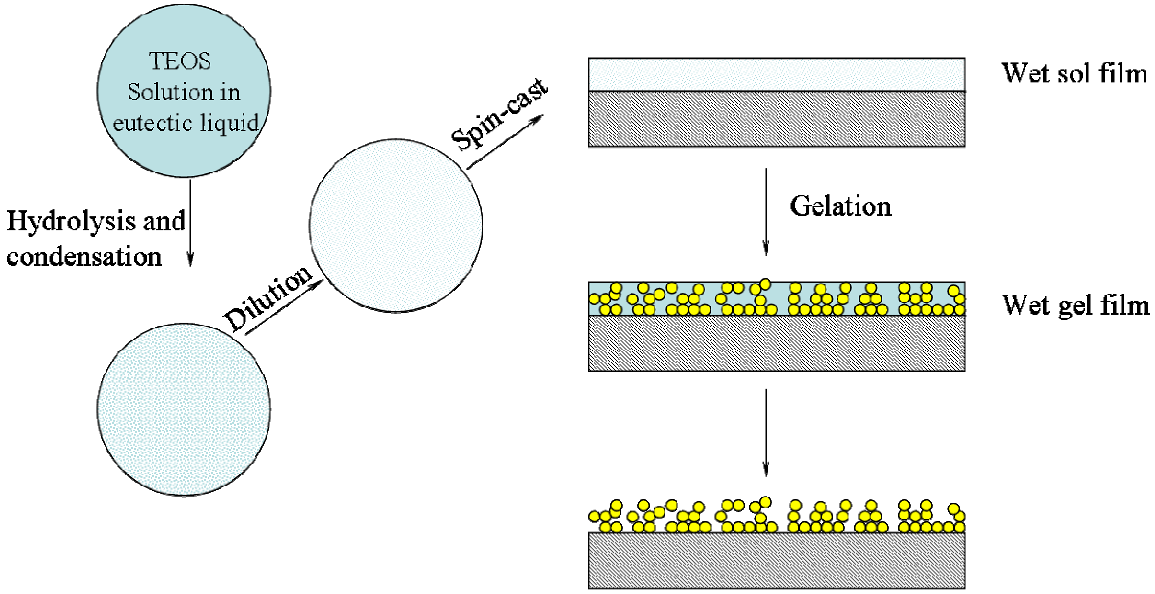

Figure 96. Schematic illustration of the procedure to prepare silica rough surfaces.

Silica thin films can be formed on glass substrates by spin-casting. However, films formed (e.g., by dipcoating, spin-casting) with the sol derived from acid catalyzed processes (e.g., TEOS, ethanol, H_2O, HCl) are usually dense and film surfaces are smooth. Therefore on such surfaces the contact angle after fluoroalkyl silane (PFOS) treatment is ~115˚. Under acid catalyzed conditions, lightly branched small polymer molecules are formed in a traditional sol-gel process. On the other hand, a eutectic liquid (e.g., urea and choline chloride) incorporated into the sol-gel process can serve as a non-volatile solvent and template for the formation of random and perhaps fractal structures in the silica. As a result, after spin-casting of the sol on glass substrates, gelation in an ammonium hydroxide atmosphere, and extraction of the eutectic liquid, asperities are formed; after a fluoroalkyl silane (PFOS) treatment, the surface contact angle can reach 170˚ with a hysteresis of 2-3˚. However, the film is thick and although it shows some optical transparency at long wavelengths, the shorter wavelength transparency is limited due to light scattering from the porous film (Figure 97).

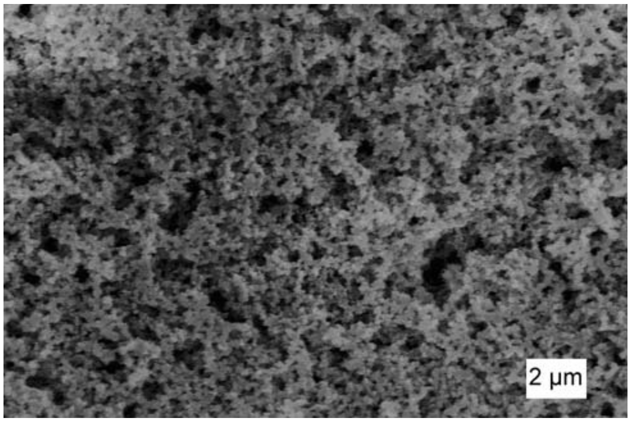

Figure 97. Surface morphology of silica films formed from the eutectic liquid/sol-gel process; tetraethoxysilane (TEOS): 0.6 g, choline chloride-urea (C-U): 2.4 g, ethanol: 3 g, 1M HCl aqueous solution: 0.3 g; film thickness: ~ 0.5 μm.

5.3.2 Reduction of the size of surface structure

In order to reduce the film thickness while maintaining superhydrophobicity, the effect of spin speed was first investigated. In the range of spin speed of 3000 rpm to 6000 rpm, the CA and hysteresis of the silica films is shown in Figure 98. As spin speed increases, although the surface contact angles do not change significantly, the contact angle hysteresis changes dramatically from a very low hysteresis (~4˚) to a very large value (~40˚). This results in the degradation of surface superhydrophobicity for ultra-thin films, which is especially deleterious for self-cleaning applications where roll-off superhydrophobicity is needed. We should note that the film thickness was essentially constant even though spinning time was increased. Apparently, the film viscosity increases substantially during the spin-casting process, due to ethanol evaporation, and a concomitant reduction in film temperature, which causes the eutectic liquid to solidify (melting point ~12 ˚C).

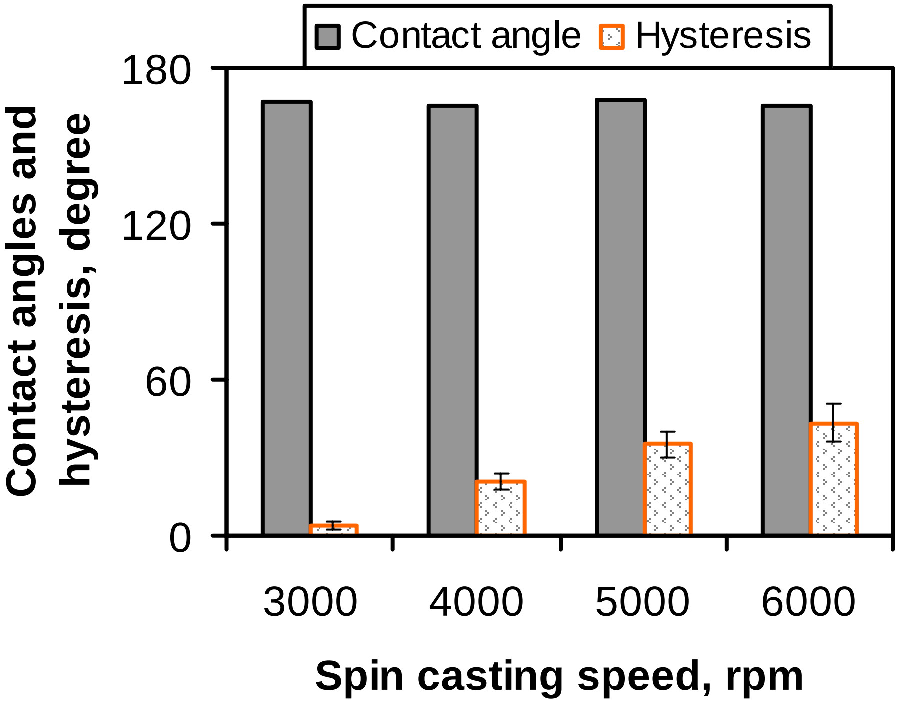

Figure 98. Effect of spin speed on contact angle and contact angle hysteresis on silica films; silica sol prepared from tetraethoxysilane (TEOS): 0.6 g, choline chloride-urea (C-U): 2.4 g, ethanol: 3 g, 1M HCl aqueous solution: 0.3 g.

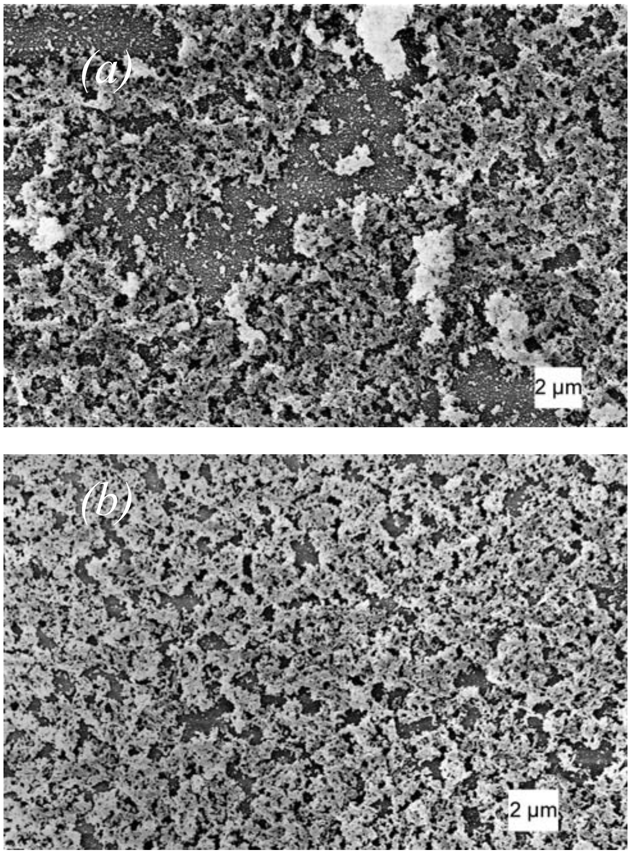

Figure 99. SEM comparison of surface morphologies for as-prepared sol-gel film without (a) and with (b) surfactant P123; diluted sol with sol: ethanol = 1:1, silica sol from tetraethoxysilane (TEOS): 0.6 g, choline chloride-urea (C-U): 2.4 g, ethanol: 3 g, 1M HCl aqueous solution: 0.3 g, P123 (for (b) only): 0.12 g; prepared at a spin speed of 3000 rpm

In order to attain transparent superhydrophobic surface coatings, the film thickness and structure size must be reduced. Achievement of thinner films by invoking a more dilute sol solution with ethanol was investigated. However, the film formed with diluted sol (sol:ethanol = 1:1) was not desirable in this regard. Under these conditions, discontinuous sol/C-U droplets formed on the surface during the gelation and aging process which led to non-uniform surfaces as shown in Figure 99a. Furthermore, the final film was not superhydrophobic after PFOS treatment. Surface roughness uniformity was improved by incorporation of the triblock copolymer P123 into the sol to lower the surface tension of the solution. After incorporation of the polymer, the surface morphology following extraction of the eutectic liquid and the polymer, was much improved as shown in Figure 99b.

In order to further reduce the surface roughness while maintaining surface superhydrophobicity, further dilution of the sol with ethanol was investigated. As shown in Figure 100, dilution of the sol with ratios of ethanol:sol = 1:1, 3:1, 5:1 to 7:1, resulted in spin-cast films that showed surface roughness wherein the surface structure sizes dropped continuously with dilution. For a ratio of 1:1, the film was thick after gelation, and silica globules coalesced, forming large agglomerates; such structures yield rough surfaces for superhydrophobicity. The corresponding water droplet contact angles and hysteresis on these surfaces after PFOS treatment are shown in Figure 101. When the surface structures decreased in size as a result of further sol dilution, the contact angles on these surfaces remained high (> 160˚), but the hysteresis increased due to the reduced surface roughness as indicated by AFM measurements (Table 18). With further dilution to ethanol:sol = 7:1, the contact angle hysteresis reached ~10˚ due to the smaller but more open structure size on the surface (Root-Mean-Square (RMS) roughness (R_{RMS}) is 69.1 nm as shown in Table 18). The thickness dependence of films spin-cast from diluted sol was also investigated. With increased dilution, the thickness dropped continously as shown in Figure 102.

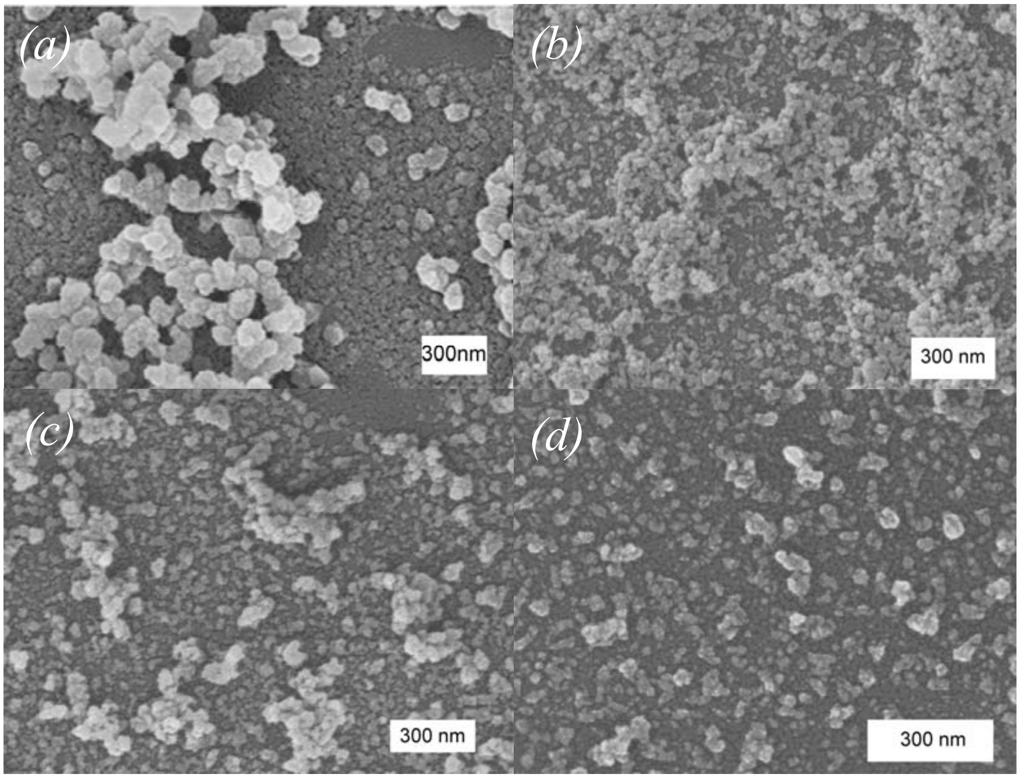

Figure 100. SEM surface images of dilute-sol-coated glass slides; ratios of ethanol:sol are: a. 1, b. 3, c. 5, and d. 7; silica sol from tetraethoxysilane (TEOS): 0.6 g, choline chloride-urea (C-U): 2.4 g, ethanol: 3 g, 1M HCl aqueous solution: 0.3 g, P123: 0.12 g; spin-cast at 3000 rpm.

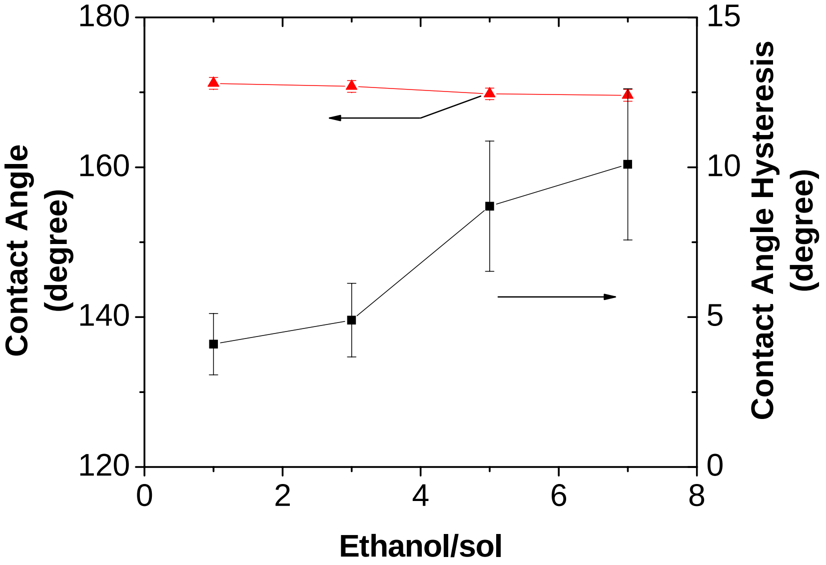

Figure 101. Dependence of contact angle and hysteresis on the ethanol:sol ratio; silica sol from tetraethoxysilane (TEOS): 0.6 g, choline chloride-urea (C-U): 2.4 g, ethanol: 3 g, 1M HCl aqueous solution: 0.3 g, P123: 0.12 g; spin-cast at 3000 rpm.

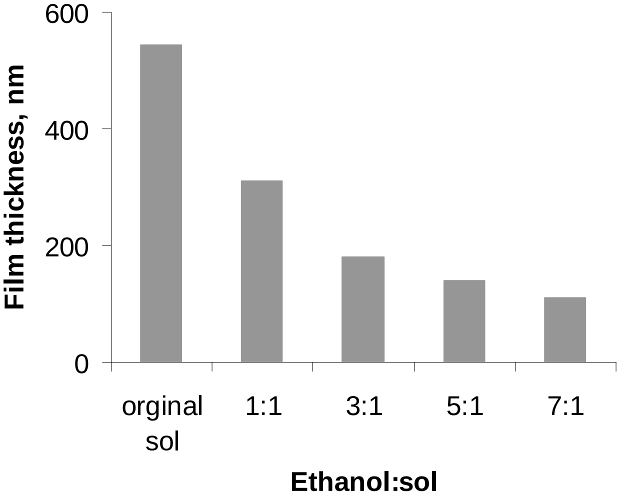

Figure 102. Film thickness with different sol dilution from cross-sectional SEM;. silica sol from tetraethoxysilane (TEOS): 0.6 g, choline chloride-urea (C-U): 2.4 g, ethanol: 3 g, 1M HCl aqueous solution: 0.3 g, P123: 0.12 g.

Table 18. RMS Roughness from AFM measurements.

Spin-cast films	R_{rms} from AFM measurement, nm
Ethanol:sol = 3:1	97.9
Ethanol:sol = 5:1	79.1
Ethanol:sol = 7:1	69.3

It has been reported that the surface structure height is very important in achieving a superhydrophobic state[195]. That is, in addition to contact areas on a rough surface, the size scale of surface structures determine the contact angle of a water droplet on the surface. Thus, to achieve superhydrophobicity, contact area, contact fraction (including structure density) and structure height are critical. This effect is demonstrated in Figure 101 where the hysteresis increases for films spin-cast from the diluted sol. Clearly, surface roughness of spin-cast films decreased continuously with dilution up to a dilution ratio of ethanol:sol = 7:1.

These observations suggest that at the composite contact interface, interaction is primarily between the contact area of water with surface structures. For long range interactions between molecules, there are generally three types of forces operative: induction, orientation and dispersion. In particular, for the interaction between two dissimilar molecules of which one is non-polar, the van der Waals energy is almost completely dominated by the dispersion contribution.[23] For the water droplet-rough surface interaction, the force is mainly dispersion due to the hydrophobic nature of the superhydrophobic surface. When surface structures are very small, the non-contacting areas where there are large separations (air cushion) between the substrate and the water droplet, van der Waals interaction across the air cushion is dominated by the properties of the bulk or substrate material. In contacting areas, adhesion energies are dominated by the properties of the surface monolayer.[23] In addition, for dispersion forces under large separations (e.g. >100 nm), interactions across the air cushion are negligible due to the retardation effect[23]. Therefore, the interaction is primarily between the contact areas of water with surface structures. However, when the surface structure size (height) is greatly reduced and the dispersion forces are not completely eliminated, the van der Waals interaction across the air cushion will inhibit the formation of the air cushion. Under this situation, a Cassie state is not attained and superhydrophobicity cannot be achieved due to a large hysteresis.

5.3.3 Optical transparency

Optically transparent and superhydrophobic coatings offer many potential applications in window glasses, auto wind shields, optical lenses and solar cell arrays. For porous films, numerous air/glass interfaces exist in the film and the transmittance of light is reduced due to light scattering; as a result such films appear white and opaque. When the film is thin and structure sizes are below ~ ¼ the wavelength of light, the film is transparent; when the structure size is even smaller, the scattered light can also be minimized. Thus, reduction of the size of surface structures and film thickness can lead to minimization of transmission losses for superhydrophobic surfaces. As the sol is diluted with ethanol from a ratio of 1:1 to 7:1, the transmittance of the resulting film increases (Figure 103). Furthermore, curve d (ethanol:sol = 5:1) indicates that at longer wavelengths (> 490 nm), the transmittance is greater than that of a bare glass slide, while at wavelengths < 490 nm, transmittance is lower than the bare glass slide. Apparently, 490 nm is the wavelength at which this specific structured film begins to scatter light. This wavelength corresponds to a rough surface layer of ~ 120 nm and the results are consistent with the thickness of ~130 nm observed from SEM images and shown in Figure 102; indeed, light scattering occurred on this surface. For a dilution of 7:1, the RMS roughness and thickness are reduced and the transmittance is always higher than that of the bare glass slide due to the antireflective property of the thin film. A photograph demonstrating the transparency of these superhydrophobic films is shown in Figure 104.

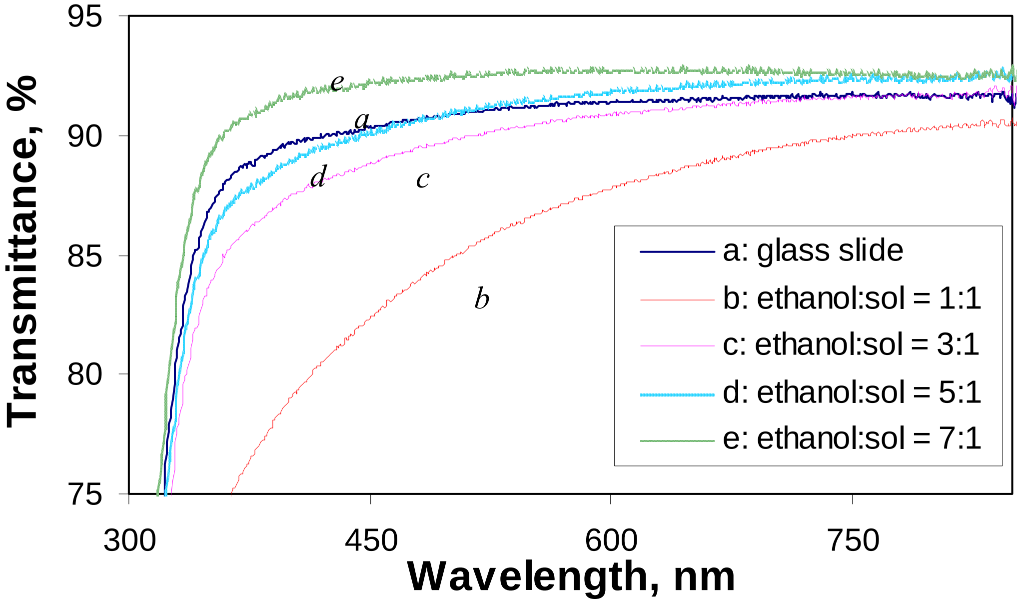

Figure 103. UV-Visible transmittance of glass microscope slides coated with superhydrophobic films generated with various ratios of ethanol:sol; silica sol from tetraethoxysilane (TEOS): 0.6 g, choline chloride-urea (C-U): 2.4 g, ethanol: 3 g, 1M HCl aqueous solution: 0.3 g, P123: 0.12 g; spin-cast at 3000 rpm.

Figure 104. Optical demonstration of a transparent superhydrophobic silica film with dilution ratio ethanol: sol of 5:1 spin-cast at 3000 rpm.

5.3.4 Non-stick property on the superhydrophobic surface

In order to quantitatively demonstrate the non-stick or reduced adhesion properties of the superhydrophobic surfaces, AFM force curves were generated using a tipless probe (with large contact area). As shown in Figure 105, with the same silane (PFOS) treatment, the adhesive force is greatly reduced between the superhydrophobic surface and the Si_3N_4 surface of the probe compared to the force experienced by the probe in contact with a smooth glass surface.

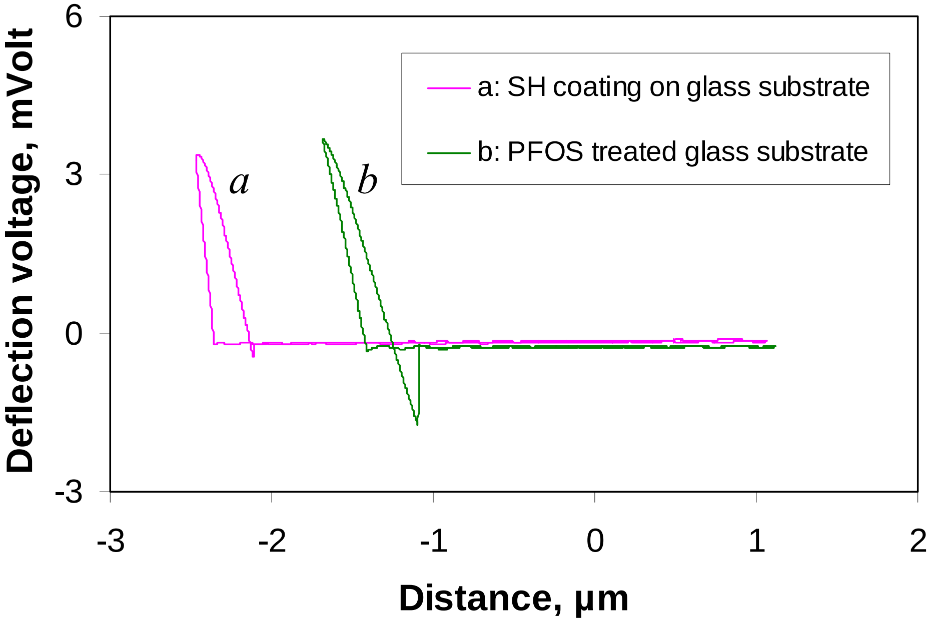

Figure 105. Surface-probe interactions as determined from AFM force measurements between a tipless Si_3N_4 probe and either a superhydrophobic film spin-casted from ethanol:sol ratio of 5:1) or a PFOS-treated glass slide.

5.3.5 Water vapor condensation on silica surfaces and comparison with micron-structured silicon surfaces

In order to compare the rough silica surfaces prepared in our study with larger roughness structures more characteristic of those typically encountered in antistiction of MEMS devices for water droplet contact angle and water vapor condensation, we prepared micron-sized structures by photolithography and plasma etching processes on silicon surfaces. Recent reports indicate that superhydrophobicity is not achieved when water vapor has condensed on such a surface [101, 204]; indeed, we observe analogous results for micron-sized surface structures. After a fluoroalkyl silane treatment of the structured surface shown in Figure 106, the contact angle is 164.4 ± 1.8˚ and the hysteresis is 25.3 ± 3.2˚. After water vapor condensation for 30 seconds on the micron-sized structured surface, the water contact angle falls to 147.1±2.9˚ and the hysteresis increases to 62.7±6.6˚, as illustrated in Figure 107. For a rough surface, the water droplet can be considered to be in either a Cassie state or a Wenzel state as shown in Figure 108.

In the Cassie regime, the surface can display superhydrophobicity. However, in the Wenzel regime, although a high contact angle can be achieved due to the increased contact area, the hysteresis is too high to establish a superhydrophobic surface. Apparently, after water vapor condensation on the surface, the surface contact with the water droplet resides in the Wenzel regime and the hysteresis increases dramatically as shown by the comparison between Figures 107a and b.

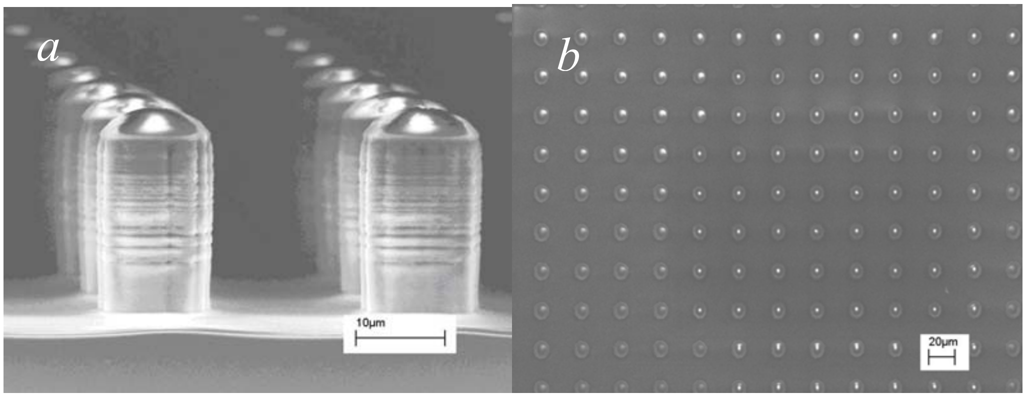

Figure 106. Silicon pillars with diameter of 12 μm, pitch size of 30 μm, and height: 25 μm; a. side view, b. top view.

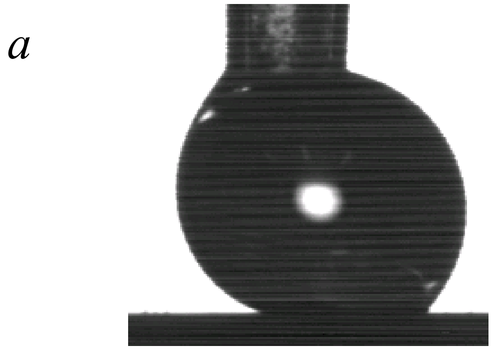

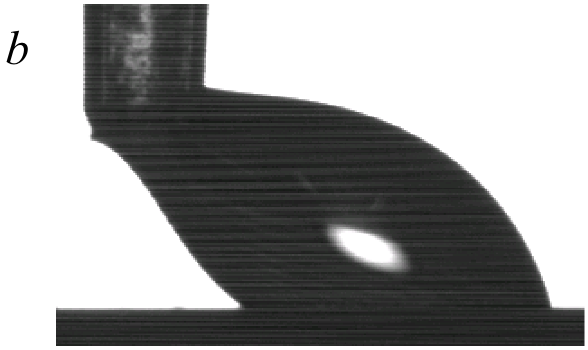

Figure 107. Contact angle hysteresis resulting from movement of a substrate in one direction (moving to right) a, before water condensation, advancing CA, 164.4˚, hysteresis, 25.3˚; b, after water condensation for 30 s, advancing CA, 147.1˚, hysteresis, 62.7˚.

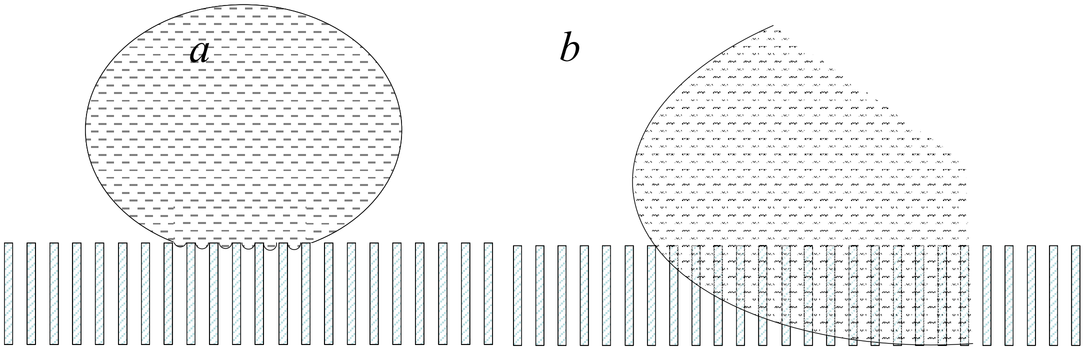

Figure 108. Schematic of a water droplet on a rough surface: a, Cassie regime, b, Wenzel regime where the edge effect is shown.

According to the Wenzel Equation, $\cos\theta_A = r\cos\theta_Y$, when the surface roughness r is known, the apparent contact angle can be calculated from Young's contact angle on a flat surface. Surface (Wenzel) roughness is 2.05 in our micron-sized model system (the ratio of the actual surface area to the projected area of a surface with pillars: height, 25 µm, diameter, 12 µm, pitch, 30 µm). For water vapor condensation on the silicon pillar surface (contact angle of 147.1^{o}), and a Young's contact angle of 115.0˚ when a layer of fluoroalkyl silane exists on the surface, the predicted contact angle according to the Wenzel Equation is 149.9˚, which is in good agreement with the value observed experimentally. This result implies that the micron-sized surface structures with water condensation behave according to that predicted in the Wenzel regime.

As shown in Figure 108, in the Cassie regime, the interface is sufficiently stable to suspend the weight of water on top of the surface because the counteractive surface tension on the liquid/air interface is large. However, when the water/air interface is not stable, the counteractive surface tension cannot confine the water on top of the surface (i.e., balance the hydraulic pressure of water) and water will flow to the bottom of the pillar valleys; this situation occurs when a surface is covered with condensed water vapor. As a result, a composite interface characteristic of the Cassie regime is not formed. This situation is also possible when, according to the Young-Laplace Equation (equation 2), Young's contact angle for water (θ) is relatively low, or the pitch size is large.

$$p_s = p - p_0 = -\frac{2\gamma\cos\theta}{r_{eff}} \tag{32}$$

where r_{eff} is the equivalent radius of a capillary, p is the pressure under the meniscus, p_0 is the ambient pressure, γ is the surface tension of liquid (water), and θ is the contact angle of water on the capillary surface. When R increases, p_s decreases, and at sufficiently large pitch, water can flow into the regions between the pillars because the surface tension can not sustain the hydraulic pressure exerted on the interface by a water droplet.

The Kelvin equation indicates that

$$RT\ln\left(\frac{p}{p^0}\right)_g = \frac{2\gamma V_m(l)}{R_0} = \frac{2\gamma M}{\rho R_0} \tag{33}$$

p: vapor pressure

M: molar molecular weight of pure liquid

ρ: density of the liquid

$Vm(l)$: molar volume of liquid

R_0: radius of curvature of the liquid droplet

Convex meniscus: R_0: > 0, contact angle $\theta > 90^\circ$

Concave meniscus: R_0: < 0, contact angle $\theta < 90^\circ$

when the radius of curvature is greater than zero (r>0), a decrease in r will result in an increase of pressure p, which means that liquid will vaporize and vapor will not condense readily on the surface. This is the surface property that is expected. However, when $r < 0$, a decrease of r will result in a decrease of the vapor pressure. Therefore, vapor will condense on the surface even at a very low vapor pressure. This is often the case in MEMS stiction failures due to the fact that a concave water meniscus is formed between the freestanding parts and the substrate. In order to effectively eliminate the failure, the surface must be hydrophobic, i.e., condensation of vapor on the surface will be inhibited, and even it does condense, the capillary force is eliminated due to the convex meniscus.

For superhydrophobic antistiction, a low contact angle hysteresis is critical to attaining reduced adhesion. According to the Young-Dupré equation[149], the work of adhesion is a measure of surface adhesion. Surface adhesion can be reduced by proper design of the surface array structures (e.g., pitch, contact area), the geometry of the individual surface structures (reduced contact line on the pillar), and the surface (material) chemistry. However, the most important characteristic is the inclusion of nanoscale roughness which is an effective approach as demonstrated by the lotus leaf structure.

From the optical micrograph in Figure 109a, it is clear that condensed water droplets on fluoroalkylsilane treated glass substrates have diameters of several microns. When water vapor condenses on the micron-sized surface structures, the droplets will simply position themselves between the structures. When more water is condensed, a greater fraction of the available surface area will be filled. Ultimately, when water essentially fills the available surface between the pillars, the contact angle falls below 120˚. Under these conditions, superhydrophobicity is lost because the water condensation has eliminated the counteracting meniscus between pillar tips.

It is well-known that if pressure is applied to the top of a water droplet on a superhydrophobic surface, the surface will not display superhydrophobic properties, since the high pressure forces water to enter the spaces between pillars[133]. This intuitive result can be described by Equation (32) [149], where r_{eff} is linearly related to the pitch size. When the pressure difference $p - p_0 < p_s$, the water droplet is stable on the tip of the structured surface and superhydrophobicity can be maintained. When $p - p_0 > p_s$, water will penetrate between the structures because the meniscus is unstable under the applied force. When $p - p_0 = p_s$, the water droplet is in a metastable state, and a slight increase of pressure on the droplet will lead to the intrusion of water between the pillars. Clearly, this also results in a loss of superhydrophobicity so that the water droplet will stick to the surface instead of rolling off.

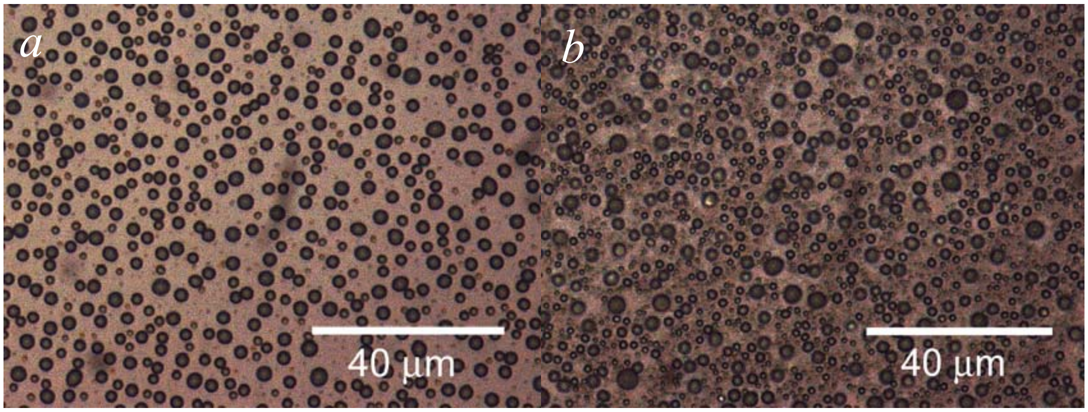

Figure 109. Water condensation on coated microscope glass slide surfaces for 30 s, a, flat surface with fluoroalkylsilane (PFOS) treatment; b, superhydrophobic surface from the modified sol-gel process with fluoroalkylsilane (PFOS) treatment.

In order to overcome these problems, nanostructures (or hierarchical structures) are necessary on superhydrophobic surfaces to establish stability. First, nanostructured surfaces have much smaller (effective) surface pitches and higher surface areas than do flat or micro-structured surfaces. According to the Young-Laplace Equation (Eqn. (32)), a meniscus on nano-structured surfaces can withstand a much higher pressure than can a meniscus on surfaces with micron-scale roughness. For example, when the radius of curvature r_{eff} is reduced to one-tenth of the original value, p_s increases a factor of 10 times relative to that for the higher roughness. For nanostructured surfaces prepared by the sol-gel process with the eutectic liquid as a templating agent (shown in Figure 110), the contact angle is 169.5 ± 1.5˚, with a hysteresis of 4.1 ± 1.3˚. In this instance, even after 30 min of water vapor condensation at 100% humidity, the contact angle is 166.0˚ and the hysteresis 19.4˚; nevertheless, a water droplet can still roll off the surface. Therefore, a reduction in surface structure size is extremely effective in increasing the stability of superhydrophobic surfaces.

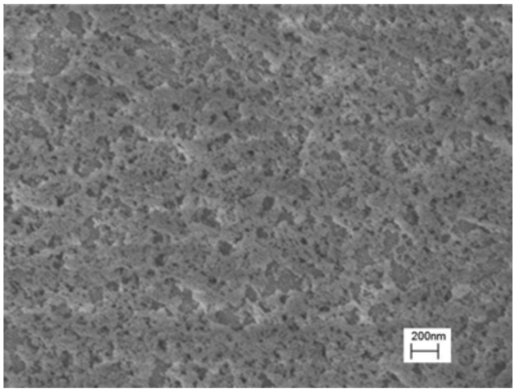

Figure 110. Example of a superhydrophobic surface with nanoroughness from the sol-gel process on a microscope glass slide, after surface treatment with fluoroalkylsilane (PFOS).

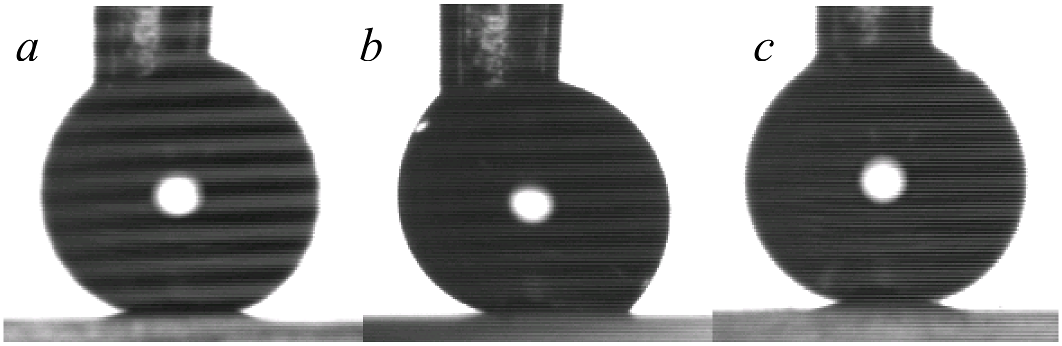

Figure 111. Hysteresis comparison immediately following water vapor condensation investigated by moving the substrate in one direction (moving to right): a, before water condensation, advancing CA: 169.5˚, hysteresis 4.1˚; b, immediately after water condensation, advancing CA: 166.0˚, hysteresis 19.4˚; c, because the previous water droplet removed the condensate, the surface shows improved hysteresis, advancing CA: 168.3˚, hysteresis 4.5˚.

The water vapor condensation tests indicate that the hysteresis is much smaller on nano-roughness surfaces than it is on micro-roughness surfaces, which demonstrates the significance of nanostructures on the reduction of CA hysteresis. After water vapor condensation on the superhydrophobic surface, although micro-water droplets were formed, the surface roughness maintained the water droplet contact in a Cassie state; when the water droplet grew, it easily rolled off the surface. This demonstrates that the surface will remain free of water and the capillary force is expected to be reduced.
To further investigate the effect of condensed water on the behavior of superhydrophobic surfaces, contact angle measurements were performed both on a dry superhydrophobic surface (surface micro-morphology as shown in Figure 110) and on the same surface immediately after condensation; Figure 111 displays contact angles on these surfaces. On the surface where water vapor has been condensed, the advancing angle is 166.0˚ with hysteresis 19.4˚ (Figure 111b). Although there is hysteresis, the water does not stick to the structured surface; rather, the water droplet picks up the condensate on the superhydrophobic surface and rolls off when the surface is tilted. The high curvature-induced pressure prevents water from penetrating between the structures. The initial hysteresis increase is due to a condensed water-induced increase of contact area which leads to an increase in the hysteresis. In addition, after picking up the micron-sized water droplets condensed on the surface (shown in Figure 109 b), the contact angle recovers to its original value as shown in Figure 111c. This sequence demonstrates that superhydrophobicity can be recovered if it was lost due to water condensation provided that the surface structure is controlled at the nano-scale. In comparison, for the micron roughness surfaces, contact angle changes are different before and after water condensation as shown in Figure 107. Furthermore, there should be a critical pitch size that either can prevent condensation within the rough structures, or after condensation, the capillary force generated can drive the water out of the structure. As a result, design

of surfaces with sufficiently small structure pitch and solid area fraction can ensure the formation of stable superhydrophobic surfaces, even when water condensate is present. Similar mechanisms are invoked by the nano scale roughness of lotus leaf surfaces which prevent the loss of superhydrophobicity in humid environments.

5.3.6 Thermal stability of the superhydrophobic surfaces

The stability of the superhydrophobic surfaces under high temperature was tested at 450˚C and 520˚C for 30 min. Contact angle data before and after the heat treatment is shown in Table 19. Clearly at 450˚C, the superhydrophobic surface is stable, but when heated to a higher temperature, the surface hydrophobic groups begin to decompose, and the superhydrophobicity is lost.

Table 19. Contact angle change after heat treatment.

Temperature (˚C)	450	520
CA before heat treatment (degree)	167.8	168.5
CA after heat treatment (degree)	166.4	10

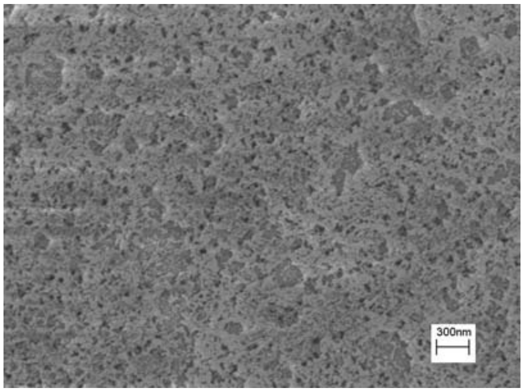

Figure 112. Surface morphology of silica surfaces after heat treatment at 520 ˚C for 30 min.

For samples treated at 520˚C, when the surface was treated with PFOS again, the water droplet contact angle is still around 166-169˚ which implied that no significant roughness change occurred. The surface morphology from SEM after heat treatment at 520 ˚C was shown in Figure 112.

5.4. Conclusions

We have demonstrated that a sol-gel process using a eutectic liquid (urea and choline chloride with molar ratio of urea:choline chloride of 2:1) can be invoked to form superhydrophobic, optically transparent films on glass slides. These properties were achieved by minimizing the surface structure length scales and film thickness while maintaining the necessary roughness for superhydrophobicity. Such results indicate that an RMS surface roughness of 70-100 nm can reduce solid/water interaction at the contact interface while allowing excellent optical transparency. Thus, by controlling the surface roughness, both superhydrophobicity (high contact angle and low hysteresis) and optical transparency can be achieved simultaneously. This silica-based superhydrophobic surface offers much potential in self-cleaning applications where optical transparency is required. However, the mechanical robustness of these layers must be improved for implementation in commercial products.

Superhydrophobic silica films formed by a sol-gel process using a eutectic liquid as a templating agent were investigated. For comparison, a micron-structured (pillared) silicon surface was also prepared. Water vapor condensation results showed that nanorough silica surfaces prepared from sol-gel processing are more stable than the micron-structured surface. Water vapor condensation onto the surface causes a loss of superhydrophobicity for micron-size surface structures. Nanostructured surfaces demonstrated that water vapor condensation does not cause a loss of superhydrophobicity, despite the fact that after water condensation, hysteresis increases. Under these circumstances, the water droplet picks up the condensed water as it rolls off the surface, thereby cleaning the surface by removing condensed water droplets. After removal of the micron-sized water droplets, the hysteresis recovered to its original value. Results from AFM force curves with a tipless probe demonstrated a negligible interaction force between the tip and the nanorough superhydrophobic surfaces. Such results indicate that adhesion forces and capillary forces can be reduced by invoking a nanostructured surface. Thermal stability tests showed that the superhydrophobic surface is stable at 450˚C and thus offers applications for high temperature environments. The surface decomposed and superhydrophobicity was lost after heating to 520˚C. These approaches offer a method to effectively reduce stiction in MEMS devices and improve the system reliability.

CHAPTER 6

SUPERHYDROPHOBIC SURFACE BY SI ETCHING

In this chapter, superhydrophobic surfaces on crystalline Si were investigated by etching techniques. The possible applications may be in the combination of superhydrophobicity with more functions from semiconductor Si.

6.1 Introduction

Artificial superhydrophobic surfaces allow the design of self-cleaning and water repellent surfaces with high water contact angles and low contact angle hysteresis. Requirements for realization of superhydrophobicity are often viewed in two different ways. One view suggests that achievement of a high water droplet contact angle may be insufficient to establish superhydrophobicity[205]. That is, in self-cleaning applications, the ease with which a droplet rolls off the surface is critical. Therefore, contact angle hysteresis/roll off angle/sliding angle must be considered when evaluating superhydrophobicity. Alternatively, it is sometimes suggested that superhydrophobicity implies only a high water droplet contact angle[133]. Although a contact angle ≥150˚ is the accepted demarcation for considering a surface to be superhydrophobic, a wide range of contact angle hysteresis values have been reported for such surfaces. Generally, superhydrophobic surfaces with contact angle hysteresis >10˚ are termed “sticky” superhydrophobic and are considered most likely to be in the Wenzel wetting regime, while superhydrophobic surfaces with contact angle hysteresis <10˚ are termed slippery/roll-off superhydrophobic and are considered to be in the Cassie regime[206, 207].

Superhydrophobic surfaces have been prepared using both organic materials such as polyethylene[208], polystyrene[209], and polyelectrolyte[210], and inorganic materials such as Al_2O_3[185], Fe_2O_3[211], ZnO[212] and Si[27, 154]. In addition to the establishment of superhydrophobicity, these materials have been further functionalized to realize electro-active surfaces with controlled wetting properties[26], transparent surfaces[58], adhesive surfaces[213], photocatalytic surfaces[98] and photonic bandgap layers[214]. However, due to its widespread use in electronic and photovoltaic devices, incorporation of superhydrophobic properties into silicon surfaces may extend and enhance the more traditional applications of these devices. Numerous approaches have been reported to generate superhydrophobic silicon surfaces[26, 58, 102, 215-217], including wet etching [154, 216, 218], creation of silicon nano wires by CVD growth[219], and plasma etching of silicon pillars[122, 144], etc. In these studies, high contact angles and reduced contact angle hysteresis were intensively investigated[17, 27, 29, 143, 156, 205, 220]. To achieve superhydrophobicity, biomimetic fabrication of two scale structures are frequently employed[14, 110, 195, 207, 221, 222]. By fabricating the nano- and micro-structures on silicon, multifunctional surfaces may be prepared that possess photoluminescence, anti-reflection, and superhydrophobic self-cleaning properties.

Over the last decade, much attention has been directed to semiconductor materials with surface micro/nano structures, primarily due to potential applications in opto-electronics, chemical and biochemical sensing and the possibility of creating material properties not readily obtained in the corresponding crystalline materials[223]. The surface micro/nano structures of semiconductors can be produced by anodic etching, where the semiconductor is biased positively in a conductive electrolyte to facilitate oxidation and subsequent removal of surface atoms. The magnitude of the applied voltage and current and the electrolyte composition are used to control etch rate and, thus, morphology and properties. This approach is hampered by the need for a conducting substrate that is stable under the electrochemical etching conditions and the need to explore the relatively large parameter space to identify the optimum etching conditions.

To circumvent these problems, an efficient chemical etching method to produce Si surface structures that requires no external bias was developed recently[132, 138], i.e., metal assisted etching of silicon surfaces has been employed to define specific structures on silicon surfaces[49, 138]. In this process, a discontinuous layer of Pt or Au (20 - 200 Å thick) is deposited on the silicon surface before immersing it in HF/H_2O_2. Reduction of the oxidant (H_2O_2) injects holes into the valence band of the semiconductor, which then participate in oxidative etching of the semiconductor surface. After deposition of a thin layer of a metal such as Au, Pt or Pt/Pd onto p- or n-type silicon surfaces, nanostructures can be formed by immersing this substrate into various mixtures of hydrofluoric acid/oxidant/solvent. This approach has been used to prepare photoluminescent surfaces[130] and ’black’ anti-reflecting silicon surfaces[49]. In fact, the reflectivity can be reduced to nearly zero if the appropriate structures are formed. Furthermore, superhydrophobic and oleophobic silicon surfaces have been reported using metal assisted etching of silicon (111) surfaces[27]. The use of etched silicon surfaces for photovoltaic applications has also been investigated, and a solar cell efficiency of 9.31% was reported[224]. Although the surface trapped most of the light incident on the silicon surface, the conversion efficiency was not as high as expected, probably due to the low current-collection efficiency of the front grid electrodes and high recombination velocity due to the large surface area.

In this study, we invoked a surface etching technique for the preparation of multi-functional (self-cleaning, non-reflecting, water repellent) surface micro/nano structures for potential photovoltaic applications. We used metal (Au) assisted etching to form nanoscale roughness and thereby form hierarchical structures by metal assisted etching of micron-size pyramid textured surfaces. By creating this two scale rough surface, it is expected that low contact angle hysteresis, robust surface structures with low light reflectivity can be achieved. To date, these functions have not been achieved simultaneously using one size scale structure. These structures yield superhydrophobic surfaces which may have important application in light harvesting, anti-reflection and light trapping properties of solar cells. It is expected that by controlled manipulation of surface structures via the etching process, multifunctional silicon surfaces can be achieved and cost-effective photovoltaics may be possible[225].

6.2 Experimental Details

p-type silicon (100) wafers with a resistivity of 1-10 Ω cm were used in all experiments. KOH etching was performed in a solution of KOH (2~3%wt), water and isopropyl alcohol (20% by volume) at 80~85˚C for 20~30 min to create pyramidal structures (2-4 μm in height). To form nanostructures, a thin discontinuous layer of Au nanoparticles (5-10 nm diameter) was deposited by e-beam evaporation. Etching was then performed for various times in a HF/H_2O_2 solution (49%HF, 30%H_2O_2 and H_2O with a volume ratio of 1:5:10). Alternatively, etching was then performed for various times in an HF/H_2O_2 solution (49%HF, 30%H_2O_2 and isopropyl alcohol with a volume ratio of 1:2:1). Subsequently, the Au nanoparticles were removed by immersing the samples in KI/I_2 (100 g KI and 25g I_2 per 1L H_2O) for 60 seconds.

Contact angle measurements were performed with a Rame-Hart goniometer that had a CCD camera equipped for image capture. Scanning Electron Microscopy (SEM) was used to investigate the surface morphology. After fabrication of the surface structures, surface fluorination was performed by treatment with perfluorooctyl trichlorosilane (PFOS). Typically, a ten millimolar solution of PFOS in hexane was used for these treatments. Specifically, the etched silicon wafer was immersed in the solution for 30 min followed by a heat treatment at 150˚C in air for 1 hour, to complete the hydrophobic surface modification. The nanostructured surface was characterized by diffuse reflectivity measurements to establish reflectivity. The weighted reflectance (WR) was calculated by normalizing the hemispherical reflectance spectrum (350 – 1100 nm) by the AM (air mass) 1.5 spectrum.

6.3 Results and Discussion: etching in aqueous solution

Au assisted etching in an HF-based etchant ($HF/H_2O_2/H_2O$)[49] was used to generate surface nanostructures in an attempt to establish superhydrophobicity and maintain reduced reflectivity. Due to the presence of Au nanoparticles, electroless etching occurs at the Au/Si contact interface. H_2O_2 decomposition causes injection of holes into the silicon surface and etching by HF proceeds in the vicinity of the Au/Si contact. As a result, pits or nanostructures are formed on the surface. Figure 113 shows a schematic of the etch process; SEM micrographs of etched silicon surfaces using different Au thicknesses with different etch times are shown in Figure 114. As the etch time increased, the etched pore structure became larger. Increasing the Au layer thickness also resulted in different surface morphologies which had a direct effect on surface superhydrophobicity after the surface was treated with fluoroalkyl silane (see below).

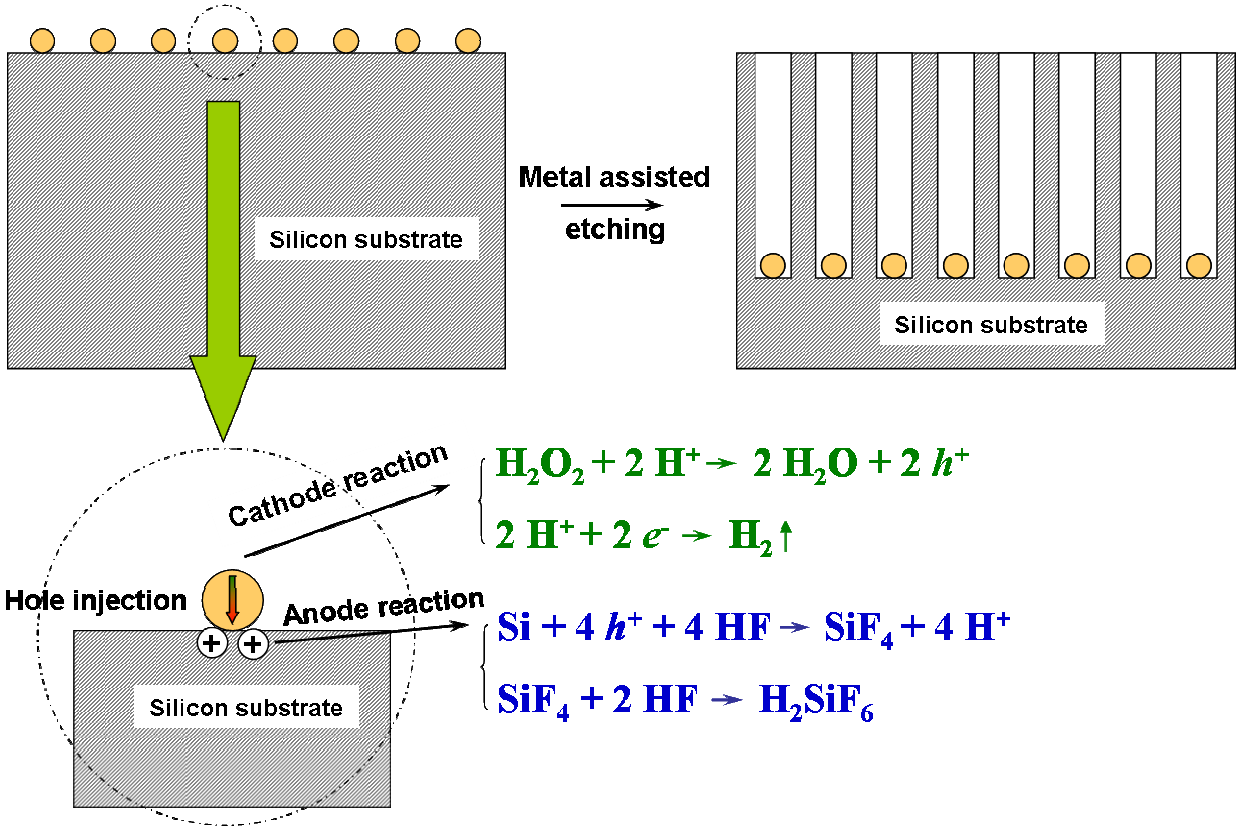

Figure 113. Schematic of the Au assisted etching process in HF:H_2O_2:H_2O = 1:5:10.

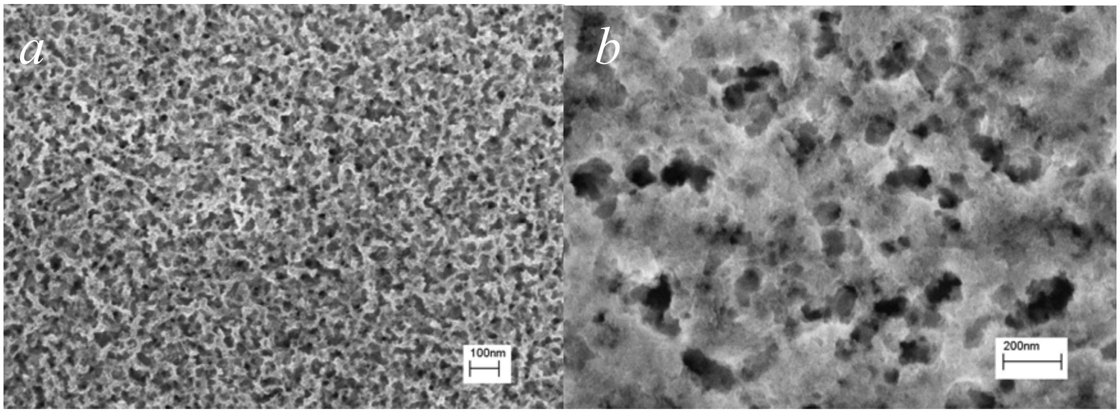

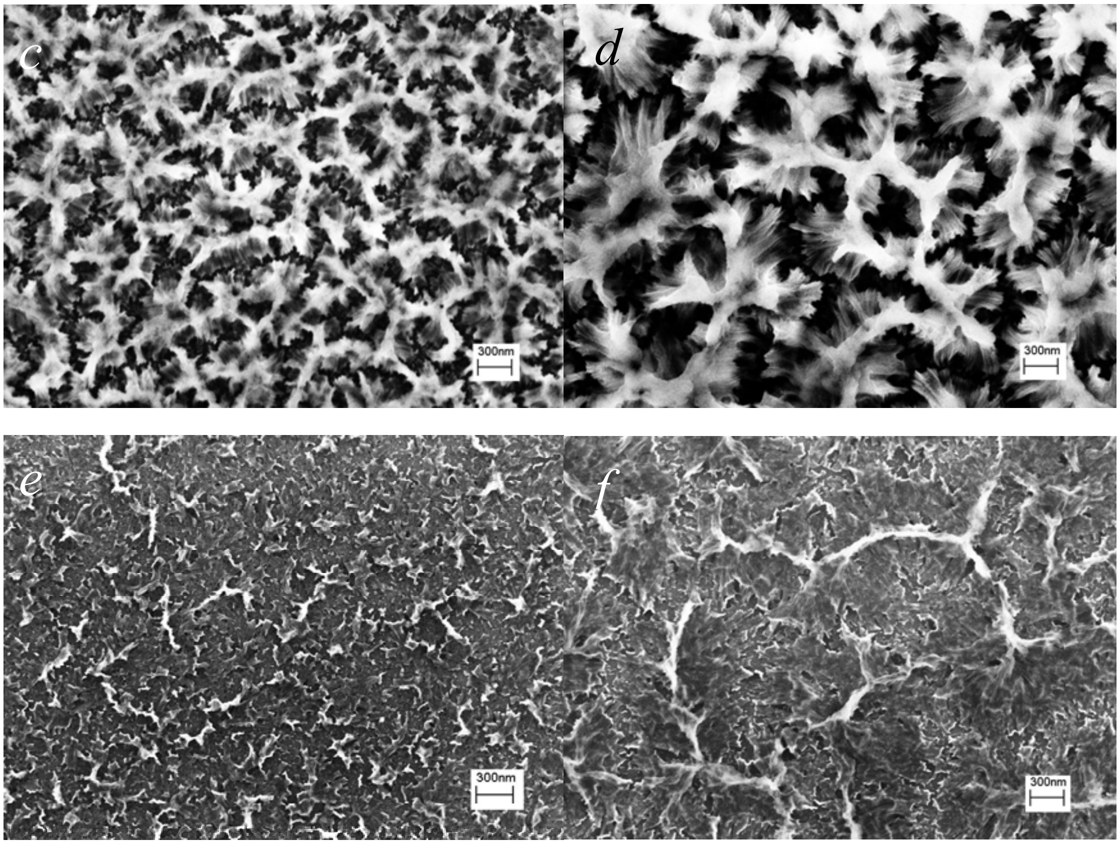

Figure 114. Au assisted etching in $HF/H_2O_2/H_2O=1:5:10$, with 2 nm Au layers after etching for 2 min (a) and 4 min (b); 5 nm Au layers for 2 min (c) and 4 min (d) etching; 10 nm Au layers for 2 min (e) and 4 min (f) etching.

Evaluation of silicon surface superhydrophobicity was made by considering both the contact angle and the contact angle hysteresis, which was used to differentiate the contact state between water droplet and the structured surface. For Si surfaces etched using 2 nm, 5 nm and 10 nm Au layers and subsequently treated with PFOS, the advancing contact angles increased with an increase of the Au layer thickness. However, the most obvious difference is in the receding contact angles as shown in Figure 115. With an increase in the Au layer thickness, the receding angle increased thereby reducing the contact angle hysteresis (difference between advancing and receding angles). Longer etch times do not reduce the hysteresis within the etching period investigated (0~4 min). Apparently, the water/solid contact is best described by a Wenzel state rather than a

Cassie state because of the large contact angle hysteresis which can be attributed to an increased contact area between water and silicon.

This observation also demonstrated that a large contact angle is not sufficient to achieve a superhydrophobic surface with roll-off characteristics. Our results indicate that for the Si surface generated by Au assisted etching, contact angle hysteresis is more important in evaluating the self-cleaning functionality. As shown in Figure 115, most of the advancing contact angles are above 150˚. However, the low receding contact angles (large hysteresis) indicate that the superhydrophobic surfaces are “sticky” since water droplets adhere to the surface even when the surface is vertical as shown in the inset to Figure 115.

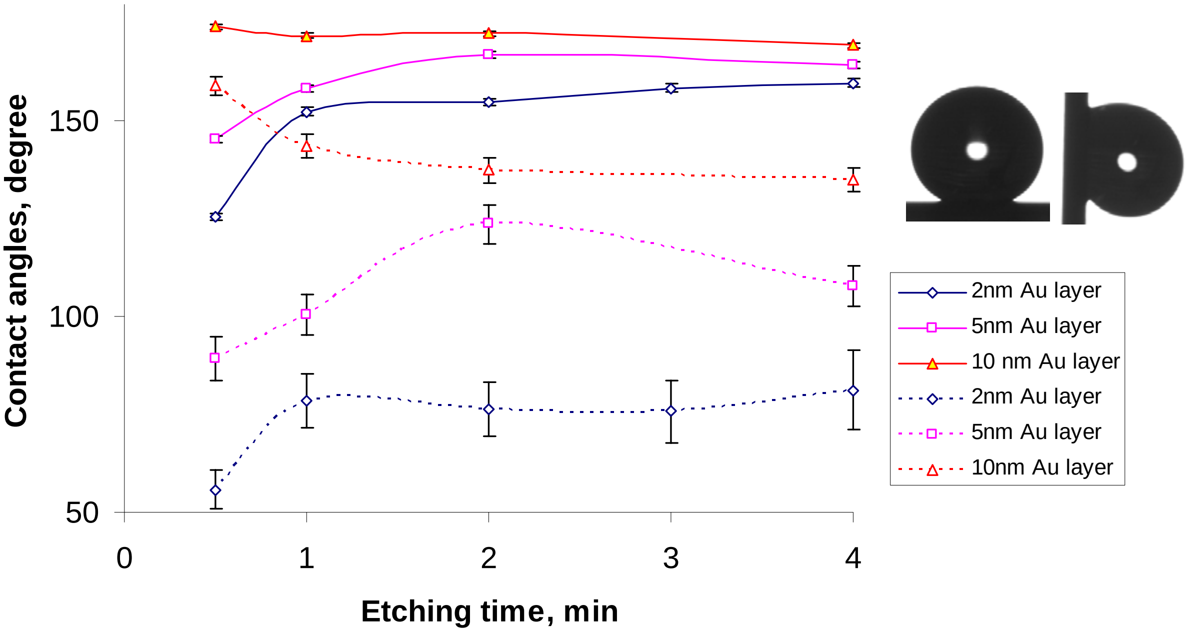

Figure 115. Contact angles after PFOS treatment of etched Si surfaces containing nanostructures. Solid lines represent advancing angles; dotted lines represent receding angles; inset: micrograph of water droplets on a silicon surface after PFOS treatment with etching conditions: Au layer 5 nm, etched 4 min; contact angle

Two scale surface structures

The above data have demonstrated that the surface nanostructures formed from Au assisted etching in $HF/H_2O_2/H_2O$ do not result in roll-off superhydrophobicity within a short (<4 min) etch time. On lotus leaf surfaces, two scale roughness generates superhydrophobic and self-cleaning leaf surfaces. Our (and others') results have shown that micron-sized silicon pyramids can be formed using KOH etching and nanostructures can be fabricated readily using Au assisted etching. It may be possible to form a hierarchical structure that allows a biomimetic superhydrophobic surface to be realized in silicon. Indeed, by first etching Si pyramids, followed by deposition of a 5 nm Au layer and subsequent Au assisted etching, micro-sized pyramids with attendant nanostructures can be generated by the two-step etching process. The pyramid Si surfaces alone cannot generate a superhydrophobic state (with a contact angle of ~140° after hydrophobization with PFOS). The nanostructure is critical on top of the pyramid surfaces to achieve both a high contact angle and low hysteresis after surface hydrophobization[154].

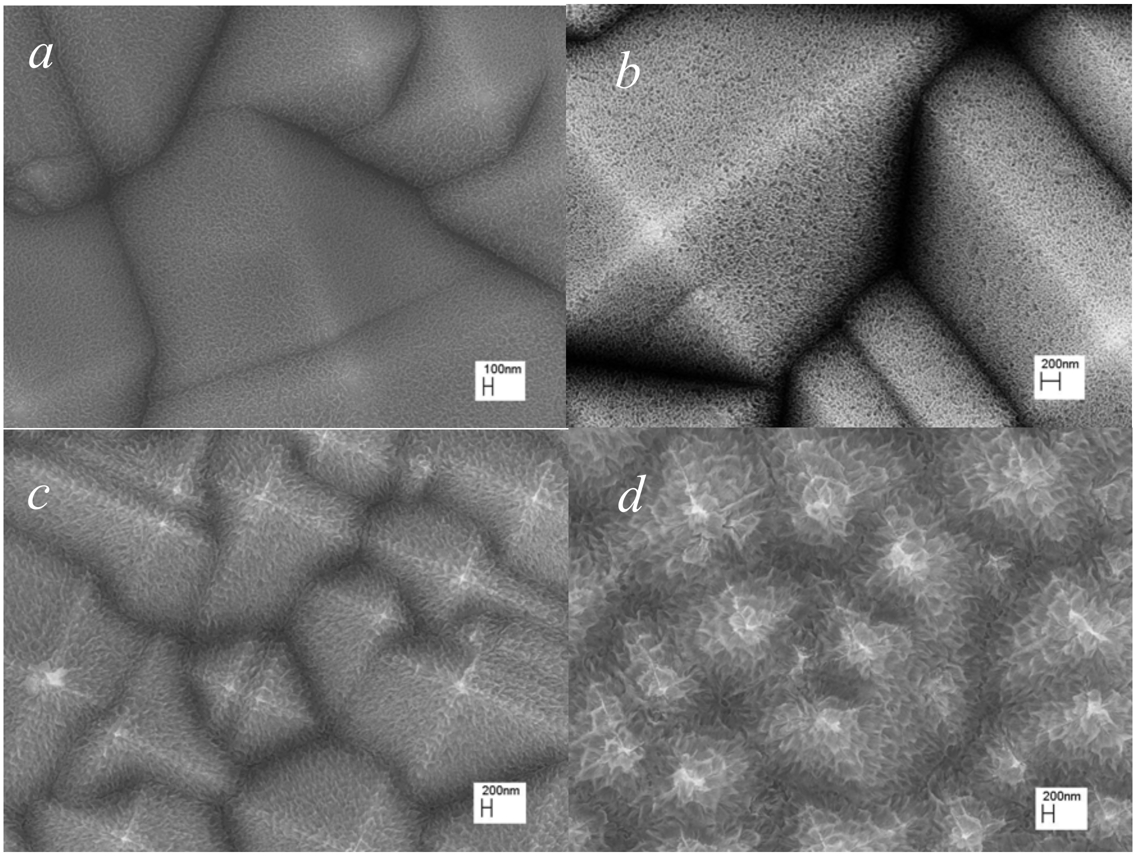

Figure 116. Si pyramid surface etched by Au assisted etching in $HF/H_2O_2/H_2O$ (v/v/v 1:5:10) for a. 30 sec, b. 1 min, c. 2 min, d. 4min; Au layer thickness: 5 nm.

As shown in Figure 116, after Au assisted etching of the silicon pyramid morphology, the surface became hierarchically rough. Treatment of the surface with PFOS to hydrophobize the surface yielded high contact angles and low hysteresis, as shown in the inset of Figure 117, water droplet falling on the surface tend to roll off the surface even the surface is horizontally positioned; this is in contrast to the contact angle results achieved on a nanostructured silicon surface created by only Au assisted etching (inset of Figure 115). Existence of the two roughness scales resulted in a roll-off superhydrophobic surface due to the reduced liquid contact area fraction. Figure 117 indicates that with increased etch time, the contact angle hysteresis first decreased then increased after 2 min of Au assisted etching. The hysteresis reduction is due to the generation of nanoscale roughness superimposed on the microscale roughness; the subsequent hysteresis increase can be attributed to a reduction of the size of the silicon pyramids due to the prolonged Au assisted etching and the loss of the nanostructures. These effects are clearly shown in Figure 118, which displays cross-sections of the etched pyramid surfaces. Despite the changes in receding contact angle, the advancing contact angles remained nearly constant.

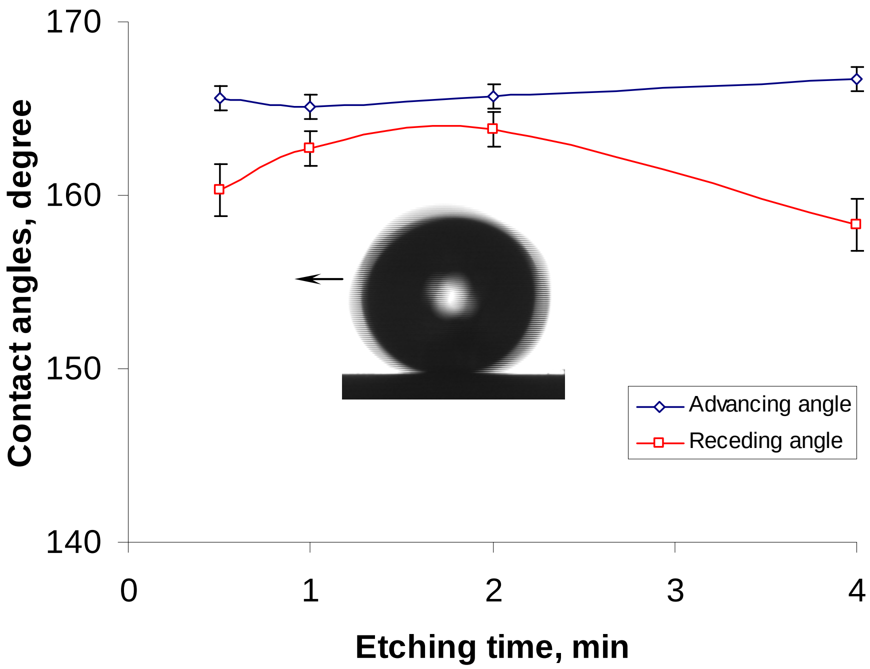

Figure 117. Contact angle and contact angle hysteresis on two-scale etched Si surfaces; inset, the dynamic water droplet moving on the superhydrophobic surfaces with two scale structures (Au assisted etching for 2 min on micro-pyramid surfaces); the droplet edge is blurred due to the fast movement of the water droplet.

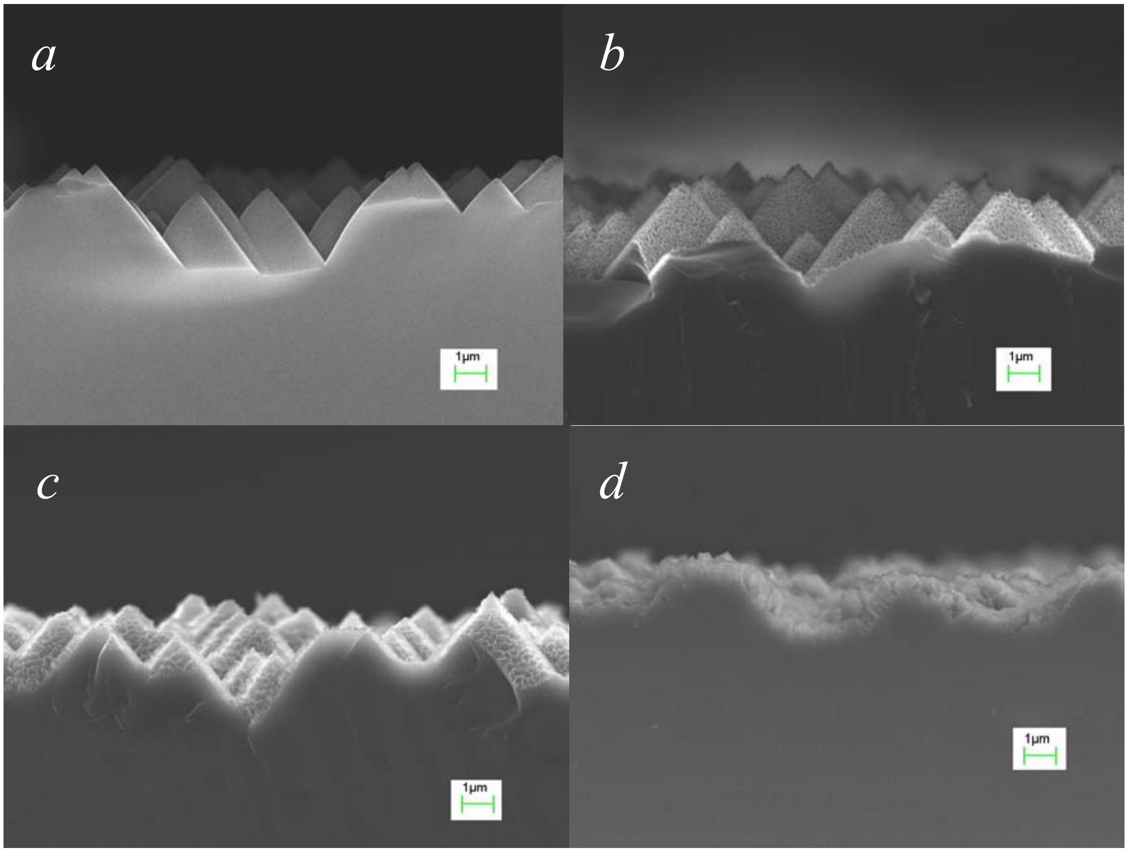

Figure 118. Cross sections of Si pyramid surfaces etched by Au assisted etching in $HF/H_2O_2/H_2O$ (v/v/v 1:5:10) for a. 30 sec, b. 1 min, c. 2 min, d. 4min, Au layer: 5 nm.

On an inclined surface as depicted in Figure 57 in chapter 2, the Laplace pressure can be expressed as[154]:

$$\Delta p = p - p_0 = -\frac{\gamma \cos(\theta - \alpha)}{R_0 + h \tan \alpha} \tag{22}$$

where γ is the surface tension of water, θ is the Young's contact angle of liquid on the surface, α is the inclination angle as illustrated in Figure 116, R_0 is half the distance between base edges of two adjacent inclined walls, p is the pressure on the liquid side of the meniscus, and p_0 is atmospheric pressure.

An effective way to increase the Laplace pressure and thus to promote superhydrophobicity is to generate nanostructures on the silicon pyramid surface[154].

According to Equation (22), the Laplace pressure is amplified when an enhanced contact angle θ can be generated on the pyramid wall surfaces; this effect can be achieved by invoking a second structure scale. In addition, the extended three phase contact line on smooth surfaces is segmented into smaller contact lines on pyramidal surfaces with nanostructures. As a result, the solid/liquid contact fraction was reduced and ultimately resulted in a stable Cassie state, which yielded superhydrophobic behavior. Such effects cannot be achieved readily by structures with only one size scale for either micron-size pyramids or nanostructures from Au assisted etching.

Low reflectivity of surfaces from Au assisted etching

The Au assisted etching of silicon surfaces can generate ‘black’ low-reflectance surfaces as shown in Figure 119, where a weighted surface reflectance of 6.4% resulted after a 2 min etch. Because of the presence of surface nanostructures, the surface absorbs most of the incident light, thus reducing reflection, especially in the 300-1000 nm wavelength regime. The nano-textured surface may also increase the path length of light as it travels through the cell, which allows thinner solar cells with reduced cost; furthermore, the surface may trap the weakly absorbed light reflected from the back surface by total internal reflection at the front surface/air interface. Pyramid textured silicon surfaces are already employed for high efficiency solar cell applications to increase light absorption by silicon surfaces[226]. Therefore, when combined with the pyramid textures on silicon surfaces, the micro/nano structured surfaces can optimize light absorption, and also establish self-cleaning properties if the surface is treated with fluoroalkylsilanes or other hydrophobic material. On the micro/nano two scale structured surfaces, the weighted light reflectance is further reduced to 3.8% as shown in Figure 119 and table 20. Longer wavelength light is reduced more. Such surface modifications should result in lowered maintenance costs and higher efficiencies due to reduction of dust/contamination build-up on solar cell surfaces.

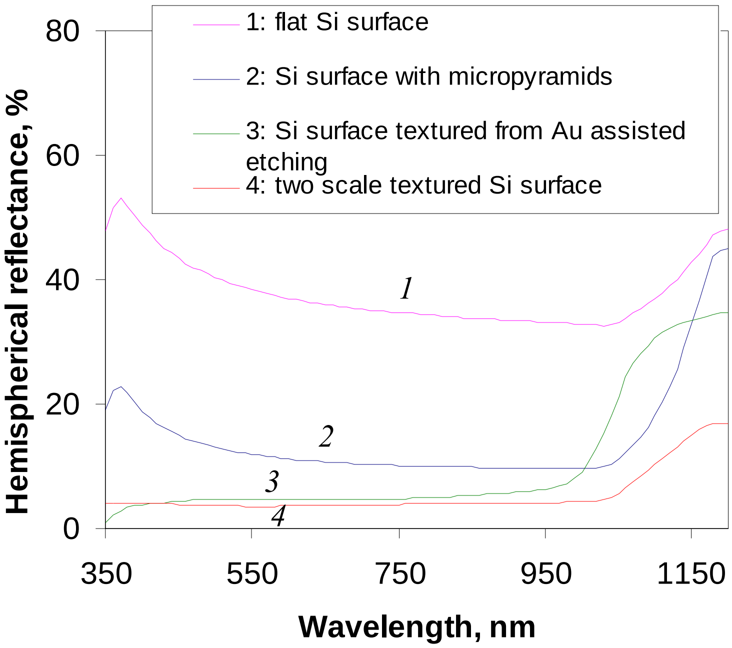

Figure 119. Light reflection on silicon nano-textured surfaces generated by Au assisted etching. Au (5 nm thickness) assisted etching in $HF:H_2O_2:H_2O$ of 1:5:10 (v/v/v) for 2 min.

Table 20. Weighted reflectance on different textured surfaces.

Sample	Weighted reflectance, %
Flat Si surface	37.3
Pyramid textured surface	12.3
Nano-textured surface (Au assisted etching)	6.4
Two scale textured surface	3.8

Conclusions

Nanostructured silicon surfaces were prepared by Au assisted etching. After a fluoroalkyl silane (PFOS) treatment, the surface showed a high (>150°) contact angle, although the contact angle hysteresis remained high, which prevented the establishment of roll-off superhydrophobicity. Au assisted etching of micron-sized silicon pyramid surfaces generated a hierarchical (micro/nano) structure which after PFOS treatment, yields a superhydrophobic surface with much reduced contact angle hysteresis. With an increase in etch time, the contact angle hysteresis increased as a result of a size reduction in the silicon pyramids. The appropriate combination of the two scale structures is effective in achieving roll-off superhydrophobicity. Silicon surfaces fabricated by Au assisted etching on Si pyramid surfaces showed low light reflection, which offers significant advantages for high efficiency solar cells with self-cleaning properties.

6.4 Results and Discussion: etching in solution contains isopropyl alcohol (IPA)

Metal assisted etching of Si surfaces is used in the preparation of black non reflecting surfaces[132]. This process may have considerable promise for light trapping in high efficiency solar cells. In this study, we investigate the application of this technique for the generation of superhydrophobicity for which structured surfaces are necessary. Au was used in our study for the metal layer on a silicon surface.

6.4.1 Etching time

To achieve superhydrophobicity, hydrophobic surface modification, density of surface structures, and height and diameter of the asperities must be controlled; only then will the hydrophobic surface show a high Young’s contact angle. The density of the surface structures can be represented by the micro three phase contact line density which yields the necessary surface forces to suspend the liquid against the forces of gravity. The topographic features must be tall enough so that the liquid does not reach the underlying surface. Also, the diameter of individual feature needs to be small enough to reduce the solid/liquid contact area so that a higher apparent contact angle results. When the etching time is increased, the etching depth the silicon surface increases. The depth of the surface structures is important in achieving better dewetting properties. The time effect on the etch depth is shown in Figure 120. With time, the etching depth increased at different rates for different thickness Au layers. For 10 nm Au layers ib silicon, the SEM images of surfaces etched at different time are shown in Figure 121.

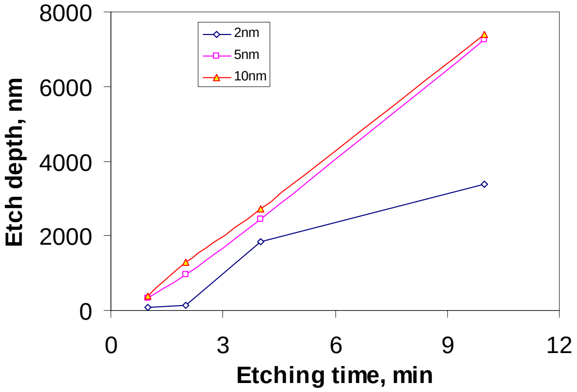

Figure 120. Etching depth of Au assisted etching of Si in HF/H_2O_2.

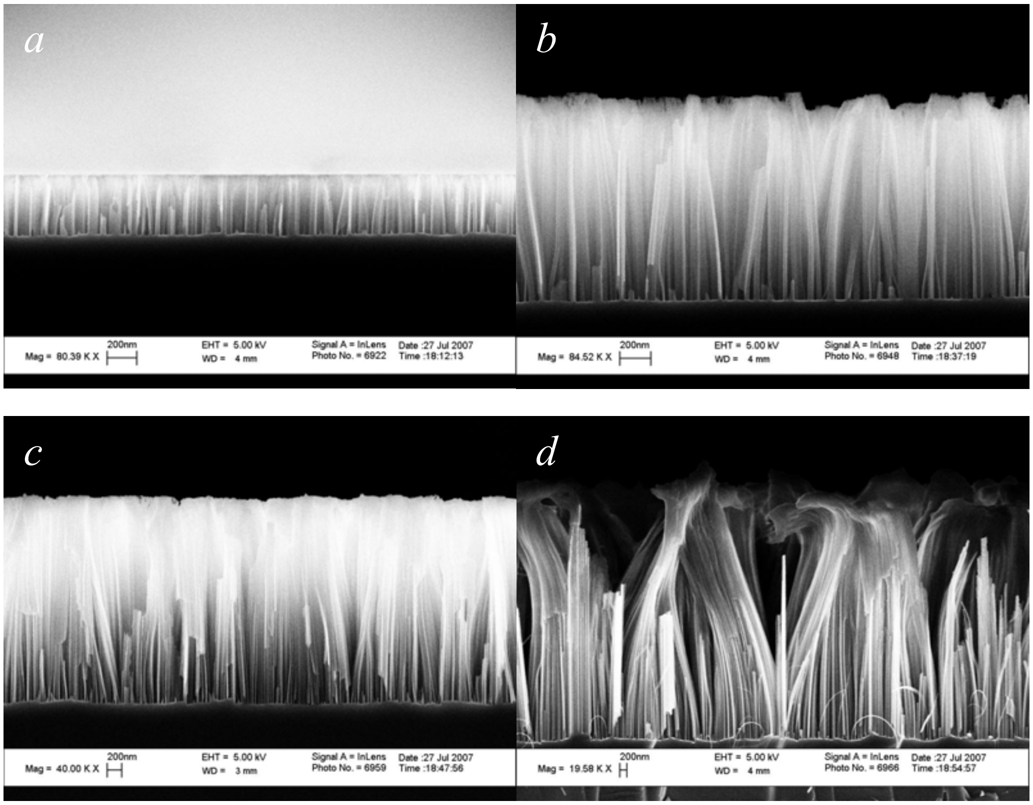

Figure 121. Cross-sections of 10nm Au layer assisted Si etching for etch times, (a) 1min, (b) 2min, (c) 4 min, and (d) 10 min.

6.4.2 Thickness of the Au layer

The thickness of the Au layer is also very important in achieving the desired surface structures. We prepared Au layers of three different thicknesses on silicon surfaces: 2 nm, 5 nm and 10 nm as shown in Figure122. The effect of the Au layer on etching is shown in Figure 123. As the Au thickness increases, the surface structures are higher. This corresponds to the difference in the etching rate shown in Figure 120. For a 2 nm Au layer (low particle density on silicon surface), the etch rate is much lower than that for 5 nm and 10 nm Au layers. This observation may be due to the low density of Au particles. However, for 5 nm and 10 nm Au layers on silicon surfaces which have a higher density than 2 nm Au, the higher density of Au particles may cause the etching to proceed at a higher speed. The etching rate for the 5 nm and 10 nm Au coated silicon surface is similar and the etching rate is also not dependent on the etching depth for thicker Au films on silicon surface. However, for 2 nm Au on silicon surface, the etching is slowed down when the etching proceeds. This also suggests a depth dependent diffusion effect on the etching process.

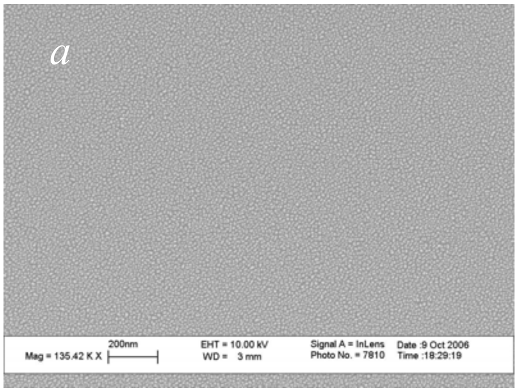

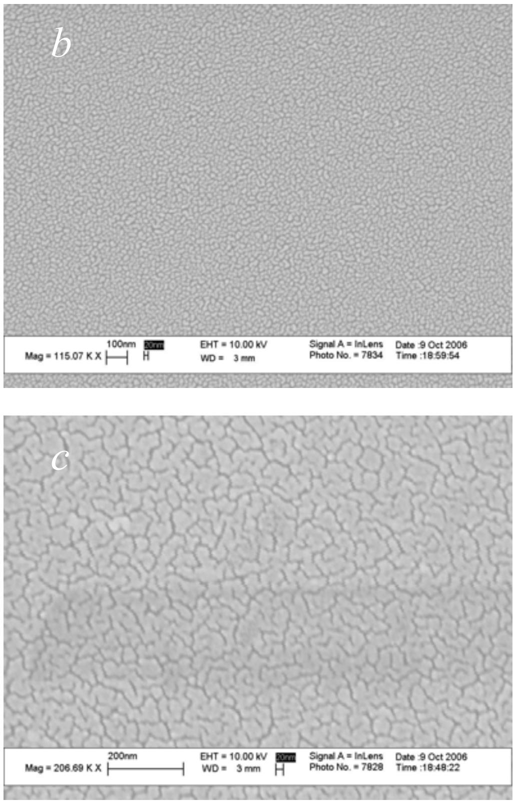

Figure 122. Silicon surface with Au layers of thickness of, 2 nm, 5 nm and 10 nm respectively.

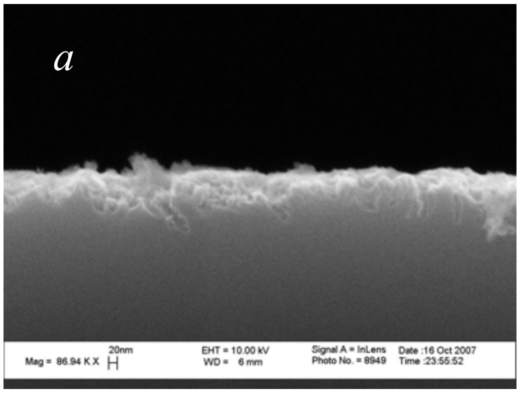

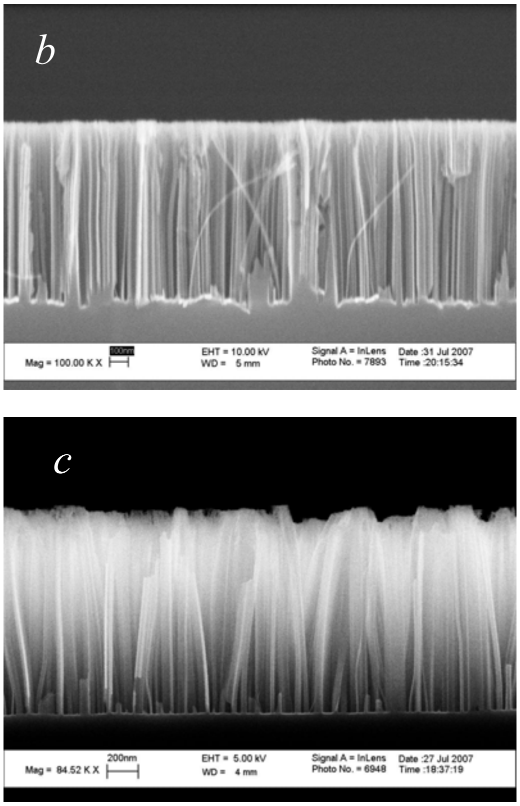

Figure 123. Cross-section of silicon etched for 2 min: 2 nm; 5 nm, 10 nm.

6.4.3 Effect of Au layer on the etching morphology

The etched silicon surfaces are shown in Figures 124, 125, and 126 for different etching times with different Au layers on top. As shown from the figures, the surface morphology size scale increased from nano scale when etched for a shorter time with thinner Au layer to submicron scale when etched at longer time with thicker Au layers. Clearly, the surface morphology can be manipulated over quite a large scale range.

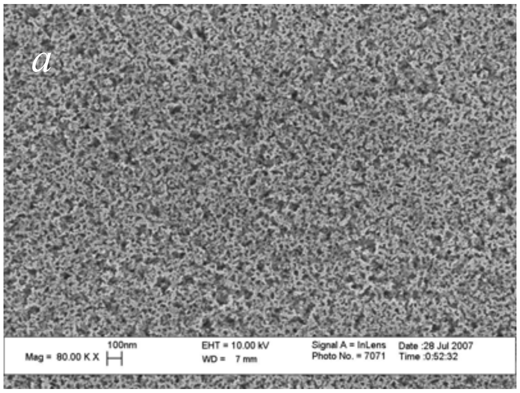

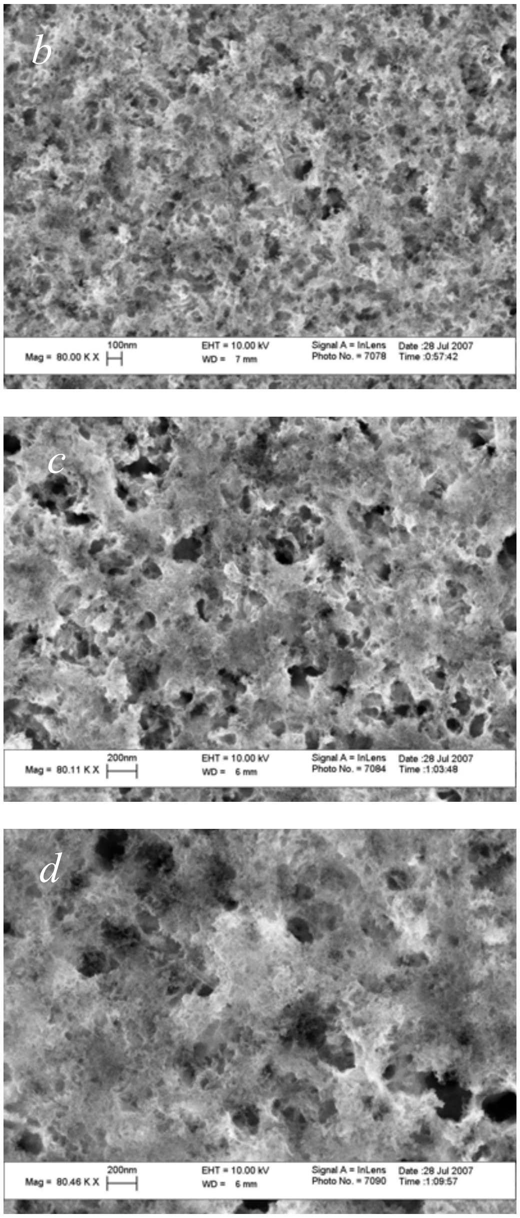

Figure 124. 2 nm Au assisted etching of Si for different times, (a) 1 min, (b) 2 min, (c) 4 min, and (d) 10 min.

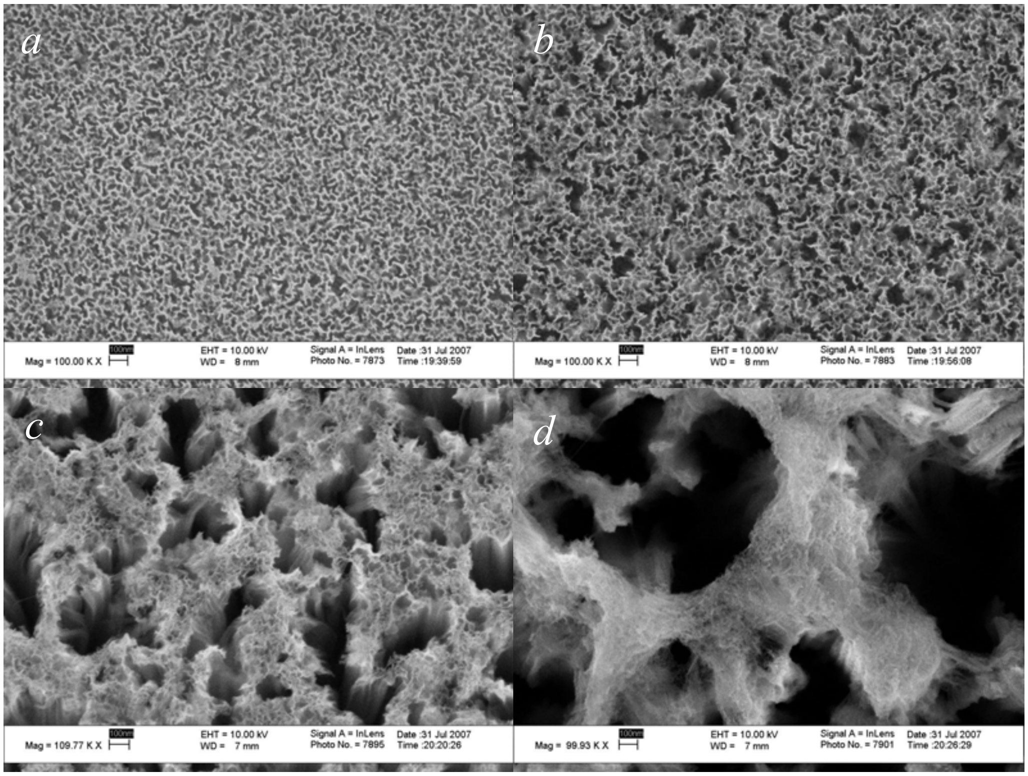

Figure 125. 5nm Au assisted etching of Si for different times, (a) 1 min, (b) 2 min, (c) 4 min, and (d) 10 min.

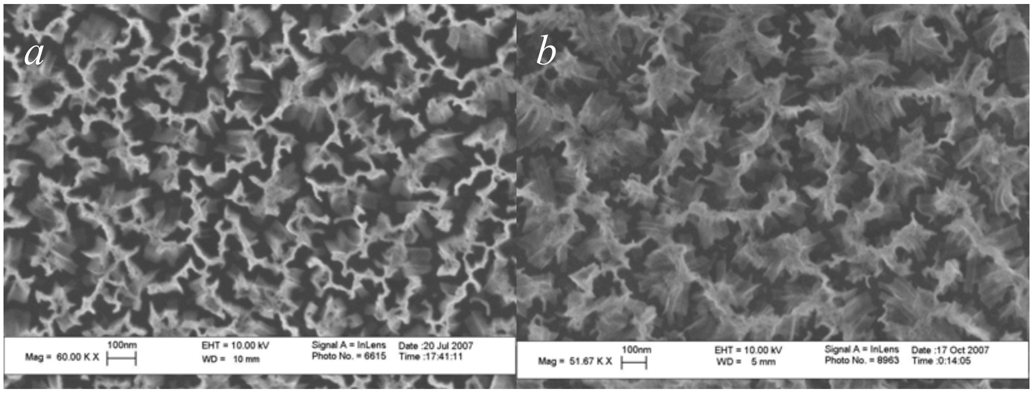

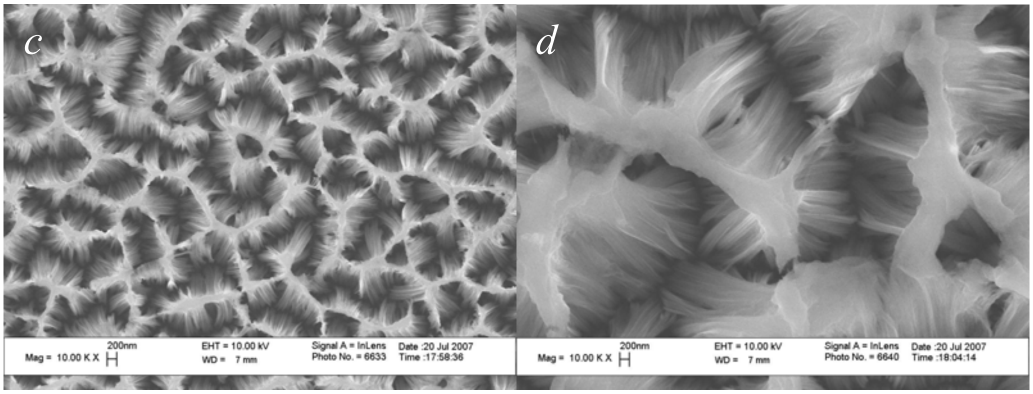

Figure 126. 10nm Au assisted etching of Si for different times, (a) 1min, (b) 2 min, and (c) 4 min and (d) 10 min.

We know that for anodic silicon etching, the voltage and current are critical. In our process electroless etching is used. The hydrogen peroxide affects the injection of holes from Au particles into silicon substrate; therefore, the particle size as well as the Au particle density may play an important role on the etching reaction since both affect the hole injection process. As a result, it is expected that for small Au particles (e.g., 2 nm), the increase in the particle size will result in an increase in the number of holes injected into silicon, while for large Au particles (5-10 nm) the size effect vanishes.

According to Wenzel and Cassie, rough surfaces facilitate the enhancement of contact angles which cannot be achieved on a flat surface even with the most hydrophobic surface coatings available. The rough silicon surfaces obtained from the metal assisted etching process were therefore treated with fluoroalkyl silane (PFOS) to render the surface hydrophobic to investigate the surface roughness effect in achieving superhydrophobicity. Contact angle and contact angle hysteresis data are shown in Figures 127 and 128. With increasing etching time, the contact angles increased. All surfaces showed contact angles greater than 140˚ while for a flat silicon surface treated with the same silane, the contact angle is only ~115˚. In addition, the contact angle hysteresis of all samples decreased with etching time, which suggests an enhanced surface roughness with longer etching times. The effect of the thickness of Au layers is also shown in Figures 127 and 128. With thicker layers, contact angles were higher and hysteresis was much reduced relative to that of thinner Au layers. For 10 nm Au layers, the silicon surface etched for 10 min showed a contact angle of 167.7˚ as shown in Figure 129 and a hysteresis of 12.4˚.

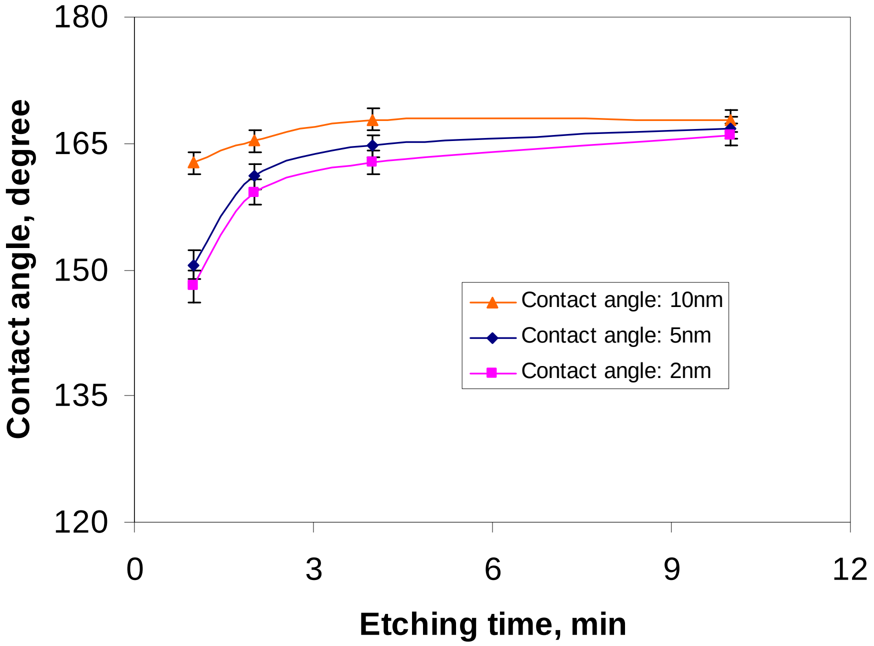

Figure 127. Contact angles for etched silicon samples.

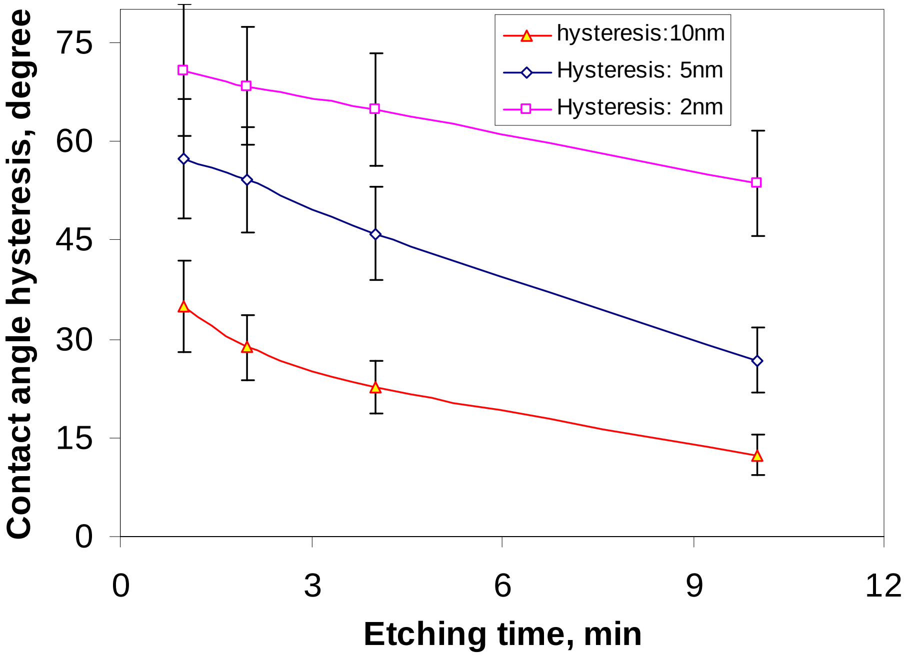

Figure 128. Contact angle hysteresis for etched silicon samples.

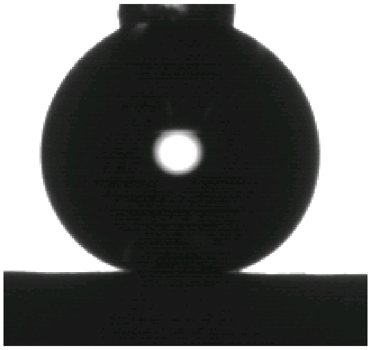

Figure 129. Shape of the water droplet on a silicon surface etched with a 10 nm Au layer for 10 min and treated with PFOS.

6.4.4 Light reflection measurement

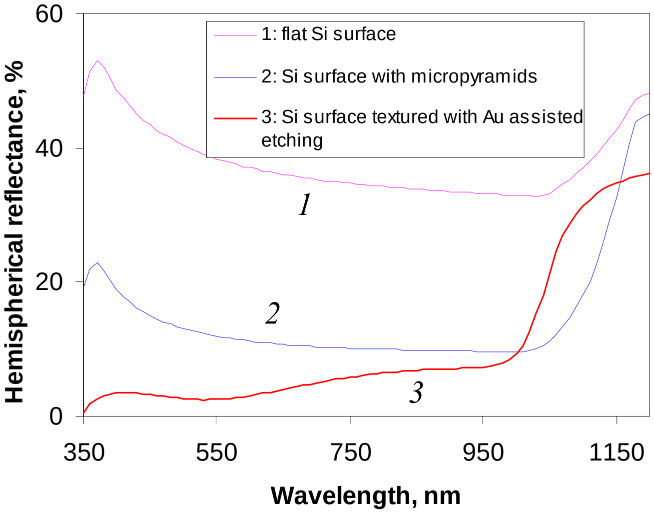

Figure 130. Surface diffuse reflectance of as etched silicon surfaces with 5 nm Au layer for 4 min with comparison to flat and pyramidal Si surfaces.

The as etched silicon surfaces appeared black (nonreflecting) due to the presence of nanostructures on the surfaces. Figure 130 shows measurement results on a flat silicon surface, pyramid textured silicon surface and an etched (nanotextured) silicon surface with a 5 nm Au layer for 4 min. Over a broad wavelength (350-980 nm) the reflectance of the nanotextured surface is lower than that of flat silicon and pyramid textured silicon and the weighted reflectance between 350-1200 nm is 6.0% which is much less than that on a micron-pyramid textured silicon surface (~12.3%), which are commonly employed in high efficiency solar cells[226]. This implies that the surface should absorb more sunlight than some other textured silicon surfaces. This property indicates a promising application of the nanotextured surfaces for photovoltaic applications with self-cleaning capability.

Conclusions

The Au assisted etching of silicon surfaces with Au layers of 2 nm, 5 nm and 10 nm was investigated. Increased etching time resulted in surface structures with greater depths. The etching rate for thicker Au layer coated silicon was constant while for a 2 nm Au layer coated silicon surface, the etching rate was dependent on etch depth which suggested a diffusion-controlled etching process. The surface morphologies changed from small nanostructures at shorter times to large submicron structures at longer etching times. When the etched surfaces were treated with PFOS, the surfaces all showed high contact angles (superhydrophobicity). An increase in etching time resulted in a higher contact angle and a reduced hysteresis. With increased thickness of the Au layer, analogous trends were observed. Reflectance measurements showed that the etched surface showed a much reduced reflectance compared to that of pyramid textured silicon surfaces which are commonly employed in high efficiency solar cells. This shows that the surfaces prepared using Au assisted etching technique is promising for light absorption for photovoltaic applications.

CHAPTER 7

HIERARCHICAL AND ROBUST SUPERHYDROPHOBIC SURFACES

Superhydrophobic surfaces offer significant advantages for many applications such as self-cleaning[125, 227], anticorrosion[228-230] and slip flow in microfluidics[91, 231]. Artificial superhydrophobic surfaces have been investigated extensively through the creation of hierarchical surface roughness design[14, 195], surface structure geometry design for superhydrophobic and superoleophobic surfaces[25, 27, 154], and designs to reduce contact angle hysteresis[29, 181]. Many different materials have been used to fabricate superhydrophobic surfaces. However, the superhydrophobic surfaces generated via current surface modification techniques are mostly not suitable for practical applications due to limited mechanical abrasion resistance of surface structures, stability to water vapor condensation, oil/surfactant repellency and surface chemical stability. Durability, chemical bonding alteration, mechanical modification, and degradation due to high energy irradiation, are major limitations to the successful application of superhydrophobic surfaces for self-cleaning and water repellence. Recent studies have begun to address the mechanical robustness to environmental[164] and UV irradiation exposure[232], chemical stability[165, 233] and water immersion stability[71]. However, little work has been reported on the investigation of mechanical abrasion/friction resistance of superhydrophobic surfaces, which is one of the most important practical limitations for self-cleaning applications.

Like on lotus leave surfaces, nature selected hierarchical structures for superhydrophobic functions. Through continuous supply of hydrophobic wax onto leave surface, a lotus leave maintained its hydrophobic coating layer. However, what is the advantage of hierarchical structures over one scale structures regarding the structure stability under mechanical abrasion or friction? Currently, most work reported is related to the hierarchical effect on the increase of contact angle and the reduction in contact angle hysteresis. Actually research is not going into the aspect of mechanical robustness. Researches regarding the improvement of superhydrophobicity (high contact angle and reduced contact angle hysteresis/sliding angle) were reported on the hierarchical surfaces[146, 154, 234-237].

7.1 Robustness Improvement on Si Hierarchical Surfaces

Pyramid surface is expected to show better mechanical strength due to its geometry compared to pillars. However, pyramid surface can not achieve a superhydrophobic state due to the fact that Cassie water/surface contact cannot be maintained. In order to achieve a stable superhydrophobic state, a second scale roughness is needed on top of pyramids. The hierarchical surface should also show certain mechanical stability. Although mechanically durable surfaces were theoretically discussed[235], the durability is mainly from the strength of individual structures on a surface. No test on mechanical durability was reported in literature. In this chapter, we will focus on understanding the mechanical stability and improvement of robustness on hierarchically structured superhydrophobic surfaces. The model Si surface we used showed two scale structures from etching techniques (micrometer size pyramids with Si nanostructures on top).

In order to investigate the abrasion resistance of the surfaces, a specific methodology was invoked as illustrated in Figure 131: Polyester/cellulose Technicloth II wipes were used as abrasion substrates and a superhydrophobic surface faces the abrasion substrate. With applying a normal pressure (~3450 Pa) on the superhydrophobic surface, the surface was moved in one direction. The contact angle and hysteresis change over abrasion length (maximum length of ~3 meters) were monitored.

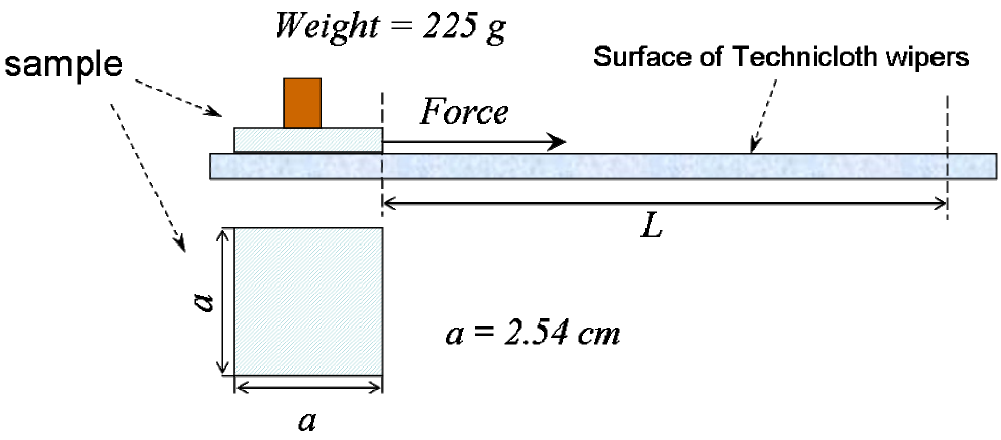

Figure 131. Illustration of the abrasion test on a superhydrophobic surface.

After preparation of the surface structures, surface fluorination was performed by treatment with perfluorooctyl trichlorosilane (PFOS). Typically, a 3 millimolar solution of PFOS in hexane was used for these treatments. Substrates were immersed in the PFOS solution for 30 min followed by a heat treatment at 150˚C in air for 1 hour, to complete the hydrophobic surface modification.

One of the limitations in the application of superhydrophobic surface coatings to commercial products is the abrasion resistance of the surface. Because of the presence of surface micro- and nano-structures, the roughness can be easily altered due to surface abrasion-induced break-down of small surface structures. In addition, abrasion may also result in removal of the hydrophobic layer on the rough surface. Both of these effects result in a failure of the self-cleaning surfaces. In order to address these issues, the abrasion test shown in Figure 131 was employed to evaluate abrasion resistance of the superhydrophobic surfaces. Initially, different superhydrophobic surfaces were tested. The data was shown in Table 21. From the test, the two scale superhydrophobic Si surfaces showed the best result with an almost constant contact angle and a hysteresis increase as shown in Figure 132 (from ~ 2˚ to 13.6 ± 3.0˚). For all other materials, contact angles decreased to below 140˚ which suggested a significant superhydrophobicity loss. Indeed, on the failed surfaces by abrasion, the self-cleaning effect vanished completely;

water droplets stuck to the surfaces even turn the superhydrophobic surface upside down. While on the two-scale structured Si surface, water droplet can still roll off while at a higher sliding angle.

Table 21. Abrasion resistance of different superhydrophobic surfaces.

Superhydrophobic surfaces	Initial contact angles	Contact angles after abrasion length of 25 cm
PU	168.1 ± 1.6°	138.7 ± 5.0°
PTFE	161.3 ± 1.0°	130.2 ± 4.0°
Silica	165.4 ± 1.5°	124.3 ± 5.0°
Si nanostructures	166.4 ± 1.5°	127.7 ± 4.5°
Si two scale structures	168.1 ± 0.7°	167.4 ± 1.5°

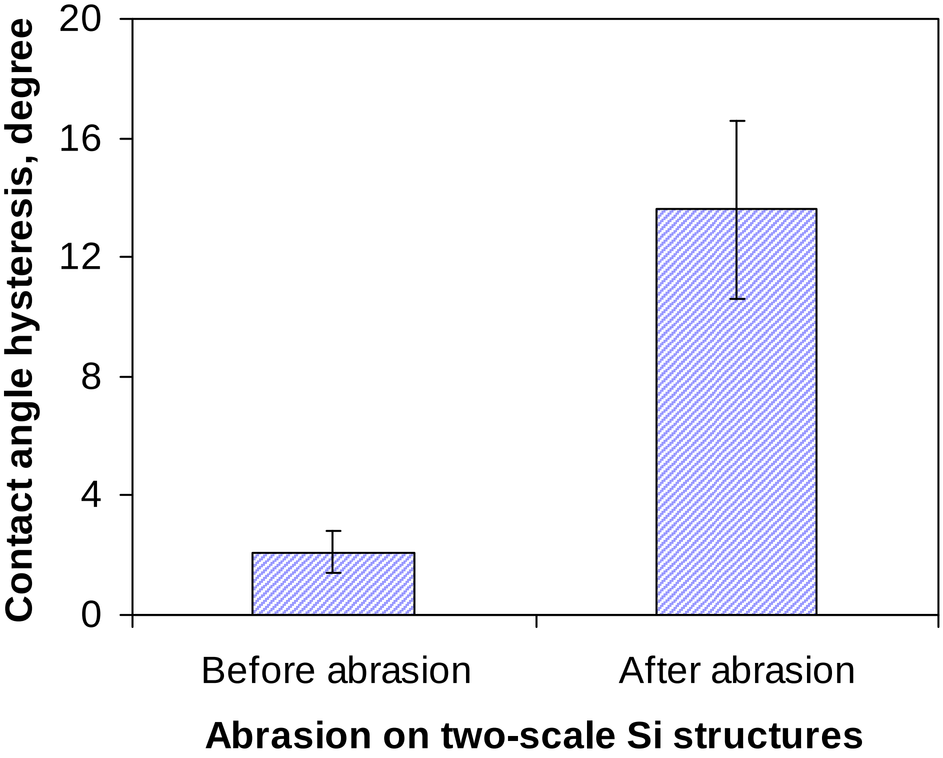

Figure 132. Contact angle hysteresis change on two-scale Si structures before and after abrasion test.

For better understanding of the good superhydrophobicity retaining effect on two-scale surfaces, microscopic investigation is necessary.

The surfaces were examined before and after abrasion test using SEM. For surfaces with only nano-scale structures, the roughness was changed greatly. Most of the surface structures were removed as shown in Figure 133b. This demonstrated that the surface nanostructures are very weak under abrasion forces. The surface structure change resulted in the decrease in water droplet contact angle on the surface. However, when the surface nanostructures were fabricated on micro-pyramid textured Si surfaces, the abrasion test showed that the surface water droplet contact angles maintained almost unchanged while there is a hysteresis increase after the test. This can also be explained by the surface structural changes. As shown in Figure 134, before abrasion test, nanostructures are uniformly covered on micro-pyramids surface. Due to abrasion, the surface structures on the top of pyramids was removed (Figure 134 b). However, the surface structures at the lower part of pyramids were retained. This two-scale structure can still maintain a high water droplet contact angle on the surface. While the top surface was depleted of nanostructures, water droplet will have a higher contact area on Si structures than that before the abrasion test, as shown in Figure 135. This corresponds to an increased contact angle hysteresis.

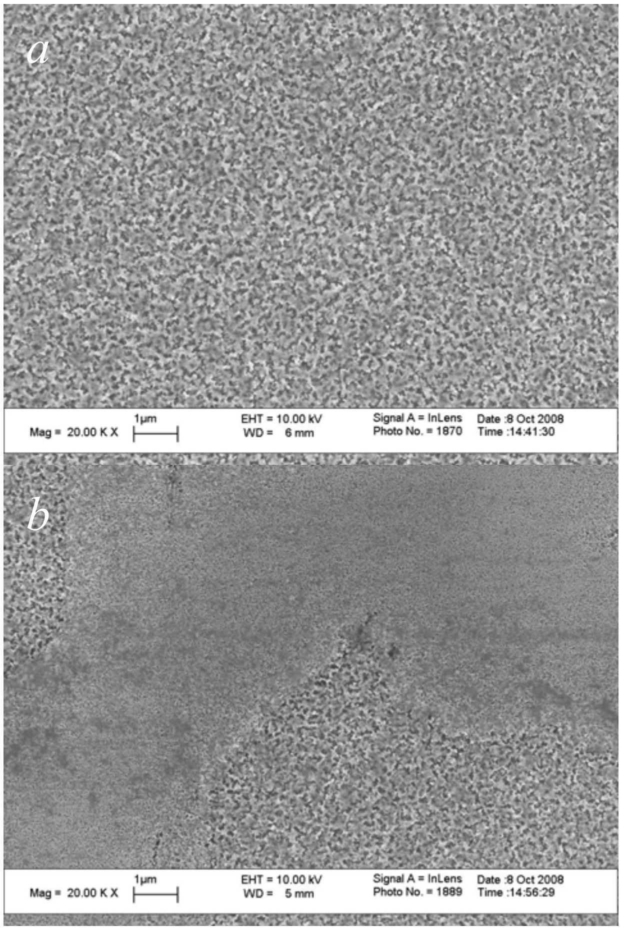

Figure 133. A Si surface with nano-scale surface structures; a. before abrasion, b. after abrasion.

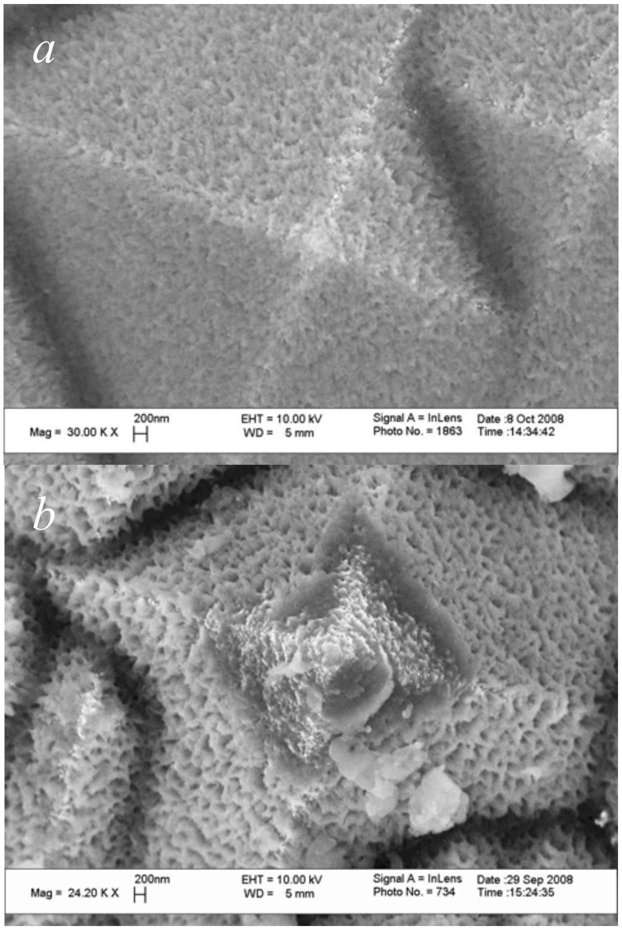

Figure 134. A Si surface with two-scale structures (micro-pyramids and nanostructures); a. before abrasion, b. after abrasion.

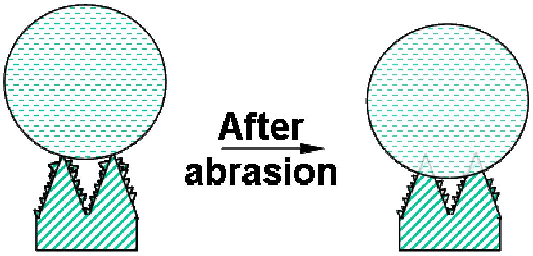

Figure 135. Illustration of water droplet contact on Si surfaces before and after abrasion.

This retain in superhydrophobicity can be explained by a protection mechanism. During abrasion, the breakdown of nanostructures is mainly on peaks of the pyramid structures where contact is inevitable. Therefore, the lower level nanostructures were protected from contacting as shown in Figure 136 and no abrasion happened on this lower part of Si micro-structures.

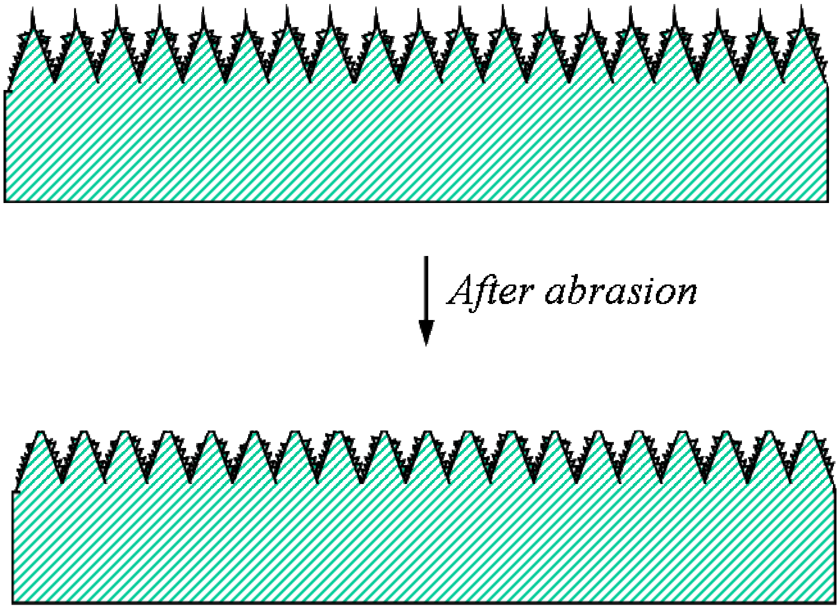

Figure 136. Illustration of the effect of abrasion on the surface structures.

7.2 Robust Superhydrophobic Surfaces from Epoxy/Silica Nanoparticles

We have reported methods to maintain a stable superhydrophobic silica surface under UV weathering conditions as described previously[232]. Based on the understanding of protection of hierarchical structures on improved robustness, in this section, we will focus on achieving the mechanical stability of superhydrophobic surface coating with the combination of silica nanoparticles and epoxy resin. For polymeric materials, intrinsic molecular structures make it difficult to overcome durability issues due to their vulnerability to UV exposure[178], and the flexibility of the materials. For inorganic materials, the brittle nature of the materials results in damage to surface micro- and nano- structures due to abrasion forces applied to the surface. In order to overcome the drawbacks of both organic and inorganic materials while maintaining adequate durability of the surface, we have combined polymeric (epoxy) material and inorganic nanoparticles for a low cost process for the fabrication of superhydrophobic surfaces. In these composite materials, the epoxy serves as an adhesion and stress relief layer, while the inorganic nanoparticles at the surface of the polymeric layer generates an abrasion resistant surface layer that possesses the nano-structure necessary to impart superhydrophobicity as shown in Figure 137.

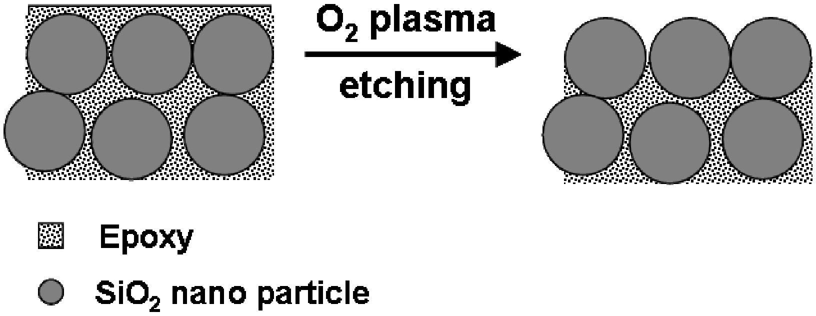

Figure 137. Illustration of O_2 plasma etching of epoxy/SiO_2 nanoparticle composite films for surface rough structures.

7.2.1 Experimental Details

One gram of silica particles (100 nm diameter) was mixed in 10 g toluene and sonicated for 5 min. Then bisphenol A diglycidyl ether (EPON 828) 1 g, hexahydro-4-methylphthalic anhydride 0.75 g, and imidazole 0.03 g were added to the silica/toluene solution and stirred for 30 min to form a final coating mixture. Glass slides were pre-cleaned by UV/ozone treatment for 5 min and then rinsed with water and ethanol. Drops of the mixture were then placed on cleaned glass slides; alternatively, the slides were also covered by the mixture via dip coating or doctor blading. After toluene vaporization, the coating was cured at 150 ˚C for 4 h. Plasma etching was conducted under the following conditions: 150 W rf power, 0.5 torr pressure and an O_2 flow rate of 75 sccm. After fabrication of the surface structures, surface fluorination was performed by treatment with perfluorooctyl trichlorosilane (PFOS). Typically, a ten millimolar solution of PFOS in hexane was used for these treatments. Specifically, the etched silicon wafer was immersed in the solution for 30 min followed by a heat treatment at 150˚C in air for 1 hour, to complete the hydrophobic surface modification.

In order to investigate the abrasion resistance of the surfaces, a specific methodology was invoked as illustrated in Figure 131.

Condensation tests were performed in a chamber at 45 ± 3˚C in the presence of water. A thermometer was used to monitor the temperature in the test chamber.

Contact angle measurements were performed with a Rame-Hart goniometer that had a CCD camera equipped for image capture. Scanning Electron Microscopy (SEM) was used to investigate the surface morphology (LEO 1530 FESEM). After preparation of the surface structures, surface fluorination was performed by treatment with perfluorooctyl trichlorosilane (PFOS). Typically, a 3 millimolar solution of PFOS in hexane was used for these treatments. Substrates were immersed in the PFOS solution for 30 min followed by a heat treatment at 150˚C in air for 1 hour, to complete the hydrophobic surface modification.

7.2.2 Results and Discussion

7.2.2.1 Superhydrophobic surfaces from Bisphenol A epoxy with silica nanoparticles

Bisphenol A epoxy is widely used in surface coatings, adhesives (microelectronics packaging), and composite materials (such as carbon fiber and fiber glass reinforced epoxy). In order to improve the abrasion resistance of epoxy coatings, silica or alumina particles are usually coated onto the epoxy surface. The adhesion between the epoxy and inorganic particles is strong due to the hydroxyl groups formed in the epoxy. In our study, we coated glass slides with epoxy mixed with silica nanoparticles; the resulting surface of this structure was expected to be rough while maintaining surface adhesion. However, we found that after coating and a surface hydrophobic treatment by PFOS, the contact angle is < 140˚; the surface is shown in Figure 138a. It is clear that the surface roughness is not sufficient to achieve a superhydrophobic self-cleaning state. In order to enhance the surface roughness, O_2 plasma etching was conducted for various times. The surface morphologies generated are shown in Figures 138b-e, where it is evident that the surface roughness increased continuously with etching time. This change yields an increase in contact angle after surface hydrophobic modification by PFOS. Contact angles and hysteresis are shown in Figure 139. The contact angles increased to establish superhydrophobicity after 5 min of etching; concomitantly, the hysteresis values dropped.

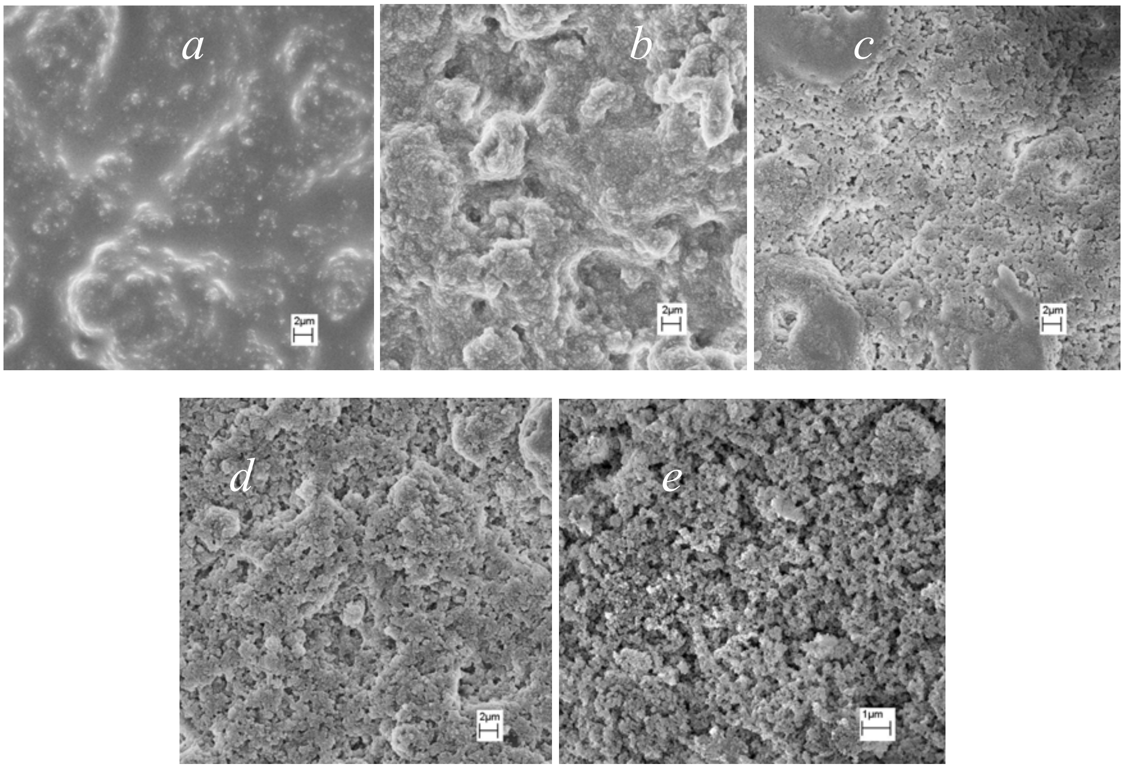

Figure 138. Surface morphology from SEM images: surface before etching (a), O_2 plasma etched for 1 min (b), 5 min (c), 10 min (d) and 15 min (e).

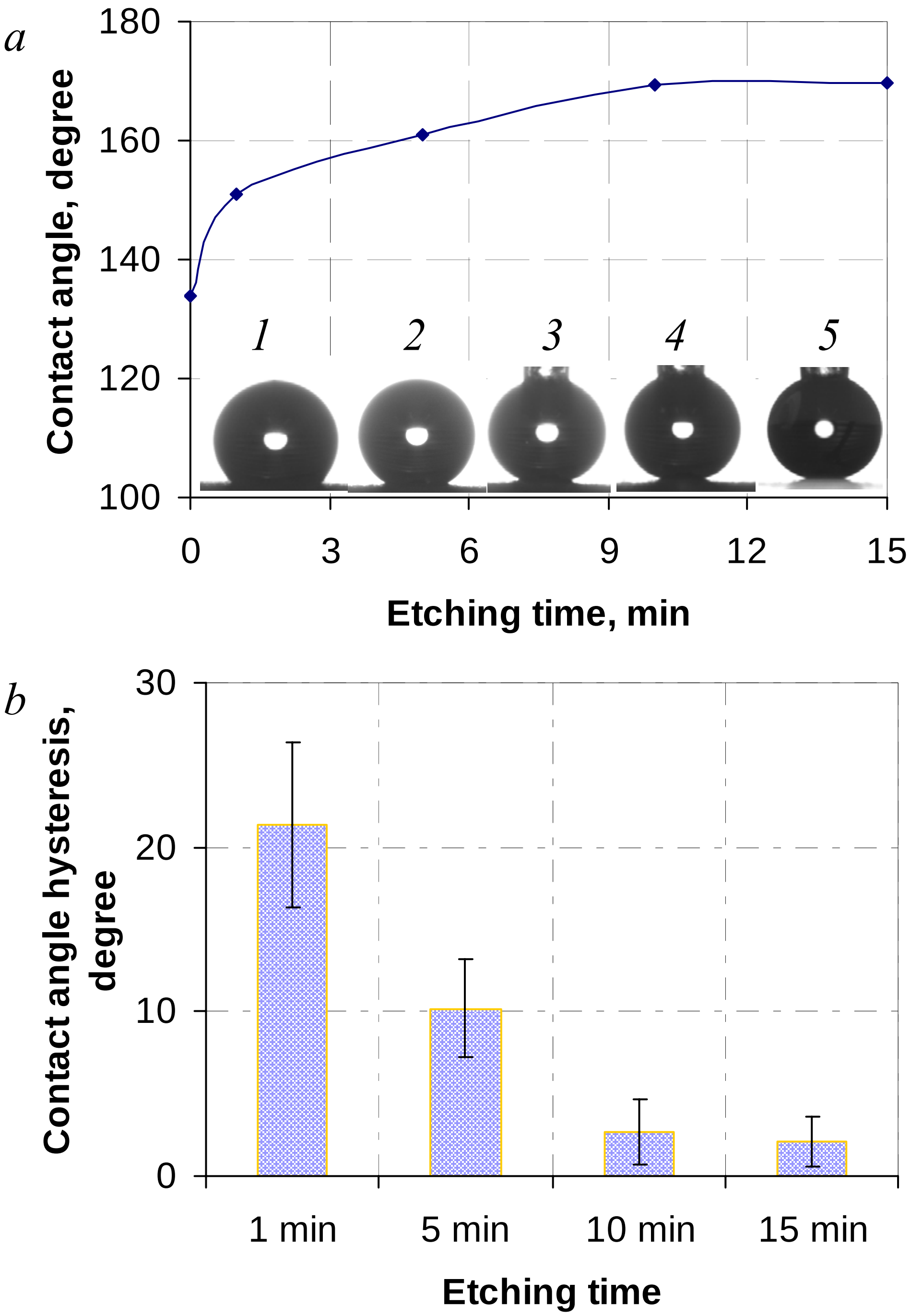

Figure 139. Contact angle (a) and hysteresis (b) for surfaces etched for various times. Inset (a): Water droplet contact angles on etched surfaces. 1) epoxy surface before etching, 2) O_2 plasma etched for 1 min, 3) O_2 plasma etched for 5 min, 4) O_2 plasma etched for 10 min, 5) O_2 plasma etched for 15 min.

Observed trends of water droplet contact angles and hysteresis can be explained by consideration of the surface morphologies generated through different etching times.

First, all surfaces have sufficient roughness to establish high (>150^o) contact angles. However, surfaces etched for short (5 min) times display nonuniformity (Figure 140) in that the micro-bump top surface epoxy (Figure 140 b) is not completely etched; therefore, most of the silica particles remain embedded in the polymeric layer. This geometry results in high contact angle hysteresis.

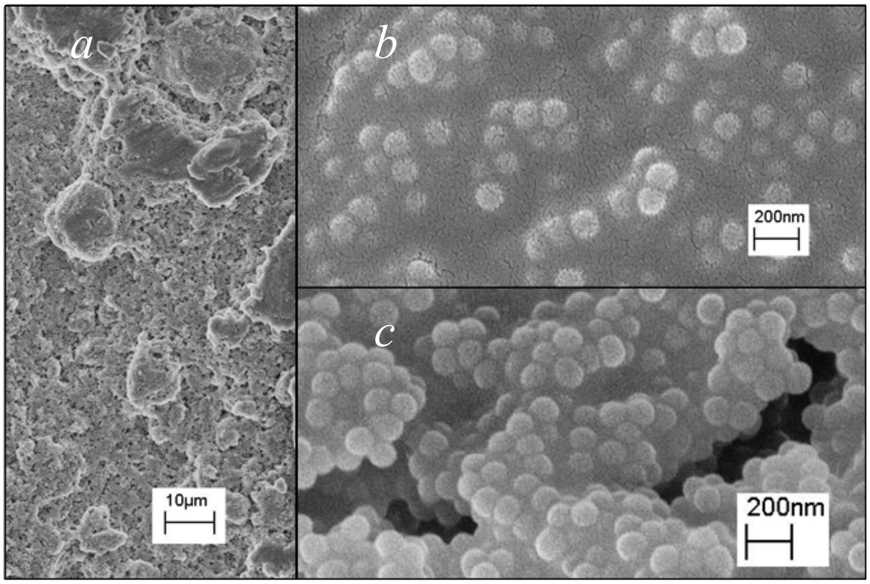

Figure 140. Surface morphology after 5 min O_2 plasma etching (a), magnified micro-bump surface (b), and magnified surface of valley areas in between the micro-bumps (c).

At etching times of 10 and 15 min, the surface is rougher as shown in Figures 141 and 142. Especially on the micro-bump surfaces, the tops of the silica particles are exposed. Therefore, both a high contact angle and a reduced hysteresis result. The difference between the 10 and 15 min etched surfaces is that for an etching time of 10 min, silica particles formed a densely packed layer while for an etching time of 15 min, the surface morphology of the micro-bump top surface is significantly roughened. The densely packed surface only gives a limited surface roughness and thus a lower water droplet contact angle compared to a rougher surface like that shown in Figure 142 b. However, the density of the micro-bumps from 10 min etching in Figure 141 is very low, and the micro-bump effect on contact angle hysteresis is not an obvious difference from the surface etched for 15 min, shown in Figure 139.

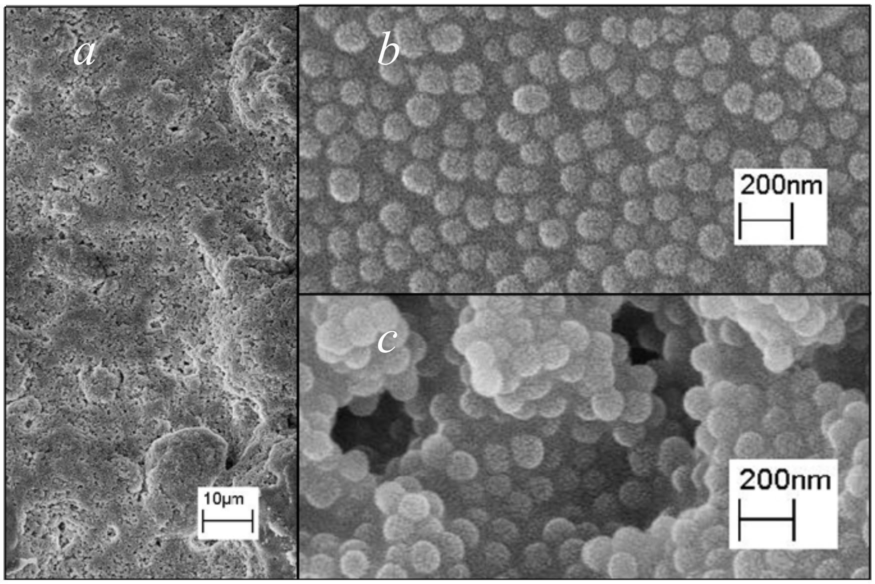

Figure 141. Surface morphology after 10 min O_2 plasma etching (a), magnified micro-bump surface (b), and magnified surface of valley areas in between the micro-bumps (c).

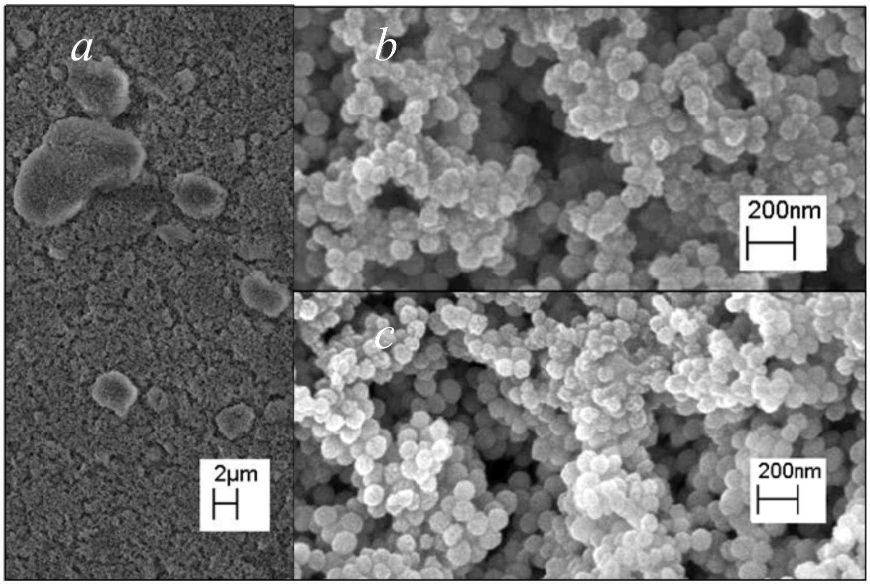

Figure 142. Surface morphology after 15 min O_2 plasma etching (a), magnified micro-bump surface (b), and magnified surface of valley areas in between the micro-bumps (c).

7.2.2.2 Abrasion test for robust structure

One of the limitations in the application of superhydrophobic surface coatings to commercial products is the abrasion resistance of the surface. Because of the presence of surface micro- and nano-structures, the roughness can be easily altered due to surface abrasion-induced break-down of small surface structures. In addition, abrasion may also result in removal of the hydrophobic layer on the rough surface. Both of these effects result in a failure of the self-cleaning surfaces. In order to address these issues, an abrasion test was designed to evaluate abrasion resistance of the superhydrophobic surfaces. Initially, different superhydrophobic surfaces were tested. The data was shown in Table 22. From the test, the epoxy/silica and Si two scale superhydrophobic surfaces showed the best result with a high contact angle. For all other materials, contact angles decreased to below 140° which suggested a significant superhydrophobicity loss.

Table 22. Abrasion resistance of different superhydrophobic surfaces.

Superhydrophobic surfaces	Initial contact angles	Contact angles after abrasion length of 25 cm
PU	168.1 ± 1.6°	138.7 ± 5.0°
PTFE	161.3 ± 1.0°	130.2 ± 4.0°
Silica	165.4 ± 1.5°	124.3 ± 5.0°
Si nanostructures	166.4 ± 1.5°	133.2 ± 4.5°
Si two scale structures	168.1 ± 0.7°	167.4 ± 1.5°
Epoxy/silica nanoparticles	169.2 ± 1.1°	168.6 ± 1.7°

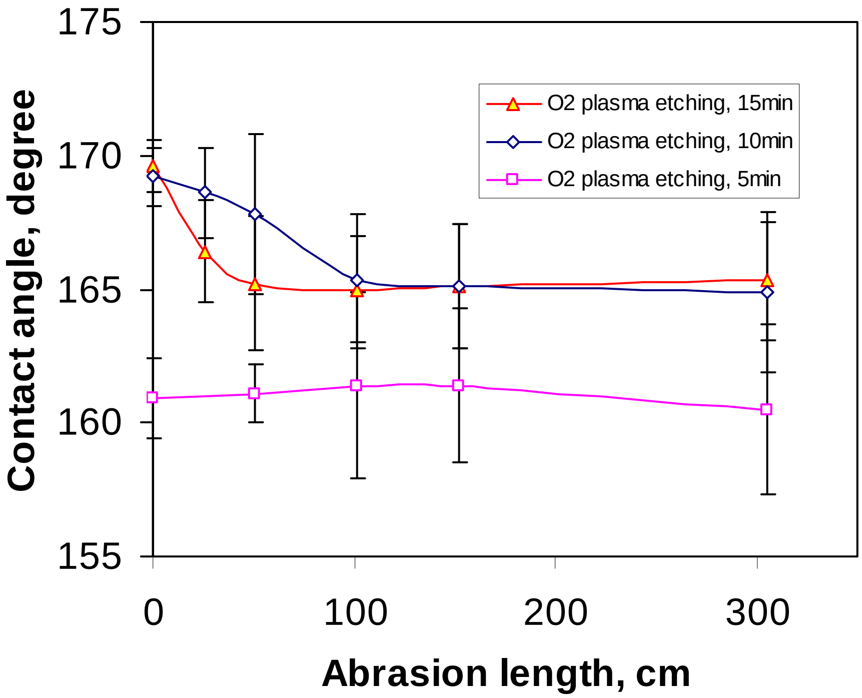

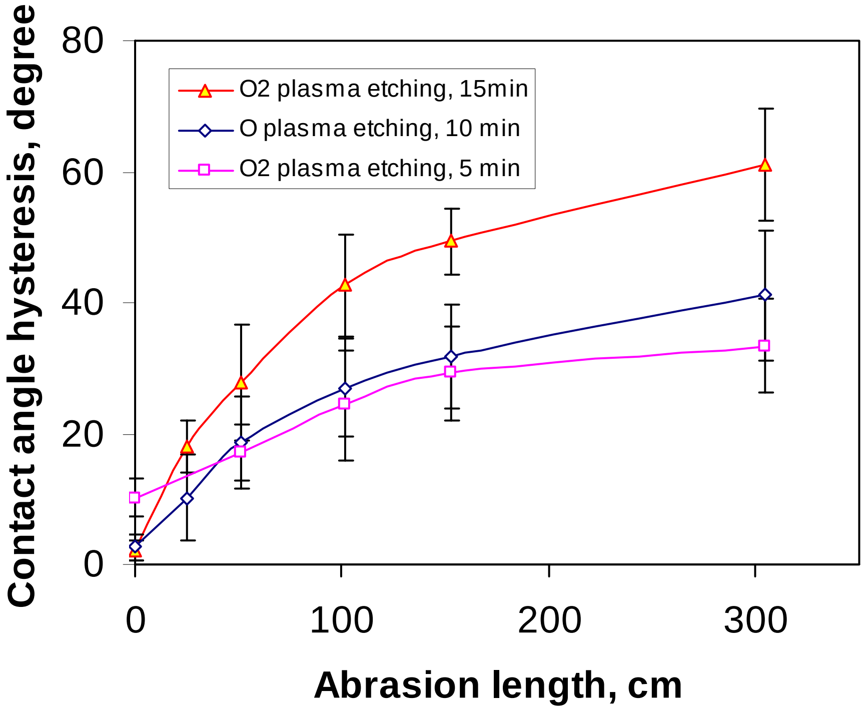

Figure 143. Contact angles and contact angle hysteresis changes after abrasion test on O_2 plasma treated epoxy/SiO_2 surfaces.

The effect of abrasion on water droplet contact angles and hysteresis was investigated on epoxy/silica superhydrophobic surfaces to investigate the mechanism of superhydrophobicity failure. The results are shown in Figures 143 and 144; three O_2 etching conditions were considered: 5, 10 and 15 min. Contact angles were essentially constant with abrasion for 5 min etching, while for 10 and 15 min etching, an initial drop in contact angles is observed. The rapid drop of contact angles for surfaces etched for 15 min suggests that the surface undergoes a surface structure change which indicates that the fragile surface structures were damaged. This observation is apparently due to the fact that for longer plasma etching times, the epoxy layer was etched extensively resulting in a loss of adhesion between the silica spheres and the epoxy. The contact angle hysteresis change with abrasion length also suggests surface structure changes which critically affect wetting and adhesion. For 15 min plasma etching, the hysteresis increased more than that for the other etched surfaces. With increasing plasma etch time, epoxy is etched more extensively and the surface is rougher, while the robustness of the surface structures is reduced. For a 5 min etched surface, although it showed the lowest increase in hysteresis with abrasion, the initial contact angle is low while the initial hysteresis is large. With 10 min etching, contact angle behavior similar to that for the15 min etched surface is observed, while the hysteresis behavior is similar to that of the 5 min etched surface.

The surface structure change with abrasion for a 15 min etched surface is shown in Figure 144 of the contact angle images with moving substrate to one direction. After abrasion, the surface morphologies were shown in Figure 145. Scratches can be seen on the whole surface (Figure 145 a).

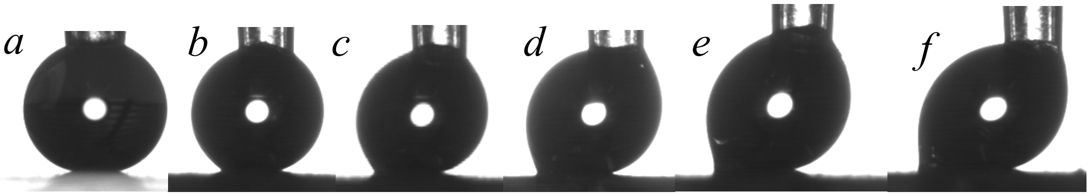

Figure 144. Contact angles hysteresis changes with abrasion; a) before abrasion test, b) 10 inch, c) 20 inch, d) 40 inch, e) 60 inch, f) 120 inch abrasion length for O_2 plasma etching of 15 min.

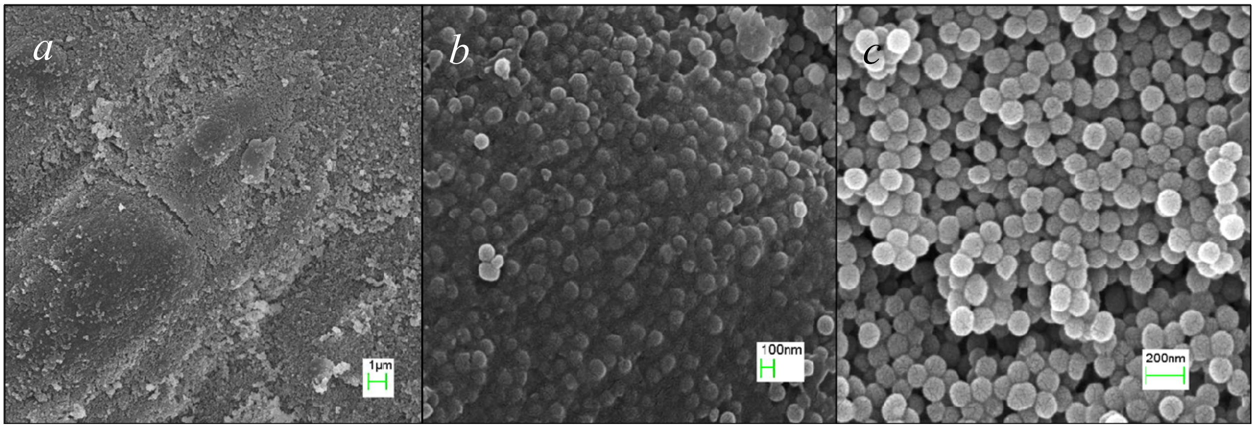

Figure 145. Surface morphology of plasma etched epoxy/silica nanoparticle surfaces after abrasion test, O_2 plasma etching for 15 min, low magnification overview of the abraded surface (a), and the high resolution images on a micro-bump (b) and on valley surfaces (c).

For surfaces etched for 10 min, the abrasion occurs mainly on the surface of the micro-bumps as shown in Figure 146. Surface morphology in the valleys is similar to those surfaces before abrasion, although minor scratches are evident as shown in Figure 146 c. High resolution SEM images of the micro-bump top surface is shown in Figure 146 b, where the surface has been scratched and flattened as a result of the mechanical friction. This flattened top gives rise to the increase in contact angle hysteresis observed (Figure 143), while the unchanged valley surface maintains a high contact angle. This effect is illustrated schematically in Figure 147. While roughness was reduced on the top (micro-bump) structures, most of the roughness was maintained in the valleys between the micro-bumps due to the fact that the top surface structures protect the valley surface from abrasion. However, for surfaces etched for 15 min, the morphology changed significantly, as shown in Figure 145. The extensive etching generated poorly adhering silica particles. After abrasion, these particles detached from the underlying epoxy layer as shown in Figure 145. Although the contact angle remains high due to the presence of loosely bonded surface structures as shown in Figure 145 c, the hysteresis has increased greatly and adhesion of the surface structures to substrates is reduced.

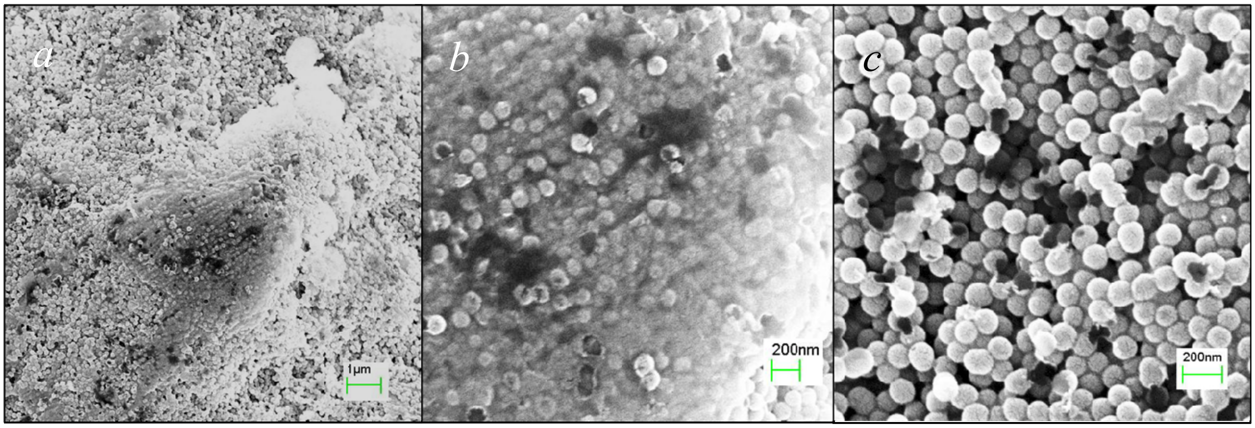

Figure 146. The surface morphology of plasma etched epoxy/silica nanoparticle surfaces after abrasion test, O_2 plasma etching for 10 min, low magnification of the abraded surface (a), and high resolution images on a micro-bump (b) and on valley surfaces (c).

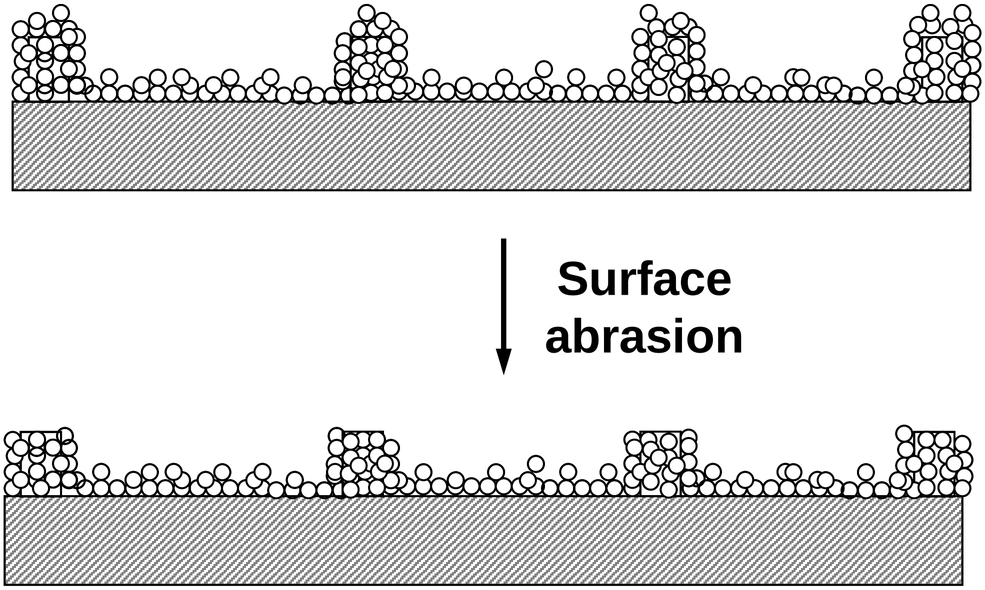

Figure 147. The surface abrasion effect on surface roughness, micro-bump surface roughness was reduced due to the mechanical abrasion while the valley surface roughness persisted.

7.2.2.3 Exposure to hot water

In order to investigate the stability of superhydrophobic surfaces in hot water, experiments were performed by soaking a superhydrophobic surface in 45˚C water for 24 hours; results are shown in Figure 148. Although the hysteresis increased immediately after the surface was removed from the water, after 4 hours of air exposure, the hysteresis decreased and approached the initial hysteresis value prior to water soaking. These results suggest that the rough surface may trap water upon soaking. Therefore, immediately after removal from the water, the trapped water increases the interaction between the surface and the water droplet. When the water vaporizes, the interaction decreases and consequently hysteresis is reduced. However, the final hysteresis is still higher than that of the initial surface without water soaking. This also suggests that there is a minor change in surface chemistry (from hydrophobic to hydrophilic in the presence of hot water) since hysteresis is very sensitive to chemical changes.

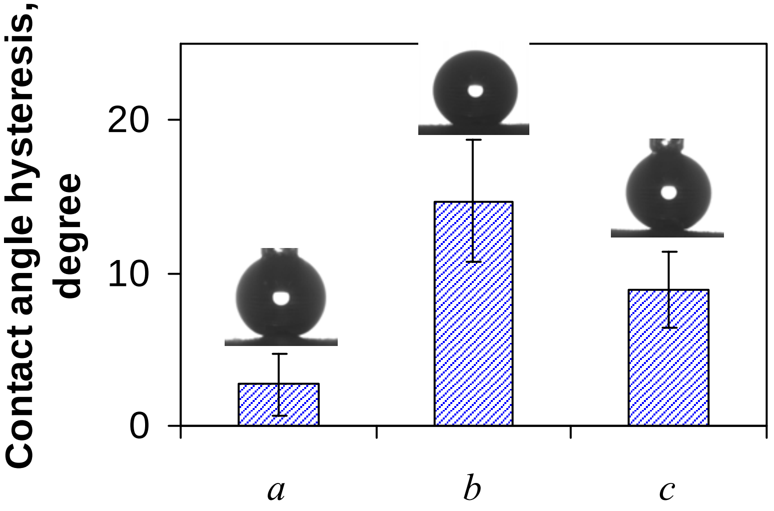

Figure 148. Contact angle hysteresis before and after 45 ˚C water soaking for 24 hours on surfaces of O_2 plasma etching for 10 min; a) before soaking in hot water, b) immediately after soaking in hot water, c) 4 h after removal from hot water. Insets: Contact angle images of water droplets.

7.2.2.4 Effect of water vapor condensation on the stability of superhydrophobic surfaces

Stability of superhydrophobic surfaces to water vapor condensation is very important because most applications for these surfaces, such as self-cleaning or water repellency, have water vapor present. For the epoxy/silica films in the current study, long term stability tests As shown in Figure 149, were performed in water vapor for ~9500 hours, the contact angles remained constant in the range of 165-166˚ while the hysteresis throughout the test period remained < 2.5˚.

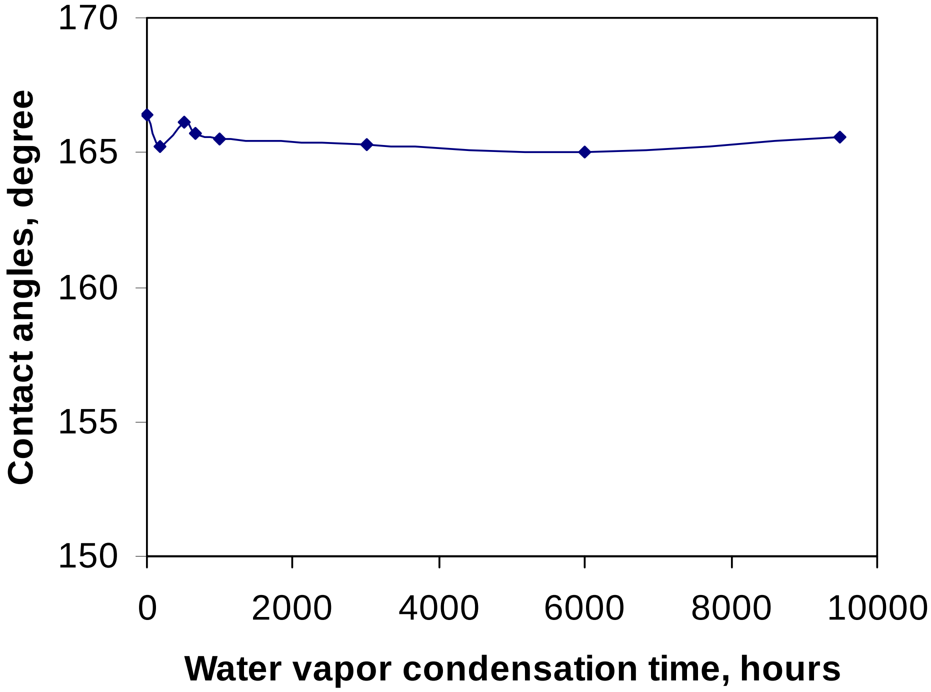

Figure 149. Water vapor condensation effect on contact angles on superhydrophobic epoxy/silica surfaces generated by O_2 plasma etching and PFOS treatment; the contact angle hysteresis throughout the test remained < 2.5˚.

Conclusions

Robust superhydrophobic surfaces were demonstrated on hierarchical Si surfaces with micro-pyramids and nanostructures. A protection mechanism of nanostructures by micro-pyramids was proposed. A mechanically robust superhydrophobic surface coating was prepared using epoxy and silica nanoparticles followed by plasma etching. Surface roughness was enhanced with O_2 plasma treatment time. Surface hydrophobicity was achieved by fluoroalkyl silane treatment. Adhesion of structures to the substrate was improved by the epoxy resin, while the mechanical stability of surface structures was improved by the inorganic silica nanoparticles with a protection mechanism from micro-bumps on the surface. By appropriate plasma etching (10 min etching in O_2), the surface roughness can be maximized while the adhesion between epoxy and silica particles is not significantly reduced. Therefore a mechanically robust superhydrophobic surface can be achieved. Abrasion on the surface mainly results in the loss of roughness on the top of the micron-scale (micro-bump) structures while the roughness in the valley between the micron structures is intact. After surface abrasion, water droplet contact angles remain high; however, the contact angle hysteresis increases significantly due to the structure change on the top of the micro-bump structures. The surface retains its superhydrophobicity even after hot water soaking. Water vapor condensation tests showed that the surface remains superhydrophobic after ~9500 hours testing time.

CHAPTER 8

SUPERHYDROPHOBICITY BY PARTICLE COATING ON SUBSTRATES WITH MOBILE AND HYDROPHOBIC SPECIES

This chapter describes the investigation of applications of superhydrophobic coatings on high voltage insulator surfaces for self-cleaning to prevent flashover and dry band arcing in outdoor applications. The weathering resistance of the surface is the first priority for successful application. Currently, the protection methods (high voltage stabilization and contamination) of polymeric insulator surfaces (EVA, silicone, EPDM) involve mobile protective coatings which incorporate oil, grease or pastes in the surface layer. The continuous supply of hydrophobic substances mitigates the contamination problem on the insulator surface.

Based on our previous research on superhydrophobicity and weathering improvement, an alternative method to resolve the UV stability issue is investigated. This method mimicks the continuous generation of superhydrophobicity on lotus leaves wherein surface self-healing occurs by continuously secreting hydrophobic species (wax) to the surface. This mechanism is applicable to surfaces that contain mobile and hydrophobic protective species. In this chapter, we attempt to establish this mechanism on silicone and EVA high voltage insulator substrates by coating an inorganic particle layer on the surface. Both silicone and EVA insulators are commercially available and are known to contain the mobile and hydrophobic species[238-240].

8.1 Sol Gel Technology for Particulates

There are numerous application areas for sol gel technologies[241]. One of the largest application areas is in film formation, which can be achieved by spin-coating or dip-coating a substrate. Other methods include spraying, electrophoresis, inkjet printing or roll coating. Optical coatings, protective and decorative coatings, and electro-optic components can be applied to glass, metal and other types of substrates with these methods.

The sol-gel process is a well-established process for making glass/ceramic materials, which involves the transition of a system from a liquid (the colloidal “sol") into a solid (the "gel") phase. This procedure allows the fabrication of materials with a large variety of properties: ultra-fine powders, inorganic membranes and thin film coatings. In a typical sol-gel process for particulate formation, the precursor is subjected to a series of hydrolysis and polymerization reactions to form soluble species; the species then condense/nucleate into a new phase in which a solid is dispersed in a solvent http://en.wikipedia.org/wiki/Macromolecule. For silica particle formation, this process is usually termed the Stöber method[242], which yields monodisperse particles. For titania particle preparation, highly reactive organometallic precursors condense in the presence of water to form particles without the need for a catalyst[243].

Monodisperse silica particles usually assume a close-packed arrangement on surfaces after coating as described in Chapter 2. We found that on such surfaces the contact angle is 130-140° after fluoroalkyl silane treatment. In order to achieve a much higher surface roughness for superhydrophobicity, we introduced titania particles into the system to achieve bimodal size distributions and thus a higher surface roughness. The process used is shown in Figure 150.

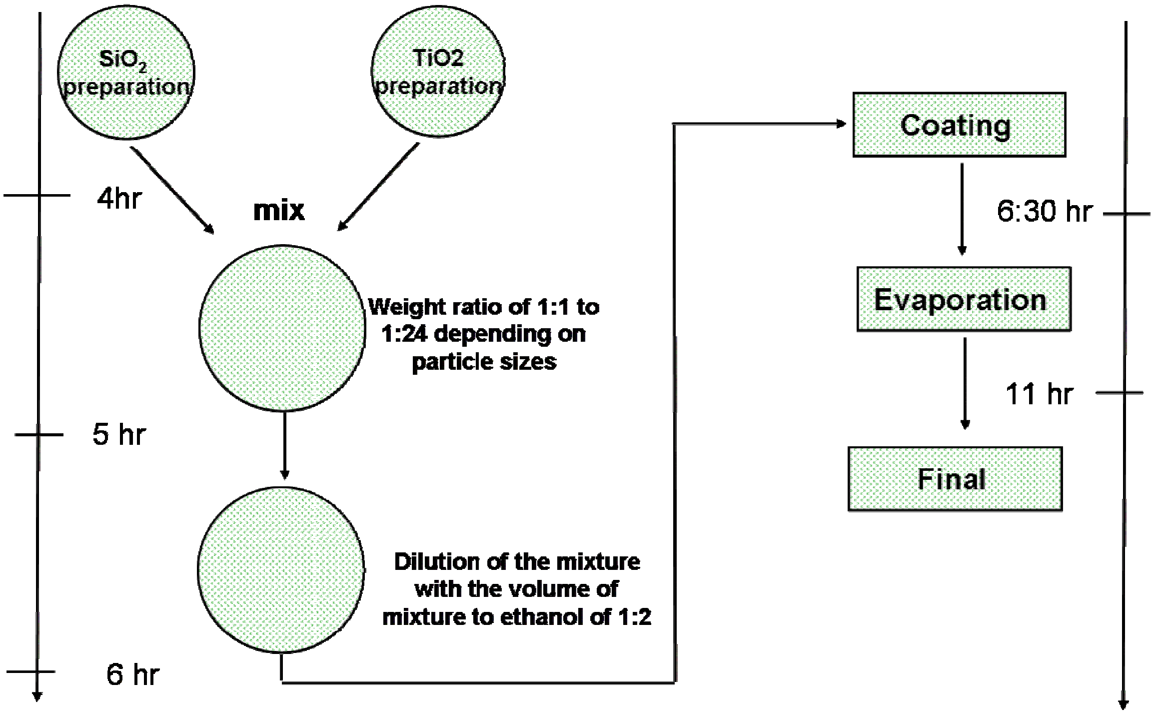

Figure 150. Process for the preparation of SiO_2/TiO_2 particle suspension in ethanol.

8.2 Experimental

Synthesis of monodisperse silica spheres is accomplished using the Stöber-Fink-Bohn method which involves using base (ammonia) as catalyst[112]. The production of monodispersed silica particles is described below.

At 60 ˚C TEOS undergoes hydrolysis to form silanol groups which are further catalyzed in the presence of ammonia to undergo condensation reactions and thereby form siloxane polymers (branched or linear depending on the reaction conditions) dissolved in solvent. When the polymer particles are sufficiently large, aggregates form which remain separated from each other by the negative surface charges. Initially, the surface charge is too small to repel the aggregates, so the aggregates undergo particle growth to form larger ones by an Ostwald ripening process wherein smaller particles dissolve and redeposit on large particles until uniform size is achieved. When more TEOS is added, the particles can grow larger due to the reaction between newly added hydrolyzed TEOS and the silica sphere surface silanol groups (seed growth). The particle size was controlled by catalyst (pH), water concentration and TEOS concentration.

A typical formulation for Silica particle formation is:

TEOS: 3 g, ethanol: 50 ml, DI water: 3 g, ammonia hydroxide (29%wt): 10 ml.

By controlling the amount of ammonia hydroxide, water, TEOS, and the reaction temperature, the silica particle size of can be controlled. Figure 151 gives the average particle diameter (*d*) in terms of the concentrations (mol/l) of water H_2O, ammonia (NH_3) and TEOS and thereby shows how the size distributions can be controlled.

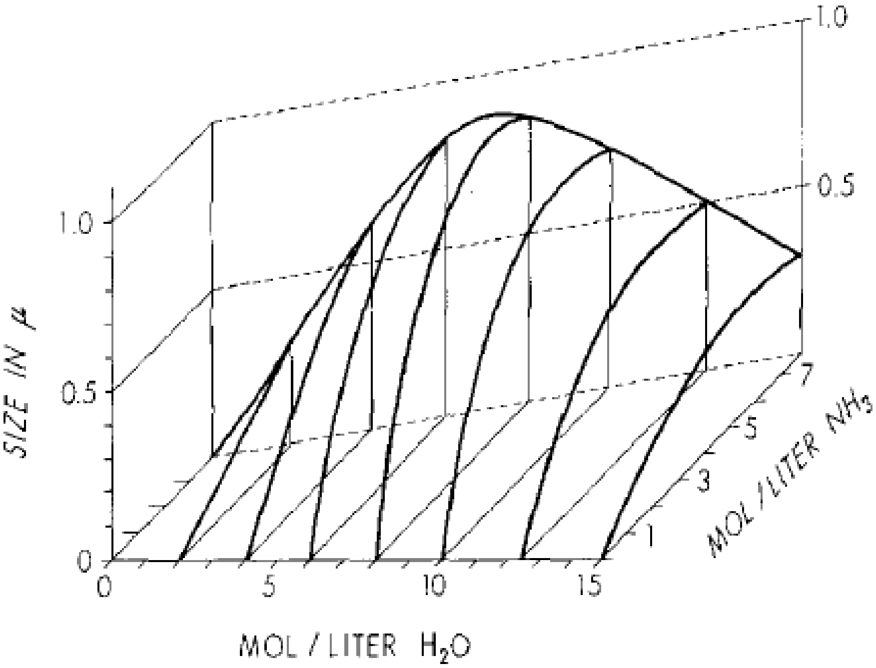

Figure 151. Control of silica particle sizes[242].

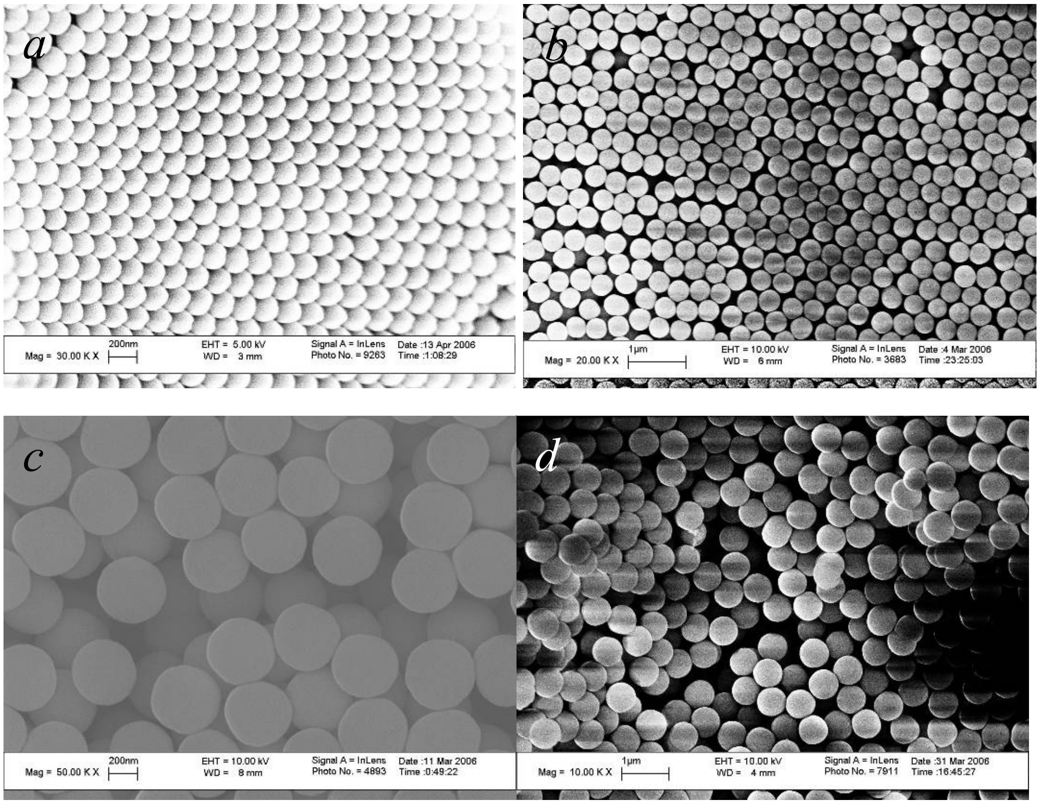

Figure 152. Monodisperse silica spheres produced using different conditions (primarily acidity); a) 200 nm, b) 300 nm, c) 370 nm, d) 600 nm by varying ammonia content in the reaction.

8.2.1 Mixing ratio determination

The particle sizes needed to form the appropriate surface structures for superhydrophobicity must first be established. For this purpose, we considered silica and titania particles as follows:

- Small particles: SiO_2, density 2.2g/mol; Large particles: TiO_2 density 4g/mol
- Assuming the silica particle size << titania particle size
- To insure that the correct surface structures can be formed the approximate minimum weight ratio of the two particles (TiO_2/SiO_2) should be calculated according to Figure 153.

Note: Safety measures should be taken when coating nanoparticles, i.e., the coating process should be performed in a well ventilated fume hood.

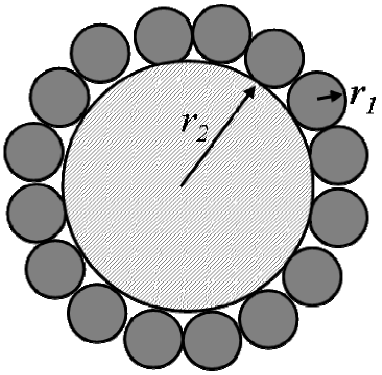

$$\frac{w_2}{w_1} = \frac{\rho_2 r_2^3}{\pi \rho_1 (r_1 + r_2)^2 r_1}$$

1: silica; 2: titania

Assume $r_1 << r_2$

$$\frac{w_2}{w_1} = \frac{\rho_2 r_2}{\pi \rho_1 r_1}$$

Figure 153. Illustration of the calculation of TiO_2/SiO_2 particle weight ratio.

In order to achieve better adhesion between the coating and the substrate, better self-cleaning, and also incorporate more functionality into the surface coating, the second species was added. Our studies mainly focused on TiO_2 formation by sol-gel processing to form bimodal TiO2 /SiO_2 particles.

Spherical TiO_2 particles were first prepared by controlled hydrolysis of titianium tetraisopropoxide in ethanol. An ethanol volume of 100 mL was mixed with 0.4-0.6 mL of aqueous salt (NaCl) followed by addition of 2.0 ml of titanium tetraisopropoxide at ambient temperature under an inert gas atmosphere, by using a magnetic stirrer. Reagents had to be mixed completely so that nucleation would occur uniformly throughout the solution. Depending on the concentration, visible particle formation started after several seconds or minutes and gave a uniform suspension of TiO_2 beads. After 5 hours the reactions were completed and the spheres were collected on a Millipore filter and washed with ethanol.

After the synthesis reaction of TiO_2 particles had proceeded for 30 min, silica sphere/ethanol dispersion (~5%wt, 10-50 ml) was added to the reaction media for another 4.5 hrs. The particles SiO_2 (shell)/TiO_2(core) formed are shown in the figure 154.

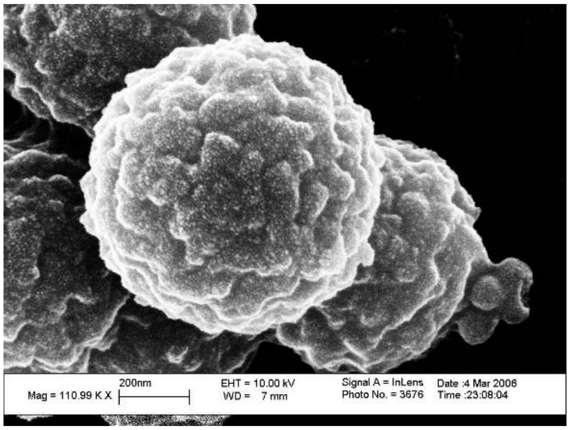

Figure 154. Particles of TiO_2 with SiO_2 particles coated on top, Titania / Silica – Large / Small, CA: 169˚.

8.3 Superhydrophobic surfaces from SiO_2/TiO_2 coatings

When using these bimodal particles to coat the surface of silicone parts from a number of manufacturers, the surfaces achieved superhydrophobicity without any further surface treatment (termed autophobicity). After the silica particles were dipcoated or painted onto the silicone surface, the surface changed over time from a hydrophilic to a hydrophobic and finally to a superhydrophobic surface as shown in Figure 155. It is most probable that diffusion of the mobile and hydrophobic species, e.g., silicone oils or other species accounts for this effect. The particles used are SiO_2 and TiO_2 with TiO_2 particle size ~800 nm and SiO_2 ~150 nm.

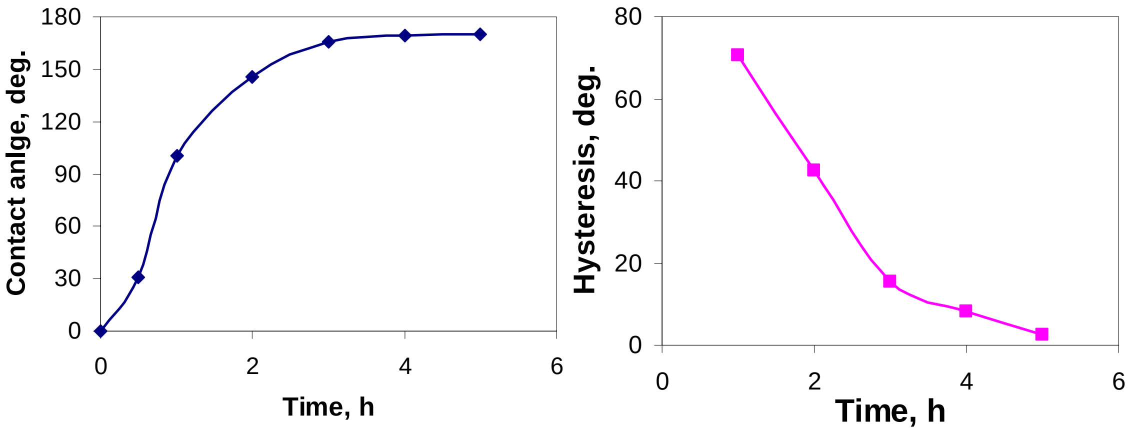

Figure 155. After Coating Process. The autophobicity (improvement in hydrophobicity with resting time) of silicone surfaces (the effect applies to all silicone surfaces). Note that the contact angle of the silicone material is 120˚ before treatment.

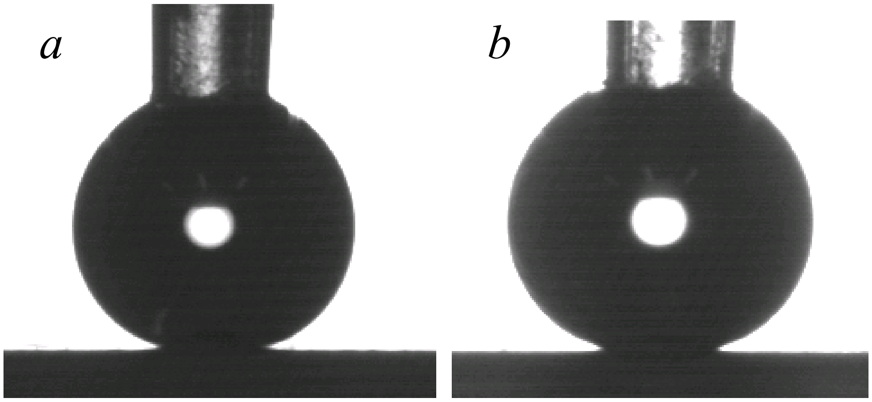

Figure 156. Particle coating (SiO_2/TiO_2) to improve the hydrophobicity of the silicone surface: figure (a) Contact angle: 167.8˚, hysteresis 6.7˚; (b) after surface treatment with PFOS, contact angle: 176˚, hysteresis< 1˚.

When the superhydrophobic silicone surface was further treated with PFOS, the contact angle increased to 176˚ as shown in Figure 156. The superhydrophobicity was improved: Contact angle: 176˚, hysteresis <1˚. The surface morphology from SEM was shown in Figure 157. Two scale roughness with micrometer sized TiO_2 and nanosized SiO_2 was formed.

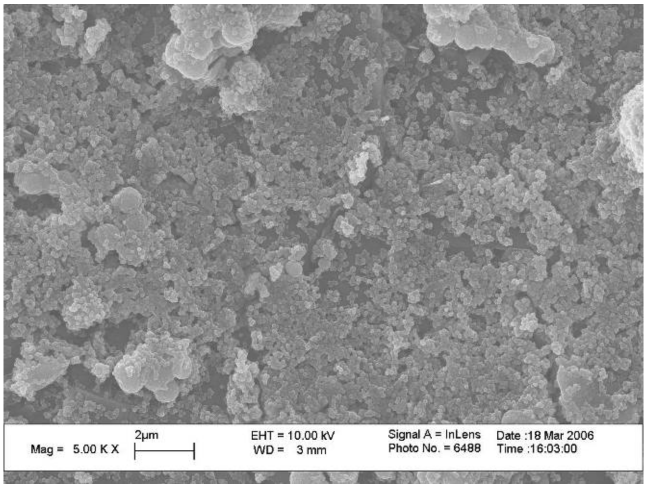

Figure 157. SEM image of the silicone plaque surface coated with the SiO_2/TiO_2 particles.

Figure 158 shows the water droplet contact angle and hysteresis on different insulator materials. For all the materials with hydrophobic mobile species, superhydrophobicity can be achieved.

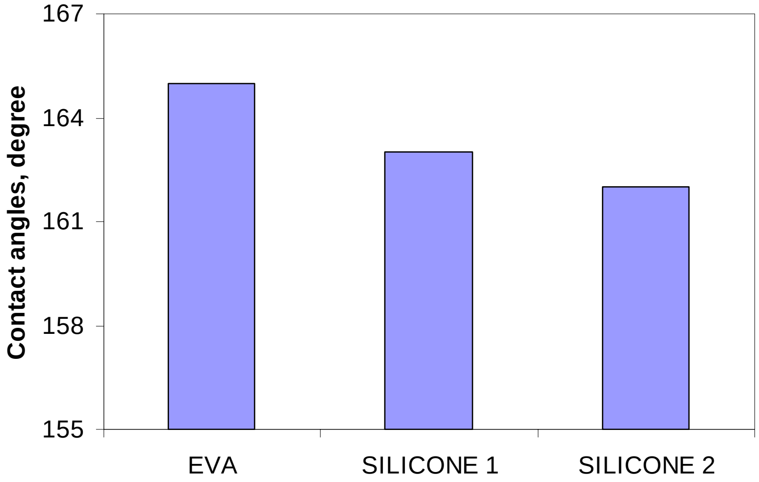

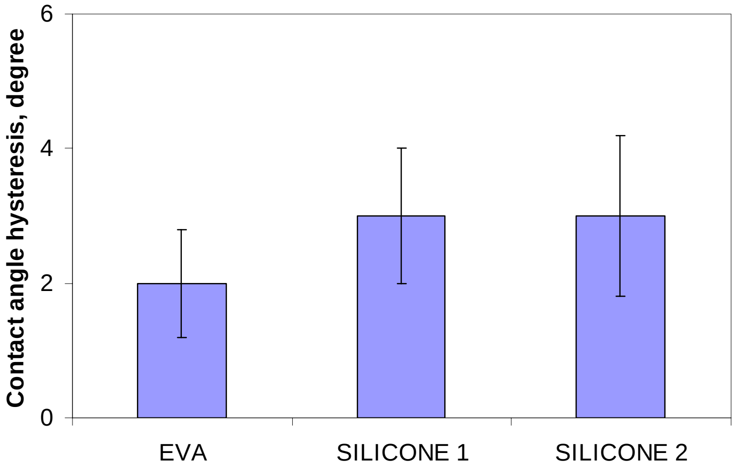

Figure 158. Contact angle and hysteresis on different surfaces coated with SiO_2/TiO_2 particles; Silicone 1 and 2 are two silicone materials from different companies, 1: Hubble, 2: Korean company.

The self-healing capability was tested on silicone surfaces by measuring the contact angle and hysteresis change upon ageing in a UV/humidity chamber for ~5500 hours; Figure 159 shows the results of contact angle and hysteresis changes with time. From the contact angle, no significant difference was observed. However, the hysteresis immediately after UV aging shows a significant difference between the exposed and unexposed regions. With increased rest time, the difference is reduced.

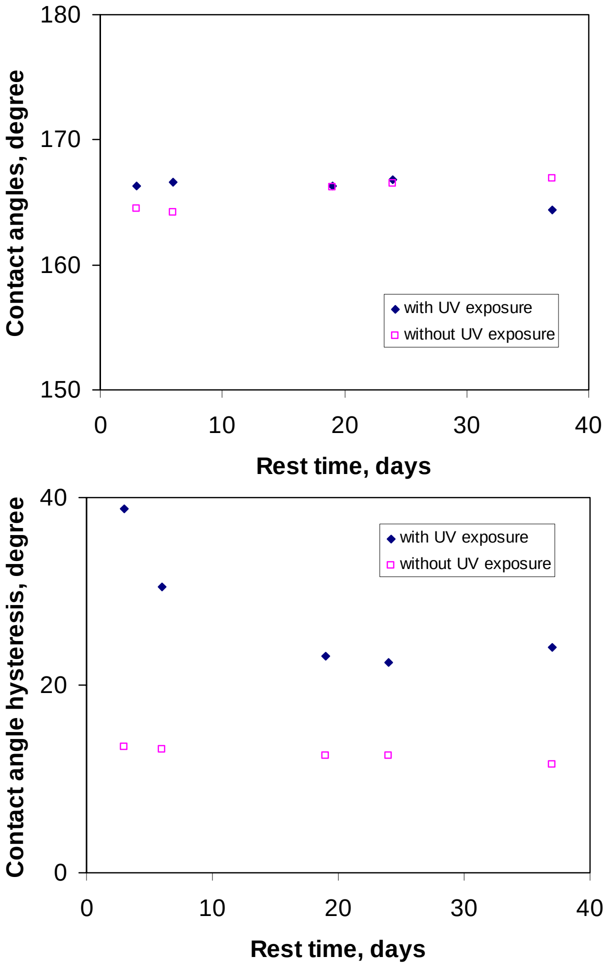

Figure 159. Self-healing effect of superhydrophobic surfaces after UV test for 5497 hours.

Figure 160. Field test of superhydrophobic coated insulators.

CHAPTER 9

FUTURE WORK

While superhydrophobic surfaces have been achieved on a variety of material surfaces with UV stability, robustness and more functionalities, considerable work remains regarding the geometry control of surface micro/nano structures for superoleophobicity, mechanical durability and incorporate more functionalities to the surface by appropriate surface treatment. In this chapter, some future work is given based mainly on geometry control of micro/nano structures.

Superoleophobicity. Regarding superoleophobic surfaces, more efforts should be focused on the surface micro and nano structure control to achieve a re-entrant structure or overhang structure to achieve nonwetting by manipulation of micro/nano structures.

Si (111) surface can be etched to form reentrant or overhang structures. We performed the Si (111) etching in $Fe(NO_3)_3$/HF by metal assisted etching technique. The etching proceeds at room temperature for 3 hours. The surface morphology and the cross-section view of the structure were shown in Figure 161 and 162 respectively.

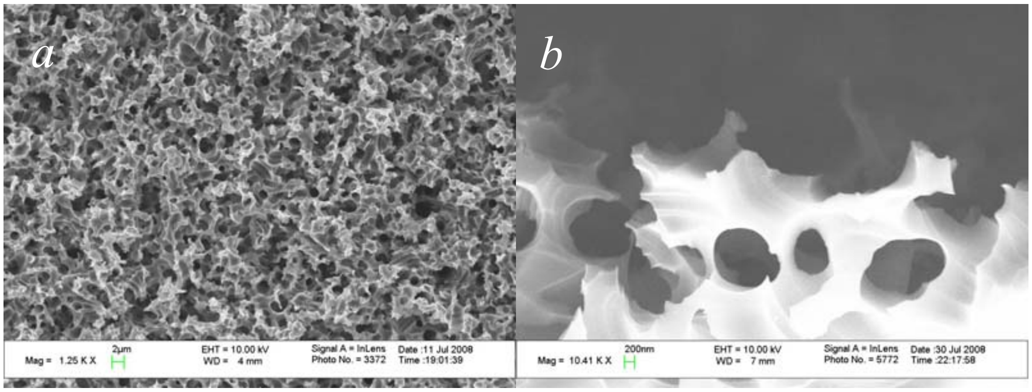

Figure 161. The surface morphology and cross-section of the etched Si (111) surfaces; a) top view, b) cross-section view of the top surfaces.

After the surface treatment with PFOS, the surface can be superhydrophobic. Surface contact angles with different liquid droplet were shown in Figure 2. One most significant observation on this surface is that the surface showed superoleophobicity. For regular superhydrophobic surfaces, the ethylene glycol showed a contact angle of < 30˚. However, on this Si surface, the ethylene glycol contact angle can go to ~160˚. When the surface tension of liquids decreased, the superhydrophobic contact angle on the rough surface also decreased and the hysteresis increased significantly when the surface tension decrease. For ethylene glycol which shows a surface tension of 47.7 mN/m, the contact angle is still high enough for a superhydrophobic surface although the contact angle hysteresis is large.

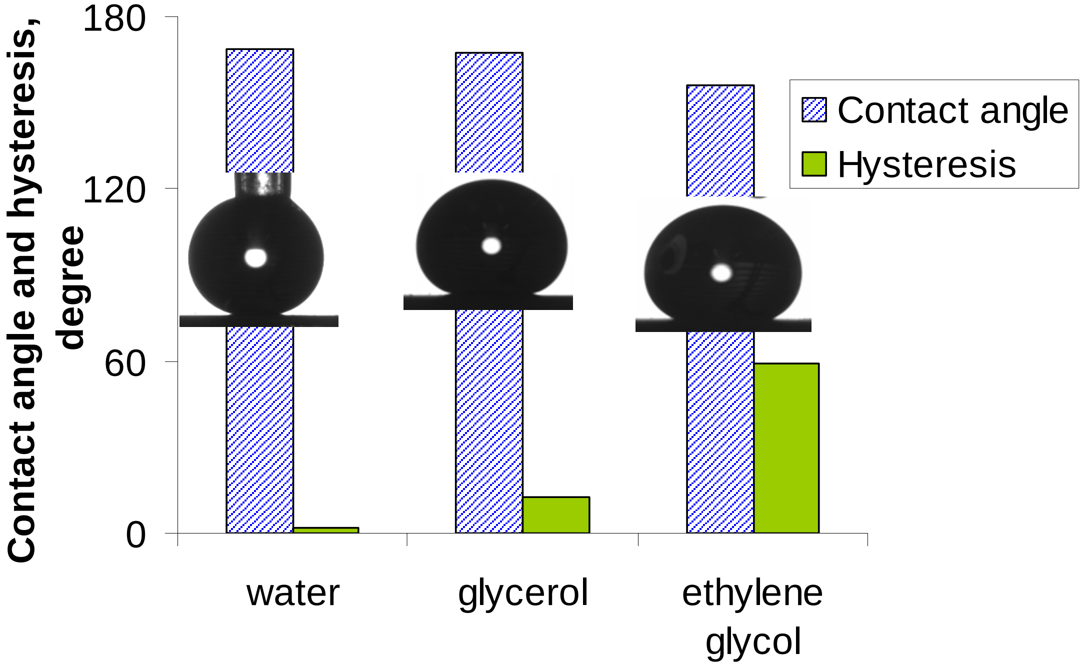

Figure 162. Contact angles of different liquids on etched Si surfaces treated by PFOS.

Table 23. Surface tensions for common liquids.

Common liquid	Surface tension, mN m^{-1} (or mJ/m^2)
Water (20˚C)	72.8
Glycerol	63.4
Ethylene glycol	47.7

Mechanical robustness. Although we have shown that robustness can be improved by appropriate hierarchical structure design on Si surfaces or using epoxy/silica nanoparticles, further investigation on using abrasive materials, such as Al_2O_3, SiC, diamond like carbon, is necessary to make a structured surface with excellent mechanical durability. Special processing approaches should be developed because of the difficulties in processing these materials. In addition, cost effective technology is another important factor in the application of superhydrophobic surfaces.

Self recovery superhydrophobic surfaces. Self-recovering surfaces are quite common on lotus leaves for both surface structures and hydrophobic species. For artificial surfaces, self recovery of structures requires is more technically demanding. However, self recovery of hydrophobic species is demonstrated achievable. Further work should be focusing on the selection of hydrophobic species which showed both a low surface energy and improved bonding on substrate surfaces, low volatility and UV and chemical stability. Functionalized polydimethyl siloxanes and fluorinated molecules are preferred for this purpose.

Self-cleaning photovoltaics. Energy is the toughest issue our society will face in the near future. Alternative clean energy solutions to oil must be brought up and applied not only for energy demand, but also for environmental protection. Photovoltaics are attracting more and more attention in this regard. Self-cleaning photovoltaic surfaces with micro/nano structures show great potential in dust cleaning, reduction in frost formation, water repellency, and added functionalities such as reduced light reflection. One drawback is the increased surface area of the semiconductor surfaces which may increase the surface recombination of electron/holes, which is a big issue in photovoltaic efficiency. Some potential methods to passivate Si surfaces are discussed below.

1) Silane solution treatment[244].

Surface treatment with silanes to form self assembled monolayer (SAM), as shown in Figure 163, to reduce the surface energy, was proposed. On the passivated surface, Si-O-C bonds are formed. In the preliminary experiments, the PI found that this monolayer (1-2 nm in thickness, dependent on the hydrophobic side chain length) can dramatically change the SiO_2/silicon surface from hydrophilic (contact angle 5-10°) to hydrophobic (contact angle 115-120°). From the point view of superhydrophobicity, the lower the surface energy is, the better self-cleaning surface can be achieved. In addition, the well-formed SAM layers will passivate the surface defects which are disadvantageous for the lifetime of free carriers (electrons/holes) in silicon semiconductor that are generated by absorbed photons. The SAM types and processing conditions require systematic exploration to fabricate well passivated and self-cleaning surfaces with reduced surface recombination rate.

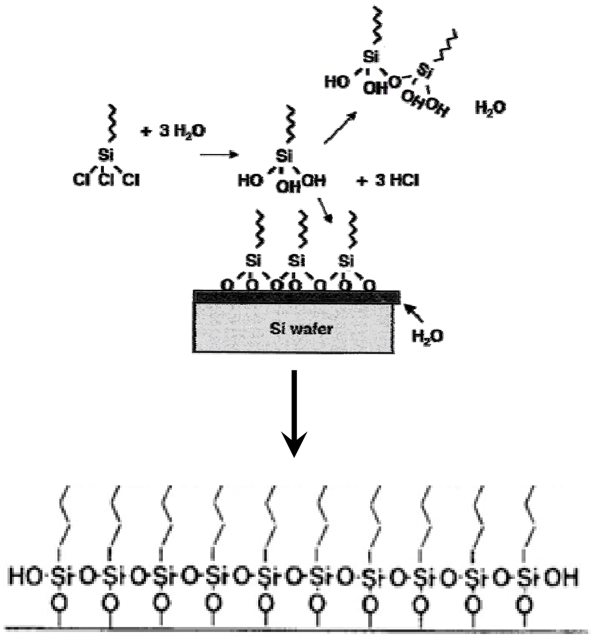

Figure 163. Silane SAM formation on silicon wafer surface.

2) HMDS vapor phase treatment[245, 246].

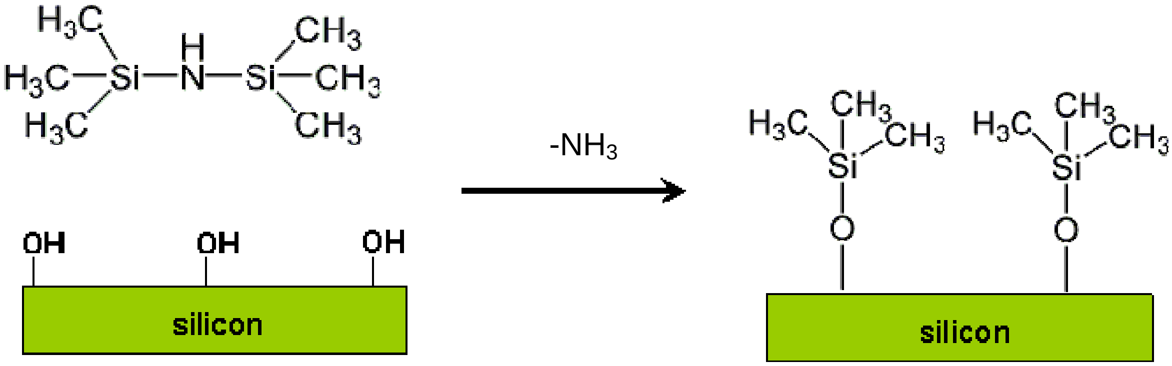

Figure 164. Illustration of the surface passivation using hexamethydisilazane (HMDS).

This surface treatment method can be conducted in HMDS vapor phase to eliminate the surface defects of SiOH groups for improved surface property while achieving hydrophobic surface through trimethyl groups as shown in Figure 164.

3) Grignard reagent solution treatment[247]. Due to the Si-C bonding, the surface electron states can be maintained. This surface treatment method leads to the production of defined organic overlayers on Si surfaces. These surface reactions have been shown to produce improved resistance to surface oxidation, while maintaining excellent electrochemical and electrical properties. In fact, the surface recombination velocity of the methylated Si surface has recently been determined to be less than 20 cm/second, which is comparable to high quality hydrogen-terminated Si surfaces but which is stable in contact with atmospheric ambient[248, 249]. This method may help to find an efficient and cost-effective way to passivate the Si surface.

4) Surface grafting of silicone[250]. (nano-patterning and doping) Picture illustration as shown in Figure 165.

Methods 1 and 2 generate surface Si-O-Si bonding at the interface. The stability of such interface should be investigated especially under direct sunlight irradiation. Methods of 3 and 4 are targeting at formation of direct Si-C bonding which is expected for improved electrical performance of devices. With the development of new surface processing techniques, new methods can also be tried with continuous literature survey. The effect can be compared with regard to the surface recombination velocity and minority carriers lifetime.

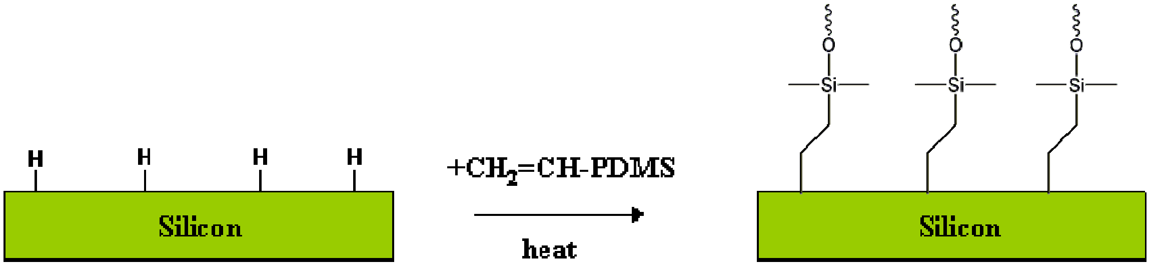

Figure 165. Illustration of the surface passivation with PDMS.

REFERENCES

[1] T. WAGNER, C. NEINHUIS, and W. BARTHLOTT, "Wettability and contaminability of insect wings as a function of their surface sculptures," *Acta Zoologica*, vol. 77, pp. 213-225, 1996.

[2] C. NEINHUIS and W. BARTHLOTT, "Characterization and distribution of water-repellent, self-cleaning plant surfaces," *Ann. Bot.*, vol. 79, pp. 667-677, 1997.

[3] E. SACHER, J. K. SAPIEHA, H. P. SCHRIEBER, N. R. WERTHEIMER, and N. S. MCINTYRE, in *Silanes, Surfaces, and Interfaces*, vol. I. London, 1986, pp. 189-202.

[4] M. MORRA, E. OCCHIELLO, and F. GARBASSI, "Contact-Angle Hysteresis in Oxygen Plasma Treated Poly(Tetrafluoroethylene)," *Langmuir*, vol. 5, pp. 872-876, 1989.

[5] S. SHIBUICHI, T. YAMAMOTO, T. ONDA, and K. TSUJII, "Super water- and oil-repellent surfaces resulting from fractal structure," *J. Colloid Interface Sci.*, vol. 208, pp. 287-294, 1998.

[6] M. NOSONOVSKY and B. BHUSHAN, "Biologically inspired surfaces: Broadening the scope of roughness," *Adv. Funct. Mater.*, vol. 18, pp. 843-855, 2008.

[7] T. L. SUN, L. FENG, X. F. GAO, and L. JIANG, "Bioinspired surfaces with special wettability," *Acc. Chem. Res.*, vol. 38, pp. 644-652, 2005.

[8] X. F. GAO and L. JIANG, "Bio Physics: Water-repellent legs of water striders," *Nature*, vol. 432, pp. 36-36, 2004.

[9] X. F. GAO, X. YAN, X. YAO, L. XU, K. ZHANG, J. H. ZHANG, B. YANG, and L. JIANG, "The dry-style antifogging properties of mosquito compound eyes and artificial analogues prepared by soft lithography," *Adv. Mater.*, vol. 19, pp. 2213-2217, 2007.

[10] S. BERTHIER, *Iridescences : the physical colors of insects*. New York: Springer, 2007.

[11] A. B. D. CASSIE and S. BAXTER, "Wettability of Porous Surfaces," *Trans. Faraday Soc.*, vol. 40, pp. 546-551, 1944.

[12] R. N. WENZEL, "Resistance of Solid Surfaces to Wetting by Water," *Industrial & Engineering Chemistry*, vol. 28, pp. 988-994, 1936.

[13] A. MARMUR, "Wetting on hydrophobic rough surfaces: To be heterogeneous or not to be?," *Langmuir*, vol. 19, pp. 8343-8348, 2003.

[14] Y. XIU, L. ZHU, D. W. HESS, and C. P. WONG, "Biomimetic creation of hierarchical surface structures by combining colloidal self-assembly and Au sputter deposition," *Langmuir*, vol. 22, pp. 9676-9681, 2006.

[15] N. A. PATANKAR, "Transition between superhydrophobic states on rough surfaces," *Langmuir*, vol. 20, pp. 7097-7102, 2004.

[16] N. A. PATANKAR, "On the modeling of hydrophobic contact angles on rough surfaces," *Langmuir*, vol. 19, pp. 1249-1253, 2003.

[17] G. MCHALE, N. J. SHIRTCLIFFE, and M. I. NEWTON, "Contact-angle hysteresis on super-hydrophobic surfaces," *Langmuir*, vol. 20, pp. 10146-10149, 2004.

[18] X. Y. LU, J. L. ZHANG, C. C. ZHANG, and Y. C. HAN, "Low-density polyethylene (LDPE) surface with a wettability gradient by tuning its microstructures," *Macromol. Rapid Comm.*, vol. 26, pp. 637-642, 2005.

[19] W. HAN, D. WU, W. H. MING, H. NIEMANTSVERDRIET, and P. C. THUNE, "Direct catalytic route to superhydrophobic polyethylene films," *Langmuir*, vol. 22, pp. 7956-7959, 2006.

[20] K. TESHIMA, H. SUGIMURA, Y. INOUE, O. TAKAI, and A. TAKANO, "Ultra-water-repellent poly(ethylene terephthalate) substrates," *Langmuir*, vol. 19, pp. 10624-10627, 2003.

[21] K. TADANAGA, J. MORINAGA, A. MATSUDA, and T. MINAMI, "Superhydrophobic-superhydrophilic micropatterning on flowerlike alumina coating film by the sol-gel method," *Chem. Mater.*, vol. 12, pp. 590-+, 2000.

[22] A. NAKAJIMA, A. FUJISHIMA, K. HASHIMOTO, and T. WATANABE, "Preparation of transparent superhydrophobic boehmite and silica films by sublimation of aluminum acetylacetonate," *Adv. Mater.*, vol. 11, pp. 1365-1368, 1999.

[23] J. ISRAELACHVILI, *Intermolecular and surface forces*, 2nd ed: Academic Press, 1991.

[24] T. NISHINO, M. MEGURO, K. NAKAMAE, M. MATSUSHITA, and Y. UEDA, "The lowest surface free energy based on -CF3 alignment," *Langmuir*, vol. 15, pp. 4321-4323, 1999.

[25] A. TUTEJA, W. CHOI, M. MA, J. M. MABRY, S. A. MAZZELLA, G. C. RUTLEDGE, G. H. MCKINLEY, and R. E. COHEN, "Designing Superoleophobic Surfaces," *Science*, vol. 318, pp. 1618-1622, 2007.

[26] A. AHUJA, J. A. TAYLOR, V. LIFTON, A. A. SIDORENKO, T. R. SALAMON, E. J. LOBATON, P. KOLODNER, and T. N. KRUPENKIN, "Nanonails: A simple geometrical approach to electrically tunable superlyophobic surfaces," *Langmuir*, vol. 24, pp. 9-14, 2008.

[27] L. L. CAO, T. P. PRICE, M. WEISS, and D. GAO, "Super water- and oil-repellent surfaces on intrinsically hydrophilic and oleophilic porous silicon films," *Langmuir*, vol. 24, pp. 1640-1643, 2008.

[28] L. L. CAO, H. H. HU, and D. GAO, "Design and fabrication of micro-textures for inducing a superhydrophobic behavior on hydrophilic materials," *Langmuir*, vol. 23, pp. 4310-4314, 2007.

[29] D. ONER and T. J. MCCARTHY, "Ultrahydrophobic surfaces. Effects of topography length scales on wettability," *Langmuir*, vol. 16, pp. 7777-7782, 2000.

[30] C. H. CHOI and C. J. KIM, "Fabrication of a dense array of tall nanostructures over a large sample area with sidewall profile and tip sharpness control," *Nanotechnology*, vol. 17, pp. 5326-5333, 2006.

[31] N. J. SHIRTCLIFFE, S. AQIL, C. EVANS, G. MCHALE, M. I. NEWTON, C. C. PERRY, and P. ROACH, "The use of high aspect ratio photoresist (SU-8) for super-hydrophobic pattern prototyping," *Journal of Micromechanics and Microengineering*, vol. 14, pp. 1384-1389, 2004.

[32] J. BICO, C. MARZOLIN, and D. QUERE, "Pearl drops," *Europhys. Lett.*, vol. 47, pp. 220-226, 1999.

[33] M. A. LIEBERMAN and A. J. LICHTENBERG, *Principles of plasma discharges and materials processing*, 2nd Translator: Lichtenberg, Allan J. ISBN: 0471720011 (hardcover) Reprint Edition: 2nd Accession Number: (OCoLC)ocm56752658 ed: Wiley-Interscience, 2005.

[34] V. STELMASHUK, H. BIEDERMAN, D. SLAVINSKA, J. ZEMEK, and M. TRCHOVA, "Plasma polymer films rf sputtered from PTFE under various argon pressures," *Vacuum*, vol. 77, pp. 131-137, 2005.

[35] J.-Y. SHIU, C.-W. KUO, and P. CHEN, "Fabrication of tunable superhydrophobic surfaces," *Proceedings of SPIE-The International Society for Optical Engineering*, vol. 5648, pp. 325-332, 2005.

[36] D. BYUN, Y. LEE, S. B. Q. TRAN, V. D. NUGYEN, S. KIM, B. PARK, S. LEE, N. INAMDAR, and H. H. BAU, "Electrospray on superhydrophobic nozzles treated with argon and oxygen plasma," *Appl. Phys. Lett.*, vol. 92, pp. -, 2008.

[37] M. LEJEUNE, M. LACROIX LISE, F. BRETAGNOL, A. VALSESIA, P. COLPO, and F. ROSSI, "Plasma-based processes for surface wettability modification," *Langmuir*, vol. 22, pp. 3057-61, 2006.

[38] M. LEJEUNE, L. M. LACROIX, F. BRETAGNOL, A. VALSESIA, P. COLPO, and F. ROSSI, "Plasma-based processes for surface wettability modification," *Langmuir*, vol. 22, pp. 3057-3061, 2006.

[39] A. D. TSEREPI, M. E. VLACHOPOULOU, and E. GOGOLIDES, "Nanotexturing of poly(dimethylsiloxane) in plasmas for creating robust super-hydrophobic surfaces," *Nanotechnology*, vol. 17, pp. 3977-3983, 2006.

[40] K. TESHIMA, H. SUGIMURA, Y. INOUE, O. TAKAI, and A. TAKANO, "Wettability of poly(ethylene terephthalate) substrates modified by a two-step plasma process: Ultra water-repellent surface fabrication," *Chem Vapor Depos*, vol. 10, pp. 295-+, 2004.

[41] K. TESHIMA, H. SUGIMURA, Y. INOUE, O. TAKAI, and A. TAKANO, "Transparent ultra water-repellent poly(ethylene terephthalate) substrates

fabricated by oxygen plasma treatment and subsequent hydrophobic coating," *Appl. Surf. Sci.*, vol. 244, pp. 619-622, 2005.

[42] K. TESHIMA, H. SUGIMURA, A. TAKANO, Y. INOUE, and O. TAKAI, "Ultrahydrophobic/ultrahydrophilic micropatterning on a polymeric substrate," *Chemical Vapor Deposition*, vol. 11, pp. 347-349, 2005.

[43] J. FRESNAIS, J. P. CHAPEL, and F. PONCIN-EPAILLARD, "Synthesis of transparent superhydrophobic polyethylene surfaces," *Surf. Coat. Technol.*, vol. 200, pp. 5296-5305, 2006.

[44] J. FRESNAIS, L. BENYAHIA, and F. PONCIN-EPAILLARD, "Dynamic (de)wetting properties of superhydrophobic plasma-treated polyethylene surfaces," *Surf Interface Anal*, vol. 38, pp. 144-149, 2006.

[45] J. FRESNAIS, L. BENYAHIA, J. P. CHAPEL, and F. PONCIN-EPAILLARD, "Polyethylene ultrahydrophobic surface: synthesis and original properties," *European Physical Journal: Applied Physics*, vol. 26, pp. 209-214, 2004.

[46] R. DI MUNDO, F. PALUMBO, and R. D'AGOSTINO, "Nanotexturing of polystyrene surface in fluorocarbon plasmas: From sticky to slippery superhydrophobicity," *Langmuir*, vol. 24, pp. 5044-5051, 2008.

[47] I. WOODWARD, W. C. E. SCHOFIELD, V. ROUCOULES, and J. P. S. BADYAL, "Super-hydrophobic surfaces produced by plasma fluorination of polybutadiene films," *Langmuir*, vol. 19, pp. 3432-3438, 2003.

[48] C. DORRER and J. RUHE, "Wetting of silicon nanograss: From superhydrophilic to superhydrophobic surfaces," *Adv. Mater.*, vol. 20, pp. 159-+, 2008.

[49] S. KOYNOV, M. S. BRANDT, and M. STUTZMANN, "Black nonreflecting silicon surfaces for solar cells," *Appl Phys Lett*, vol. 88, pp. 203107/1-203107/3, 2006.

[50] K. Q. PENG, Y. WU, H. FANG, X. Y. ZHONG, Y. XU, and J. ZHU, "Uniform, axial-orientation alignment of one-dimensional single-crystal silicon nanostructure arrays," *Angew Chem Int Edit*, vol. 44, pp. 2737-2742, 2005.

[51] K. Q. PENG, Y. J. YAN, S. P. GAO, and J. ZHU, "Dendrite-assisted growth of silicon nanowires in electroless metal deposition," *Adv Funct Mater*, vol. 13, pp. 127-132, 2003.

[52] B. T. QIAN and Z. Q. SHEN, "Fabrication of superhydrophobic surfaces by dislocation-selective chemical etching on aluminum, copper, and zinc substrates," *Langmuir*, vol. 21, pp. 9007-9009, 2005.

[53] Z. G. GUO, F. ZHOU, J. C. HAO, and W. M. LIU, "Effects of system parameters on making aluminum alloy lotus," *J. Colloid Interface Sci.*, vol. 303, pp. 298-305, 2006.

[54] N. J. SHIRTCLIFFE, G. MCHALE, M. I. NEWTON, and C. C. PERRY, "Wetting and wetting transitions on copper-based super-hydrophobic surfaces," *Langmuir*, vol. 21, pp. 937-943, 2005.

[55] F. RUPP, L. SCHEIDELER, N. OLSHANSKA, M. DE WILD, M. WIELAND, and J. GEIS-GERSTORFER, "Enhancing surface free energy and hydrophilicity through chemical modification of microstructured titanium implant surfaces," *Journal of Biomedical Materials Research Part A*, vol. 76A, pp. 323-334, 2006.

[56] Y. K. LAI, C. J. LIN, J. Y. HUANG, H. F. ZHUANG, L. SUN, and T. NGUYEN, "Markedly controllable adhesion of superhydrophobic spongelike nanostructure TiO2 films," *Langmuir*, vol. 24, pp. 3867-3873, 2008.

[57] H. KIM SEONG, J.-H. KIM, B.-K. KANG, and S. UHM HAN, "Superhydrophobic CFx coating via in-line atmospheric RF plasma of He-CF4-H2," *Langmuir*, vol. 21, pp. 12213-7, 2005.

[58] G. R. J. ARTUS, S. JUNG, J. ZIMMERMANN, H. P. GAUTSCHI, K. MARQUARDT, and S. SEEGER, "Silicone nanofilaments and their application as superhydrophobic coating," *Adv. Mater.*, vol. 18, pp. 2758-2762, 2006.

[59] J. ZIMMERMANN, M. RABE, G. R. J. ARTUS, and S. SEEGER, "Patterned superfunctional surfaces based on a silicone nanofilament coating," *Soft Matter*, vol. 4, pp. 450-452, 2008.

[60] L. ZHU, Y. XIU, J. XU, P. A. TAMIRISA, D. W. HESS, and C.-P. WONG, "Superhydrophobicity on Two-Tier Rough Surfaces Fabricated by Controlled

Growth of Aligned Carbon Nanotube Arrays Coated with Fluorocarbon," *Langmuir*, vol. 21, pp. 11208-11212, 2005.

[61] K. K. S. LAU, J. BICO, K. B. K. TEO, M. CHHOWALLA, G. A. J. AMARATUNGA, W. I. MILNE, G. H. MCKINLEY, and K. K. GLEASON, "Superhydrophobic carbon nanotube forests," *Nano Lett.*, vol. 3, pp. 1701-1705, 2003.

[62] A. ROIG, E. MOLINS, E. RODRIGUEZ, S. MARTINEZ, M. MORENO-MANAS, and A. VALLRIBERA, "Superhydrophobic silica aerogels by fluorination at the gel stage," *Chem. Comm.*, pp. 2316-2317, 2004.

[63] K. TADANAGA, N. KATATA, and T. MINAMI, "Formation process of super-water-repellent Al2O3 coating films with high transparency by the sol-gel method," *J. Am. Ceram. Soc.*, vol. 80, pp. 3213-3216, 1997.

[64] D. A. DOSHI, P. B. SHAH, S. SINGH, E. D. BRANSON, A. P. MALANOSKI, E. B. WATKINS, J. MAJEWSKI, F. VAN SWOL, and C. J. BRINKER, "Investigating the interface of superhydrophobic surfaces in contact with water," *Langmuir*, vol. 21, pp. 7805-7811, 2005.

[65] A. V. RAO, S. D. BHAGAT, H. HIRASHIMA, and G. M. PAJONK, "Synthesis of flexible silica aerogels using methyltrimethoxysilane (MTMS) precursor," *J. Colloid Interface Sci.*, vol. 300, pp. 279-285, 2006.

[66] N. J. SHIRTCLIFFE, G. MCHALE, M. I. NEWTON, and C. C. PERRY, "Intrinsically superhydrophobic organosilica sol-gel foams," *Langmuir*, vol. 19, pp. 5626-5631, 2003.

[67] H. WANG, J. FANG, T. CHENG, J. DING, L. QU, L. DAI, X. WANG, and T. LIN, "One-step coating of fluoro-containing silica nanoparticles for universal generation of surface superhydrophobicity," *Chem. Comm.*, pp. 877-879, 2008.

[68] L. C. GAO and T. J. MCCARTHY, "A perfectly hydrophobic surface (theta(A)/theta(R)=180 degrees/180 degrees)," *J. Am. Chem. Soc.*, vol. 128, pp. 9052-9053, 2006.

[69] H. ZHENG, H. OKADA, S. NOJIMA, S. SUYE, and T. HORI, "Layer-by-layer assembly of enzymes and polymerized mediator on electrode surface by

electrostatic adsorption," *Science and Technology of Advanced Materials*, vol. 5, pp. 371-376, 2004.

[70] J. JI, J. H. FU, and J. C. SHEN, "Fabrication of a superhydrophobic surface from the amplified exponential growth of a multilayer," *Adv. Mater.*, vol. 18, pp. 1441-1444, 2006.

[71] L. ZHAI, F. C. CEBECI, R. E. COHEN, and M. F. RUBNER, "Stable superhydrophobic coatings from polyelectrolyte multilayers," *Nano Lett.*, vol. 4, pp. 1349-1353, 2004.

[72] J. Y. SHIU, C. W. KUO, P. L. CHEN, and C. Y. MOU, "Fabrication of tunable superhydrophobic surfaces by nanosphere lithography," *Chem. Mater.*, vol. 16, pp. 561-564, 2004.

[73] M. L. MA, R. M. HILL, J. L. LOWERY, S. V. FRIDRIKH, and G. C. RUTLEDGE, "Electrospun poly(styrene-block-dimethylsiloxane) block copolymer fibers exhibiting superhydrophobicity," *Langmuir*, vol. 21, pp. 5549-5554, 2005.

[74] M. L. MA, M. GUPTA, Z. LI, L. ZHAI, K. K. GLEASON, R. E. COHEN, M. F. RUBNER, and G. C. RUTLEDGE, "Decorated electrospun fibers exhibiting superhydrophobicity," *Adv. Mater.*, vol. 19, pp. 255-259, 2007.

[75] Y. ZHU, J. C. ZHANG, Y. M. ZHENG, Z. B. HUANG, L. FENG, and L. JIANG, "Stable, superhydrophobic, and conductive polyaniline/polystyrene films for corrosive enviromnents," *Adv. Funct. Mater.*, vol. 16, pp. 568-574, 2006.

[76] Y. LI and G. SHI, "Electrochemical Growth of Two-Dimensional Gold Nanostructures on a Thin Polypyrrole Film Modified ITO Electrode," *J. Phys. Chem. B*, vol. 109, pp. 23787-23793, 2005.

[77] M. LI, J. ZHAI, H. LIU, Y. L. SONG, L. JIANG, and D. B. ZHU, "Electrochemical deposition of conductive superhydrophobic zinc oxide thin films," *J. Phys. Chem. B*, vol. 107, pp. 9954-9957, 2003.

[78] L. WANG, S. J. GUO, and S. J. DONG, "Facile electrochemical route to directly fabricate hierarchical spherical cupreous micro structures: Toward superhydrophobic surface," *Electrochemistry Communications*, vol. 10, pp. 655-658, 2008.

[79] L. B. XU, Z. W. CHEN, W. CHEN, A. MULCHANDANI, and Y. S. YAN, "Electrochemical synthesis of perfluorinated ion doped conducting polyaniline films consisting of helical fibers and their reversible switching between superhydrophobicity and superhydrophilicity," *Macromol. Rapid Comm.*, vol. 29, pp. 832-838, 2008.

[80] W. LEE, M. K. JIN, W. C. YOO, and J. K. LEE, "Nanostructuring of a polymeric substrate with well-defined nanometer-scale topography and tailored surface wettability," *Langmuir*, vol. 20, pp. 7665-7669, 2004.

[81] B. LIU, Y. N. HE, Y. FAN, and X. G. WANG, "Fabricating super-hydrophobic lotus-leaf-like surfaces through soft-lithographic imprinting," *Macromol. Rapid Comm.*, vol. 27, pp. 1859-1864, 2006.

[82] H. YABU and M. SHIMOMURA, "Single-step fabrication of transparent superhydrophobic porous polymer films," *Chem. Mater.*, vol. 17, pp. 5231-5234, 2005.

[83] F. SHI, Z. Q. WANG, and X. ZHANG, "Combining a layer-by-layer assembling technique with electrochemical deposition of gold aggregates to mimic the legs of water striders," *Adv. Mater.*, vol. 17, pp. 1005-+, 2005.

[84] T. ONDA, S. SHIBUICHI, N. SATOH, and K. TSUJII, "Super-Water-Repellent Fractal Surfaces," *Langmuir*, vol. 12, pp. 2125-7, 1996.

[85] L. FENG, Z. Y. ZHANG, Z. H. MAI, Y. M. MA, B. Q. LIU, L. JIANG, and D. B. ZHU, "A super-hydrophobic and super-oleophilic coating mesh film for the separation of oil and water," *Angew. Chem Int. Ed.*, vol. 43, pp. 2012-2014, 2004.

[86] H. Y. UENG and C. Y. LIU, "The aluminum bond-pad corrosion in small outline packaged devices," *Materials Chemistry and Physics*, vol. 48, pp. 27-35, 1997.

[87] C. W. TAN, A. R. DAUD, and M. A. YARMO, "Corrosion study at Cu-Al interface in microelectronics packaging," *Applied Surface Science*, vol. 191, pp. 67-73, 2002.

[88] R. B. COMIZZOLI, R. P. FRANKENTHAL, K. J. HANSON, K. KONSTADINIDIS, R. L. OPILA, J. SAPJETA, J. D. SINCLAIR, K. M. TAKAHASHI, A. L. FRANK, and A. O. IBIDUNNI, "Electrochemical Aspects of Corrosion-Resistance and Etching of Metallizations for Microelectronics,"

Materials Science and Engineering a-Structural Materials Properties Microstructure and Processing, vol. 198, pp. 153-160, 1995.

[89] G. TRABANELLI, "Inhibitors - an Old Remedy for a New Challenge," *Corrosion*, vol. 47, pp. 410-419, 1991.

[90] C. H. MASTRANGELO and C. H. HSU, "Mechanical stability and adhesion of microstructures under capillary forces. I. Basic theory.," *J. Microelectromech. S.*, pp. 33-43, 1993.

[91] S. GOGTE, P. VOROBIEFF, R. TRUESDELL, A. MAMMOLI, F. VAN SWOL, P. SHAH, and C. J. BRINKER, "Effective slip on textured superhydrophobic surfaces," *Physics of Fluids*, vol. 17, pp. -, 2005.

[92] R. D. DEEGAN, O. BAKAJIN, T. F. DUPONT, G. HUBER, S. R. NAGEL, and T. A. WITTEN, "Capillary flow as the cause of ring stains from dried liquid drops," *Nature*, vol. 389, pp. 827-829, 1997.

[93] L. ZHAI, M. C. BERG, F. C. CEBECI, Y. KIM, J. M. MILWID, M. F. RUBNER, and R. E. COHEN, "Patterned superhydrophobic surfaces: Toward a synthetic mimic of the Namib Desert beetle," *Nano Lett.*, vol. 6, pp. 1213-1217, 2006.

[94] G. M. WHITESIDES and A. D. STROOCK, "Flexible methods for microfluidics," *Physics Today*, vol. 54, pp. 42-48, 2001.

[95] P. ROACH, N. J. SHIRTCLIFFE, and M. I. NEWTON, "Progess in superhydrophobic surface development," *Soft Matter*, vol. 4, pp. 224-240, 2008.

[96] M. DU, R. L. OPILA, V. M. DONNELLY, J. SAPJETA, and T. BOONE, "The interface formation of copper and low dielectric constant fluoro-polymer: Plasma surface modification and its effect on copper diffusion," *Journal of Applied Physics*, vol. 85, pp. 1496-1502, 1999.

[97] M. KIURU and E. ALAKOSKI, "Low sliding angles in hydrophobic and oleophobic coatings prepared with plasma discharge method," *Mater. Lett.*, vol. 58, pp. 2213-2216, 2004.

[98] X. T. ZHANG, M. JIN, Z. Y. LIU, S. NISHIMOTO, H. SAITO, T. MURAKAMI, and A. FUJISHIMA, "Preparation and photocatalytic wettability conversion of TiO2-based superhydrophobic surfaces," *Langmuir*, vol. 22, pp. 9477-9479, 2006.

[99] Y. Y. WU, H. SUGIMURA, Y. INOUE, and O. TAKAI, "Preparation of hard and ultra water-repellent silicon oxide films by microwave plasma-enhanced CVD at low substrate temperatures," *Thin Solid Films*, vol. 435, pp. 161-164, 2003.

[100] E. HOSONO, S. FUJIHARA, I. HONMA, and H. ZHOU, "Superhydrophobic Perpendicular Nanopin Film by the Bottom-Up Process," *J. Am. Chem. Soc.*, vol. 127, pp. 13458-13459, 2005.

[101] K. A. WIER and T. J. MCCARTHY, "Condensation on ultrahydrophobic surfaces and its effect on droplet mobility: Ultrahydrophobic surfaces are not always water repellant," *Langmuir*, vol. 22, pp. 2433-2436, 2006.

[102] R. M. JISR, H. H. RMAILE, and J. B. SCHLENOFF, "Hydrophobic and ultrahydrophobic multilayer thin films from perfluorinated polyelectrolytes," *Angew. Chem. Int. Ed.*, vol. 44, pp. 782-785, 2005.

[103] L. VOGELAAR, R. G. H. LAMMERTINK, and M. WESSLING, "Superhydrophobic surfaces having two-fold adjustable roughness prepared in a single step," *Langmuir*, vol. 22, pp. 3125-3130, 2006.

[104] G. ZHANG, D. WANG, Z.-Z. GU, and H. MOEHWALD, "Fabrication of Superhydrophobic Surfaces from Binary Colloidal Assembly," *Langmuir*, vol. 21, pp. 9143-9148, 2005.

[105] H. M. SHANG, Y. WANG, S. J. LIMMER, T. P. CHOU, K. TAKAHASHI, and G. Z. CAO, "Optically transparent superhydrophobic silica-based films," *Thin Solid Films*, vol. 472, pp. 37-43, 2005.

[106] Q. XIE, G. FAN, N. ZHAO, X. GUO, J. XU, J. DONG, L. ZHANG, Y. ZHANG, and C. C. HAN, "Facile creation of a bionic super-hydrophobic block copolymer surface," *Adv. Mater.*, vol. 16, pp. 1830-1833, 2004.

[107] L. JIANG, Y. ZHAO, and J. ZHAI, "A lotus-leaf-like superhydrophobic surface: A porous microsphere/nanofiber composite film prepared by electrohydrodynamics," *Angew. Chem Int. Ed.*, vol. 43, pp. 4338-4341, 2004.

[108] M. JIN, X. FENG, J. XI, J. ZHAI, K. CHO, L. FENG, and L. JIANG, "Super-hydrophobic PDMS surface with ultra-low adhesive force," *Macromol. Rapid Comm.*, vol. 26, pp. 1805-1809, 2005.

[109] N. TAKESHITA, L. A. PARADIS, D. OENER, T. J. MCCARTHY, and W. CHEN, "Simultaneous Tailoring of Surface Topography and Chemical Structure for Controlled Wettability," *Langmuir*, vol. 20, pp. 8131-8136, 2004.

[110] L. C. GAO and T. J. MCCARTHY, "The "lotus effect" explained: Two reasons why two length scales of topography are important," *Langmuir*, vol. 22, pp. 2966-2967, 2006.

[111] L. GAO and T. J. MCCARTHY, "\"Artificial Lotus Leaf\" Prepared Using a 1945 Patent and a Commercial Textile," *Langmuir*, vol. 22, pp. 5998-6000, 2006.

[112] W. STOEBER, A. FINK, and E. BOHN, "Controlled growth of monodisperse silica spheres in the micron size range," *Journal of Colloid and Interface Science*, vol. 26, pp. 62-9, 1968.

[113] G. H. BOGUSH, M. A. TRACY, and C. F. I. ZUKOSKI, "Preparation of monodisperse silica particles: control of size and mass fraction," *Journal of Non-Crystalline Solids*, vol. 104, pp. 95-106, 1988.

[114] M. ISHII, H. NAKAMURA, H. NAKANO, A. TSUKIGASE, and M. HARADA, "Large-Domain Colloidal Crystal Films Fabricated Using a Fluidic Cell," *Langmuir*, vol. 21, pp. 5367-5371, 2005.

[115] Y. YIN and Y. XIA, "Growth of large colloidal crystals with their (100) planes oriented parallel to the surfaces of supporting substrates," *Advanced Materials (Weinheim, Germany)*, vol. 14, pp. 605-608, 2002.

[116] N. DENKOV, O. VELEV, P. KRALCHEVSKI, I. IVANOV, H. YOSHIMURA, and K. NAGAYAMA, "Mechanism of formation of two-dimensional crystals from latex particles on substrates," *Langmuir*, vol. 8, pp. 3183-90, 1992.

[117] S. MAENOSONO, C. D. DUSHKIN, Y. YAMAGUCHI, K. NAGAYAMA, and Y. TSUJI, "Effect of growth conditions on the structure of two-dimensional latex crystals: modeling," *Colloid and Polymer Science*, vol. 277, pp. 1152-1161, 1999.

[118] Y. A. VLASOV, X.-Z. BO, J. C. STURM, and D. J. NORRIS, "On-chip natural assembly of silicon photonic bandgap crystals," *Nature (London, United Kingdom)*, vol. 414, pp. 289-293, 2001.

[119] H. NAKAE, R. INUI, Y. HIRATA, and H. SAITO, "Effects of surface roughness on wettability," *Acta Materialia*, vol. 46, pp. 2313-2318, 1998.

[120] J. L. ZHANG, W. H. HUANG, and Y. C. HAN, "Wettability of zinc oxide surfaces with controllable structures," *Langmuir*, vol. 22, pp. 2946-2950, 2006.

[121] W. CHEN, A. Y. FADEEV, M. C. HSIEH, D. OENER, J. YOUNGBLOOD, and T. J. MCCARTHY, "Ultrahydrophobic and Ultralyophobic Surfaces: Some Comments and Examples," *Langmuir*, vol. 15, pp. 3395-3399, 1999.

[122] D. OENER and T. J. MCCARTHY, "Ultrahydrophobic Surfaces. Effects of Topography Length Scales on Wettability," *Langmuir*, vol. 16, pp. 7777-7782, 2000.

[123] Y. G. CHUSHAK and L. S. BARTELL, "Melting and Freezing of Gold Nanoclusters," *Journal of Physical Chemistry B*, vol. 105, pp. 11605-11614, 2001.

[124] K. KOGA, T. IKESHOJI, and K.-I. SUGAWARA, "Size- and temperature-dependent structural transitions in gold nanoparticles," *Physical Review Letters*, vol. 92, pp. 115507/1-115507/4, 2004.

[125] W. BARTHLOTT and C. NEINHUIS, "Purity of the sacred lotus, or escape from contamination in biological surfaces," *Planta*, vol. 202, pp. 1-8, 1997.

[126] C. NEINHUIS, K. KOCH, and W. BARTHLOTT, "Movement and regeneration of epicuticular waxes through plant cuticles," *Planta*, vol. 213, pp. 427-434, 2001.

[127] B. BHUSHAN and Y. C. JUNG, "Micro- and nanoscale characterization of hydrophobic and hydrophilic leaf surfaces," *Nanotechnology*, vol. 17, pp. 2758-2772, 2006.

[128] C. COTTIN-BIZONNE, J.-L. BARRAT, L. BOCQUET, and E. CHARLAIX, "Low-friction flows of liquid at nanopatterned interfaces," *Nat. Mater.*, vol. 2, pp. 237-240, 2003.

[129] S. T. WANG, L. FENG, and L. JIANG, "One-step solution-immersion process for the fabrication of stable bionic superhydrophobic surfaces," *Adv. Mater.*, vol. 18, pp. 767-+, 2006.

[130] S. CHATTOPADHYAY, X. L. LI, and P. W. BOHN, "In-plane control of morphology and tunable photoluminescence in porous silicon produced by metal-assisted electroless chemical etching," *J Appl Phys*, vol. 91, pp. 6134-6140, 2002.

[131] P. CAMPBELL and M. A. GREEN, "Light Trapping Properties of Pyramidally Textured Surfaces," *J Appl Phys*, vol. 62, pp. 243-249, 1987.

[132] S. KOYNOV, M. S. BRANDT, and M. STUTZMANN, "Black nonreflecting silicon surfaces for solar cells," *Appl Phys Lett*, vol. 88, pp. -, 2006.

[133] A. LAFUMA and D. QUERE, "Superhydrophobic states," *Nat. Mater.*, vol. 2, pp. 457-460, 2003.

[134] X. F. GAO, X. YAO, and L. JIANG, "Effects of rugged nanoprotrusions on the surface hydrophobicity and water adhesion of anisotropic micropatterns," *Langmuir*, vol. 23, pp. 4886-4891, 2007.

[135] Y. M. ZHENG, X. F. GAO, and L. JIANG, "Directional adhesion of superhydrophobic butterfly wings," *Soft Matter*, vol. 3, pp. 178-182, 2007.

[136] L. BARBIERI, E. WAGNER, and P. HOFFMANN, "Water wetting transition parameters of perfluorinated substrates with periodically distributed flat-top microscale obstacles," *Langmuir*, vol. 23, pp. 1723-1734, 2007.

[137] E. BORMASHENKO, R. POGREB, G. WHYMAN, and M. ERLICH, "Cassie-Wenzel Wetting Transition in Vibrating Drops Deposited on Rough Surfaces: Is the Dynamic Cassie-Wenzel Wetting Transition a 2D or 1D Affair?," *Langmuir*, vol. 23, pp. 6501-6503, 2007.

[138] X. LI and P. W. BOHN, "Metal-assisted chemical etching in HF/H2O2 produces porous silicon," *Appl Phys Lett*, vol. 77, pp. 2572-2574, 2000.

[139] Y. TSORI, "Discontinuous liquid rise in capillaries with varying cross-sections," *Langmuir*, vol. 22, pp. 8860-8863, 2006.

[140] D. QUERE, "Surface chemistry - Fakir droplets," *Nat. Mater.*, vol. 1, pp. 14-15, 2002.

[141] C. G. FURMIDGE, "Studies at Phase Interfaces .1. Sliding of Liquid Drops on Solid Surfaces and a Theory for Spray Retention," *J Coll Sci Imp U Tok*, vol. 17, pp. 309-&, 1962.

[142] R. N. WENZEL, "Surface Roughness and Contact angle," *J. Phys. Colloid Chem.*, vol. 53, pp. 1466-1467, 1949.

[143] C. W. EXTRAND, "Model for contact angles and hysteresis on rough and ultraphobic surfaces," *Langmuir*, vol. 18, pp. 7991-7999, 2002.

[144] M. NOSONOVSKY and B. BHUSHAN, "Biomimetic superhydrophobic surfaces: Multiscale approach," *Nano Lett.*, vol. 7, pp. 2633-2637, 2007.

[145] D. QUERE, "Rough ideas on wetting," *Physica a-Statistical Mechanics and Its Applications*, vol. 313, pp. 32-46, 2002.

[146] M. NOSONOVSKY, "Multiscale roughness and stability of superhydrophobic biomimetic interfaces," *Langmuir*, vol. 23, pp. 3157-3161, 2007.

[147] S. A. MCAULEY, H. ASHRAF, L. ATABO, A. CHAMBERS, S. HALL, J. HOPKINS, and G. NICHOLLS, "Silicon micromachining using a high-density plasma source," *J Phys D Appl Phys*, vol. 34, pp. 2769-2774, 2001.

[148] L. C. GAO and T. J. MCCARTHY, "Contact angle hysteresis explained," *Langmuir*, vol. 22, pp. 6234-6237, 2006.

[149] A. W. G. ADAMSON, ALICE P., *Physical chemistry of surfaces*, 6th ed, 1997.

[150] W. LI and A. AMIRFAZLI, "A thermodynamic approach for determining the contact angle hysteresis for superhydrophobic surfaces," *J. Colloid Interface Sci.*, vol. 292, pp. 195-201, 2005.

[151] P. S. SWAIN and R. LIPOWSKY, "Contact angles on heterogeneous surfaces: A new look at Cassie's and Wenzel's laws," *Langmuir*, vol. 14, pp. 6772-6780, 1998.

[152] G. WOLANSKY and A. MARMUR, "The actual contact angle on a heterogeneous rough surface in three dimensions," *Langmuir*, vol. 14, pp. 5292-5297, 1998.

[153] A. W. NEUMANN, *Adv Colloid Interfac*, vol. 4, pp. 105, 1974.

[154] Y. XIU, L. ZHU, D. W. HESS, and C. P. WONG, "Hierarchical silicon etched structures for controlled hydrophobicity/superhydrophobicity," *Nano Lett.*, vol. 7, pp. 3388-3393, 2007.

[155] G. MCHALE, "Cassie and Wenzel: Were they really so wrong?," *Langmuir*, vol. 23, pp. 8200-8205, 2007.

[156] N. ANANTHARAJU, M. V. PANCHAGNULA, S. VEDANTAM, S. NETI, and S. TATIC-LUCIC, "Effect of three-phase contact line topology on dynamic contact angles on heterogeneous surfaces," *Langmuir*, vol. 23, pp. 11673-11676, 2007.

[157] J. GENZER and K. EFIMENKO, "Creating long-lived superhydrophobic polymer surfaces through mechanically assembled monolayers," *Science*, vol. 290, pp. 2130-2133, 2000.

[158] D. SCHONDELMAIER, S. CRAMM, R. KLINGELER, J. MORENZIN, C. ZILKENS, and W. EBERHARDT, "Orientation and self-assembly of hydrophobic fluoroalkylsilanes," *Langmuir*, vol. 18, pp. 6242-6245, 2002.

[159] Y. C. HONG and H. S. UHM, "Superhydrophobicity of a material made from multiwalled carbon nanotubes," *Appl. Phys. Lett.*, vol. 88, pp. 244101/1-244101/3, 2006.

[160] L. FENG, Z. L. YANG, J. ZHAI, Y. L. SONG, B. Q. LIN, Y. M. MA, Z. Z. YANG, L. JIANG, and D. B. ZHU, "Superhydrophobicity of nanostructured carbon films in a wide range of pH values," *Angew. Chem Int. Ed.*, vol. 42, pp. 4217-4220, 2003.

[161] J.-Y. SHIU, C.-W. KUO, P. CHEN, and C.-Y. MOU, "Fabrication of Tunable Superhydrophobic Surfaces by Nanosphere Lithography," *Chem Mater*, vol. 16, pp. 561-564, 2004.

[162] Y. REN, T. P. LODGE, and M. A. HILLMYER, "A simple and mild route to highly fluorinated model polymers," *Macromolecules*, vol. 34, pp. 4780-4787, 2001.

[163] P. FAVIA, G. CICALA, A. MILELLA, F. PALUMBO, R. ROSSINI, and R. D'AGOSTINO, "Deposition of super-hydrophobic fluorocarbon coatings in modulated RF glow discharges," *Surf. Coat. Technol.*, vol. 169, pp. 609-612, 2003.

[164] J. ZIMMERMANN, F. A. REIFLER, U. SCHRADE, G. R. J. ARTUS, and S. SEEGER, "Long term environmental durability of a superhydrophobic silicone nanofilament coating," *COLLOID SURFACE A*, vol. 302, pp. 234-240, 2007.

[165] J. ZIMMERMANN, G. R. J. ARTUS, and S. SEEGER, "Long term studies on the chemical stability of a superhydrophobic silicone nanofilament coating," *Appl. Surf. Sci.*, vol. 253, pp. 5972-5979, 2007.

[166] H. ZHANG, G. C. HARDY, Y. Z. KHIMYAK, M. J. ROSSEINSKY, and A. I. COOPER, "Synthesis of hierarchically porous silica and metal oxide beads using emulsion-templated polymer scaffolds," *Chem. Mater.*, vol. 16, pp. 4245-4256, 2004.

[167] J. L. GU, J. L. SHI, G. J. YOU, L. M. XIONG, S. X. QIAN, Z. L. HUA, and H. R. CHEN, "Incorporation of highly dispersed gold nanoparticles into the pore channels of mesoporous silica thin films and their ultrafast nonlinear optical response," *Adv. Mater.*, vol. 17, pp. 557-+, 2005.

[168] R. RICHER and L. MERCIER, "Direct synthesis of functional mesoporous silica by neutral pH nonionic surfactant assembly: Factors affecting framework structure and composition," *Chem Mater*, vol. 13, pp. 2999-3008, 2001.

[169] N. J. SHIRTCLIFFE, G. MCHALE, M. I. NEWTON, C. C. PERRY, and P. ROACH, "Superhydrophobic to superhydrophilic transitions of sol-gel films for temperature, alcohol or surfactant measurement," *Mater. Chem. Phys.*, vol. 103, pp. 112-117, 2007.

[170] Z. G. GUO, F. ZHOU, and W. M. LIU, "Preparation of biomimetic superhydrophobic silica film by sol-gel technique," *Acta Chimica Sinica*, vol. 64, pp. 761-766, 2006.

[171] J. SHIRTCLIFFE NEIL, G. MCHALE, I. NEWTON MICHAEL, C. PERRY CAROLE, and P. ROACH, "Porous materials show superhydrophobic to superhydrophilic switching," *Chemical communications (Cambridge, England)*, pp. 3135-7, 2005.

[172] S. PILOTEK and H. K. SCHMIDT, "Wettability of microstructured hydrophobic sol-gel coatings," *Journal of Sol-Gel Science and Technology*, vol. 26, pp. 789-792, 2003.

[173] A. V. RAO and M. M. KULKARNI, "Hydrophobic properties of TMOS/TMES-based silica aerogels," *Mater. Res. Bull.*, vol. 37, pp. 1667-1677, 2002.

[174] B. M. DEWITTE, D. COMMERS, and J. B. UYTTERHOEVEN, "Distribution of organic groups in silica gels prepared from organo-alkoxysilanes," *J Non-Cryst Solids*, vol. 202, pp. 35-41, 1996.

[175] N. D. HEGDE, H. HIRASHIMA, and A. V. RAO, "Two step sol-gel processing of TEOS based hydrophobic silica aerogels using trimethylethoxysilane as a co-precursor," *Journal of Porous Materials*, vol. 14, pp. 165-171, 2007.

[176] C. C. PERRY and X. C. LI, "Structural Studies of Gel Phases .1. Infrared Spectroscopic Study of Silica Monoliths - the Effect of Thermal History on Structure," *J Chem Soc Faraday T*, vol. 87, pp. 761-766, 1991.

[177] H. F. MARK, *Encyclopedia of polymer science and technology. Encyclopedia of polymer science and engineering*, 2nd Translator: Mark, H. F. Kroschwitz, Jacqueline I. ISBN: 0471895407 (v. 1) : Reprint Edition: 2nd Accession Number: ocm11158119 ed, 1985.

[178] W. L. HAWKINS, *Polymer stabilization. Edited by W. Lincoln Hawkins. City: New York, Publisher: Wiley-Interscience Number of Pages: viii, 452 p. Translator: Hawkins, W. Lincoln*, 1972.

[179] N. J. TURRO, *Modern molecular photochemistry*: University Science Books, 1991.

[180] A. B. D. CASSIE, "Contact Angles," *Disc. Faraday Soc.*, vol. 3, pp. 11-16, 1948.

[181] Y. XIU, L. ZHU, D. W. HESS, and C. P. WONG, "Relationship between Work of Adhesion and Contact Angle Hysteresis on Superhydrophobic Surfaces," *J. Phys. Chem. C*, vol. 112, pp. 11403-11407, 2008.

[182] A. NAKAJIMA, K. HASHIMOTO, T. WATANABE, K. TAKAI, G. YAMAUCHI, and A. FUJISHIMA, "Transparent superhydrophobic thin films with self-cleaning properties," *Langmuir*, vol. 16, pp. 7044-7047, 2000.

[183] G. GU, H. DANG, Z. ZHANG, and Z. WU, "Fabrication and characterization of transparent superhydrophobic thin films based on silica nanoparticles," *Appl. Phys. A-Mater.*, vol. 83, pp. 131-132, 2006.

[184] M. KEMELL, E. FARM, M. LESKELA, and M. RITALA, "Transparent superhydrophobic surfaces by self-assembly of hydrophobic monolayers on nanostructured surfaces," *Phys. Status Solidi, A Appl. Mater. Sci.*, vol. 203, pp. 1453-1458, 2006.

[185] K. TADANAGA, N. KATATA, and T. MINAMI, "Super-water-repellent Al2O3 coating films with high transparency," *J. Am. Ceram. Soc.*, vol. 80, pp. 1040-1042, 1997.

[186] J. BRAVO, L. ZHAI, Z. WU, R. E. COHEN, and M. F. RUBNER, "Transparent Superhydrophobic Films Based on Silica Nanoparticles," *Langmuir*, vol. 23, pp. 7293-7298, 2007.

[187] A. P. ABBOTT, G. CAPPER, D. L. DAVIES, and R. RASHEED, "Ionic Liquids Based upon Metal Halide/Substituted Quaternary Ammonium Salt Mixtures," *Inorg. Chem.*, vol. 43, pp. 3447-3452, 2004.

[188] A. P. ABBOTT, G. CAPPER, D. L. DAVIES, R. K. RASHEED, and V. TAMBYRAJAH, "Novel solvent properties of choline chloride/urea mixtures," *Chem. Comm.*, pp. 70-71, 2003.

[189] X. F. WU and G. Q. SHI, "Fabrication of a lotus-like micro-nanoscale binary structured surface and wettability modulation from superhydrophilic to superhydrophobic," *Nanotechnology*, vol. 16, pp. 2056-2060, 2005.

[190] Z.-G. GUO, F. ZHOU, J.-C. HAO, Y.-M. LIANG, W.-M. LIU, and W. T. S. HUCK, "\"Stick and slide\" ferrofluidic droplets on superhydrophobic surfaces," *Appl. Phys. Lett.*, vol. 89, pp. 081911/1-081911/3, 2006.

[191] Y. XIU, L. ZHU, D. W. HESS, and C. P. WONG, "Superhydrophobic durable silica thin films from sol-gel processing for the application in antistiction of MEMS devices," *Abstracts of Papers, 231st ACS National Meeting, Atlanta, GA, United States, March 26-30, 2006*, pp. IEC-196, 2006.

[192] A. DUPARRE, M. FLEMMING, J. STEINERT, and K. REIHS, "Optical coatings with enhanced roughness for ultrahydrophobic, low-scatter applications," *Appl. Opt.*, vol. 41, pp. 3294-3298, 2002.

[193] L. ZHU, Y. XIU, J. XU, D. W. HESS, and C. P. WONG, "Optimizing Geometrical Design of Superhydrophobic Surfaces for Prevention of Microelectromechanical System (MEMS) Stiction," presented at Electronic Components and Technology Conference, San Diego, CA, 2006.

[194] M. L. MA, Y. MAO, M. GUPTA, K. K. GLEASON, and G. C. RUTLEDGE, "Superhydrophobic fabrics produced by electrospinning and chemical vapor deposition," *Macromolecules*, vol. 38, pp. 9742-9748, 2005.

[195] L. ZHU, Y. XIU, J. XU, P. A. TAMIRISA, D. W. HESS, and C. P. WONG, "Superhydrophobicity on two-tier rough surfaces fabricated by controlled growth of aligned carbon nanotube arrays coated with fluorocarbon," *Langmuir*, vol. 21, pp. 11208-11212, 2005.

[196] T. SUN, G. J. WANG, H. LIU, L. FENG, L. JIANG, and D. B. ZHU, "Control over the wettability of an aligned carbon nanotube film," *J. Am. Chem. Soc.*, vol. 125, pp. 14996-14997, 2003.

[197] H. LIU, L. FENG, J. ZHAI, L. JIANG, and D. B. ZHU, "Reversible wettability of a chemical vapor deposition prepared ZnO film between superhydrophobicity and superhydrophilicity," *Langmuir*, vol. 20, pp. 5659-5661, 2004.

[198] J. C. LOVE, B. D. GATES, D. B. WOLFE, K. E. PAUL, and G. M. WHITESIDES, "Fabrication and wetting properties of metallic half-shells with submicron diameters," *Nano Lett.*, vol. 2, pp. 891-894, 2002.

[199] W. R. ASHURST, C. YAU, C. CARRARO, C. LEE, G. J. KLUTH, R. T. HOWE, and R. MABOUDIAN, "Alkene based monolayer films as anti-stiction coatings for polysilicon MEMS," *Sensor Actuat a-Phys*, vol. 91, pp. 239-248, 2001.

[200] C. H. MASTRANGELO and C. H. HSU, "Mechanical stability and adhesion of microstructures under capillary forces. II. Experiments," *Journal of Microelectromechanical Systems*, pp. 44-55, 1993.

[201] S. A. KULKARNI, S. A. MIRJI, A. B. MANDALE, and K. P. VIJAYAMOHANAN, "Thermal stability of self-assembled octadecyltrichlorosilane monolayers on planar and curved silica surfaces," *Thin Solid Films*, vol. 496, pp. 420-425, 2006.

[202] C. C. LEE and W. HSU, "Method on surface roughness modification to alleviate stiction of microstructures," *J Vac Sci Technol B*, vol. 21, pp. 1505-1510, 2003.

[203] Y. XIU, D. W. HESS, and C. P. WONG, "UV and thermally stable superhydrophobic coatings from sol-gel processing," *J. Colloid Interface Sci.*, vol. doi:10.1016/j.jcis.2008.06.042, 2008.

[204] Y. T. CHENG, D. E. RODAK, A. ANGELOPOULOS, and T. GACEK, "Microscopic observations of condensation of water on lotus leaves," *Appl. Phys. Lett.*, vol. 87, pp. -, 2005.

[205] W. CHEN, A. Y. FADEEV, M. C. HSIEH, D. ONER, J. YOUNGBLOOD, and T. J. MCCARTHY, "Ultrahydrophobic and ultralyophobic surfaces: Some comments and examples," *Langmuir*, vol. 15, pp. 3395-3399, 1999.

[206] B. BALU, V. BREEDVELD, and D. W. HESS, "Fabrication of "roll-off" and "sticky" superhydrophobic cellulose surfaces via plasma processing," *Langmuir*, vol. 24, pp. 4785-4790, 2008.

[207] D. QUERE, A. LAFUMA, and J. BICO, "Slippy and sticky microtextured solids," *Nanotechnology*, vol. 14, pp. 1109-1112, 2003.

[208] W. HAN, D. WU, W. MING, H. NIEMANTSVERDRIET, and P. C. THUENE, "Direct Catalytic Route to Superhydrophobic Polyethylene Films," *Langmuir*, vol. 22, pp. 7956-7959, 2006.

[209] M. H. JIN, X. J. FENG, L. FENG, T. L. SUN, J. ZHAI, T. J. LI, and L. JIANG, "Superhydrophobic aligned polystyrene nanotube films with high adhesive force," *Adv. Mater.*, vol. 17, pp. 1977-1981, 2005.

[210] J. JI, J. FU, and J. SHEN, "Fabrication of a superhydrophobic surface from the amplified exponential growth of a multilayer," *Advanced Materials (Weinheim, Germany)*, vol. 18, pp. 1441-1444, 2006.

[211] A. CAO, L. CAO, and D. GAO, "Fabrication of nonaging superhydrophobic surfaces by packing flowerlike hematite particles," *Appl. Phys. Lett.*, vol. 91, pp. 034102/1-034102/3, 2007.

[212] M. LI, J. ZHAI, H. LIU, Y. SONG, L. JIANG, and D. ZHU, "Electrochemical Deposition of Conductive Superhydrophobic Zinc Oxide Thin Films," *J. Phys. Chem. B*, vol. 107, pp. 9954-9957, 2003.

[213] A. MAHDAVI, L. FERREIRA, C. SUNDBACK, J. W. NICHOL, E. P. CHAN, D. J. D. CARTER, C. J. BETTINGER, S. PATANAVANICH, L. CHIGNOZHA, E. BEN-JOSEPH, A. GALAKATOS, H. PRYOR, I. POMERANTSEVA, P. T. MASIAKOS, W. FAQUIN, A. ZUMBUEHL, S. HONG, J. BORENSTEIN, J. VACANTI, R. LANGER, and J. M. KARP, "A biodegradable and biocompatible gecko-inspired tissue adhesive," *Proc. Natl. Acad. Sci. U. S. A.*, vol. 105, pp. 2307-2312, 2008.

[214] J. X. WANG, Y. Q. WEN, X. J. FENG, Y. L. SONG, and L. JIANG, "Control over the wettability of colloidal crystal films by assembly temperature," *Macromol. Rapid Comm.*, vol. 27, pp. 188-192, 2006.

[215] P. H. TUNG, S. W. KUO, K. U. JEONG, S. Z. D. CHENG, C. F. HUANG, and F. C. CHANG, "Formation of honeycomb structures and superhydrophobic surfaces by casting a block copolymer from selective solvent mixtures," *Macromol. Rapid Comm.*, vol. 28, pp. 271-275, 2007.

[216] T. BALDACCHINI, J. E. CAREY, M. ZHOU, and E. MAZUR, "Superhydrophobic surfaces prepared by microstructuring of silicon using a femtosecond laser," *Langmuir*, vol. 22, pp. 4917-4919, 2006.

[217] M. F. WANG, N. RAGHUNATHAN, and B. ZIAIE, "A nonlithographic top-down electrochemical approach for creating hierarchical (micro-nano) superhydrophobic silicon surfaces," *Langmuir*, vol. 23, pp. 2300-2303, 2007.

[218] M. W. CAO, X. Y. SONG, J. ZHAI, J. B. WANG, and Y. L. WANG, "Fabrication of highly antireflective silicon surfaces with superhydrophobicity," *J. Phys. Chem. B*, vol. 110, pp. 13072-13075, 2006.

[219] N. VERPLANCK, E. GALOPIN, J. C. CAMART, V. THOMY, Y. COFFINIER, and R. BOUKHERROUB, "Reversible electrowetting on superhydrophobic silicon nanowires," *Nano Lett.*, vol. 7, pp. 813-817, 2007.

[220] B. KRASOVITSKI and A. MARMUR, "Drops down the hill: Theoretical study of limiting contact angles and the hysteresis range on a tilted plate," *Langmuir*, vol. 21, pp. 3881-3885, 2005.

[221] S. HERMINGHAUS, "Roughness-induced non-wetting," *Europhys. Lett.*, vol. 52, pp. 165-170, 2000.

[222] A. PATANKAR NEELESH, "Mimicking the lotus effect: influence of double roughness structures and slender pillars," *Langmuir : the ACS journal of surfaces and colloids*, vol. 20, pp. 8209-13, 2004.

[223] K. W. KOLASINSKI, "Silicon nanostructures from electroless electrochemical etching," *Curr Opin Solid St M*, vol. 9, pp. 73-83, 2005.

[224] K. Q. PENG, Y. XU, Y. WU, Y. J. YAN, S. T. LEE, and J. ZHU, "Aligned single-crystalline Si nanowire arrays for photovoltaic applications," *Small*, vol. 1, pp. 1062-1067, 2005.

[225] S. KOYNOV, M. S. BRANDT, and M. STUTZMANN, "Black multi-crystalline silicon solar cells," *Phys Status Solidi-R*, vol. 1, pp. R53-R55, 2007.

[226] M. A. GREEN, *Solar cells : operating principles, technology, and system applications*. Kensington, NSW: University of New South Wales, 1998.

[227] R. BLOSSEY, "Self-cleaning surfaces - virtual realities," *Nat. Mater.*, vol. 2, pp. 301-306, 2003.

[228] K. S. LIU, M. L. ZHANG, J. ZHAI, J. WANG, and L. JIANG, "Bioinspired construction of Mg-Li alloys surfaces with stable superhydrophobicity and improved corrosion resistance," *Appl. Phys. Lett.*, vol. 92, pp. -, 2008.

[229] F. Z. ZHANG, L. L. ZHAO, H. Y. CHEN, S. L. XU, D. G. EVANS, and X. DUAN, "Corrosion resistance of superhydrophobic layered double hydroxide films on aluminum," *Angew. Chem Int. Ed.*, vol. 47, pp. 2466-2469, 2008.

[230] P. M. BARKHUDAROV, P. B. SHAH, E. B. WATKINS, D. A. DOSHI, C. J. BRINKER, and J. MAJEWSKI, "Corrosion inhibition using superhydrophobic films," *Corros. Sci.*, vol. 50, pp. 897-902, 2008.

[231] C. COTTIN-BIZONNE, J. L. BARRAT, L. BOCQUET, and E. CHARLAIX, "Low-friction flows of liquid at nanopatterned interfaces," *Nat. Mater.*, vol. 2, pp. 237-240, 2003.

[232] Y. XIU, D. W. HESS, and C. P. WONG, "UV and Thermally Stable Superhydrophobic Coatings from Sol-Gel Processing," *J. Colloid Interface Sci.*, vol. 326, pp. 465-470, 2008.

[233] X. H. ZHOU, G. L. CUI, L. J. ZHI, and S. S. ZHANG, "Large-area helical carbon microcoils with superhydrophobicity over a wide range of pH values," *New Carbon Materials*, vol. 22, pp. 1-6, 2007.

[234] X. Q. FENG, X. F. GAO, Z. N. WU, L. JIANG, and Q. S. ZHENG, "Superior water repellency of water strider legs with hierarchical structures: Experiments and analysis," *Langmuir*, vol. 23, pp. 4892-4896, 2007.

[235] W. LI and A. AMIRFAZLI, "Hierarchical structures for natural superhydrophobic surfaces," *Soft Matter*, vol. 4, pp. 462-466, 2008.

[236] C. W. EXTRAND, "Modeling of ultralyophobicity: Suspension of liquid drops by a single asperity," *Langmuir*, vol. 21, pp. 10370-10374, 2005.

[237] N. A. PATANKAR, "Mimicking the lotus effect: Influence of double roughness structures and slender pillars," *Langmuir*, vol. 20, pp. 8209-8213, 2004.

[238] M. N. WHYATT, J. D. STOKER, M. E. HINTON, and S. DAY, "High voltage electrical insulation material," U. S. Patent, Ed. USA: Tyco Electronics, 2003, pp. 8.

[239] E. P. EVERAERT, H. C. VANDERMEI, J. DEVRIES, and H. J. BUSSCHER, "Hydrophobic Recovery of Repeatedly Plasma-Treated Silicone-Rubber .1. Storage in Air," *Journal of Adhesion Science and Technology*, vol. 9, pp. 1263-1278, 1995.

[240] E. P. EVERAERT, H. C. VANDERMEI, and H. J. BUSSCHER, "Hydrophobic recovery of repeatedly plasma-treated silicone rubber .2. A comparison of the hydrophobic recovery in air, water, or liquid nitrogen," *Journal of Adhesion Science and Technology*, vol. 10, pp. 351-359, 1996.

[241] C. J. BRINKER and G. W. SCHERER, *Sol-gel science : the physics and chemistry of sol-gel processing*, 1990.

[242] W. STÖBER, A. FINK, and E. BOHN, "Controlled growth of monodisperse silica spheres in the micron size range," *J. Colloid Interface Sci.*, vol. 26, pp. 62-9, 1968.

[243] S. EIDEN-ASSMANN, J. WIDONIAK, and G. MARET, "Synthesis and characterization of porous and nonporous monodisperse colloidal TiO2 particles," *Chem. Mater.*, vol. 16, pp. 6-11, 2004.

[244] M. J. WANG, K. M. LIECHTI, Q. WANG, and J. M. WHITE, "Self-assembled silane monolayers: Fabrication with nanoscale uniformity," *Langmuir*, vol. 21, pp. 1848-1857, 2005.

[245] A. KAWAI and J. KAWAKAMI, "Characterization of SiO2 surface treated by HMDS vapor and O-2 plasma with AFM tip," *Journal of Photopolymer Science and Technology*, vol. 16, pp. 665-668, 2003.

[246] A. MACCARINI, M. HIMMELHAUS, S. STOYCHEVA, and M. GRUNZE, "Characterisation and stability of hydrophobic surfaces in water," *Appl. Surf. Sci.*, vol. 252, pp. 1941-1946, 2005.

[247] T. YAMADA, T. INOUE, K. YAMADA, N. TAKANO, T. OSAKA, H. HARADA, K. NISHIYAMA, and I. TANIGUCHI, "Detection of C-Si covalent bond in CH3 adsorbate formed by chemical reaction of CH3MgBr and H : Si(111)," *Journal of the American Chemical Society*, vol. 125, pp. 8039-8042, 2003.

[248] W. J. ROYEA, A. JUANG, and N. S. LEWIS, "Preparation of air-stable, low recombination velocity Si(111) surfaces through alkyl termination," *Appl Phys Lett*, vol. 77, pp. 1988-1990, 2000.

[249] E. J. NEMANICK, P. T. HURLEY, L. J. WEBB, D. W. KNAPP, D. J. MICHALAK, B. S. BRUNSCHWIG, and N. S. LEWIS, "Chemical and electrical

passivation of single-crystal silicon(100) surfaces through a two-step chlorination/alkylation process," *J Phys Chem B*, vol. 110, pp. 14770-14778, 2006.

[250] J. C. HO, R. YERUSHALMI, Z. A. JACOBSON, Z. FAN, R. L. ALLEY, and A. JAVEY, "Controlled Nanoscale Doping of Semiconductors Via Molecular Monolayers," *Nature Materials*, vol. 7, pp. 62-67, 2008.

RELATED PUBLICATIONS

Journal papers

1. Y. Xiu, Fei Xiao, D. W. Hess, C. P. Wong, “Superhydrophobic Optically Transparent Silica Films Formed with a Eutectic Liquid”, Thin Solid Films, in press.
2. Y. Xiu, D. W. Hess, C. P. Wong, “UV and Thermally Stable Superhydrophobic Coatings from Sol-Gel Processing”, Journal of colloid and Interface Science, vol. 326, (2) 465-470.
3. Y. Xiu, Shu Zhang, Vijay Yelundur, Ajeet Rohatgi, Dennis. W. Hess, C. P. Wong, “Superhydrophobic and Low Light Reflectivity Silicon Surfaces Fabricated by Hierarchical Etching”, Langmuir, 2008, 10421-10426.
4. Y. Xiu, D. W. Hess, C. P. Wong, “UV Resistant and Superhydrophobic Self-Cleaning Surfaces Using Sol-Gel Processes”, Journal of Adhesion Science and Technology, in press.
5. Y. Xiu, Lingbo Zhu, Dennis W. Hess, C. P. Wong, “Sol-Gel Derived Superhydrophobic Silica Thin Films for Antistiction of MEMS Devices”, Microelectronics Reliability, in press.
6. Y. Xiu, L. Zhu, D. W. Hess, C. P. Wong, “Relationship between Work of Adhesion and Contact Angle Hysteresis on Superhydrophobic Surfaces”, Journal of Physical Chemistry C, 2008, 112, 11403-11407.
7. Y. Xiu, Lingbo Zhu, Dennis W. Hess, C. P. Wong, “Hierarchical silicon etched structures for controlled hydrophobicity/superhydrophobicity”, Nano Letters. 2007, 7(11), 3388-3393.
8. Y. Xiu, L. Zhu, D. W. Hess, C. P. Wong, “Biomimetic Creation of Hierarchical Surface Structures by Combining Colloidal Self-Assembly and Au Sputter Deposition” Langmuir, 2006, 22, p. 9676-9681.

Collaborated Journal Papers

9. Y. Ding, S. Xu, Y. Zhang, A. C. Wang, M. H. Wang, Y. Xiu, C. P. Wong, Z. L. Wang, Nanotechnology 19, 355708/1-7(2008)
10. F. Xiao, Y. Sun, Y. Xiu, and C. P. Wong, "Preparation, thermal and mechanical properties of POSS epoxy hybrid composites," Journal of Applied Polymer Science, vol. 104, pp. 2113-2121, 2007.
11. L. Zhu, J. Xu, Y. Xiu, Y. Sun, D. W. Hess, and C. P. Wong, "Electrowetting of

Aligned Carbon Nanotube Films," Journal of Physical Chemistry B, vol. 110, pp. 15945-15950, 2006.

12. L. Zhu, J. Xu, Y. Xiu, Y. Sun, D. Hess, and C. P. Wong, "Growth and Electrical Characterization of High Aspect-Ratio Aligned Carbon Nanotube Arrays," Carbon, vol. 44, pp. 253-258, 2006.

13. L. Zhu, J. Xu, Y. Xiu, D. Hess, and C. P. Wong, "A Rapid Growth of Aligned Carbon Nanotube Films and High-Aspect-Ratio Arrays," Journal of Electronic Materials, vol. 35, pp. 195-199, 2006.

14. W. Lin, Y. Xiu, H. Jiang, R. Zhang, O. Hildreth, K. S. Moon, C. P. Wong, "Self-Assembled Monolayer-Assisted Chemical Transfer of In Situ Functionalized Carbon Nanotubes", Journal of the American Chemical Society (2008), 130(30), 9636-9637.

15. L. Zhu, Y. Xiu, D. Hess, and C. P. Wong, "Aligned Carbon Nanotube Stacks by Water-Assisted Selective Etching," Nano Letters, vol. 5, pp. 2641-2645, 2005.

16. L. Zhu, Y. Xiu, J. Xu, P. A. Tamirisa, D. W. Hess, and C. P. Wong, "Superhydrophobicity on Two-Tier Rough Surfaces Fabricated by Controlled Growth of Aligned Carbon Nanotube Arrays Coated with Fluorocarbon," Langmuir, vol. 21, pp. 11208-11212, 2005.

Patent and Invention Disclosures

1. Y. Xiu, Jack K. Moon, C. P. Wong, "Abrasion Resistant Superhydrophobic Coatings via the Combination of Epoxy and Inorganic Nanoparticles", US provisional patent, serial No.: 61/100,863, Sept. 29, 2008.

2. Y. Xiu, L. Zhu, F. Xiao, D. W. Hess, C. P. Wong, N. Hampton, F. Lambert, "Superhydrophobic Surface and Method for Forming Same", US patent, Serial No.: 11/610,111, Filing Date: December 13, 2006.

3. Y. Xiu, L. Zhu, F. Xiao, D. W. Hess, C. P. Wong, N. Hampton, F. Lambert, "Superhydrophobic Surface And Method For Forming Same", WO/2007/126432.

4. Y. Xiu, Jack K. Moon, C. P. Wong, "Abrasion Resistant Superhydrophobic Coatings via the Combination of Epoxy and Inorganic Nanoparticles", GT Invention Disclosure ID 4306, Georgia Institute of Technology, 2007.

5. Y. Xiu, L. Zhu, N. Hampton, F. Lambert, C.P. Wong, "Multi-Modal Size Distribution Superhydrophobic Surface", GT Invention Disclosure ID 3846, Georgia Institute of Technology, 2006.

6. Y. Xiu, L. Zhu, N. Hampton, F. Lambert, Dennis W. Hess, C.P. Wong, "Multi Species Superhydrophobic Surface", GT Invention Disclosure ID 3847, Georgia Institute of

Technology, 2006.

7. Y. Xiu, L. Zhu, N. Hampton, F. Lambert, Dennis W. Hess, C.P. Wong, “Post Treatment with Coupling Agent to Manufacture Superhydrophobic Surface” GT Invention Disclosure ID 3848, Georgia Institute of Technology, 2006.

8. Y. Xiu, L. Zhu, N. Hampton, F. Lambert, Dennis W. Hess, C.P. Wong, “Transparent Superhydrophobic Self-Cleaning and UV Resistant Coatings”. GT Invention Disclosure ID 3928, Georgia Institute of Technology, 2006.

Proceedings and Presentations

1. Y. Xiu, L. Zhu; Dennis, W. Hess, C. P. Wong., “Superhydrophobic Silica Thin Films Prepare by Sol-Gel Process for Antistiction of MEMS Devices” High Density packaging and Microsystem Integration, 2007. HDP '07. International Symposium on 26-28 June 2007 Page(s):1 – 5.

2. Y. Xiu, L. Zhu; Dennis, K. S. Moon, W. Hess, C. P. Wong., “Eutectic liquid in Sol-Gel process for superhydrophobic silica thin films - antistiction of MEMS devices” Advanced Packaging Materials: Processes, Properties, and Interfaces, 2007. APM 2007. 12th International Symposium on 3-5 Oct. 2007 Page(s):172 - 179

3. Y. Xiu, L. Zhu; Dennis, W. Hess, C. P. Wong., “Sol-gel process derived superhydrophobic silica thin films for antistiction of MEMS devices”, Materials Research Society Symposium Proceedings, 2007, 990(Materials, Processes, Integration and Reliability in Advanced Interconnects for Micro- and Nanoelectronics), 303-311.

4. Y. Xiu, L. Zhu, D. W. Hess, C. P. Wong, "Preparation of Superhydrophobic Silica Thin Films From a Novel Sol-Gel Processing for the Application in Antistiction of MEMS devices” Proceedings of 57th IEEE Electronic Components and Technology Conference, Reno, Nevada, May 29- June 1, p.1135-1142 (2007).

5. Y. Xiu, Dennis, W. Hess, C. P. Wong., A Novel Method to Prepare Superhydrophobic, Self-Cleaning and Transparent Coatings for Biomedical Applications Electronic Components and Technology Conference, 2007. ECTC '07. Proceedings. 57th May 29 2007-June 1 2007 Page(s):1218 – 1223.

6. Y. Xiu, L. Zhu, D. W. Hess, C. P. Wong, “Superhydrophobic Silicone/PTFE Films for Biocompatible Applications in Encapsulation of Implantable Microelectronics Devices” in Proceedings of 56th IEEE Electronic Components and Technology Conference. San Diego, CA. May30- June 2, 2006, pp. 686-692.

7. L. Zhu, Y. Xiu, J. Xu, D. W. Hess, and C. P. Wong, "Optimizing Geometrical Design of Superhydrophobic Surfaces for Prevention of Microelectromechanical System (MEMS) Stiction," presented at Electronic Components and Technology Conference, San Diego, CA, 2006.

8. Y. Xiu, L. Zhu, D. W. Hess, and C. P. Wong, "Superhydrophobic durable silica thin films from sol-gel processing for the application in antistiction of MEMS devices," Abstracts of Papers, 231st ACS National Meeting, Atlanta, GA, United States, March 26-30, 2006, pp. IEC-196, 2006.

9. Y. Xiu, L. Zhu, D. Hess, and C. P. Wong, "Superhydrophobicity and UV stability of polydimethylsiloxane/polytetrafluoroethylene (PDMS/PTFE) coatings," IEEE CPMT International Symposium and Exhibition on Advanced Packaging Materials: Processes, Properties and Interfaces, 11th, Atlanta, GA, United States, Mar. 15-17, 2006, pp. 98-103, 2006.

10. Y. Xiu, L. Zhu, D. W. Hess, and C. P. Wong, "Superhydrophobic Durable Self-Cleaning Surfaces from sol-gel processing," presented at Strategic Energy Initiative (Sei) Energy Research Exposition, Atlanta, 2006.

11. B. C. Englert, Y. Xiu, and C. P. Wong, "Deposition and surface treatment of microparticles to produce lotus-effect surface," IEEE CPMT International Symposium and Exhibition on Advanced Packaging Materials: Processes, Properties and Interfaces, 11th, Atlanta, GA, United States, Mar. 15-17, 2006, pp. 73-78, 2006.

12. L. Zhu, Y. Xiu, J. Xu, D. W. Hess, and C. P. Wong, "Optimizing geometrical design of superhydrophobic surfaces for prevention of microelectromechanical system (MEMS) stiction," Proceedings - Electronic Components & Technology Conference, vol. 56th, pp. 1129-1135, 2006.

13. L. Zhu, J. Xu, Y. Xiu, D. W. Hess, and C. P. Wong, "Controlled Growth of Well-aligned Carbon Nanotubes and Their Assembly," presented at IEEE CMPT International Symposium and Exhibition on Advanced Packaging Material, Atlanta, GA, 2006. Advanced Packaging Materials: Processes, Properties and Interface, 200611th International Symposium on 15-17 March 2006 Page(s):123 – 127.

14. L. Zhu, Y. Xiu, D. Hess, and C. P. Wong, "Growth of Aligned Carbon Nanotube Arrays for Electrical Interconnect," presented at 7th Electronics Packaging Technology Conference, Singapore, 2005.

15. Y. Xiu, L. Zhu, D. Hess, and C. P. Wong, "Coprecursor Method to Make Superhydrophobic Durable Self-Cleaning Silica Surfaces," presented at 7th Electronics Packaging Technology Conference, Singapore, 2005.